

**UNIVERSIDADE DE LISBOA**  
**INSTITUTO SUPERIOR TÉCNICO**

Controlled plasma wakefield acceleration for particle acceleration  
towards the energy frontier

Lígia Diana Pinto de Almeida Amorim

**Supervisor:** Doctor Jorge Miguel Ramos Domingues Ferreira Vieira

**Co-Supervisor:** Doctor Luís Miguel de Oliveira e Silva

**Thesis approved in public session to obtain the PhD Degree in  
Technological Physics Engineering**

**Jury final classification: Pass with Distinction**

**Jury**

**Chairperson:** Doctor Luís Paulo da Mota Capitão Lemos Alves, Instituto Superior Técnico, Universidade de Lisboa

**Members of the Committee:**

Doctor Robert Bingham, Faculty of Science, University of Strathclyde, Glasgow, UK

Doctor Patric Muggli, Max-Planck-Institut für Physik, Germany

Doctor João Pedro Saraiva Bizarro, Instituto Superior Técnico, Universidade de Lisboa

Doctor Jorge Miguel Ramos Domingues Ferreira Vieira, Instituto Superior Técnico, Universidade de Lisboa

**Funding Institutions - Fundação para a Ciência e Tecnologia and EuPRAXIA European project**



***"Whenever we proceed from the known into the unknown we may hope to understand, but we may have to learn at the same time a new meaning of the word "understanding."***

Werner Heisenberg

***"If I have seen further it is by standing on the shoulders of Giants."***

Isaac Newton

***"We can only see a short distance ahead, but we can see plenty there that needs to be done."***

Alan Turing

***"Better is the enemy of good."***

Voltaire / François-Marie Arouet

***"Melhor é experimentá-lo que julgá-lo,  
Mas julgue-o quem não pode experimentá-lo."***

Luís de Camões

***"Eles não sabem, nem sonham,  
que o sonho comanda a vida,  
que sempre que um homem sonha  
o mundo pula e avança  
como bola colorida  
entre as mãos de uma criança."***

Antônio Gedeão / Rómulo de Carvalho



# Acknowledgments

As a Ph.D student one of the main lessons I have learned is that all my results, discoveries and understandings of physical phenomena were the product of many questions, discussions held with and the teachings from every extraordinary scientist I crossed paths with not only here at IST - GoLP, but also at SLAC and UCLA and in all the conferences I attended. In this acknowledgments I try to do justice to all of those who contributed significantly to my research for the past years.

I am mostly indebted to my supervisor Dr. Jorge Vieira for the patience and persistence with which he introduced me to and thoroughly explained the fundamental concepts of my field of study. Not only his continuous guidance and positive criticism have shaped me into a more professional and efficient student, as his ambition and devotion have awakened my ever growing motivation and fascination for the topic of this Ph.D. work. I would like to thank my co-supervisor professor Luís Silva for his support and acceptance into the outstanding atmosphere and enlightening meetings shared at GoLP years ago.

For the first years of my Ph.D. studies I had the privilege of sharing my working hours, in an office with no windows, with my amazing and interesting colleagues, Paulo Ratinho, Dr. Elisabetta Boella, Dr. Gareth Williams, Axel Huebl, Andrea Ciraci, André Lopes and Fábio Cruz, who is currently hosting the young students: Rui Torres, Rui Calado, Lucas Sá and Mariana Moreira. My days there would not have been such an indulging supply of physics discussions without the great scientists Dr. Joana Martins, Dr. Paulo Alves, Dr. Kevin Schoeffler, Dr. Ujjwal Sinha, Dr. Thales Silva, Dr. Anne Stockhem, Dr. Bandhu Pathak, Dr. Timon Mehring, Dr. Thomas Grismayer, Dr. Marija Vranic and Pedro Carneiro. Furthermore, my lunch breaks at the student canteen would have not been the same without the fascinating Paulo Ratinho and our fellow MEFT students. I appreciate how professor Ricardo Fonseca showed me that being friendly teased does not necessarily stop once one is over high school, which is delightfully rejuvenating. I am grateful to have faced the time and challenges of this Ph.D. program in the company of soon to be Dr. Nitin Shukla, whom has been an admirable friend who never got tired of showing me the best Lisbon sights and restaurants.

I am thankful for being welcomed into the groups of Professors Warren Mori and Chan Joshi, during my one year stay at UCLA. Both professors, whom were responsible for the main and the initial development of our field of study, always dedicated their time and interest to teaching me with knowledge that was vital for me to tackle the new phenomena we were analyzing and to deepen and broaden my knowledge of the field. The exemplary professionalism and motivation of Dr. Weiming

An and Dr. Nuno Lemos, who supervised my work there, allied to: the fruitful interactions with the plasma simulation group, Thamine Dalichaouch, Dr. Fei Li, Dr. Asher Davidson, Dr. Peicheng Yu, Dr. Archis Joglekar, Dr. Michaël Touati, Dr. Paul-Quentin Elias, Dr. Xinlu Xu, Dr. Benjamin J. Winjum, Dr. Frank Tsung and Dr. Viktor Decyk; the collaboration with the hard-working 3rd floor lab, Chen-keng Huang, Dr. Jessica Shaw, Prof. Navid Vafaei-Najafabadi, Ken Marsh and the creativity of the Neptune lab, Eric Welch, Jeremy Pigeon and Dr. Sergei Tochitsky drove me to improve my own approach in science. My stay in Los Angeles during that time was a great experience, including the Friday pizza x-box matches with the plasma simulation group, the dinners with the 3rd floor and Neptun lab's and the very special, lovely, trip to Death Valley with the kind couple Betsy and Dr. Viktor Decyk.

In the first years of my Ph.D. I had the unique opportunity to participate in the E-209 experiment at FACET/SLAC, led by Dr. Patric Muggli and Dr. Jorge Vieira. That extraordinary experience was enriched by Dr. Patric Muggli and Dr. Navid Vafaei-Najafabadi teachings in not only plasma and laser physics, but also on subjects ranging from gastronomy to ethics for which I am profoundly thankful. The complications presented by each run time were solved by the combined team effort of mainly Dr. Patric, Dr. Jorge, Dr. Mark Hogan, Dr. Vitaly Yakimenko, Professor Eric Adli, Dr. Navid Vafaei-Najafabadi, Dr. Veronica Olsen, Dr. Christine Clarke, Dr. Mike Litos, Dr. Spencer Guessner, Dr. Sébastien Corde and Dr. Brendon D. O'Shean in a way that inspired the scientist in me.

My deepest gratitude goes to all the people who have accompanied me throughout life's highs and lows, work and fun, of these past years. To my inspiring and extraordinary family. In particular, to my brother for surprising me everyday with his admirable character and endless strength while being more than Sancho Pança is to Don Quixote to me. To my dad for teaching me *Voltaire's* saying that "o ótimo é inimigo do bom" and to my mom for making the 6 year old me study english even when I only aspired to becoming a single housewife. To my tough and kind sister and her conscious husband who were exploring their own fields of physics in Belgium but always just "an email away" from daring and encouraging me to push forward. To my dear cousins Tiago Fonseca, Mário Pinto de Almeida, Vandinha Sá Dias and Marco Robalo who also graduated (or are graduating) from IST. To the best young women, Inês F. Mota and Matilde Neves. To my companions of the working nights at IST, Ricardo Teixeira and Tiago Frederico and to my dearest school friends who've been there for me in many of my adventures, Gonçalo Forjaz, João Pinto, João Dias, Miguel Rebelo, Emanuel Pires, Joana Marques, Marta Forte, João Gil, João Lousada, David Laginha, Sofia Tully and Ricardo Magro.

## Computing resources

For all the numerical work done for this dissertation, the large multi dimensional parallel numerical codes ran on millions of cores that our research group was granted access to in the following international high performance computing clusters:

- Accelerates of the Extreme Plasma Physics group of the Institute of Plasmas and Nuclear Fusion, University of Lisbon, Portugal [1],
- Hoffman2 cluster of the Institute for Digital Research and Education of the University of California Los Angeles (University of California Los Angeles (UCLA) in California, United States [2],
- Fermi and Marconi at the Super Computing Applications and Innovation centre developed by the Cineca consortium in Bologna, Roma and Milano, Italy [3],
- SuperMuc Petascale system at the Leibniz Supercomputing centre of the Bavarian Academy of Sciences and Humanities in Garching, Germany [4] and
- Blue Waters Sustained Petascale Computing managed by the National Centre for Supercomputer Applications at the University of Illinois, United States [5].

## Grants

The work done for this dissertation would not have been possible without the support of the grants of the Fundação para a Ciência e Tecnologia SFRH/BD/84851/2012 and of the EuPRAXIA European project EuPRAXIA-GA No.653782.



# Abstract

The maximum energy with which elementary particle bunches collide at international scientific research laboratories is key to the progress of particle physics and astrophysics. Several techniques for particle acceleration are being explored as alternatives to the traditional devices, where material breakdown limits the maximum particle kinetic energy attainable. From those techniques, accelerators using plasmas to mediate the energy transfer are promising compact and affordable candidates.

This dissertation aims at describing the study of different plasma based electron and positron acceleration configurations resorting to numerical simulations done with the codes OSRIS, QuickPIC and the post-processing tool jRad to evaluate emitted radiation, and to experimental results from the collaborations with SLAC (E-209), CERN (AWAKE), LBNL (JLF) and UCLA.

In this work the regime in which a laser pulse is sent through the plasma driving a wake of electron density oscillations with electromagnetic fields capable of accelerating charged particles is analyzed. In particular, when the laser duration allows it to overlap and directly accelerate particles within the wake and to undergo the self-modulation instability, where each laser section is responsible for linearly intensifying the wakefields. The properties of the hard x-rays produced in these accelerating processes are examined.

Moreover, a proof-of-principle experimental and numerical study of the self-modulation of electron and positron beams in plasmas is also included in this dissertation. The obtained results highlighted the relevance of controlling the beam longitudinal profile, its rise time and front shape, for more efficient seeding of the instability.

To conclude, a novel configuration where a tightly focused positron bunch is able to excite the electron plasma wake as well as to repel the plasma ions forming a hollow channel is proposed and discussed. The main advantage being that positron bunches can propagate inside the channel without being subject to defocusing forces and jeopardizing their emittance.

## Keywords

Particle accelerators; Plasma accelerators; Laser pulses; Particle beams; Numerical simulations



# Resumo

A energia máxima com que partículas elementares colidem nos laboratórios de investigação científica é vital para os avanços da física de partículas e astrofísica. Por isso, várias técnicas de aceleração de partículas estão ser exploradas como alternativas aos dispositivos comuns, onde o risco de destruição dos materiais limita a aceleração máxima possível. Sendo as que utilizam plasmas para a transmissão da energia potenciais candidatas.

Serve a presente dissertação para descrever o estudo de diferentes configurações de aceleração de leptões em plasmas recorrendo a simulações numéricas com os códigos OSIRIS, QuickPIC e a ferramenta de processamento posterior que determina a radiação emitida, jRad, e às experiências do SLAC (E-209), CERN (AWAKE), LBNL (JLF) e UCLA.

Neste trabalho o regime em que um impulso de laser enviado pelo plasma origina uma esteira (ou rasto) de regiões com diferentes densidades de electrões com campos electromagnéticos capazes de acelerar partículas carregadas é analisado. O regime em que a largura do impulso é tal que o próprio campo do laser é sobreposto aos da esteira, contribuindo directamente para a aceleração e verificando a instabilidade de auto modelação, consoante o período do plasma. Examinámos a radiação de raios-x gerada ao longo dos processos de aceleração.

Esta dissertação inclui também o estudo, com base em simulações e numa experiência de teste, do conceito da ocorrência da instabilidade de auto modelação de feixes longos de electrões e positrões. Os resultados realçaram a necessidade do controle do perfil longitudinal, particularmente da forma da frente do feixe, para despoletar a instabilidade com maior eficiência.

Por fim, é proposta e desenvolvida numericamente e com base um modelo analítico uma configuração original em que um feixe de positrões estreito e com densidade suficiente cria uma esteira nos electrões e também um canal vazio nos iões do plasma. A propagação e aceleração de feixes de positrões nesse canal vazio é possível por longas distâncias sem comprometer as suas divergências.

## Palavras Chave

Aceleradores de partículas; Plasmas; Pulsos de laser; Feixes de partículas; Simulações numéricas



# Contents

<b>1 Introduction</b>	<b>1</b>
1.1 Brief history and applications of particle accelerators	2
1.1.1 The Plasma Wakefield Accelerator	4
1.2 Dissertation Outline	6
1.3 Original Contributions	6
1.3.1 Peer-reviewed publications	7
1.3.2 Published proceedings	8
1.3.3 Oral communications	9
1.3.4 Poster communications	9
<b>2 Overview of analytical background and numerical resources</b>	<b>11</b>
2.1 Plasma Wakefield Accelerator operating in the linear regime	12
2.2 Wakefields in the standard nonlinear bubble/blowout regime	17
2.3 Nonlinear plasma wakefield regime driven by a positron beam	20
2.4 Betatron radiation	23
2.5 Numerical infrastructures	24
2.5.1 Particle-In-Cell code OSIRIS 3.0 and 4.0	24
2.5.1.A Hybrid Particle-In-Cell and a girdles azimuthal description code version of OSIRIS Quasi-3D	26
2.5.2 QuickPIC and PGC	26
2.5.2.A Post processing radiation computing code - jRad	27
<b>3 Laser direct and indirect energy transfer in a wakefield accelerator scheme</b>	<b>29</b>
3.1 Process of Direct Laser Acceleration in non-linear plasma wakefields	31
3.1.1 Direct energy gain from the laser	32
3.2 Experimental investigation of the role of Direct Laser Acceleration	35
3.2.1 Laser apparatus	35
3.2.2 Plasma injector gas cell	37
3.2.3 Experimental results	37
3.3 Numerical analysis of the Direct Laser Acceleration signatures found in Laser Wakefield Acceleration experiments	39
3.3.1 OSIRIS 2D study	39

3.3.2 OSIRIS 3D simulations setup . . . . .	39
3.3.3 OSIRIS 3D simulations results . . . . .	41
3.4 X-ray emission from Direct Laser Acceleration in Plasma Wakefield accelerators . . . . .	66
3.5 Conclusions and future options . . . . .	72
<b>4 X-ray production in self modulated laser plasma wakefields</b>	<b>73</b>
4.1 Long laser pulse propagation in plasma wakes . . . . .	75
4.1.1 Laser pulse relativistic self-channeling . . . . .	79
4.2 Numerical study of long laser pulse propagation in plasmas . . . . .	81
4.3 Radiation from long laser plasma wakefield accelerator . . . . .	92
4.4 Experimental investigation of x-ray generation in the long laser wakefield setup . . . . .	92
4.5 Conclusions and future direction . . . . .	95
<b>5 Positron beam based Plasma Wakefield Acceleration in a self-driven Plasma Hollow</b>	
<b>Channel</b>	<b>97</b>
5.1 Analytical model for self-driven hollow channel wakefields . . . . .	100
5.1.1 Particle acceleration inside pre-formed plasma hollow channels . . . . .	100
5.1.2 Hollow channel formation by tightly focused positron bunches . . . . .	102
5.2 Simulations of the positron self-channeling accelerator . . . . .	105
5.2.1 Limits of the linear theory for positron acceleration inside a pre-formed channel . . . . .	105
5.2.2 Positron self-driven plasma hollow channel numerical results . . . . .	106
5.2.3 Preliminary results and future research directions . . . . .	110
5.2.3.A Beam loading in hollow channel linear to nonlinear electron wakes . . . . .	110
5.2.3.B Field mode excitation in the hollow channel by propagating azimuthal . . . . .	
modes 0 and 1 electron beam . . . . .	112
5.3 Concluding remarks . . . . .	112
<b>6 Proof-of-principle experiment and numerical investigation of the self-modulation of long</b>	
<b>lepton beams</b>	<b>115</b>
6.1 Self-modulation instability of long particle bunches propagating in plasmas . . . . .	117
6.2 Experimental setup of the self-modulation of lepton bunches at SLAC - FACET experi- . . . . .	
ment E-209 . . . . .	119
6.3 Numerical simulations of the positron acceleration . . . . .	121
6.3.1 Long lepton beams and plasma configuration . . . . .	123
6.4 Conclusions . . . . .	129
<b>7 Conclusions and Future Work</b>	<b>131</b>
<b>8 Appendix: State of the art laser and x-ray sources</b>	<b>135</b>
<b>Bibliography</b>	<b>139</b>

# List of Figures

2.1 Illustration of beam driven plasma wakefield scheme . . . . .	13
2.2 Illustration of a plasma wakefield scheme . . . . .	18
2.3 Nonlinear electron vs positron excitation of the plasma wake . . . . .	22
3.1 Laser Wakefield Acceleration configuration with Direct Laser Acceleration . . . . .	31
3.2 Experimental setup for Direct Laser Acceleration in the Laser Wakefield Accelerator . . . . .	36
3.3 Schematic of the Direct Laser Acceleration experimental configuration . . . . .	36
3.4 Experimental transverse electron spectra dispersed in the two orthogonal directions transverse to laser propagation . . . . .	38
3.5 Laser setups explored to understand the impact of Direct Laser Acceleration . . . . .	42
3.6 Helium and Nitrogen plasma density evolution in the wakefield of a 25fs laser pulse . . . . .	44
3.7 Helium and Nitrogen plasma density evolution in the wakefield of a 45fs laser pulse . . . . .	45
3.8 Helium and Nitrogen plasma density evolution in the wakefield of a 45fs laser pulse . . . . .	46
3.9 Helium and Nitrogen plasma density evolution in the wakefield of a plasma with higher density . . . . .	47
3.10 Helium and Nitrogen plasma density evolution in the wakefield of a plasma with highest density studied . . . . .	48
3.11 Nitrogen core electrons total charge evolution in the Direct Laser Acceleration of elec- trons in plasma wakefields (DLA) assisted Laser Wakefield Acceleration (LWFA) . . . . .	49
3.12 Accelerated Nitrogen core electrons final 3D density . . . . .	50
3.13 Final accelerated electron bunch charge as a function of the laser length to wake wa- velength ratio . . . . .	53
3.14 Numerical longitudinal laser driven plasma wakefield evolution . . . . .	55
3.15 Energy histogram of the simulated laser accelerated electrons . . . . .	56
3.16 Laser longitudinal wakefield acceleration contribution . . . . .	58
3.17 Laser transverse wakefield and direct acceleration contribution . . . . .	59
3.18 Simulated transverse position spectra in the directions orthogonal to laser propagation direction . . . . .	60
3.19 Simulated transverse position spectra for the laser pulse with circular polarization si- mulation . . . . .	61

3.20 Simulated transverse position spectra for the laser pulse with linear polarization simulations . . . . .	62
3.21 Simulated transverse position spectra for the laser pulse with circular polarization simulation . . . . .	63
3.22 Initial position of the trapped and followed electrons along the different simulations . . . . .	64
3.23 Direct Laser Acceleration resonance condition for a single trapped electron trajectory . . . . .	65
3.24 Radiation emitted by the 20 highest final energy electrons in the Laser Wakefield Accelerator . . . . .	68
3.25 Spectra of the radiation emitted by the 20 electrons in the laser polarization direction . . . . .	69
3.26 Spectra of the radiation emitted by the 20 electrons perpendicular to the laser polarization direction . . . . .	70
3.27 Radiation emitted by all the selected electrons in the Laser Wakefield Accelerator . . . . .	71
4.1 Illustration of a self-modulated and self-channeling laser plasma wakefield scheme . . . . .	80
4.2 Initial simulated electron/ion density, laser electric field and electron phase space . . . . .	84
4.3 Simulated electron/ion density, laser self-modulated electric field and phase space . . . . .	85
4.4 Initial simulated electron and ion density and laser electric field . . . . .	86
4.5 Laser normalized axis vector potential value evolution and 512 electrons picking criteria . . . . .	88
4.6 Longitudinal electric field, 512 electrons trajectory and energy evolution . . . . .	89
4.7 512 picked electrons DLA contribution to final energy . . . . .	91
4.8 Transverse spectra of the transverse electric field (laser) . . . . .	91
4.9 Radiation emitted by the 512 picked electrons in the Long Laser Wakefield Accelerator . . . . .	93
4.10 Radiation spectra emitted by the 512 picked electrons . . . . .	94
4.11 Radiation spectra emitted by the 512 picked electrons at the centre of the virtual detector . . . . .	94
5.1 Illustration of the positron self-driven hollow channel acceleration scheme . . . . .	100
5.2 Plot of the normalised channel excited wake frequency and radius . . . . .	101
5.3 Scheme of the hollow channel formation used to develop analytical model for respective fields . . . . .	104
5.4 Electron driven wake in pre-formed channel simulated with OSIRIS and QuickPIC . . . . .	105
5.5 3D simulation scheme of the plasma hollow channel generated by tightly focused positron beam . . . . .	107
5.6 Plasma wakefields inside the hollow channel behind the tightly focused positron beam . . . . .	108
5.7 Positron test particle accelerated in the hollow channel energy gain and final characteristics . . . . .	109
5.8 Two bunch sets of electrons and positrons beam loading the wakefields inside the plasma hollow channel . . . . .	111
5.9 Sketch of the 3D simulated mode 0 and 1 lepton beam that is sent into a pre-formed hollow channel plasma . . . . .	112

6.1	Illustrating of the sequence of self-modulated beamlets	117
6.2	3D simulation results illustrating the competition between hosing and self-modulation instabilities	119
6.3	Sketch of the experimental setup for the SLAC E-209 self-modulation plasma wakefield setup	119
6.4	Experimental dispersed spectrum of the electron bunch with and without plasma	120
6.5	Experimental detection of the transverse halo formed around the electron bunch when it self-modulated	121
6.6	Experimental FFT of the electron bunch highlighting longitudinal bunching at the plasma periodicity	122
6.7	Initial electron bunch profile as given by Eq. 6.2	123
6.8	Self-modulated electron beam simulation results reproducing experiment at SLAC E-209	124
6.9	Accelerating wakefield evolution along the propagation direction	124
6.10	Final beam energy spectrum	125
6.11	Self-modulation differences due to the sign of the charge of the beam driving the plasma wakefields	126
6.12	Corrected longitudinal model of the experimental bunch parameters for FACET's E-209 run 2	126
6.13	Density plot showing the self-modulated electron and positron bunches	127
6.14	Expected signal relative intensity at the plasma frequency harmonics for the simulated bunches	127
6.15	Comparison of the acceleration longitudinal wakefields evolution when excited by electron and positron bunches in narrow finite plasmas	128
6.16	Additional comparison of the acceleration longitudinal wakefields evolution when excited by electron and positron bunches in narrow finite plasmas	129



# List of Tables

3.1 Laser and plasma configurations for the 3D OSIRIS numerical simulations . . . . .	40
3.2 3D OSIRIS numerical simulations characteristic lengths and laser pulse powers . . . . .	41
3.3 3D OSIRIS numerical simulations resulting accelerated electron bunch charge . . . . .	52
3.4 Simulated final bunch energy values . . . . .	54
3.5 Configurations of the virtual detector for the radiation numerical diagnostic . . . . .	66
4.1 Spacial criteria for the selection of accelerated electrons . . . . .	90
6.1 Values of the parameters of the profile specified in Eq. 6.2 used in the simulation. . . . .	123
8.1 State-of-the-art laser international planned and operational systems . . . . .	136
8.2 State-of-the-art laser international planned and operational systems part II . . . . .	137



# Abbreviations

**ADK** *Ammosov Delone Krainov* ionization model

**ATF** Accelerator Test Facility

**AWAKE** Proton Driven Plasma Wakefield Acceleration Experiment

**BELLA** Berkeley Lab Laser Accelerator

**BNL** Brookhaven National Laboratory

**CC** Complex Conjugate

**CCD** Charge-Coupled Device

**CERN** European Organization for Nuclear Research

**CLF** Central Laser Facility

**CTR** Coherent Transition Radiation

**CGS** centimeter-gram-second unit system

**DC** Direct Current

**DESY** Deutsches Elektronen-Synchrotron

**DLA** Direct Laser Acceleration of electrons in plasma wakefields

**ELETTRA** Multidisciplinary research centre Elettra Sincrotrone Trieste

**ELI** Extreme Light Infrastructure

**EM** Electromagnetic

**EuPRAXIA** European Plasma Research Accelerator with eXcellence In Applications

**FACET** Facility for Advanced Accelerator Experimental Tests

**FEL** Free Electron Laser

**FFT** Fast Fourier Transform algorithm

**FLASH** Free-Electron LASer in Hamburg

**FWHM** Full Width Half Maximum measurement

**GHHG** Gas High Harmonic Generation

**HWHM** Half Width Half Maximum measurement

**HZDR** Helmholtz- Zentrum Dresden-Rossendorf

**IFEL** Inverse Free Electron Laser

**IST** Instituto Superior Técnico - Universidade de Lisboa

**LCLS** Linac Coherent Light Source

**LESM** Laser Envelope Self-Modulation (or laser saussaging)

**LHC** Large Hadron Collider

**LLNL** Lawrence Livermore National Laboratory

**LRFS** Laser Raman Forward Scattering

**LRSPM** Laser Relativistic Self-Phase Modulation

**LRSF** Laser Relativistic Self-Focusing

**LRSC** Laser Relativistic Self-Channeling

**LULI** Laboratoire pour l'Utilisation des Lasers Intenses

**LWFA** Laser Wakefield Acceleration

**NIF** National Ignition Facility

**OAMs** Orbital Angular Momentum laser beams

**PIC** Particle-In-Cell

**PGC** Ponderomotive Guiding Center approximation

**PHPCWA** Positron self-driven Hollow Plasma Channel Wakefield Acceleration

**PDPWFA** Proton Driven Plasma Wakefield Acceleration

**PBWA** Plasma Beat-Wave Acceleration

**PWFA** Plasma based Wakefield Acceleration

**QED** Quantum Electrodynamics

**QST** National Institute for Quantum and Radiological Science and Technology

**RF** Radio Frequency

**RMS** Root Mean Square

**SACLA** SPring-8 Angstrom Compact Free Electron Laser

**SLAC** National Accelerator Laboratory in California

**SM-LWFA** Self-Modulated Laser Wakefield Accelerator

**SM-PWFA** Self-Modulated Particle beam driven Wakefield Accelerator

**SPS** Super Proton Synchrotron

**UCLA** University of California Los Angeles



# List of Symbols

$\lambda_D$	Plasma typical <i>Debye</i> length	4
$n_0$	Plasma background electron and ion density	4
$e$	Electron charge	4
$I$	Laser pulse peak intensity	4
$\vec{E}$	Electric field vector	12
$\vec{B}$	Magnetic field vector	12
$\lambda_0$	Laser pulse wavelength	12
$\omega_0$	Laser pulse frequency	13
$c$	Speed of light in vacuum	13
$a_0$	Electromagnetic (EM) vector potential amplitude normalized to the plasma properties	13
$\gamma$	Relativistic electron <i>Lorentz</i> factor	13
$H$	Relativistic particle <i>Halmiltonian</i> in an Electromagnetic field	13
$\omega_p$	Plasma electron density oscillations frequency	14
$v_{th}$	Plasma electron thermal velocity	14
$\xi$	Longitudinal coordinate in the frame co-moving with the driver	15
$\tau$	Time coordinate in the frame co-moving with the driver	15
$v_p$	Plasma wakefield phase velocity in the blowout regime	15
$W_{\parallel}$	Longitudinal plasma wakefield force per unit charge	16
$W_{\perp}$	Transverse plasma wakefield force per unit charge	16
$W_0$	Gaussian laser spot size	16
$E_{WB}$	Cold wave breaking electric field non relativistic limit	17
$\Psi$	Plasma wake pseudo potential	18
$r_b$	Plasma wake bubble radius for the standard blowout regime	19
$\gamma_p$	Relativistic <i>Lorentz</i> factor associated with the plasma wake group velocity	19
$\omega_{\beta}$	Electron betatron oscillation frequency in a plasma wake	20
$\omega_c$	Critical frequency beyond which the emitted betatron radiation intensity diminishes	23
$n_c$	Critical plasma density for laser propagation	32
$I_{rel}$	Laser pulse peak intensity	32
$\eta(r, z)$	Refractive index of light propagating in an uniform plasma	32
$v_{ph}$	Laser pulse phase velocity	33
$v_g$	Laser pulse group velocity in the plasma	33

$L_{\text{Diff}}$	Diffraction Length	33
$Z_R$	Gaussian laser <i>Rayleigh</i> length	33
$P_c$	Critical laser power for self-focusing	33
$L_d$	Particle dephasing length	34
$L_{\text{pd}}$	Laser pump depletion length	34
$v_{\text{etch}}$	Velocity of laser front etching	34
$\Gamma_{\text{LRFS}}$	Growth rate of the Laser Raman Forward Scattering Instability	77
$\Gamma_{\text{LRSPM}}$	Growth rate of the Laser Relativistic Self-Phase Modulation	78
$\tau_c$	Time interval for axis plasma ions to be radially expelled beyond the laser pulse	81
$\epsilon$	Medium electric permittivity normalized to the value in vacuum	100
$Z$	Plasma ion atomic number	102
$q_i$	Ion electric charge	102
$A$	Plasma ion atomic mass	103
$r_c$	Plasma ion hollow channel limiting radius	104
$I_A$	Álfven magnetohydrodynamic current	105
$N_b$	Number of charged particles constituting the bunch	106
$k_\beta$	Wavenumber associated with the betatron oscillations frequency	118
$P_L$	Laser pulse power	136
$En_L$	Laser pulse peak energy	136
$\tau_L$	Laser pulse length/duration	136
$R_L$	Laser pulse system repetition rate	136

# 1

## Introduction

### Contents

---

<b>1.1 Brief history and applications of particle accelerators</b> . . . . .	<b>2</b>
<b>1.2 Dissertation Outline</b> . . . . .	<b>6</b>
<b>1.3 Original Contributions</b> . . . . .	<b>6</b>

---

## 1.1 Brief history and applications of particle accelerators

The evolution of particle accelerators is characterised by the increase in the acceleration of more luminous particle beams to higher energies and the development of technology and the application of new concepts. An important first step was the extension of the vacuum tube, invented by *Heinrich Geissler* in the 1850s, by *William Crookes* that showed the deflection of cathode rays by magnetic fields in 1879. In 1895, the *Crookes* cathode discharge tubes accelerated electrons up to a few KeV and sent them into a platinum anode target emitting x-ray radiation, allowing the field of radiography to arise in medicine, material sciences and research. Cathode ray tubes were used in the well-known fundamental physics discovery of the first subatomic particle with negative electric charge, the electron, by *Joseph John Thompson* in 1897. At that time *Karl Ferdinand Braun* built the first cold cathode-ray tube that paved the way to the electronic television era. Those television devices became commercially available already in the 1930s and, until recently, cathode ray tubes are used in our university's laboratories oscilloscopes, where the ray deflection process is electrostatic instead of magnetic.

Naturally accelerated particle beams, with energies reaching  $10^{20}$  eV, were found in the Earth's atmosphere by *Victor Hess* in his ballon expedition between Vienna and Berlin between 1911 and 1913 and were named cosmic rays. The search for the source of cosmic rays and for understanding its production mechanism is still ongoing and yet these accelerated beams already provided particle and nuclear physics with the first detection of the positron and the muon, as part of *Carl David Anderson's* work. The gap between the highly energetic cosmic rays and beams accelerated in ground worldwide laboratories was reduced with *Robert Van de Graaff* apparatus, in 1929. It sends a gas of positive ions (and also negatively charged ions if it is the *Tandem Van de Graaff* version) through a tube with an accelerating Direct Current (DC) voltage, produced by a moving belt, until they strike the bottom. In 1937 the attained final energy of the ions was of about 5 MeV (the voltage applied is limited by the tube gas ionization field limit) and it was the cornerstone to making x-rays and accelerated particle beams available for nuclear physics and medical research since then and nowadays for educational purposes. In 1932 the *John D. Cockcroft and Ernest T. S. Walton* multiplier machine was operated with linear stages applying successfully higher electric voltages to accelerate protons. These are still used today to inject high current into other particle accelerators, however, voltage breakdown limits energy gain to a few MeV.

The 1920s witnessed the implementation of varying and oscillating electric potentials in accelerating models. In 1924, *Gustav Ising* idea and *Rolf Wideröe* construction resulted in first Linac linear particle accelerator in which ions got to 50 KeV as they passed by tubes of different lengths and voltages. Later, in 1966, the Stanford Linear Accelerator Center linac of over 3 km accelerated electrons to 20 GeV and positrons to 13 GeV. The cyclotron scheme, where particles perform half circular trajectories in a static magnetic field while being resonantly accelerated by an electric field, in the Radio Frequency (RF) region of the Electromagnetic (EM) wave frequency spectrum, that was reversed every half-cycle, was conceived in 1931 and attained about 80 KeV proton energy. That first not linear

configuration was created by *Ernest O. Lawrence* and was limited due to the difficulty of keeping the beam stable as the orbit radius became wider. The stability concern led researchers, such as *Edwin McMillan* and *Vladimir Veksler*, by 1944, to include a separate alternating gradient focusing, through varying the magnetic field strength in time, system. By 1953 over 3 GeV proton beams were produced in the *Bevatron* and *Cosmotron* accelerators and several naturally unstable rare isotopes found. At this point particle accelerators started to be used for beam high-energy collisions and, since then, electrons and positrons collided in the PEP Storage Ring (where the same synchrotron was used for both lepton species) Electron-Positron Collider in 1980 with 29 GeV and in the 27 km Large Electron Positron collider storage ring in 1995 with 209 GeV, almost 1 TeV protons and anti-protons were generated at the Tevatron synchrotron in 2008 and, more recently, 14 TeV collisions were obtained at the 27 km Large Hadron Collider ring in 2012 when the *Higgs* boson, particle that corroborates the theory of the Standard model, presence was finally measured.

Charged particles in non linear trajectories emit incoherent synchrotron radiation proportional to their velocities electrons will be subject to greater deceleration than protons in synchrotron-like infrastructures. Therefore, when in 1971 *John Madey* invented the Free Electron Laser (FEL) where a relativistic beam of electrons passes an undulator or wiggler, periodic set of magnets that bend its trajectory transversely in alternate directions, describing a sinusoidal-like trajectory, its applicability as a tunable high-power coherent fs radiation source was evident. The undulator is composed of a periodic set of magnets that transversely bend the trajectory of the particles in alternate directions so that it describes a sinusoidal like motion.

Just as the accelerator technology has evolved so did its applications and societal impact of (and need for) their progress. Nowadays, material compounds and isotopes can be detected also non-destructively using nuclear resonance fluorescence activated with a Laser-Compton scattering  $\gamma$  ray source without the need for the materials to be removed from their heavy cm thick iron shields, allowing for nuclear waste hazard to be evaluated safely [6]. Radiotherapy is now being complemented by clinical high-energy proton beam therapy in hospitals for the complex pediatric long time treatments, including embryonal tumors, due to the greater precision in radiation doses without damage to surrounding, healthy, tissues [7]. Biological processes, for example that of the photosynthesis through which plants create the air we live of, can be viewed with 3D highly resolved (2.25 Å) picture frames without freezing the sample and hampering its evolution with the use of 40 fs intense x-rays produced in an X-ray FEL [8]. The  $\beta$  decay of a  $^{32}\text{Cl}$  beam accelerated at the National Superconducting Cyclotron Laboratory is being studied in view of explaining the puzzling isotope ratios present in the silicon carbide remains of some meteorites [9]. This year, 2017, a forevacuum-pressure range 1-15 Pa, plasma hollow-cathode discharge source produced up to 15 KeV, 200 mA and kW power wide aperture electron beams and was used in the evaporation of aluminum oxide ceramic that was evaporated and then deposited as a protective ceramic large area coating for industrial applications [10].

In the accelerators described above, where RF fields are employed, the main limitation on the accelerating gradient or, in other words, the minimum distance needed for particles to achieve a fixed

final energy, results from the gas breakdown in the gap sections, generating dark current, or/and the surface breakdown due to high electric-field forces exceeding the tensile strength of the metal materials, the binding potential of its atoms to its crystal, melting and evaporating it. The limit for **RF** cavities made of, for example copper is a surface field of 170 MV/m and for Molybdenum it is of about 430 MV/m [11]. This is the reason why for electrons to gain 1 TeV energy in them, a 6 km long structure of copper is required. To build such a particle accelerator for all the medical, industrial, research applications, like the ones mentioned above, in developing countries with economical constrains, like Portugal, where the cost and place further restricts the maximum energy attainable, is not possible. This motivates developing new, more compact and efficient, alternative accelerating technologies is vital to our community and ultimately, the goal of the work discussed in this dissertation.

### 1.1.1 The Plasma Wakefield Accelerator

A solution, proposed back in 1956, to the accelerator wall material breakdown is to use plasmas as the energy transfer medium [12]. Plasma is constituted by a collection of free ions and electrons that exhibits collective behavior and represents the state of about 99% of all matter in the universe [13]. A plasma can be created either by ionizing baryonic matter with strong electrical fields, for example with intense laser pulses or electrical discharges, or by thermal heating. The advantage of using a plasma to sustain strong fields, which can be used to accelerate charged particles, is that it is not limited by the breakdown limit. The plasma *Debye* shielding effect prevents strong fields from reaching or damaging its surrounding material. It occurs when electric forces (associated with the fields) attract or repel electrons and ions to or from any perturbative charges (or potentials) in order to neutralize those forces. That effect happens in the characteristic *Debye* length  $\lambda_D = \sqrt{\frac{KT}{4\pi n_0 e^2}}$ , that depends on the background density,  $n_0$ , on the plasma temperature in thermal equilibrium,  $T$ , to which corresponds an energy of  $KT$ , where  $K$  is the *Boltzmann* constant and  $e$  stands for the electron negative electric charge value.

The pioneer work done by *Toshi Tajima* and *John Dawson* in 1979 [14], showed a plasma based acceleration concept that was since capable of reaching tens of GeV/m accelerating gradients. Thereafter, similar techniques were explored in which the energy from state-of-the art intense laser pulses or high current charged particle beams were used to excite accelerating fields in plasmas that surpassed those of the previously mentioned standard devices [15–20]. This section covers the main plasma based configurations explored and their primary implications and breakthroughs for developing future linear colliders, producing new x-ray beam sources and reaching beyond the energy frontier (TeV). The sections that follow will then be dedicated to the detailed description of the two most effective schemes: the Laser Wakefield Acceleration (**LWFA**) and the Plasma based Wakefield Acceleration (**PWFA**).

In 1985 the Plasma Beat-Wave Acceleration (**PBWA**) scheme accelerating fields ranging from 0.3 to 1 GV/m, propagating close to the speed of light were demonstrated. In such scheme the beat wave of two frequencies co-propagating<sup>1</sup> long (2 ns) laser pulses (with intensities of  $I \approx 1.7 \times 10^{13}$  W/cm<sup>3</sup>)

<sup>1</sup>Note that the same setup with only one laser would not have sufficed, due to the available lasers low intensity, to excite

was sent into Hydrogen pre-ionized plasmas, with  $n_0$  on the order of  $10^{17}\text{cm}^{-3}$  (and  $T \approx 30$  eV) [21]. Another alternative configuration involved relativistic particle beams instead of laser pulses and it used the PWFA scheme [22]. The PWFA was demonstrated experimentally in 1988 with a 21 MeV electron beam [23]. Later in 1995 yet another setup was tested in which single laser pulses were sent into plasmas where they underwent the self phase modulation due to the local variations of phase velocity correlated to plasma density oscillations induced by the pulse itself [24, 25]. The LWFA scheme could only be explored after the advent of the laser chirped pulse amplification technique by Donna Strickland and Gerard Mourou [26] with which ultra-short (when compared to the plasma wavelength,  $< 1\text{ps}$ ), ultra-intense ( $I > 10^{17}$  W/cm<sup>2</sup>) high-power laser pulses were created. Those specialized lasers were used for the first time in a LWFA configuration with a  $10^{17}\text{cm}^{-3}$  plasma in 1993 [27]. By 2004 it had been shown how different table-top plasma wakefield acceleration techniques could produce a mono energetic high-energy "Dream Beam" [28-31].

One of the most exciting results of plasma based acceleration was obtained at National Accelerator Laboratory in California (SLAC) in 2007. In it an electron drive beam excited PWFA accelerating gradients of 52 GeV/m and its tail gained over 42 GeV in only 85cm of plasma [32]. An electron PWFA more recent experiment accelerated a second trailing 20.35 GeV bunch of electrons with 200 pC up to  $21.95 \pm 0.1$  GeV, on average, in a 36 cm Lithium plasma, also at SLAC, representing an extraction efficiency reaching 50% and a 4.4 GV/m average accelerating gradient in some events [33]. The experiment, also done at SLAC, published in 2015 [34] proved similar efficiency of a PWFA scheme driven by a positron bunch instead. The front of the short (between 30 to 50  $\mu\text{m}$  long)  $1.4 \times 10^{10}$  positrons bunch transferred about 30% of its energy to the tail, containing around 200 pC of the bunch, in a 1.15m long Lithium plasma with density up to  $10^{16}\text{cm}^{-3}$ . The corresponding energy gain was over 3 GeV with the accelerated positrons exhibiting a Root Mean Square (RMS) energy spread close to 2%. In 2016, two independent compact LWFA configurations constituted two separate stages. The first was responsible for producing a  $\approx 34$  pC electron beam that was injected into the second stage where the energy from the Berkeley Lab Laser Accelerator (BELLA) Center TREX laser pulse produced a final electron bunch of 1.2 pC with energies between 110 to 150 MeV (85% efficiency) [35].

While the plasma based accelerator scheme is still being optimized to produce industry level high quality particle beams (high current, low emittance) to be used in, for example, future linear colliders, their application to diagnostics and imaging has already been shown. In 2015, the 3D full reconstruction of the bone tissue, with resolution below 50  $\mu\text{m}$  was made possible with the use of hard (with energies above 30 KeV) x-rays with divergency of  $10 \times 20$  mrad<sup>2</sup> generated by electrons that were accelerated to  $\approx 700$  MeV in the LWFA machine employing a 1.2 cm,  $3 \times 10^{18}\text{cm}^{-3}$  density Helium plasma and the 300 TW Astra-Gemini laser pulse of the Central Laser Facility [36]. In 2011, that result extended the applicability of the LWFA for x-ray beam sources that had already been proved with the contrast imaging of an orange tetra fish by x-ray absorption produced also in a LWFA experiment using the Hercules laser at the Center for Ultrafast Optical Science at the University of

---

comparable fields.

Michigan, Ann Arbor[37].

In 2010 the idea of utilizing the TeV proton beam available at European Organization for Nuclear Research (CERN) for the Large Hadron Collider (LHC) infrastructure to excite the plasma wake and transfer its energy to plasma electrons was explored numerically [38]. For it the long proton beam undergoes the self-modulation instability and is divided by the plasma transverse wakefields into a sequence of segments that contribute resonantly to the wake excitation. Four years later the E-209 self-modulation of electron and positron long bunches proof-of-principle experiment was done at SLAC [39] and the relevance of seeding that instability was highlighted [40]. In the summer of 2016 the first Super Proton Synchrotron (SPS) accelerated to 400 GeV long (12cm) proton beam was sent into the Proton Driven Plasma Wakefield Acceleration Experiment (AWAKE) self-modulated PWFA experiment at CERN containing a 10 m long plasma gas cell [41] successfully exciting the plasma wake. The international collaboration behind the experiment is now working on the external injection and acceleration of 40% of those electrons up to 1.8 GeV in AWAKE [42] aiming to later reach TeVs.

## 1.2 Dissertation Outline

The work presented in the different chapters of this document does not follow the chronological order in which it was made but an order that was found fit to help the reader go through it. Firstly, the study of the direct laser acceleration of the electrons trapped in the nonlinear blowout bubble driven by a laser pulse with a length that is comparable to the plasma wake density oscillations wavelength will be explained in detail. That chapter contains the motivation for the experimental and numerical investigation that are enclosed. Secondly, the understanding of the direct laser impact on the trapped electrons was used to find the hard x-ray radiation that is generated in the laser self modulated plasma wakefield regime through numerical simulations. The third chapter includes the discussion of a novel scheme that we proposed, in which a hollow channel is generated by a tightly focused positron beam propagating in an initially uniform pre-ionized plasma where it also excites the electron plasma density wake and associated wakefields. Next we investigated through numerical simulations and also the proof-of-principle experiment E-209 done at the SLAC Laboratory how long lepton beams undergo self-modulation of their density profile according to the sign of their charge and to their initial longitudinal shape. Final remarks and the future direction of the different work topics are listed at the end of this dissertation.

## 1.3 Original Contributions

Of the topics described in this dissertation my main contributions were numerical simulation analysis to support the experimental findings by J. Shaw, Nuno Lemos et al. and F. Albert et al.; the complete numerical framework and the analytical model determining how a focused drive positron bunch can excite a plasma wake and generate a hollow channel in the ion density profile; simulations done to understand long particle beam longitudinal shape influence on its self-modulation instability seeding in the plasma wakefields and the experiment that was done at SLAC, E-209 with P. Muggli et al. The

resulting international and national publications and communications are listed below.

### 1.3.1 Peer-reviewed publications

1. **L. D. Amorim**, J. Vieira, R. A. Fonseca and L. O. Silva, *Self-driven Plasma Hollow Channels for Positron Acceleration*, To be submitted to PHYS REV LETT (2017)
2. **L. D. Amorim**, F. Peano, J. Vieira and L. O. Silva, *Isotope Separation using Chirped Laser Acceleration*, To be submitted to APPL PHYS LETT (2017)
3. F. Albert, N. Lemos, J. L. Shaw, B. B. Pollock, C. Goyon, W. Schumaker, A. M. Saunders, K. A. Marsh, A. Pak, J. E. Ralph, J. L. Martins, **L. D. Amorim**, R. W. Falcone, S. H. Glenzer, J. D. Moody, and C. Joshi, *Observation of Betatron X-Ray Radiation in a Self-Modulated Laser Wakefield Accelerator Driven with Picosecond Laser Pulses*, PHYS REV LETT **118** 134801 (2017)
4. J. L. Shaw, N. Lemos, **L. D. Amorim**, N. Vafei-Najafabadi, K. A. Marsh, F. S. Tsung, W. B. Mori and C. Joshi, *Role of Direct Laser Acceleration of Electrons in a Laser Wakefield Accelerator with Ionization Injection*, PHYS REV LETT. **118** 064801 (2017)
5. A. Caldwell and the AWAKE collaboration, *Path to AWAKE: Evolution of the concept*, NUCL INSTRUM METH A **829** (2016)
6. E. Gschwendtner and the AWAKE collaboration, *AWAKE, The Advanced Proton Driven Plasma Wakefield Acceleration Experiment at CERN*, NUCL INSTR. METH PHYS RES A **829** (2016) 76-82
7. C. Bracco and the AWAKE collaboration, *AWAKE: A Proton-Driven Plasma Wakefield Acceleration Experiment at CERN*, Nuclear and Particle Physics Proceedings **273-275** (2016) 175-180, 37th International Conference on High Energy Physics, Valencia, Spain, 2 - 9 Jul 2014
8. **L. D. Amorim**, J. Vieira, R. A. Fonseca and L. O. Silva, *Positron plasma wakefield acceleration in a self-driven hollow channel*, AIP Conference Proceedings **1777**, 070001 (2016) of the 6th AAC in San Jose, California, USA July 2014
9. E. Adli, V.K. Berglyd Olsen, C.A. Lindstrøm, P. Muggli, O. Reimann, J.M. Vieira, **L.D. Amorim**, C.I. Clarke, S.J. Gessner, S.Z. Green, M.J. Hogan, M.D. Litos, B.D. O'Shea, V. Yakimenko, C. Clayton, K.A. Marsh, W.B. Mori, C. Joshi, N. Vafei-Najafabadi and O. Williams, *Progress of plasma wakefield self-modulation experiments at FACET*, NUCL INSTRUM METHODS **829**, 334 (2016)
10. K. V. Lotov, A. P. Sosedkin, A. V. Petrenko, **L. D. Amorim**, J. Vieira, R. A. Fonseca, L. O. Silva, E. Gschwendtner and P. Muggli, *Electron trapping and acceleration by the plasma wakefield of a self-modulating proton beam*, PHYS PLASMAS **21**, 123116 (2014)

11. J. Vieira, **L. D. Amorim**, Y. Fang, W. B. Mori, P. Muggli and L. O. Silva, *Self-modulation instability of ultrarelativistic particle bunches with finite rise times*, PLASMA PHYS CONTR F **56**, 084014 (2014)
12. Y. Fang, J. Vieira, **L. D. Amorim**, W. Mori and P. Muggli, *The effect of plasma radius and profile on the development of self-modulation instability of electron bunches*, PHYS PLASMAS **21**, 056703 (2014)

### 1.3.2 Published proceedings

1. V.K.B. Olsen, E. Adli, P. Muggli, **L.D Amorim**, J.M. Vieira, *Loading of a plasma-wakefield accelerator section driven by a self-modulated proton bunch*, **WEPWA026**, Proceedings of the 6th IPAC Conference Richmond, VA - USA, June 2015
2. P. Muggli, O. Reimann, **L.D. Amorim**, N.C. Lopes, L.O. Silva, J.M. Vieira, J. Allen, S.J. Gessner, M. Hogan, S.Z. Green, M.D. Litos, B.D. O'Shea, V. Yakimenko, G. Andonian, C. Joshi, K. Marsh, W. B. Mori, N. Vafaei-Najafabadi, O. Williams, E. Adli, C.A. Lindstrom, V.B. Olsen, *Measuring the self-modulation instability of electron and positron bunches in plasmas*, **WEPWA008**, Proceedings of the 6th IPAC Conference Richmond, VA - USA, June 2015
3. **L. D. Amorim**, J. Vieira, R. A. Fonseca, L. O. Silva, *Positron acceleration in non-linear plasma wakefields driven by tightly focused particle bunches*, Proceeding of the 41st EPS Conference on Plasma Physics Berlin, Germany, **O5.224**, 23-27 June 2014
4. P. Muggli, O. Reimann, **L.D. Amorim**, N.C. Lopes, J.M. Vieira, S.J. Gessner, M. Hogan, S.Z. Li, M.D. Litos, K. Marsh, W. Mori, C. Joshi, N. Vafaei-Najafabadi, E. Adli, V.K. Berglyd Olsen, *Electron Bunch Self-modulation in a Long Plasma at SLAC FACET*, **TUPME050**, Proceeding of the IPAC Conference Dresden, Germany, 15-20 June 2014
5. **L. D. Amorim**, J. Vieira, L. O. Silva, P. Muggli, *Numerical Modeling of the E-209 Self-modulation Experiment at SLAC - FACET*, **TUPME076**, Proceeding of the IPAC Conference Dresden, Germany, 15-20 June 2014
6. P. Muggli, N. C. Lopes, **L. D. Amorim**, J. Vieira, L. O. Silva, S. Karsh, *Injection of a LWFA Electron Bunch in a PWFA Driven by a Self-modulated Proton Bunch*, **TUPME048**, Proceeding of the IPAC Conference Dresden, Germany, 15-20 June 2014
7. P. Muggli, O. Reimann, J. Vieira, N. Lopes, **L. D. Amorim**, L. O. Silva, S. Gessner, M. J. Hogan, S. Li, M. Litos, N. Vafaei-Najafabadi, C. Joshi, W. B. Mori, K. Marsh, E. Adli, V. K. B. Olsen, Y. Fang, *Self-modulation of ultra-relativistic SLAC electron and positron bunches*, Proceeding on the ICOPS/BEAMS 2014 - 41st IEEE International Conference on Plasma Science and XX International Conference on High-Power Particle Beams, May 2014

### 1.3.3 Oral communications

- L. D. Amorim, R. A. Fonseca, J. Vieira and L. O. Silva, *Plasma Based Accelerators of the Future*, PhD Open Days at Instituto Superior Técnico, University of Lisbon, Portugal, April 2017
- L. D. Amorim, W. An, W. B. Mori and J. Vieira, *Transverse evolution of positron beams accelerating in hollow plasma channel non-linear wakefields*, XXVII Advanced Accelerator Concepts Workshop (AAC) in Maryland, USA, August 2016
- L. D. Amorim, J. Vieira, R. Fonseca and L. O. Silva, *Wakefield structure of plasma hollow channels self-driven by tightly focused beams*, 57th Annual Meeting of the American Physical Society (APS) Division of Plasma Physics in Savannah, GA, USA, November 2015
- L. D. Amorim, J. Vieira, R. Fonseca and L. O. Silva, *Nonlinear wakefield structure of a hollow channel driven by a tightly focused positron bunch*, 42nd European Physical Society (EPS) Conference on Plasma Physics in Lisbon, Portugal, June 2015
- L. D. Amorim, J. Vieira, R. A. Fonseca and L. O. Silva, *Positron acceleration in hollow channels self-driven by tightly focused positron beams*, Laser Plasma Acceleration Workshop (LPAW) in Guadeloupe, May 2015
- L. D. Amorim, J. Vieira, R. A. Fonseca and L. O. Silva, *Positron plasma wakefield acceleration in a self-driven hollow channel*, 6th Advanced Accelerator Concepts Workshop (AAC) in San Jose, California, USA July 2014
- L. D. Amorim, J. Vieira and L. O. Silva, *Positron acceleration in non-linear plasma wakefields driven by tightly focused particle bunches*, 41st European Physical Society (EPS) Conference on Plasma Physics in Berlin, Germany June 2014

### 1.3.4 Poster communications

- L. D. Amorim, R. A. Fonseca, J. Vieira and L. O. Silva, *Plasma Based Accelerators of the Future*, PhD Open Days at Instituto Superior Técnico, University of Lisbon, Portugal, April 2017
- L. D. Amorim, W. An, W. B. Mori and J. Vieira, *Linear to non linear analysis for positron acceleration in plasma hollow channel wakefields*, 58th Annual Meeting of the American Physical Society (APS) Division of Plasma Physics in San Jose, California, USA, November, 2016
- L. D. Amorim, J. Vieira and L. O. Silva, *Mitigation of transverse instabilities for efficient positron acceleration in non-linear wakefields excited in hollow plasma channels*, 43rd European Physical Society (EPS) Conference on Plasma Physics in Leuven, Belgium, July 2016
- L. D. Amorim, W. An, W. B. Mori and J. Vieira, *Transverse evolution of positron beams accelerating in hollow plasma channel non-linear wakefields*, XXVII Advanced Accelerator Concepts Workshop (AAC) in Maryland, USA, August 2016

- L. D. Amorim, J. Vieira, P. Muggli and L. O. Silva, *Numerical investigation of the lepton self-modulation plasma wakefield acceleration for the E-209 experiment at SLAC-FACET*, II European Advanced Accelerator Concepts Workshop (EAAC) in Elba, Italy, September 2015
- L. D. Amorim, J. Vieira, R. A. Fonseca and L. O. Silva, *Positron self-driven hollow channel in non-linear plasma wakefields*, 56th Annual Meeting of the American Physical Society (APS) Division of Plasma Physics in New Orleans, Louisiana, USA October 2014
- L. D. Amorim, J. Vieira, P. Muggli and L. O. Silva, *Numerical Modeling of the E-209 Self-Modulation Experiment at SLAC - FACET*, V International Particle Accelerator Conference (IPAC) in Dresden, Germany, June 2014
- L. D. Amorim, J. Vieira, P. Muggli and L. O. Silva, *Full scale simulations of the E-209 self-modulation experiment*, XXVI Advanced Accelerator Concepts Workshop (AAC) in San Jose, California, USA, July 2014
- L. D. Amorim, J. Vieira and L. O. Silva, *Self-modulation instability of ultra-relativistic SLAC electron and positron bunches in plasmas*, 40th European Physical Society (EPS) Conference on Plasma Physics in Finland, July 2013
- L.D. Amorim, J. Vieira, P. Muggli, R. Fonseca, W. B. Mori, L. O. Silva. *Ultra-relativistic electron and positron bunches in plasmas in the linear and blow-out/suck-in regime*, 55th Annual Meeting of the American Physical Society (APS) Division of Plasma Physics, Denver, Colorado, November 2013.

# 2

## Overview of analytical background and numerical resources

### Contents

---

<a href="#">2.1 Plasma Wakefield Accelerator operating in the linear regime</a>	12
<a href="#">2.2 Wakefields in the standard nonlinear bubble/blowout regime</a>	17
<a href="#">2.3 Nonlinear plasma wakefield regime driven by a positron beam</a>	20
<a href="#">2.4 Betatron radiation</a>	23
<a href="#">2.5 Numerical infrastructures</a>	24

---

In light of the recent relevant advances in plasma wakefield accelerators, presented in the previous chapter, it became timely to investigate how to surpass their challenges. This chapter aims at explaining the basic notions and concepts of the plasma wakefield accelerator technology operating in the linear (Sec. 2.1) and the nonlinear regimes driven by laser pulses and electron beams (Sec. 2.2) excited by a laser pulse and beam of charged particles. The detail of the information herein contained was chosen in order to alleviate the subsequent chapters, i.e. so that in these the focus would be mostly on the original work for this dissertation. The nonlinear wakefields excited when a positron bunch is sent through the plasma are described in Sec. 2.3. Section 2.4 contains the characterization of the betatron radiation emitted by particles accelerated in plasma wakefields and Sec. 2.5 introduces the numerical codes and models used for the work of this dissertation. The main contributions of my past years work to the field of plasma wakefield acceleration are listed in Sec. 1.3. Finally, the outline of the next chapters is written in Sec. 1.2. Each of the following chapters of this dissertation contain further theoretical and experimental considerations that were not detailed in the present one.

## 2.1 Plasma Wakefield Accelerator operating in the linear regime

A plasma wakefield accelerator can be driven by a short drive laser pulse, Laser Wakefield Acceleration (LWFA) or an electron beam, Plasma based Wakefield Acceleration (PWFA), in the linear regime depicted in Fig. 2.1. In the case of the short laser pulse (in a red circle), its radiation pressure expels charged particles. As a result, when the laser is sent into a pre-formed initially uniform and in electrostatic equilibrium plasma of electrons (in blue) and ions, it radially repels the plasma electrons thus reducing their local density (white region). The heavier ions behave as stationary in the electron motion time frame. Therefore, after the laser left the low electron density region, the total space charge (of the ions and electrons) is positively charged and focuses the plasma electrons back to the propagation axis. When electrons return to the axis they have transverse velocity and so overshoot the axis, generating a local region of high concentration of electrons (dark blue region). That region's corresponding total space charge is negatively charged and radially repels other plasma electrons creating a subsequent lower electron density region, turning the electron density perturbations into a cycle. Similarly, when an electron beam (red circle) is used to excite this scheme, its electric space charge also repels plasma electrons radially starting the cycle.

This electron density oscillations, named the plasma wake structure driven by a laser or electron beam, have associated electric fields, called the plasma wakefields, that are capable of accelerating and focusing charged particles (represented in Fig. 2.1 a) and b) by dashed orange square).

For the analytical derivation of the linear regime plasma wakefields, consider a single electron immersed in the laser pulse inhomogeneous and oscillating Electromagnetic (EM) fields will follow the *Lorentz* equation of motion that can be written in centimeter-gram-second unit system (CGS) as:

$$\frac{d\vec{p}}{dt} = \frac{\partial \vec{p}}{\partial t} + (\vec{v} \cdot \nabla) \vec{p} = q(\vec{E} + \vec{v}/c \times \vec{B}) \quad (2.1)$$

where  $q = -4.8 \times 10^{-10}$  statC,  $\vec{p}$ ,  $\vec{v}$  are the electron charge, momentum and velocity, respectively,  $t$  the time, and  $\vec{E}$  and  $\vec{B}$  are the laser electric and magnetic fields oscillating at wavelength  $\lambda_0$  and

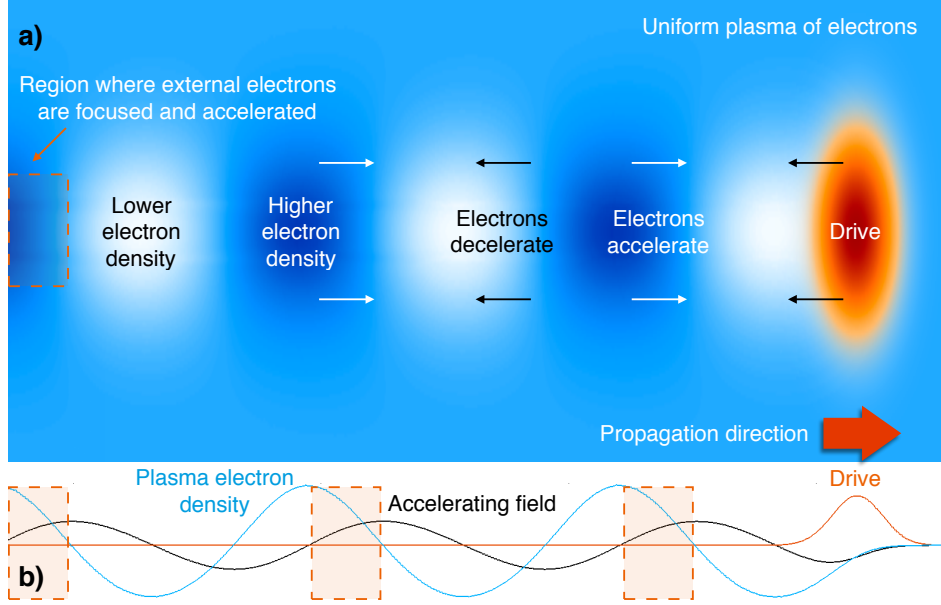


**Figure 2.1:** a) 2D Illustration of the plasma wakefield accelerator where a drive laser pulse/particle beam (red tones) propagates into the plasma of electrons (in blue) and approximately immobile ions exciting the wake electron density oscillations (sequence of white and dark blue regions). b) on-axis lineout of the pulse/beam envelope/density (orange line), the plasma electron density (blue line) and the reversed ( $\times -1$ ) longitudinal wakefield. Orange squares (dashed lines) highlight the accelerating and focusing wakefield regions for electrons.

frequency  $\omega_0 = 2\pi c/\lambda_0$ .  $c = 3 \times 10^{10}$  cm/s is the speed of light propagating in vacuum. In the absence of other charged particles (or in a quasi-neutral plasma that has negligible density perturbations,  $n(\vec{r}, t) = n_0 + n_1(\vec{r}, t) + \dots$ , with  $n_1 \ll n_0$ ) it is possible to find the laser **EM** fields vector potential so that  $\vec{E} = -\frac{1}{c} \frac{d\vec{A}}{dt}$  that can be weighted relative to the electron rest mass energy through the adimensional amplitude  $a_0 = \frac{|q\vec{A}|}{m_e c^2} \approx 8.5 \times \lambda_0 [\mu\text{m}] \sqrt{I [10^{20} \text{W/cm}^2]}$ . In a regime where the fields direct perturbations to the electron trajectory are small, i.e.  $a_0 \ll 1$  the equation of motion of the electron starting from rest,  $|\vec{v}_0| = |\vec{v}|(t=0) = 0$ , and without any static fields,  $|\vec{E}_0| = |\vec{B}_0| = 0$ , to describe an initial electrostatic equilibrium situation (for eg. plasma), can be linearized. The second order  $\vec{v}_1/c \times \vec{B}_1$  and  $(\vec{v}_1 \cdot \nabla) \vec{p}_1$  terms are neglected to yield the electron quiver velocity  $\frac{\partial \vec{p}_1}{\partial t} = m_e \gamma_0 \frac{\partial \vec{v}_1}{\partial t} = q \vec{E}_1$  where the relativistic electron *Lorentz* factor,  $\gamma$  is given, using the **EM** *Hamiltonian*,  $H$ , mechanics canonical (conjugate) momentum  $\vec{P}_H = m_e \gamma \vec{v} + \frac{q}{c} \vec{A}$ , by the relation:  $\gamma = \sqrt{1 + \left( \frac{\vec{P}_H}{m_e c} - \frac{q\vec{A}}{m_e c^2} \right)^2}$ .

Linear oscillating **EM** fields can be expressed by  $\vec{E}_1 = \vec{E}_1(\vec{r}) \cos(\omega_0 t) = \vec{E}_{1r} \cos(\omega_0 t)$  and, from *Faraday's* law,  $\vec{B}_1 = -\frac{\nabla \times \vec{E}_{1r}}{c\omega_0} \sin(\omega_0 t)$ . From here the first order result gives  $\vec{v}_1 = \frac{q\vec{E}_{1r}}{m_e \gamma_0 \omega_0} \sin(\omega_0 t)$  and also  $\vec{r}_1 = -\frac{q\vec{E}_{1r}}{m_e \gamma_0 \omega_0^2} \cos(\omega_0 t)$ , the electron quiver velocity and position. The second order evaluation of the equation of motion is then  $m_e \gamma_0 \frac{d\vec{v}_2}{dt} + m_e \gamma_1 \frac{d\vec{v}_1}{dt} = q(\vec{r}_1 \cdot \nabla) \vec{E}_{1r} \cos(\omega_0 t) + \left( \frac{q\vec{E}_{1r}}{m_e \gamma_0 \omega_0 c} \sin(\omega_0 t) \right) \times \left( -\frac{\nabla \times \vec{E}_{1r}}{c\omega_0} \sin(\omega_0 t) \right)$ , from where we drop the  $m_e \gamma_1 \frac{d\vec{v}_1}{dt}$  term by assuming that the electron energy varies at a slower time scale, and where we introduced the second order expansion of  $\vec{E}_2 = \vec{r}_1 \cdot \nabla \vec{E}_{1r}$ . With simple algebra the second order electron equation of motion can be simplified into:  $m_e \gamma_0 \frac{d\vec{v}_2}{dt} = -\frac{q^2}{m_e \gamma_0 \omega_0^2} \left( \left( \vec{E}_{1r} \cdot \nabla \right) \vec{E}_{1r} \cos(\omega_0 t)^2 + \vec{E}_{1r} \times \nabla \times \vec{E}_{1r} \sin(\omega_0 t)^2 \right)$ . Performing the time average of the quantities, making use of the vector identity  $\nabla \left( \vec{E}_{1r} \cdot \vec{E}_{1r} \right) = 2\vec{E}_{1r} \times \nabla \times \vec{E}_{1r} + 2 \left( \vec{E}_{1r} \cdot \nabla \right) \vec{E}_{1r}$ , and generalizing to all the plasma electrons leads to the effective nonlinear relativistic ponderomotive

force, or radiation pressure, averaged over a laser period, acting equally on every electron:

$$\langle \vec{F}_p \rangle = n_0 m_e \gamma_0 \left\langle \frac{d\vec{v}_2}{dt} \right\rangle = -\frac{1}{4} \frac{q^2 n_0}{\gamma_0 m_e \omega_0^2} \nabla \vec{E}_{1r}^2 \implies \vec{F}_p = -\frac{1}{2} \frac{n_0 m_e c^2}{\gamma_0} \nabla \langle a_0^2 \rangle \quad (2.2)$$

Equation (2.2) can be interpreted as the laser EM fields of a wave with longitudinally varying amplitude. Infinite plane waves will not generate this force. Introducing a non-uniform first order transverse quiver motion in the electrons leads to their pile up over each half cycle. The need of an additional second order net longitudinal, i.e. in the laser propagation direction, secular type of drift from the magnetic field that results from *Faraday's* law of induction and the field amplitude longitudinal dependence [13]. A transversely finite laser pulse induces a radial ponderomotive force that radially repels the plasma electrons creating the plasma wake. In the LWFA the plasma electrons will feel the ponderomotive force of the laser and the space charge effect from the excited plasma density oscillations and so a cold nonrelativistic (meaning low thermal velocity and  $\gamma_0 \approx 1$ ) plasma equation of motion becomes  $\frac{d\vec{p}}{dt} = q\vec{E}_{\text{wake}} + \langle \vec{F}_p \rangle$ . Using the other vector identity  $\nabla \times \nabla \times \vec{E}_{\text{wake}} = \nabla (\nabla \cdot \vec{E}_{\text{wake}}) - \nabla^2 \vec{E}_{\text{wake}}$ , *Ampère's* law:  $\nabla \times \vec{B}_{\text{wake}} = \frac{1}{c} \frac{\partial \vec{E}_{\text{wake}}}{\partial t} + \frac{4\pi n_0 q \vec{v}}{c}$  and *Faraday's* law  $\nabla \times \vec{E}_{\text{wake}} = -\frac{1}{c} \frac{\partial \vec{B}_{\text{wake}}}{\partial t}$ , allows to derive the resulting plasma wave equation [43, 44]:

$$\nabla (\nabla \cdot \vec{E}_{\text{wake}}) - \nabla^2 \vec{E}_{\text{wake}} + \frac{\omega_p^2}{c^2} \vec{E}_{\text{wake}} + \frac{1}{c^2} \frac{\partial^2 \vec{E}_{\text{wake}}}{\partial t^2} = -\frac{\omega_p^2}{\omega_0^2} \frac{q}{4m_e c^2} \nabla \vec{E}_{\text{laser}}^2 = \frac{\omega_p^2 m_e}{2q} \nabla \langle a_0^2 \rangle \quad (2.3)$$

where  $\vec{E}_{1r} = \vec{E}_{\text{laser}}$  and  $\omega_p \equiv \lambda_D / v_{th} = \sqrt{4\pi n_0^2 / m_e}$  corresponds to the plasma density wake perturbations frequency for the thermal velocity  $v_{th} = \sqrt{KT/m_e}$ . The dispersion relations in the plasma can be computed through *Fourier* and *Laplace* analysis according to the laser frequency and wavenumber values, with  $\vec{E}_{\text{wake}} = \vec{E}_w \exp i(\vec{k} \cdot \vec{r} - \omega t)$ , of the homogeneous solution ( $\langle \vec{F}_p \rangle = 0$ ). The longitudinal (i.e. along the laser propagation direction) quantities are labeled with the index  $\parallel$  and with  $\perp$  those perpendicular to it. The dispersion relations are:  $\omega^2 - \omega_p^2 = 0$ , and the wakefields oscillate at a frequency of  $\omega_p$ , or  $\omega^2 - \omega_p^2 - k_{\parallel}^2 c^2 - k_{\perp}^2 c^2 = 0$ . If the plasma response time,  $1/\omega_p$ , exceeds the period of oscillation of an external light wave,  $1/\omega_0$ , the plasma acts as a mirror, shielding the light out and reflects the wave.

If instead a relativistic particle beam with density profile  $n_b(\vec{r})$  of charges  $q_b$ , all with velocity  $v_b$ , is sent into the plasma, i. e. in a PWEA, then the motion of a single plasma electron is still governed by Eq. (2.1) with the fields resulting from the beam space charge instead of from the laser pulse, according to *Gauss' law* in the *Coulomb* gauge,  $\nabla \cdot \vec{A} = 0$ , gives  $\nabla \cdot \vec{E}_{\text{beam}} = \nabla^2 \Phi = 4\pi n_b q_b$ , where the scalar potential can be normalized to  $\phi_0 = \frac{1q\Phi}{m_e c^2}$ . A finite beam of electrons (or other negatively charged particles) will then be responsible for repelling plasma electrons radially whilst a positron beam (or other positively charged particles, such as protons) will attract them. The plasma ions are again considered immobile and their space charge generates the restoring force to sustain the wake. In this linear regime the superposition principle is valid and Eq. (2.3) would be [22, 45]:

$$-\nabla^2 \vec{E}_{\text{tot}} + \frac{\omega_p^2}{c^2} \vec{E}_{\text{tot}} + \frac{1}{c^2} \frac{\partial^2 \vec{E}_{\text{tot}}}{\partial t^2} = -\nabla (4\pi n_b q_b + 4\pi n_1 q) \quad (2.4)$$

The linearized plasma density wake fluctuations can be determined, for the case of a LWFA or a PWEA, from the time derivative of the plasma cold-fluid (cold here represents the restriction to

$\frac{1}{2}mv_1^2 \gg \frac{3}{2}k_B T$ ) continuity equation,  $\frac{\partial n_1 q}{\partial t} = -\nabla \cdot \vec{J} = -\nabla \cdot nq\vec{v}_1$  and the equation of motion, assuming the total force to only be due to the drivers, i.e.  $q\vec{E}_{\text{tot}} = q\vec{E}_{\text{beam}} + q\vec{E}_{\text{plasma}} + \langle \vec{F}_p \rangle / n_0$ , of each plasma electron to yield:

$$\frac{1}{n_0} \frac{\partial^2 n_1}{\partial t^2} + \omega_p^2 \frac{n_1}{n_0} = -\omega_p^2 \frac{n_b}{n_0} \frac{q_b}{q} + \frac{1}{2} c^2 \nabla^2 \langle a_0^2 \rangle \quad (2.5)$$

The corresponding homogeneous solution (computed taking the right side of the equation as null) is a harmonic oscillator at  $\omega_p$ ,  $G = A \sin(\omega_p(t-t')) + B \cos(\omega_p(t-t'))$ . Taking the right side of Eq. (2.5) as a the  $\delta$  function and integrating in time  $\int_{t'-\epsilon}^{t'+\epsilon} \frac{\partial^2 G}{\partial t'^2} dt + \int_{t'-\epsilon}^{t'+\epsilon} \omega_p^2 G dt = n_0$  in the limit of  $\epsilon \rightarrow 0$  yields  $\frac{\partial G}{\partial t} \Big|_0 = n_0$  and hence the retarder *Green's* function plasma density response  $G = \frac{n_0}{\omega_p} \sin(\omega_p(t-t'))$ . From  $G$  the general solution to Eq. (2.5), considering a drive particle beam or laser pulse, respectively, becomes  $n_1 = \frac{n_0}{\omega_p} \int_0^t dt' \sin(\omega_p(t-t')) \left( \omega_p^2 \frac{n_b}{n_0} \frac{q_b}{q} + \frac{1}{2} c^2 \nabla^2 \langle a_0^2 \rangle \right)$  and its transverse profile is directly related to the particle beam and the laser pulse envelope profiles.

In the **LWFA** setup where a finite laser pulse propagating in the  $z$  direction, having  $B_z = 0, E_z \rightarrow -\frac{\partial A_z}{\partial t} \rightarrow \omega_0 A_z = 0$ <sup>1</sup>, excites the plasma wake, the associated scalar potential is governed by  $\frac{\partial^2 \phi}{\partial t^2} + \omega_p^2 \phi = \frac{\omega_p^2}{2} \langle a_0^2 \rangle$  from where, applying the same *Green* function as before, the longitudinal wake electric field is:

$$E_{z\text{wake}} = -\frac{\partial}{\partial z} \Phi + 0 = \frac{\omega_p m_e c^2}{2q} \int_0^t dt' \sin(\omega_p(t-t')) \frac{\partial}{\partial z} \langle a_0^2 \rangle (t') \quad (2.6)$$

The laser ponderomotive force displaces the plasma electrons radially and so there is no significant longitudinal current nor azimuthal magnetic field to balance it (*Biot-Savart's* law),  $B_{\theta\text{wake}} = 0$ . Consequently, the oscillating radial field can be computed:

$$E_{r\text{wake}} = -\frac{\partial \Phi}{\partial r} = -\frac{\partial}{\partial r} \Phi + 0 = \frac{\omega_p m_e c^2}{2q} \int_0^t dt' \sin(\omega_p(t-t')) \frac{\partial}{\partial r} \langle a_0^2 \rangle (t') \quad (2.7)$$

To find the plasma wakefields formed behind a relativistic particle beam in the **PWFA** it is convenient to work in the coordinate system co-moving with the beam instead of the laboratory cartesian space-time variables<sup>2</sup>,  $(x, y, z, t) \rightarrow (x, y, \xi = z - ct, \tau = t)$ , for which the derivatives become  $\frac{\partial}{\partial z} = \frac{\partial}{\partial \xi}$  and  $\frac{\partial}{\partial t} = \frac{\partial}{\partial \tau} - c \frac{\partial}{\partial \xi}$ . The quasi-static beam approximation allows to assume that there is no variation in time of the beam, and so wakefields, in its reference frame,  $\frac{\partial}{\partial \tau} \rightarrow 0$ . Reducing Eq. (2.4) for the wakefield in the longitudinal direction to:

$$\left( -\nabla_{\perp}^2 + \frac{\omega_p^2}{c^2} \right) E_{z\text{total}} = -\frac{\partial}{\partial \xi} (4\pi n_b q_b + 4\pi n_1 q) \quad (2.8)$$

The homogeneous equation is  $\left( (k_p r)^2 \frac{\partial^2}{\partial (k_p r)^2} + k_p r \frac{\partial}{\partial k_p r} - k_p^2 r^2 \right) G_{E_z} = 0$  for an axis symmetric particle beam, corresponding to the zeroth-order modified *Bessel* differential equation, with solutions  $G_{E_z} = c_0 I_0(k_p r) + c_1 K_0(k_p r)$ . Applying the same reasoning as before gives the *Green's* function for a  $\frac{1}{k_p r} \delta(k_p(r-r_0))$  perturbation, with radial extent  $r_0$ . For the drive beams  $r_0$  corresponds to the radial effective size of the beam as perceived by the plasma electrons. The fields must vanish for  $r \rightarrow \infty$  and must be finite for  $r \rightarrow 0$ , thus the solution is piecewise,  $c_0 I_0(k_p r)$  for  $r < r_0$  and  $c_0 \frac{I_0(k_p r)}{K_0(k_p r_0)} K_0(k_p r)$

<sup>1</sup>There is no longitudinal field for a plane like wave front, which is the case for plane waves and for *Gaussian* laser pulses close to their beam waist region.

<sup>2</sup>The frame co-moving with the relativistic particle beam is considered to follow the plasma wake velocity,  $v_p$ , so that  $z - v_p t \approx z - ct$ , which is dictated by its velocity,  $v_b$  or for the frame following the laser its phase velocity.

otherwise. Here the  $r_0$  represents the beam transverse width. The integration of the field equation around  $r_0$  according to the *Bessel* function differentiation properties then yields  $c_0 = K_0(k_p r_0)$ . Behind the particle beam  $-\frac{\partial}{\partial \xi} 4\pi n_1 q = -\int_{\xi}^{\infty} d\xi' 4\pi n_b q_b k_p^2 \cos(k_p(\xi - \xi'))$  and the longitudinal electric field is  $E_{z\text{total}} = 4\pi k_p q_b \int_{\infty}^{\xi} d\xi' \int_0^{\infty} dr' r' \cos(k_p(\xi - \xi')) G_{E_z} n_b(\xi', r')$  [15, 22, 45].

The *Panofsky - Wenzel* theorem, of 1956, states that the integrated momentum gained by a relativistic electron,  $\Delta \vec{p} = \int_{t_0}^t \frac{d\vec{p}}{dt'} dt'$ , moving parallel to the propagation axis in a cavity excited in either a TE (no component of the electric field parallel to the axis) or TM mode (no component of the magnetic field parallel to the axis) is irrotational. Defining the plasma wakefields as the fields with which a paraxial electron, a relativistic electron propagating in the beam axis direction,  $v_0 \approx c$ ) in the **LWFA** or **PWFA** interacts, i.e.  $W_{\parallel} = E_z$  and  $W_{\perp} = E_{\perp} + v_0 \times B_{\theta}$  and the total momentum transferred to it  $\Delta \vec{p} = \int_{t_{-\infty}}^{\infty} q \vec{E} + q \frac{v_0}{c} \times B_{\theta} dt' = \int_{t_{-\infty}}^{\infty} W_{\parallel} + W_{\perp}$  verifies in the *Coulomb* gauge  $\nabla \times \Delta \vec{p} = q \int_{t_{-\infty}}^{\infty} -\nabla \times \nabla \Phi - \frac{1}{c} \frac{\partial B_{\theta}}{\partial t} + \frac{v_b}{c} \frac{\partial B_{\theta}}{\partial z} dt' = \int_{-\infty}^{\infty} -\frac{1}{c} \frac{\partial B_{\theta}}{\partial \tau'}$  which is null given that the plasma is in electrostatic equilibrium away from the beam,  $\vec{B}(\tau \rightarrow \pm\infty) = 0$ . Thus the *Panofsky - Wenzel* theorem translates into:

$$\frac{\partial \Delta p_{\perp}}{\partial \xi} = \nabla_{\perp} \partial \Delta p_{\parallel} \Rightarrow \frac{\partial W_{\perp}}{\partial \xi} = \nabla_{\perp} \partial W_{\parallel} \quad (2.9)$$

and a relativistic electron experiences the oscillating radial force proportional to  $W_{\perp}$ . In the case of the **PWFA** the radial force is given by  $W_{\perp} = 4\pi k_p q_b \int_{\infty}^{\xi} d\xi' \int_0^{\infty} dr' r' \sin(k_p(\xi - \xi')) \frac{\partial G_{E_z}}{\partial r} n_b(\xi', r')$  with  $\frac{\partial G_{E_z}}{\partial r} = \frac{k_p I_0(k_p r)}{I_0(k_p r_0)}$  for  $r < r_0$  and  $-\frac{k_p K_0(k_p r)}{K_0(k_p r_0)}$  for  $r > r_0$  otherwise. Thus, the transverse wakefield strength decreases for particles beyond the beam radius,  $r_0$ .

The general simpler profile of the drivers can be described with cylindrical symmetry,  $\frac{\partial}{\partial \theta} \rightarrow 0$ , a sinusoidal like function in its reference frame,  $\sin(\pi \xi / L_b)$ , valid in the interval  $[0, L_b]$ , with the beam length  $L_b$ , and a *Gaussian* radial profile of  $\exp\left(-\frac{r^2}{W^2}\right)$  when hitting the plasma, where  $W = \sqrt{2} \sigma_r$  and  $\sigma_r$  is the particle beam standard deviation or  $W \approx W_0$  that is the laser pulse spot size (beam evolution will be tackled in the next chapters) of amplitudes  $n_{b0}$  and  $a_0$ . Therefore, for the standard laser pulse  $\langle a_0^2 \rangle_{\omega_0} = \frac{a_0^2}{2} \exp\left(-\frac{2r^2}{W_0^2}\right) \sin^2(\pi \xi / L_b)$  and the wakefields are given by [43]:

$$W_{\parallel} = \frac{k_p m_e c^2 a_0^2}{4q} \exp\left(-\frac{2r^2}{W_0^2}\right) \frac{\pi}{4\pi^2 - k_p^2 L_b^2} \begin{cases} 2\pi \sin(k_p(L_b - \xi)) + 2\pi \sin(k_p \xi), & \xi \leq 0 \\ k_p L_b \sin\left(\frac{2\pi \xi}{L_b}\right) + 2\pi \sin(k_p(L_b - \xi)), & 0 \leq \xi \leq L_b \\ 0, & \text{otherwise} \end{cases} \quad (2.10)$$

$$W_{\perp} = -r \frac{k_p m_e c^2 a_0^2}{q W_0^2} \exp\left(-\frac{2r^2}{W_0^2}\right) \frac{\pi}{4k_p \pi^2 - k_p^3 L_b^2} \begin{cases} 4\pi \sin\left(\frac{k_p L_b}{2}\right) \sin\left(k_p\left(\frac{L_b}{2} - \xi\right)\right), & \xi \leq 0 \\ \frac{k_p^2 L_b^2}{2} \cos\left(\frac{2\pi \xi}{L_b}\right) - 2\pi^2 \cos(k_p(L_b - \xi)), & 0 \leq \xi \leq L_b \\ 0, & \text{otherwise} \end{cases} \quad (2.11)$$

The transverse force is 0 along the laser propagation axis. If the laser pulse length is the double of the plasma wavelength,  $L_b = 2\lambda_p = \frac{4\pi}{k_p}$ , then both wakefields vanish behind the pulse and the setup is no longer useful for acceleration of electrons. If instead it is equal,  $L_b = \lambda_p = \frac{2\pi}{k_p}$  then the wakefields have maximum amplitude and it follows that  $W_{\parallel}(L_b = \frac{2\pi}{k_p}) = \frac{\pi k_p m_e c^2 a_0^2}{8q} \exp\left(-\frac{2r^2}{W_0^2}\right) \cos(k_p \xi)$  while  $W_{\perp}(L_b = \frac{2\pi}{k_p}) = -r \frac{\pi m_e c^2 a_0^2}{2q W_0^2} \exp\left(-\frac{2r^2}{W_0^2}\right) \sin(k_p \xi)$ . Moreover, the on-axis amplitude of  $W_{\parallel}$  is

$\frac{\pi m_e c^2 k_p a_0^2}{8q} \cos(k_p \xi)$  that introduces the longitudinal motion in each electron starting close to the laser pulse propagation axis, from Eq. (2.2), of  $\xi = \xi_0 + \frac{\pi a_0^2}{8k_p} \cos(k_p \xi)$ . Numerically solving this equation shows that as  $a_0$  approaches  $\sqrt{\frac{8}{\pi}}$  the trajectory becomes nonlinear and sawtooth like. For higher  $a_0$  values, the plasma fluid velocity can locally exceed the phase velocity, the plasma wake breaks and there is electron sheet crossing (instead of secular motion). The cold plasma non relativistic wave breaking field amplitude then is  $E_{WB} \equiv \frac{k_p m_e c^2}{|q|}$  corresponding to  $96.1 \sqrt{n_0 [\text{cm}^{-3}]} [\text{V/m}]$  [46]. The linear regime of the LWFA is thus limited to the laser pulse strength of  $a_0 \ll \sqrt{\frac{8}{\pi}} = 1.6$ .

For the general particle beam profile it is advantageous to focus on the longitudinal beam configuration influence in the wakefields it excites, separating the normalized ( $\times k_p^2$ ) radial integration into  $R(r)$  and getting:

$$W_{\parallel} = 4\pi q_b n_{b0} R(r) \frac{L_b \pi}{\pi^2 - k_p^2 L_b^2} \begin{cases} \cos(k_p(L_b - \xi)) + \cos(k_p \xi), & \xi \leq 0 \\ \cos(k_p(L_b - \xi)) + \cos\left(\frac{\pi \xi}{L_b}\right), & 0 \leq \xi \leq L_b \\ 0, & \text{otherwise} \end{cases} \quad (2.12)$$

$$W_{\perp} = -4\pi q_b n_{b0} \frac{\partial R(r)}{\partial r} \frac{L_b}{\pi^2 k_p - k_p^3 L_b^2} \begin{cases} 2\pi \cos\left(\frac{k_p L_b}{2}\right) \sin\left(k_p \left(\frac{L_b}{2} - \xi\right)\right), & \xi \leq 0 \\ \pi \sin(k_p(L_b - \xi)) - k_p \sin\left(\frac{\pi \xi}{L_b}\right), & 0 \leq \xi \leq L_b \\ 0, & \text{otherwise} \end{cases} \quad (2.13)$$

If the particle beam length (in the case of the profile mentioned here that is a first approximation to realistic scenarios) is 3/2 of the plasma wavelength,  $L_b = \frac{3}{2} \lambda_p = \frac{3\pi}{k_p}$  then both PWFA wakefields vanish behind the beam. The peak field is found when  $L_b \approx \frac{2}{3} \lambda_p = \frac{4\pi}{3k_p}$ . If instead  $L_b = \frac{1}{2} \lambda_p = \frac{\pi}{k_p}$  then it is possible to simplify the wakefields behind the beam to  $W_{\parallel} = 2\pi^2 \frac{1}{k_p} q_b n_{b0} R(r) \sin(k_p \xi)$  and  $W_{\perp} = -2\pi^2 \frac{1}{k_p^2} q_b n_{b0} \frac{\partial R(r)}{\partial r} \cos(k_p \xi)$ . In this case the wave breaking limit is reached when the beam charge density relative to the plasma is  $\frac{q_b n_{b0}}{q n_0} = \frac{2}{\pi} \approx 0.6$  close to which the PWFA wakefields become nonlinear. In the linear regime the difference between using a positive or a negative charge beam translates into making a shift of  $\pi$  in the plasma wakefields phase, because instead of repelling the plasma electrons, positive charges will attract them. On the beam propagation axis the radial function is given by  $R(0) = k_p^2 \int_0^{\infty} dr' r' K_0(k_p r') \exp\left(-\frac{r'^2}{2\sigma_r^2}\right)$  and for narrow beams,  $k_p \sigma_r \ll 1$ , it can be approximated by  $k_p^2 \sigma_r^2 (0.05797 - \ln(k_p \sigma_r))$  [47, 48].

The  $\pi/2$  phase difference between the peak longitudinal and transverse wakefields,  $W_{\parallel}$  and  $W_{\perp}$ , imposes that the simultaneously focusing and accelerating regions are confined within 1/4 of the plasma wake, i. e. within a  $\xi$  range of  $\frac{\pi}{4k_p}$ , for both PWFA or LWFA techniques.

Different interesting bunch shapes, with triangular or longitudinal gaussian profiles, have been carefully explored in the past and are detailed, for example, in [19, 22, 45, 47] where tailored particle beams are used to beam load the plasma wake, i.e. to extract all the energy from the wake oscillations (absorbing the wakefields after it).

## 2.2 Wakefields in the standard nonlinear bubble/blowout regime

To take full advantage of using the plasma as the medium to transfer the energy, the highest fields possible are desirable. That is why the nonlinear LWFA bubble [49-51] and electron driven PWFA [48]

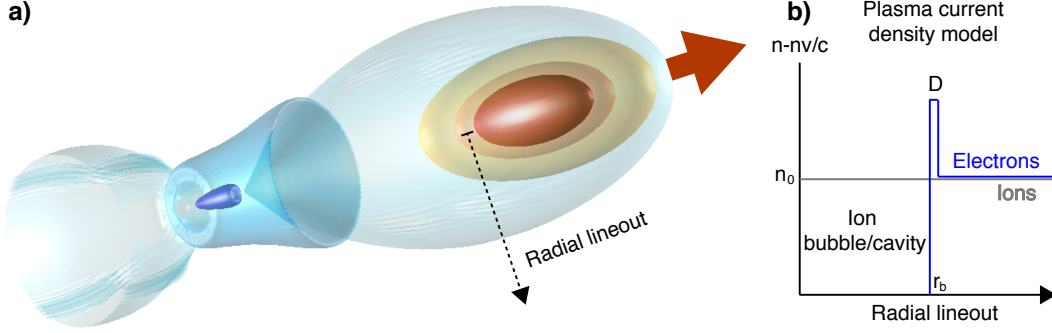


**Figure 2.2:** a) 3D visualization of a plasma based wakefield acceleration scheme close to the nonlinear regime, where the plasma electron density isosurfaces are represented by the blue envelopes and the beam, which propagates in the direction of the red arrow, density in the red ones (higher density regions have darker colors). This simulation was done, in collaboration with professor Olle Lundh and using the real electron beam parameters available at the MAX IV injector facility in the Lund University [53], to explore the capability of a possible PWFA to be built there. b) Approximate model of the lineout of the radial current density of plasma electrons (blue) and ions (gray) at the center of the bubble/cavity (dashed line of plot a).

[52] blowout scenarios, associated with sheath crossing and wave breaking [46], have been extensively studied. Figure 2.2 a) depicts the 3D image of the plasma being radially expelled from the front of the energetic high intensity laser pulse or very dense electron beam driver, as discussed above, leaving behind a cavity completely void of electrons, also referred to as bubble, forming a nonlinear density wake. For the following arguments the plasma electron and ion density profile are modeled by a sphere without electrons, a thin spherical sheath of high density of electrons surrounding it and a further region where the plasma is quasi-neutral and the perturbations are linear, see Fig. 2.2 plot b).

The *Hamiltonian* of a charged relativistic particle, with  $q_i$  charge, in the reference frame co-moving with the LWFA is given by  $H(x, y, \xi = z - v_p t, \tau) = m_e c^2 \gamma + q\Phi - v_p P_z$ . The quasi-static approximation, valid when the plasma wakefields and drive beam or pulse do not evolve significantly in the time scale of the accelerated particle motion, leads to the integral  $\int \frac{dH}{dt} dt = \int \frac{dH}{d\xi} \frac{d\xi}{dt} d\xi = \int \frac{dH}{d\xi} \frac{1}{v_z - v_p} d\xi = 0$  and using the canonical momentum evolution,  $\vec{P}_H$ , to the general condition of  $\int (m_e c^2 \gamma - v_p p_z - v_p \frac{q_i}{c} A_z + q_i \Phi) d\xi = 0$ . Taking the average over the fast oscillations of the laser field (or the beam perturbations) that its transverse oscillations in the laser field are negligible, that  $v_p \rightarrow c$ , and considering that the particle started from rest,  $\gamma_0, p_{z0} = 0$ , means that its constant of motion is given by [54]:

$$\langle \gamma \rangle m_e c - \langle p_z \rangle = \langle \gamma \rangle m_e c \left( 1 - \left\langle \frac{v_z}{c} \right\rangle \right) = m_e c + \frac{q_i}{c} (\langle A_z \rangle - \langle \Phi \rangle) \equiv mc + \frac{q_i}{c} \langle \Psi \rangle \quad (2.14)$$

where  $\Psi$  is the commonly designated in literature as the plasma wake pseudo potential,  $E_z = \frac{\partial \Psi}{\partial \xi}$ , that, in, for simplicity, the Lorentz gauge,  $\nabla \cdot \vec{A} = \frac{\partial \Phi}{\partial \xi} \Rightarrow \nabla_{\perp} \cdot A_{\perp} = -\frac{\partial \Psi}{\partial \xi}$ , and obeying Maxwell's equations, verifies the Poisson like equation:

$$\nabla_{\perp}^2 \Psi = -4\pi(nq + n_b q_b + n_0 q_{ion}) + \frac{4\pi}{c}(nq v_z + n_b q_b v_b) \quad (2.15)$$

, where  $n_0 q_{ion}$  represents the plasma ion charge density. Equation 2.14 shows that when the particle is counter-propagating in respect to the wakefields  $\Psi \rightarrow \infty$  whilst if it is trapped so that  $v_z \rightarrow v_p \approx c$  then would have to see  $\Psi \rightarrow -1$ . For convenience we drop the  $\langle \rangle$  in the following discussion. The time

<sup>3</sup>Extra care must be taken when determining the trapping condition because longitudinally trapped particles violate the limit

total derivative can then be written as a function of the longitudinal co-moving derivative  $\frac{d}{dt} = \frac{1+\Psi}{\gamma} \frac{d}{d\xi}$ . Resorting once again to cylindrical symmetry, plus the idea that the plasma density oscillations and hence wakefields can be separated into a purely longitudinal, depending solely on  $(\xi)$ , and a radial,  $r$ , function and the logic of the cylindrical *Green* functions as in Sec. 2.1, results in the following form of *Ampère's* law:

$$\left(\nabla^2 \vec{A}\right)_{\perp} = \frac{4\pi}{c} (nq\vec{v} + n_b q_b \vec{v}_b) \quad (2.16)$$

In the nonlinear regime inside the ion bubble  $nq$ ,  $nq \frac{v_z}{c}$  vanishes (see the model depicted in Fig. 2.2 b)). Assuming a very short drive is used then the electromagnetic potentials behind it and in the center of the bubble are:  $A_r = A_{r0}(\xi)r$ ,  $A_z = A_{z0}(\xi) - 2\pi \left(\int_0^\infty r' n_b(r', \xi) q_b \frac{v_b}{c} dr'\right) \log r$ ,  $\Phi = \Phi_0(\xi) - 2\pi \left(\int_0^\infty r' n_b(r', \xi) q_b dr'\right) \log r - r^2 \pi n_0 q_{ion}$  and also, for the case that  $\frac{v_b}{c} \rightarrow 1$ , the value of  $\Psi = \Psi_0(\xi) - r^2 \pi n_0 q_{ion}$  as long as  $A_{r0} = -\frac{1}{2} \frac{\partial \Psi_0}{\partial \xi}$ . The continuity equation in this regime reads  $\frac{\partial}{\partial \xi} (nq + n_0 q_{ion}) = \frac{\partial}{\partial \xi} nq \frac{v_z}{c} + \frac{1}{r} \frac{\partial}{\partial r} r nq \frac{v_r}{c}$  that integrated over all transverse space yields  $\frac{\partial}{\partial \xi} \int_0^\infty r' (nq + n_0 q_{ion} - nq \frac{v_z}{c}) dr' = 0$  so that the source term of  $\Psi$  is, behind the driver, conserved.

Using the radial equation of motion, from the *Lorentz* force with the ponderomotive force or the electron beam space charge and current contributions, of the plasma electrons sheath at  $(r, \xi)$  we can determine the maximum radius of the ion, sphere like, bubble  $r_b$  region as  $r_b k_p \approx 2\sqrt{a_0}$ , in the case of an intense laser pulse and  $r_b k_p \approx 2$  for narrow,  $\sigma_r \ll r_b$  electron bunches. The plasma continuity equation behind the beam allows to write the current density of the narrow region, width  $D$ , that surrounds the ion bubble (Fig. 2.2 b)). If  $D \gg r_b$  then it is but a small (linear) perturbation to the plasma equilibrium current density ( $n_0$ ) and the plasma response is said to be non-relativistic, this is usually the case of wakes excited by particle bunches. On the other hand, if  $D \ll r_b$  then in a very short region the current density spikes. This latter ultra-relativistic nonlinear plasma blowout regime is generally driven by laser pulses. The source terms to find  $\Psi$  were determined for both scenarios in [48] and close to the center of the bubble, where the radius is maximum, the plasma wakefields behind the driver were found to follow:

$$\begin{aligned} W_{\parallel \text{Blowout}}(\xi) &= E_z = -\frac{m_e \omega_p^2 \xi}{2q} \\ W_{\perp \text{Blowout}}(r) &= E_r - B_\theta = -\frac{m_e \omega_p^2}{2q} r \end{aligned} \quad (2.17)$$

The momentum evolution of a plasma electron within the  $D$  sheath region, with the parameterization  $r^2 + \xi^2 \approx r_b^2$  and so  $\int_0^\xi d\xi' \rightarrow \int_{r_b^2 - \xi^2}^{r_b^2} \frac{r'}{\xi} dr'$ , immersed in those nonlinear wakefields becomes  $p_z = -\frac{m_e \omega_p^2}{4q} (r_b^2 - \xi^2)$ . The peak accelerating field is at the back of the bubble  $E_{zmax} \approx -\frac{m_e \omega_p^2}{2q} r_b$ . These wakefields can be derived from the wake associate **EM** potential  $\Phi_w = \frac{m_e \omega_p^2}{q} |\vec{r}|^2$ .

To discover the radial motion of particles that are trapped and clustered at the back of the bubble (moving mostly inside an ion column) and radially away from the laser pulse or beam propagation axis, with charge  $q_t$  and mass  $m_t$ , plus the *Lorentz* relativistic factor  $\gamma_p$  at the phase velocity of the plasma wake,  $\gamma_p \approx \frac{\omega_0}{\omega_p}$  for a **LWFA** and  $\gamma_p \approx \gamma_b$  for a **PWFA**, we return to the co-moving *Hamiltonian* written above and linearize around the case of  $p_{\perp} \ll p_z \approx m_t c$ , i.e.  $\gamma \approx \frac{P_{Hz}}{m_t c}$ . To zeroth order that for the ponderomotive force approach [54]. In [48] the more accurate trapping condition is taken to be  $1 + \Psi = \frac{\gamma}{\gamma_p}$ .

yields  $H_0 m_0 c \approx P_{Hz} + \frac{1}{2P_{Hz}} + \frac{1}{4} \frac{m_e q_t}{m_0 q} \omega_p^2 \xi^2$  and to first order  $H_1 = \frac{(\vec{P}_{H\perp} - \frac{q_t}{c} \vec{A})^2}{2P_{Hz} m_0 c} + \frac{1}{4} \frac{m_e q_t}{m_0 q} \omega_p^2 r_{\perp}^2$ . The resulting equations of motion describe a longitudinal drift coupled to a driven harmonic oscillator at the betatron (almost fixed) frequency  $\omega_{\beta} = \frac{\omega_p \sqrt{m_e c}}{\sqrt{2P_{Hz}}} \approx \omega_p \sqrt{2\gamma_p}$ , through the relativistic mass effect<sup>4</sup>.

The transverse betatron motion of accelerated particles and of particles of the drive beam (in the case of the [PWFA](#)) lead to the spontaneous emission of radiation, see Sec. [2.4](#), in similar fashion as in a synchrotron, in particular of collimated broadband beam of x-rays [\[56–58\]](#). These are crucial for multiple applications, from radiotherapy and nuclear medicine to diagnostics for industry and the defence sectors to plasma radiography, material and isotope detection, nuclear waste treatment and semiconductor imaging [\[20\]](#). One plasma wakefield scheme that has been proposed to generate directional, small-divergence, and short-duration picosecond x-ray probe beam with an energy greater than 50 keV is the Self-Modulated Laser Wakefield Accelerator ([SM-LWFA](#)) driven by relativistic long laser pulses [\[59, 60\]](#) where the electrons perform betatron oscillations in a nonlinear plasma electron density wake region and in a plasma hollow channel, generated by the resonant wakefields and laser fields repelling the plasma ions over the length of the long laser pulse, while being accelerated directly by the laser [\[61, 62\]](#). The Direct Laser Acceleration of electrons in plasma wakefields ([DLA](#)) and the x-ray radiation phenomena in that nonlinear plasma wakefield scheme are understood through experiments done at University of California Los Angeles ([UCLA](#)) and Lawrence Livermore National Laboratory ([LLNL](#)) and numerical simulations using the Particle-In-Cell ([PIC](#)) code OSIRIS and the jRad post-processing tool that are briefly described in Section [2.5](#), explained in Chapters [3](#) and [4](#).

## 2.3 Nonlinear plasma wakefield regime driven by a positron beam

Lee et al. introduced in [\[63\]](#) the suck-in regime obtained when instead of the intense laser pulses or electron beams a positron beam is used to excite the nonlinear plasma electron density wake oscillations. The positron driven linear scenario can be understood as the positron beam strongly attracts the plasma electrons that get sucked into it to neutralise its space charge. Those electrons are later dispersed by their own electromagnetic repulsion as the beam travels through, starting the plasma wake. Consequently, the difference between having electrons or positrons driving the wake is simple the sign change in the force, leading to a phase shift in the wakefields of  $\frac{\pi}{2}$  in the linear regime. Intuitively this would make us believe that the analytical description of the nonlinear regime could be taken from a mere sign change of the bubble or blowout predicted wakefields, Eq. [\(2.17\)](#), but simulations and experiments showed that a different analytical model is required to characterise the suck-in regime. The physical origin of the difference comes from the phase mixing that occurs when the electrons are radially sucked-in by the beam, even before the first bubble is formed.

For simplicity we take the beam to be infinitely long thin cylinder of radius  $r_b$  and using *Gauss's* theorem we can find the radial field to be  $E_r = 2\pi r [n_b q_b + n_i q_i + nq]$ . Considering that after the electrons collapsed into the beam it is completely neutralized, meaning that  $n = n_0 + n_1$  with  $n_0 = n_i$  and that the charge is conserved in each electron ring-like structure,  $\pi n_1 q r^2 = -\pi n_b q_b r_b^2$ . When the

<sup>4</sup>Explicit analysis of the betatron induced motion of electrons trapped in the bubble excited by a (circularly polarized) high intensity laser follows the *Wentzel-Kramers-Brillouin* (WKB) method [\[55\]](#) ([\[54\]](#)).

beam passes by the resulting electron density is still close to  $n_1 = -\frac{n_b q_b r_b^2}{qr}$  and so the transverse field becomes  $-2\pi \frac{n_b q_b r_b^2}{qr}$ . For the plasma electrons this results in the radial force (assuming the motion of these electrons has  $v_1 \ll c$  and so the magnetic influence being negligible):

$$\frac{d^2 r}{dt^2} = -\omega_p^2 \frac{n_b q_b}{n_0 |q|} \frac{r_b^2}{r} \equiv -\omega_b^2 \frac{r_b^2}{r} \quad (2.18)$$

Electrons that are close to the beam propagation axis, at  $r(t=0) = r_0 \approx 0$ , will reach (and cross) the axis in a very short time  $\frac{d}{dt} \approx \frac{1}{\Delta t}$  that can be estimated from Eq. (2.18) as  $\Delta t \approx \frac{\Delta r}{\omega_b r_b} = \frac{r_0}{\omega_b r_b}$ . This time period is not directly dependent on the plasma density but the beam one. Moreover, as long as the beam radius and density are fixed, which is valid in scales shorter than the beam's betatron distance, the compression phase region is too. Different initial positions inside the beam,  $r_0$ , lead to different travel time periods for the respective plasma electrons collapsing on the axis and, consequently, to phase mixing. This limits the attainable longitudinal accelerating wakefield, [63, 64].

Preliminary experiments showed that the propagation of positron beams in underdense plasmas results in their distortions and deflections and that are mitigated if instead a plasma hollow channel, where the particles beneath a certain radius,  $r_c < r_b$ , were not ionized, is utilised to guide the positron beam and generate plasma wakes without the risk of phase mixing [64, 65]. More recent studies corroborated those results and that the positron beam suffers emittance growth, manifested in a halo formation and an increase in beam spot size with plasma density (going from linear to the nonlinear regime), as it travels through an uniform plasma [66].

Figure 2.3 contains the illustrations, from simulations done with the PIC code OSIRIS-3D version 4, see Sec. 2.5.1, of the mildly nonlinear regime, that was explored in [63], excited by an electron, plot a) corresponding almost to the bubble regime and positron, plot b) the suck-in case, bi-gaussian beams propagating in an uniform plasma. These show two clear distinct plasma wake structures being formed. This is because phase mixing occurs in the beam already for case b) whilst it only occurs at the end of the first bubble of plot a). Scenario b) shows doughnut like regions with the lowest (lighter blue/white) and highest (darker blue) plasma electron concentrations. Therefore, any charge particles that propagate along the same axis as the drive positron beam will not feel the peak accelerating wakefield and will defocus making this scheme unsuitable for the purpose of acceleration.

In Fig. 2.3 c) the on-axis accelerating wakefields are plotted for both operating regimes. The suck-in has lower accelerating wakefields, (dashed green line) the positive peaks reach less than half than in the blowout (solid red line). But the bubble regime is also not ideal for accelerating a trailing positron beam because the region that it provides for its propagation to have mainly focusing, so without jeopardising its emittance, and accelerating forces is narrower and shorter (green dashed and shaded box in plot c)) than the equivalent region for an electron beam (red dashed and shaded box). Thus the amount of positron charge the blowout PWFA can accelerate is less than the electron charge and it is technically demanding to create a positron beam to fit in that region making it overall very inefficient for positron acceleration. For this reason, we proposed a novel plasma wakefield technique in which a drive tightly focused positron bunch generates a hollow plasma channel in its tail, forcing the electron and ion density and consequently the defocusing wakefields to vanish on the propagation

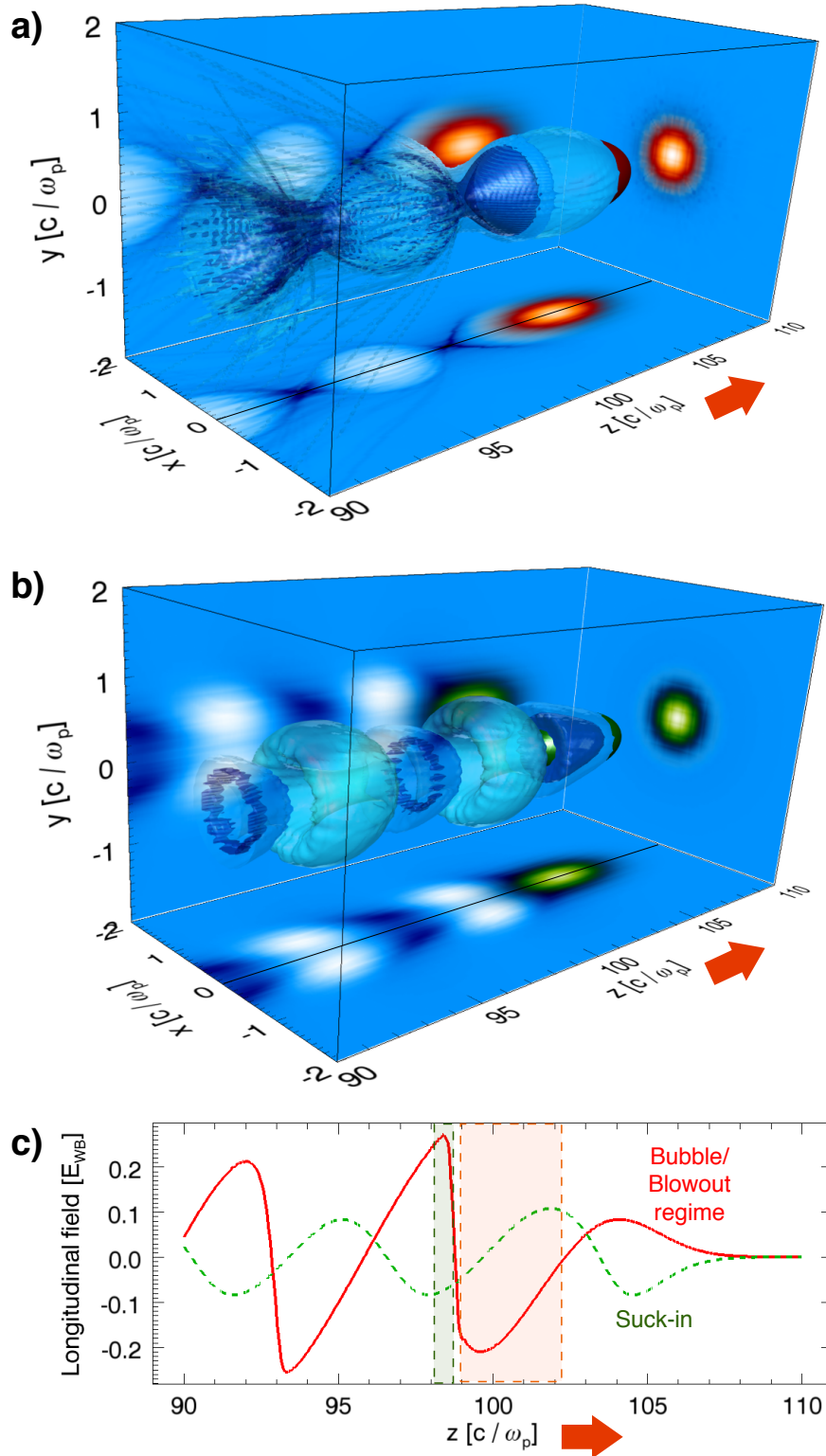


**Figure 2.3:** 3D OSIRIS 4 simulation results showing the mildly nonlinear plasma wake density perturbations by a) an electron beam (red color scale represents its density) and b) a positron beam (green color scale) propagating in an uniform plasma with  $n_0 \approx 4.3 \times 10^{14}$  (blue color scale). Isosurfaces were coloured for the plasma densities of  $0.85, 1.2$  and  $1.7 \times n_0$  and for the beam density of  $0.2 \times n_0$ . Projections show the integrated charge density along their respective perpendicular direction. The beam parameters were set as  $n_b = 1.3n_0$ ,  $\sigma_z = 1.5c/\omega_p$ , and  $\sigma_r = 0.28c/\omega_p$  following [63]. Plot c) represent the on-axis (indicated by the black solid line in the 3D a) and b) plots) longitudinal electric field for both scenarios. Dashed squares roughly depict focusing and accelerating regions for trailing positron (green) and electron (red) beams placed in the bubble of a).

axis, as well as highly nonlinear accelerating gradients that are ideal for accelerating trailing positron beams, see Chapter 5.

To take advantage of the extremely high energy, up to several TeVs, but too long when compared to the suitable plasma wake wavelength for the suck-in regime, proton beams available at European Organization for Nuclear Research (CERN)'s Large Hadron Collider (LHC) and Super Proton Synchrotron (SPS), to accelerate electron beams another operating scheme was studied, the Self-Modulated Particle beam driven Wakefield Accelerator (SM-PWFA), in which the plasma defocusing wakefields split the long beam into a sequence of beamlets distanced by the plasma wavelength, in what is named the beam self-modulation instability, that resonantly excite the accelerating wakefields up to nonlinear-like values. Firstly, to study how the instability applies to positive charges we participated in the E-209 experiment at National Accelerator Laboratory in California (SLAC) and provided numerical support for the CERN AWAKE experiment. This work integrates Chapter 6.

## 2.4 Betatron radiation

In general, a single particle, an electron for example, in an arbitrary motion,  $\vec{r}$  with velocity  $\vec{v} = \beta c$ , emits radiation - an irreversible flow of EM energy to the universe - according to the *Lienard-Wiechert* potentials from which the energy spectrum can be computed through [67]:

$$\frac{d^2W}{d\omega d\Omega} = \frac{e^2\omega^2}{4\pi^2c} \left| \int_{-T/2}^{T/2} [\vec{n} \times (\vec{n} \times \vec{\beta})] \exp[i\omega(t - \vec{n} \cdot \vec{r}/c)]^2 dt \right. \quad (2.19)$$

where the left side represents the energy per photon frequency,  $\omega$ , per solid angle  $\Omega$ , during the interaction time,  $T$ , that is radiated along the unit vector  $\vec{n}$  direction.

For an electron trapped in the LWFA or PWFA, performing a high number of transverse  $N_\beta = \frac{\omega_\beta L}{2\pi c}$  betatron oscillations, within the radius  $r_\beta$ , in a plasma of length  $L$ , characterised by a high wiggler (betatron) strength parameter  $a_\beta^2 = (\gamma_{z0} k_\beta r_\beta)^2 \gg 1$ , and for a detector placed in the plane perpendicular to the propagation axis of the drivers capturing photons that came at the angle  $\theta$ , the total radiation emitted does not consist of a sequence of several narrow bandwidth harmonics but of a broadband spectrum that peaks around the critical frequency  $\omega_c \approx 3a_\beta \gamma_{z0}^2 \omega_\beta$  and is given by [56]:

$$\frac{d^2W}{d\omega d\Omega} \approx N_\beta \frac{6e^2}{\pi^2 c} \frac{\gamma_{z0}^2 \zeta^2}{(1 + \gamma_{z0}^2 \theta^2)} \left[ \frac{\gamma_{z0}^2 \theta^2}{(1 + \gamma_{z0}^2 \theta^2)} K_{1/3}^2(\zeta) + K_{2/3}^2(\zeta) \right] \quad (2.20)$$

where  $K_{1/3}, K_{2/3}$  are the modified *Bessel* functions of second kind of fractional orders and  $\zeta = \frac{\omega}{\omega_c} (1 + \gamma_{z0}^2 \theta^2)^{3/2}$ . At the center of the detector,  $\theta = 0$ , the radiation peaks at  $\omega = \frac{1}{2}\omega_c$ . Eq. (2.20) is maximum for  $\omega \approx 0.45\omega_c$  whilst the spectrum emitted integrated over the full space,  $\frac{dW}{d\omega}$ , peaks at  $\omega \approx 0.3\omega_c$ . Note that, from the analytical standpoint, more energetic particles, with higher  $\gamma_{z0}$ , have higher  $a_\beta$  and  $\zeta$  values and emit more radiation/photons. The width of the betatron oscillations influences  $a_\beta$  and determines the critical frequency of the photons.

The first experimental observation of betatron x-ray production in plasma wakefield acceleration schemes was in a PWFA driven by a 28.5 GeV electron beam propagating in an underdense 1.4 m long plasma at SLAC in 2002, [68]. The forwards emitted radiation had a divergence angle of 0.1-0.3 mrad and peak brightness at 14.2 KeV located at the hard x-ray portion of the light spectrum.

Because the electrons trajectories are not simple and their initial conditions vary within the wakefields framework several techniques and models have been proposed to corroborate the experimental measurements. In our group Joana L. Martins has developed a post-processing tool capable of determining the radiation generated in different laser-beam-plasma regimes, with and without Quantum Electrodynamics (QED) effects for example [69], where Eq. (2.19) is applied to the trajectory, momentum and field information of hundreds of particles determined by the PIC code OSIRIS, named jRad [70–72]. Both numerical tools were used for the work of this dissertation and will be briefly introduced in the following sections.

## 2.5 Numerical infrastructures

In pursuit of a better understanding and modeling of the complex phenomena that occur in plasma based compact acceleration environments, in which non-linear plasma wakes interplay with powerful lasers to induce the motion of billions of particles, such as the ones described this far, several numerical codes have been utilized. In particular, the topic of wakefield acceleration has advanced greatly with the development of kinetic particle calculation PIC codes, where electric and magnetic fields, particle currents and charges are discretized and stored on a multi-dimensional spacial grid of multiple cells simulation domain whilst the particles are represented in a statistical finite-sized cloud of an ensemble, named macro-particle, that is initialized in each grid cell and that moves continuously in space but discretely through time. By not relying in particle-particle calculations and by resorting to the use of macro-particles the computational cost and is greatly reduced.

For the work summarised in this dissertation the code OSIRIS with 2D, 3D and Quasi-3D cartesian particle and grid coordinate systems, in versions 3.0 and 4.0, and code QuickPIC was employed and thus it will be carefully described in the following paragraphs. Moreover, the visualization infrastructure utilized was the IDL data software provided by Harris Geospatial Solutions, with tools that have been developed internally, VisXD.

### 2.5.1 Particle-In-Cell code OSIRIS 3.0 and 4.0

For over a decade the OSIRIS consortium, consisting of Instituto Superior Técnico - Universidade de Lisboa (IST) and UCLA, has been dedicated to the improvement of the wide array of features and physics models present in the state-of-the-art multi-dimensional fully relativistic massively parallel PIC code OSIRIS [73]. The standard PIC technique, dating to the 50s, is used to self-consistently solve *Maxwell's* partial differential equations (i.e. their finite difference version) in a grid of points, named cells. The particles (or their ensemble representation, which is more useful for modeling plasmas that contain, for example,  $10^{19}$  electrons and/or ions in a  $\text{cm}^3$  electrons and ions) are pushed over all the space of the grid whilst their density and current information is deposited on each of the (field) grid cell position.

Different PIC algorithms have been implemented for more efficient modeling including the moving window technique, [74], the Lorentz boosted frame domain [75–78], the hybrid PIC geometry

and gridless description in the azimuthal direction [79, 80], the hybrid finite difference Yee [81] and Fast Fourier Transform algorithm (FFT) Maxwell solver [82, 83], the particle merging method [84, 85] and the ponderomotive guiding center Ponderomotive Guiding Center approximation (PGC) theory for modeling laser propagation [54, 86–88]. Furthermore, OSIRIS enables the use of distinct models including the *Ammosov Delone Krainov* ionization model (ADK) [89], binary collisions [90] and quantum electrodynamics physics [91]. A spherical coordinate system and a co-rotating sheering mode are being implemented into OSIRIS to model different astrophysical interesting scenarios like pulsar magnetospheres and the turbulence originated in the magneto-rotating-instability by Fabio Cruz et al., and Giannandrea Inchingolo et al.

In OSIRIS the algorithm cycle can be viewed as a sequence of:

- a) finite difference integration of *Maxwell's* partial differential equations to determine the electric and magnetic fields in the grid,
- b) interpolation of those fields values from the grid points to the position of each particle,
- c) finite difference integration of each particle *Lorentz* equation of motion,
- d) particle pushing to new position at subsequent time step and
- e) particle current deposition in the grid points to be used in *Maxwell's* equations in a).

For all these operations the used units are normalized to the characteristic laser and plasma parameters so that each simulation represents physical phenomena occurring over a wide range of realistic laboratory configurations.

The numerical finite difference methods used in the OSIRIS algorithm can only be stable, and accurately model the relativistic particle motion, **PWFA** and **LWFA** devices and the numerical dispersion relation for the propagation of **EM** waves in the grid, if the physical speed of light is smaller than the simulation spreading velocity (finite difference time operator over the finite difference space one). In other words, the *Courant-Friedrichs-Lewy* condition [92] must be respected<sup>5</sup>. For 3D rectangular grid cell dimensions given by  $\Delta x \times \Delta y \times \Delta z$ , in normalized units (with respect to the scale of interest - typically for our work the plasma equilibrium frequency), the *Courant* time step is:

$$\Delta t = \frac{100\%}{\sqrt{1/\Delta x^2 + 1/\Delta y^2 + 1/\Delta z^2}} \quad (2.21)$$

we usually use 99.8% $\Delta t$  for the simulation time step, for 2D runs 95% and for 2D runs employing cylindrical symmetry 67%.

The simulations of Sec. 3.3, done respecting Eq. 2.21 also used the optical field ionization **ADK** (quasi-static tunneling / barrier suppression ionization) model that takes place when the Keldysh parameter<sup>6</sup> is small ( $\ll 1$ ). That parameter measures the ration between the tunneling time and the laser period and is used to define the transition between the regimes where the tunnel ionization

<sup>5</sup>This is, intuitively, in one dimension simulations, equivalent to the notion that the time step chosen must be smaller than the time taken for the wave to travel the distance of the spatial step

<sup>6</sup>The Keldysh adimensional parameter is the ratio between the ionization potential and the electron quiver energy in the laser field.

process is more efficient than multi-photon ionization and vice versa. This model can be applied as long as the laser pulse can be considered static, i.e., when its frequency is much lower than the atomic transitions frequency ( $\sim$  PHz). The laser field deforms the nuclear potential barrier of the electron in the atom. If the optical laser field is strong enough the electron can overcome the barrier and becomes free - is ionized.

The ionization is calculated on the simulation grid. This implies that in every time step the code calculates the ionization rate based in the **ADK** coefficients and model using the **EM** field values for each cell. Neutral macro particles are initialized and move through the grid. The computed rates are used along with the neutral integrated density of each cell to determine the total ionization density (i.e. the percentage of ions that have been ionized) within that cell. When the level of ionization density reaches the minimum threshold for ionization an electron macro particle is injected in that cell. If the neutral associated electron species was configured to have only 1 particle per cell then only when the ionization density is above 50% will the electron be injected. With multiple particles per cell a more gradual and accurate ionization process is modeled. The code can account for multiple ionization levels of neutrals, calculating the ionization rates and ionization densities for each of those levels.

### 2.5.1.A Hybrid Particle-In-Cell and a girdles azimuthal description code version of OSIRIS Quasi-3D

Fully 3D simulations done with OSIRIS become computationally demanding for modelling long laser plasma interactions or high density beam driven hollow channels. For that reason a model of OSIRIS was created by Asher Davidson et. al., [80] where the fields were solved in  $(r, z)$  grids, for as many azimuthal modes as selected by the user and the particles were then pushed in the 3D grid space. This code was necessary for the field azimuthal analysis of complex scenarios. The correct *Courant* time step for the simulations using the Quasi-3D framework is complex to define analytically and we tested a fraction of that of the 2D-cylindrical setup.

### 2.5.2 QuickPIC and PGC

QuickPIC is a highly efficient and parallelized fully relativistic 3D **PIC** code for simulating **PWFA** (the model for **LWFA** is currently being developed at **UCLA** [93, 94]. The algorithm applies a quasi-static field approximated equation model that allows to consider two time scales: a fast one for the plasma evolution and a slow one for the beam evolution. In this way the code computes the effect of the 3D beam space charge resulting fields on each plasma macroparticle, that is initialized over a 2D slab grid, that runs through the box (and beam fields) discretely over  $z$ . Then it updates the beam charge distribution according to the total fields, beam + plasma slab at each  $z$  location. This allows a speed up of over 2 orders of magnitude, when compared with OSIRIS, to solve the standard blowout scenario, but at the cost of introducing an approximation.

A 3D **PGC** algorithm has also been implemented into a model of OSIRIS 4 OSIRIS-PGC. In it the **EM** fields of the laser are split from the wakefields and the laser component evolves in time following its the envelope evolution. The optimisation of this model is still in-progress [88]. For this

dissertation QuickPIC and OSIRIS-PGC were employed to benchmark their modelling of the plasma hollow channel wakefield accelerator and the direct laser acceleration of trapped electrons against OSIRIS-3D and quasi-3D, respectively.

### 2.5.2.A Post processing radiation computing code - jRad

The output of selected simulations done using the OSIRIS PIC code was vital to understand and calculate the radiation emitted in the plasma based accelerator configurations modeled. For that we used the macro particles trajectory information (momentum, energy, position, charge weight factor etc.), at each time step, from some of our OSIRIS simulations to input in the post processing diagnostic tool developed at IST by J. L. Martins et al., [70] that accurately computes the radiation that they generate, according to Eq. (2.19) (reviewed in the next chapter), in a virtual detector as well as the corresponding spectra and their energy loss. This code includes the features of incoherent radiation, radiation reaction and quantum effects in the final calculations [69, 72].



# 3

## Laser direct and indirect energy transfer in a wakefield accelerator scheme

### Contents

---

<b>3.1 Process of Direct Laser Acceleration in non-linear plasma wakefields</b> . . . . .	31
<b>3.2 Experimental investigation of the role of Direct Laser Acceleration</b> . . . . .	35
<b>3.3 Numerical analysis of the Direct Laser Acceleration signatures found in Laser Wakefield Acceleration experiments</b> . . . . .	39
<b>3.4 X-ray emission from Direct Laser Acceleration in Plasma Wakefield accelerators</b>	66
<b>3.5 Conclusions and future options</b> . . . . .	72

---

Since the first laser operation held at Hughes Research Laboratory in California for Maiman's 1960 experiment, that our understanding of molecular and atomic structure of matter has been shaped by advances in both laser power and duration. Nowadays state of the art lasers are being devised to deepen our knowledge in nuclear, high-energy, vacuum and quantum physics. The ELI-NP facility, for instance, will use a multi-petawatt ultrashort (tens of fs) laser pulse system with peak electric fields reaching 100 TV/m [95], see Table 8.2. In our work we focus on the use of such powerful lasers in plasma-based particle acceleration techniques.

As mentioned in 1.1, plasmas can sustain accelerating gradients that surpass the limit after which standard radio frequency acceleration cavities breakdown (100 MeV/m). In 1979, the Laser Wakefield Acceleration (LWFA) concept was proposed [14] to use a plasma to mediate the energy transfer between a short laser pulse and charged particles. In it the laser ponderomotive force displaces the plasma electrons away from its higher intensity regions in a short time scale, at which ions remain immobile, exciting a space-charge density wave, the wake, with associated wakefields suitable for electron acceleration. This scheme was tested experimentally in 1994 in the Institute of Laser Engineering at the Osaka University with a 1 ps laser pulse amplified to a peak power of 30 TW that accelerated externally injected electrons in 1.7 GeV/m gradients up to 18 MeV [96]. Later the laser at Laboratoire pour l'Utilisation des Lasers Intenses (LULI) was used to accelerate externally injected electrons in a 1.5 GeV/m accelerating gradient, 25 mm long plasma [97].

Several other mechanisms<sup>1</sup> for laser plasma acceleration were explored [15, 17, 19]. The introduction of the non-linear bubble regime [50], also known as the blowout regime [48, 52, 99] and analogous to the non-linear regime of the Plasma based Wakefield Acceleration (PWFA) scheme [100] (see Sec. 2.2 of the LWFA) in 2002, where a laser with sufficiently high intensity completely expels the plasma electrons creating a cavity of positively charged ions behind it. In the rear of the cavity the plasma electrons were self-injected and subsequently trapped and accelerated in highly nonlinear strong accelerating fields [101, 102]. This enabled highly relativistic quasi-monoenergetic electron bunches to be produced [103] across the globe [28-30, 104, 105]. Thereafter electron bunches were accelerated in bubble wakefields to energies reaching the GeV [106-111]. In fact, in recent experiments the 300 TW peak power Berkeley Lab Laser Accelerator (BELLA) pulse was used to drive wakefields in a 9 cm long plasma discharge of  $6 - 7 \times 10^{17} \text{ cm}^{-3}$  and accelerate self-injected and trapped about 6 pC plasma electrons up to 4.25 GeV with a resulting energy spread of 5% [112].

In view of current laser technological developments and the above scientific breakthroughs and proof-of-principle experimental results the European Plasma Research Accelerator with eXcellence In Applications (EuPRAXIA) collaboration was initiated in 2015 to devise a future compact plasma based linear accelerator for science, industry and medicine [113]. It is, therefore, timely to investigate the properties of efficient LWFA configurations.

In collaboration with the Laser Plasma Group of University of California Los Angeles (UCLA), a

<sup>1</sup>MeV electron bunches were produced in other LWFA configurations including: the laser beat-wave [21], where the wake is excited when the frequency difference between two co-propagating laser pulses is the plasma frequency; the self-modulated regime [25], when the laser pulse duration exceeds the plasma period and the laser power exceeds the critical power for self-focusing; the forced regime [98], where a plasma wavelength long laser pulse is optically compressed in its initially linear wake.

LWFAs mechanism, the Direct Laser Acceleration of electrons in plasma wakefields (DLA) [61, 62, 114-116] has been, for the first time, both experimentally and numerically investigated and evidenced. When the laser pulse length is long enough for it to encompass the first bubble region that the ionized, self-injected and trapped electrons gain energy from the laser both directly (like in laser-driven sub-critical plasma channels [117, 118]) and through the plasma non-linear wake. In section 3.1 this process is discussed in detail and in the following sections, 3.2 and 3.3, we present the experimental and simulation results, respectively. These results show how DLA makes the energy transfer more efficient, with the generated accelerated electron bunch having an energy spectra tail with higher energy than in the standard bubble regime and how the resulting bunch has a transverse modulation, micro-bunching, at the laser wavelength. The final section will cover the main findings regarding the x-ray radiation produced [68, 119, 120] as the higher energy electrons perform wide amplitude betatron oscillations in the transverse wake and laser fields [121].

### 3.1 Process of Direct Laser Acceleration in non-linear plasma wakefields

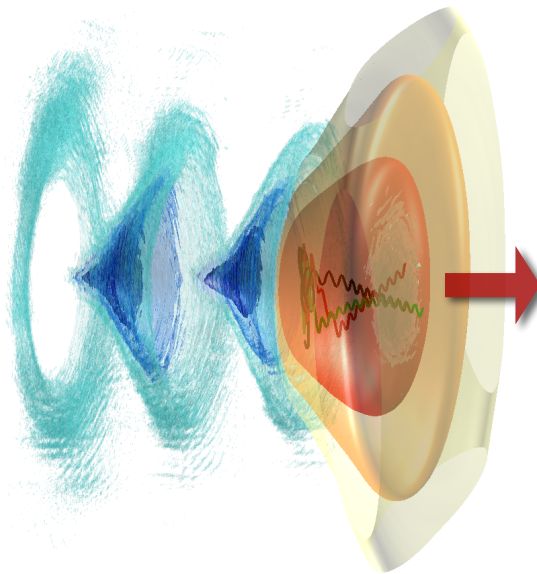


**Figure 3.1:** Illustration of the LWFA scheme explored. In the picture a laser pulse (red regions) propagates through a plasma (white) generating a wake of electron density oscillations, bubbles, (blue) with trapped electrons that are accelerated in the wakefields (indirectly by the laser) and the laser fields (direct). Three single electron (red, green and orange lines) trajectories are shown since their origin, the laser front to highlight their transverse oscillations in the laser fields until they get trapped at the back of the bubble and laser pulse.

Figure 3.1 illustrates the LWFA configuration operating in the nonlinear regime when DLA occurs. The laser pulse (whose envelope regions are featured in red) is linearly polarized in the page plane propagates (following the arrow direction) in a homogenous gas mixture of Helium and Nitrogen (in black). The laser high intensity ionizes the plasma. Its ponderomotive force generates the non-linear wake, where each bubble has the ion cavity that is surrounded by the high electron density pinched

region (in shades of blue).

It is technically challenging to inject a bunch of electrons into the back of the plasma bubble (typically  $< 20\mu\text{m}$  long) where they can remain trapped and be accelerated both by the wakefields and the laser, [DLA](#) to relativistic energies. For that reason the study of this chapter relies on the use of the ionization injection process. For the experiment of relevance to this chapter the plasma used for that end is composed of Helium with a Nitrogen dopant. The Helium and outer shell electrons of Nitrogen are quickly ionized by the laser front and form the bubble structure. The inner shell Nitrogen electrons are ionized on the propagation axis and can be injected and trapped (in green) [\[108, 122–125\]](#) in the back of the bubble.

The laser pulse encompasses the whole first bubble and overlaps the trapped electrons region. Therefore, its electric field increases the electrons transverse momenta and the magnetic fields converts it into longitudinal momentum. As a consequence of such resonant interplay of both laser fields and wakefields the electrons reach higher final energies than if shorter laser pulses had been used. A randomly chosen [DLA](#) and wakefield accelerated electron trajectory is shown (red color scale represents energy gain) since the point of ionization (darker red) close to the laser front to the point where it joins the bulk of the trapped electrons.

### 3.1.1 Direct energy gain from the laser

In order to understand the [DLA](#) concept in the [LWFA](#), it is useful to review the first work in which the laser plasma setup used resulted in [DLA](#) being the main energy transfer mechanism to determine the final energy of the accelerated electrons. The pioneer numerical work of 1999, [\[118\]](#), analyzed the resonance coupling of laser energy and plasma electrons and ions. In that work linearly polarized relativistic Gaussian laser pulses of duration  $\tau_L = 150$  fs (commonly measured at the Full Width Half Maximum measurement ([FWHM](#))), wavelength  $\lambda = 1 \mu\text{m}$  and power values of  $P = 1, 10, 100$  and  $1000$  TW were sent into  $L \sim 30 \mu\text{m}$  long pre-formed plasmas of electrons and ions (with charge to mass ratio equivalent to that of Deuterium) that followed an exponentially increasing profile,  $n(z) = n_0 \exp(z/L)$  where the plasma peak density,  $n_0$ , is such that at  $z = L a$ ,  $a$  being an integer, surpasses the critical density for those pulses,  $n_c = \pi m_e c^2 / (\lambda_0^2 e^2) = 1.12 \times 10^{21} \text{ cm}^{-3}$ , where  $c$  is the speed of light in vacuum. We employ the concept of the threshold to relativistic laser electron plasma interactions given by the pulse intensity:  $I_{\text{rel}} = 1.37 \times 10^{18} / \lambda^2 \text{ W } \mu\text{m}^2 \text{ cm}^{-2}$  that corresponds to the case where the kinetic energy of a quivering electron gains from the laser becomes comparable to its rest mass energy.

The laser pulses encompassed over 27 plasma oscillations, of length  $\lambda_{p0} \approx 2\pi c / \omega_p(0)$ , therefore the laser pulse underwent the laser self-modulation instability [\[25, 60, 126–129\]](#) at the plasma period, in which case the acceleration process is designated by Self-Modulated Laser Wakefield Accelerator ([SM-LWFA](#)). At the front of the laser the electrons are subject to the ponderomotive expulsive force of the pulse and are radially, as a function of  $r$ , expelled (in similar fashion as the bubble regime [\[50, 51\]](#)) generating the initial plasma wake density oscillations. The wake is associated with perturbations in the local refractive index,  $\eta(r, z)^2 = 1 - \omega_p(r, z)^2 / \omega_0^2 = c / v_{\text{ph}}(r, z)$  which affects the laser phase velocity,

$v_{ph} \approx v_g$ , and group velocity that is given by  $v_g = c \sqrt{1 - \frac{\omega_p^2}{\omega_0^2}}$ , derived from the Electromagnetic (EM) wave, with wavenumber  $k$ , dispersion relation in a plasma  $\omega_0^2 = \omega_p^2 + c^2 k^2$  [13]. In this way the laser pulse envelope modulated periodically and a train of laser pulses, separated by  $\approx \lambda_{p0}$ , compressed in  $z$  and focused in  $r$  is generated. Each sub pulse resonantly contributes to increasing the subsequent bubbles density oscillations and wakefields.

The increase in the effective relativistic mass of the accelerated electrons combined with the wake refractive index perturbations<sup>2</sup> induce the relativistic laser spot size Laser Relativistic Self-Focusing (LRSF) phenomena in the modulated laser pulses [130, 131] that opposes the diffraction (which would occur if the laser propagated in vacuum instead). LRSF is further explained in chapter 4. In the absence of that optical guiding, the interaction length of a Gaussian laser pulse and an electron is limited by the diffraction length,

$$L_{Diff} = \pi Z_R \quad (3.1)$$

where  $Z_R = \pi W_0^2 / \lambda_0$  corresponds to the pulse Rayleigh length and  $W_0$  the Gaussian laser spot size. The critical power for the laser intensity to balance its diffraction is  $P_c \approx 17 \frac{nc}{n(z)}$  [GW] [132] which remains in the order of GW, which is lower than the pulse power values used,  $P$ . Consequently, the train of laser sub-pulses ponderomotive force is strengthened. The total expelling force, from the plasma wakefields and the ponderomotive force, that is exerted on the ions is enough to introduce significant ion motion and the process known as Laser Relativistic Self-Channelling (LRSC) takes place [117, 133, 134], leading to the formation of a plasma depleted channel. LRSC is further explained in chapter 4. While the relativistic and ponderomotive effects on the plasma electrons are responsible for the radial and longitudinal electric fields ( $E_r$  and  $E_z$ ) inside the channel formed, the trapped electrons current contributes to the azimuthal magnetic field  $B_\phi$ . These self-generated fields are key for DLA.

In this scenario [118], plasma electrons that oscillate transversely due to the radial expulsive ponderomotive force, performing betatron oscillations, also accelerate in the generated fields and if their velocity in the laser propagation direction matches the laser pulse local phase velocity,  $v_z(z) \approx v_{ph}(z)$  they become trapped in the effective potential [48, 99, 135]. A single relativistic trapped plasma electron trajectory follows the Lorentz equation of motion (2.1) with  $\vec{E}$  and  $\vec{B}$  corresponding to the superposition of the electric and magnetic fields from the laser and the plasma wake. The trapped electron is accelerated up to relativistic velocities by the self-generated longitudinal electric field  $E_z$ . As its velocity approaches  $c$  the second term in Eq. (2.1) becomes relevant. Assuming, for simplicity, a laser pulse linearly polarized in the  $x$  direction, when the electron oscillates in the laser transverse electric field,  $E_x^l$ , with increasing their transverse momentum  $p_x$  significantly, the orthogonal magnetic fields  $B_y$  will transform that gain into longitudinal acceleration. Therefore the trapped relativistic electron is accelerated by the longitudinal field,  $E_z$  (which is excited by the plasma wave driven by the laser pulse) and also directly by the laser, DLA, field  $E_x^l$ . The DLA process is equivalent to the Inverse Free Electron Laser (IFEL) [136] at the betatron frequency

The plasma transverse wakefields act as an IFEL periodic magnetic wiggler and accelerate the electrons in the direction of  $E_x^l$ . The trapped electrons form bunches at half the laser period, micro-

<sup>2</sup>The index of refractive can include a relativistic correction that is associated with the effective relativistic mass.

bunching, where the laser electric field is aligned with the transverse velocity and are expected to exhibit higher divergence in the polarization direction of the linearly polarized laser pulses than in its orthogonal transverse direction.

Assuming that, for the majority of the trapped electron trajectory, the above described fields in which they are immersed can be considered as quasi static then there will be electron net energy variation through [DLA](#) if the resonance condition:

$$N\omega_\beta = \gamma(1 - v_{\parallel}/v_{ph})\omega_0 \quad (3.2)$$

is verified. In other words a harmonic,  $N$ , of the electron, with relativistic *Lorentz* factor  $\gamma$ , betatron frequency<sup>3</sup>  $\omega_\beta$ , has to match the relativistic electron perceived *Doppler* shifted laser frequency [\[137\]](#) for an electron, in a point in its betatron oscillation that is in opposite phase to  $E_x^l$ , to be continuously accelerated by the laser field.

Ideally the local values of  $v_{ph}$ ,  $\omega_0$  and  $\omega_\beta$  do not vary and the trapped electron can constantly respect the betatron resonance of Eq. [3.2](#) throughout the acceleration distance. The trapped electrons can be accelerated for as long as they remain in the accelerating region, i.e. during the dephasing length  $L_d$ , and the laser energy is not completely depleted so it can still drive the plasma wake, i.e. during the depletion length  $L_{pd}$ . Typically, in the blowout regime,  $L_{pd}$  corresponds to the distance after which the laser transfers all its energy to the plasma and is related to the rate at which the leading edge etches (transfers its field energy to the plasma),  $v_{etch} = c\omega_0^2/\omega_p^2$  [\[138\]](#). It is given by<sup>4</sup>

$$L_{pd} = v_{etch}\tau_{LFWHM} = \frac{\omega_0^2}{\omega_p^2}c\tau_{LFWHM} \quad (3.3)$$

Also, in the blowout regime, a laser propagates and generates a wake of bubbles with approximate characteristic radii  $r_b$  (see Sec. [2.2](#)). The dephasing length is the distance until the accelerating particle overcomes the accelerating phase of the wakefield that is given by  $v_p = v_g - v_{etch}$ , yielding:

$$L_d = \frac{c r_b}{c - v_p} = \frac{2\omega_0^2}{3\omega_p^2}2\sqrt{a_0}c/\omega_p \quad (3.4)$$

In the framework of [\[118\]](#), the self-generated [EM](#) fields  $B_y$  and  $E_x$  that the electron was subject to were assumed to be quasi-static and the laser pulse was approximated by a plane [EM](#) wave,  $E_x^l$ . In [\[118\]](#) these simplifying considerations associated with a single particle model were used to attempt to describe the phenomena of [DLA](#) alone, without accounting for the laser pulse evolution, the relativistic and ponderomotive effects on those parameters. However, to truly understand the final energy spectrum of the electrons accelerated in those conditions, mainly the interplay of [DLA](#) with the plasma wakefields, we explored the role of these effects self-consistently by performing full-scale, one-to-one, Particle-In-Cell ([PIC](#)) simulations with the code OSIRIS, with shorter and more powerful laser pulses.

<sup>3</sup>In plasma wakefields of the standard blowout regime the betatron frequency can be computed from Eq. [\(2.1\)](#):

$$\frac{d}{dt}\vec{p} = \frac{d}{dt}\gamma m_e \vec{v} = -m_e \omega_p^2 / 2\vec{r} \equiv \omega_\beta \Rightarrow \omega_\beta \approx \omega_p / \sqrt{2\gamma}$$

<sup>4</sup>This commonly applied definition of  $L_{pd}$  considers that the back of the pulse is mostly unperturbed and is valid as long as the laser energy that is transferred directly to the trapped electrons is much lower than that transferred to the wake.

Moreover, with the development of more advanced laser and plasma systems technology it became possible and relevant to experimentally determine the role of **DLA** in **LWFAs**. The experiment done by J. Shaw, N. Lemos et al. at **UCLA** [61, 139] compared different scenarios characterized by: a laser pulse duration of the order of the bubble size ( $r_b/c$  [48, 52]) and normalized  $T_p$ , which is given by:

$$T_p = \frac{\omega_p \tau_L}{2\pi \sqrt{a_0}} \quad (3.5)$$

and ranging from 0.8 to 1.4. They could compare **LWFAs** with and without significant expected **DLA** impact in the trapped electron acceleration [61, 139]. This experiment allowed, for the first time, to study the properties of the generated microbunched electron beams operating close to the standard nonlinear blowout regime, using high intensity laser pulses that could encompass the full length of the first excited plasma bubble.

The following section, 3.2 will briefly describe selected experimental results obtained at **UCLA** [61, 139]. Because of the complexity of the explored scheme, the validation of the influence and impact that **DLA** has on the non-linear **LWFA** mechanism when  $T_p$  reaches values close to and above 1, observed in the experiment, could not be provided through theoretical and analytical descriptions only. Numerical simulations, [114, 115], were thus critical to support the experimental findings and identify the main physical processes. My main contribution was in performing and analyzing full 3D numerical simulations, [62], in the supercomputers FERMI and SUPERMUC (see Sec. 3.3). I investigated numerically, with the post-processing code jRad, the radiation emitted by the accelerated electrons in order to find further signatures of the **DLA** assisted **LWFA** mechanism. Those can be compared to future planned experiments where the emitted radiation will be measured.

## 3.2 Experimental investigation of the role of Direct Laser Acceleration

The experiments were performed at the **UCLA** Xtream Plasma Laboratory and resorted to laser pulses that were too short for both self-modulation and relativistic channeling to take place in the generated plasmas [61, 62, 114, 115, 139]. Figure 3.2 is the picture of the experimental setup (taken from Fig. 3.1 of [61]). For a better understanding of the scheme used, all the components are explained in the following paragraphs and an illustrative diagram is shown in Fig. 3.3.

### 3.2.1 Laser apparatus

In the Laboratory the Ti:Sapphire laser system has  $\lambda_0 = 0.815\mu\text{m}$  with pulse length fixed to  $45 \pm 5$  fs (at the **FWHM** of intensity) and focused to a spot size of  $6.7\mu\text{m}$ . The power of the laser reached 20 TW. In each shot the laser beam travels through a beam splitter and the resulting pulses travel two beam lines. In the first one, the pulse is focused, by an off-axis parabola, which is a reflector with the surface generated by a parabola revolving around the focal axis. The focal position is set inside the gas cell where the intense laser pulse ionizes and excites the plasma nonlinear wake. The outgoing laser light is absorbed by an aluminum foil. In the second beam line there is a second beam splitter and part of the

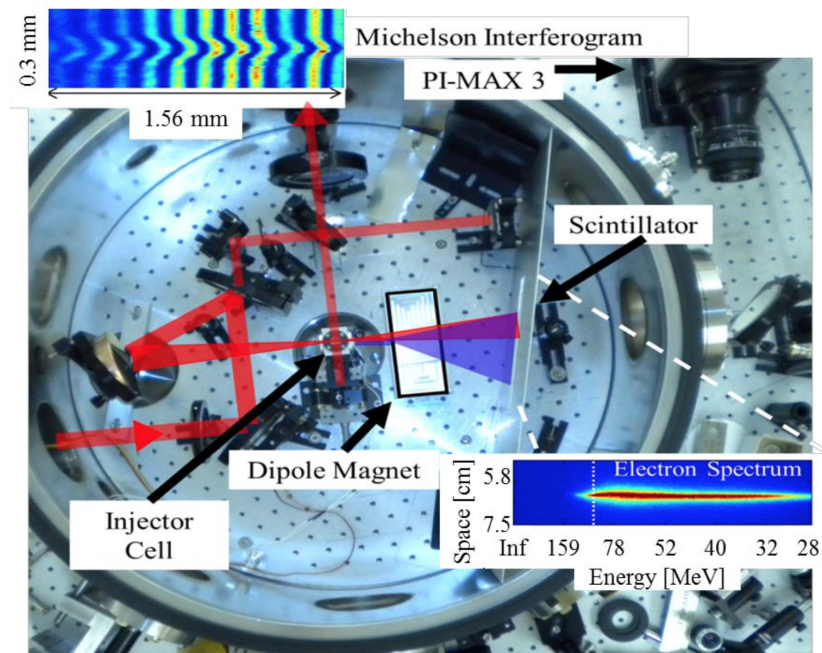


**Figure 3.2:** Photograph of the experimental setup used at the Xstream Plasma Laboratory shown in [61]. The red line shows the trajectory of the incident laser pulse. The insets show a typical plasma interferogram result on the top left corner and the resulting plasma density profile inside the gas cell on the bottom right.

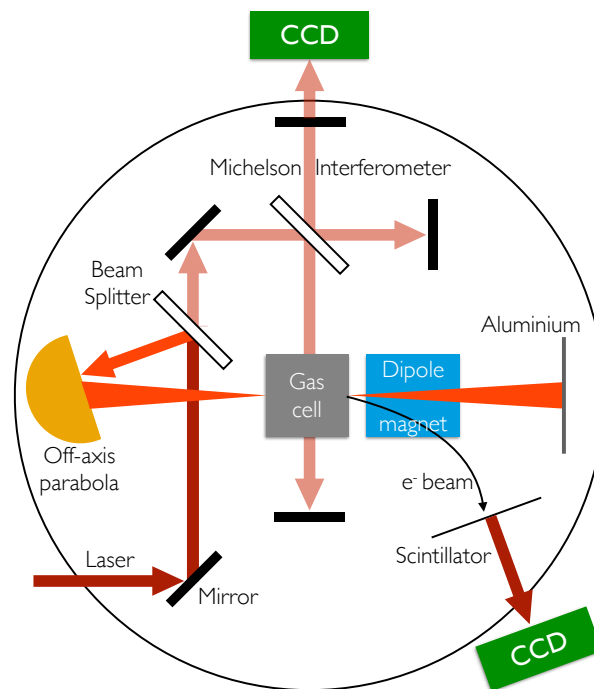


**Figure 3.3:** Schematic of the laser pulse trajectory into the chamber and following the main beam lines, including the gas cell, dipole magnet and of the different diagnostics used [61].

pulse reaches the gas cell, without being focused, in the direction perpendicular to the previous pulse while the other part travels in vacuum until, following the concept of the *Michelson* interferometer, both parts interfere, containing information on the plasma density profile, that is collected in a PI-MAX intensified Charge-Coupled Device (CCD) camera for imaging and spectroscopy that converts the incident light characteristics into digital values.

### 3.2.2 Plasma injector gas cell

The plasma gas cell was developed to allow for variable gas length ranging from 0.1 to 2mm, with short up and down ramps of the density profile [139]. The cell was self-aligned and the gas source was a mixture of neutral Helium and Nitrogen in the proportions of 95:5. After ionization by the laser pulse in the main beam line, the measured plasma densities typically ranged from  $n_0 = 8 \times 10^{18} \text{ cm}^{-3}$  to  $2.8 \times 10^{19} \text{ cm}^{-3}$  and were controllable by changing the gas filling pressure (which is higher than the density explored in the work mentioned in Sec. 3.1.1 [118]).

This configuration was chosen so that the ionized Helium and outer shell Nitrogen electrons contributed to the quasi-static plasma wake in the nonlinear blowout regime whilst most of the inner shell Nitrogen electrons would be injected in the optimal phase-space position to be trapped. This mechanism is known as ionization-injection in the LWFA [108, 140]. The resulting trapped and accelerated electron bunch escaped the gas cell and was dispersed in energy, in one of the two directions orthogonal to each other and to the laser propagation direction, by a dipole magnet (0.92 tesla) onto a plastic scintillator or a lanex screen. The beam energy profile, correlated to the radiation it produced in the screen, was then recorded using another CCD camera.

### 3.2.3 Experimental results

This section, for comprehension sake only, briefly mentions the experimental results that are relevant in determining the principal signatures of DLA. The full outputs of the investigation led by the Xtream Plasma Laboratory team can be found in detail in [61].

The initial DLA indicator found was the greater maximum energy that trapped and collected electrons exhibited when higher  $T_p$  values were tested, for which it differed significantly from the estimates done for a solely LWFA setup. Subsequent tests showed the measurement of the transverse position of undispersed (which means they were collected without being subject to the dipole magnetic force) electrons that exit the gas cell, for ( $\sim 10$ ) consecutive shots with laser pulses emitted linearly polarized in the two directions orthogonal to the propagation of the pulses,  $x$  or  $y$ , with ellipticity where the major axis was aligned with the selected polarization direction. The Half Width Half Maximum measurement (HWHM) divergence values for each ellipse axis, which were transverse to the laser pulse propagation, differed in about 50% for the experiments done with a plasma with  $n_0 = 1.7 \times 10^{19} \text{ cm}^{-3}$  density over  $900 \mu\text{m}$  with laser power  $\sim 20 \text{ TW}$ . This evidence can be attributed to the increase in electron momentum gain along the laser polarization direction when DLA has a significant impact in the acceleration, as discussed in Sec. 3.1.1.

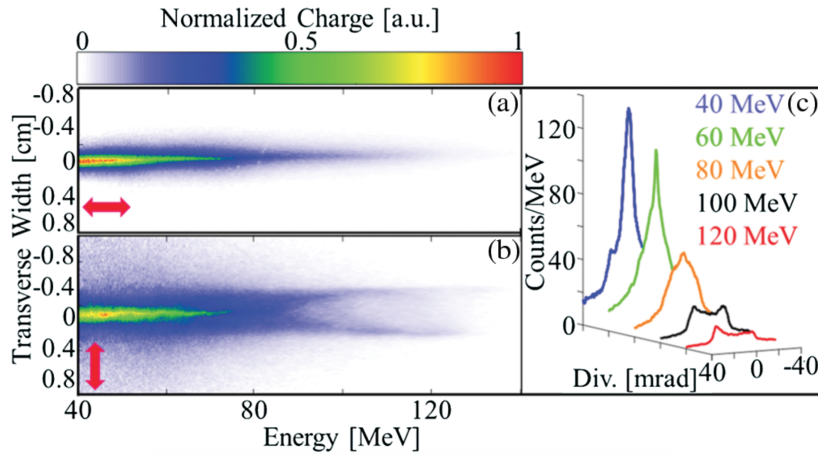


**Figure 3.4:** Experimental electron transverse spectra dispersed transversely to the laser pulse propagation direction: a) parallel to and b) perpendicular to its polarization direction, as is indicated by the red arrows. c) represents the lineouts, from plot b), for different energy values for a clearer interpretation of the results. The two spectra are of electron beams generated in two separate experiments with plasma and linearly polarized laser configurations: a) a neutral gas cell length of about  $800\mu\text{m}$  with measured total electron density  $n_0 = 1.7 \times 10^{19}\text{cm}^{-3}$  and laser power of about 12 TW and b) a  $900\mu\text{m}$  long gas with  $n_0 = 1.4 \times 10^{19}\text{cm}^{-3}$  electron density, laser power of about 13 TW. Both scenarios corresponded to a value of  $T_p \sim 1$  [61] [62].

Polarized preferential divergence of accelerated electrons can also be due to the electrons being tunnel ionized and injected over a phase range of the laser. When the laser local vector potential amplitude is enough to ionize the core Nitrogen electrons, even off its axis of propagation, they can receive an initial transverse linear momentum from the laser, which is, for that reason, parallel to the laser polarization direction. However, in Sec. 3.3 the comparison of numerical simulations describing the experimental process with a laser pulse that is short and another that is long enough for DLA assisted LWFA to occur, at the back of the bubble where the trapped electrons are, showed that DLA effectively strengthens the ellipticity in the polarization direction that might arise from tunnel ionization.

An additional evidence that DLA was interplaying with the LWFA process was found experimentally by comparing the accelerated electron bunch energy vs final position, transverse to the propagation direction, spectra collected on the screen<sup>5</sup> when the electrons were dispersed, according to their longitudinal velocity,  $v_z$  through the  $v_z \times B_{x,y}$  contribution to the electron Lorentz force, by the dipole magnet,  $B_{x,y}$ , in each one of the two orthogonal directions,  $x, y$ , to the laser pulse propagation direction,  $z$ . Figure 3.4 shows the preferential divergence in the polarization direction, b), which is justified by an ellipticity in the electron beam transverse (in  $x, y_{\text{screen}}$ ) profile. This indicates that laser transverse electric field direction is correlated with the transverse increase of the displacement of the accelerated electrons.

Moreover, taking into account the highest energy electrons in plot b) of Fig. 3.4 with energies above 90 MeV (corresponding to the black and red lineout curves present in plot c) ) it is possible to see a "fork"like structure of the electron spectra. In other words, electrons that are accelerated to higher energies have greater transverse position spread associated with higher divergence levels. This structure is not present in the case of dispersion in the direction parallel to the polarization direction, a), which indicates that it can be a signature of laser electric field induced momentum gain.

<sup>5</sup>The lanex screen was placed at the distance from the gas cell and the dipole magnet of (3.2 + 7cm).

The fork structure was experimentally reproduced and clearly observed consistently in separated runs done on several days, with plasma densities varying between  $n_0 = 1.1$  to  $1.5 \times 10^{19} \text{cm}^{-3}$  and laser power values between 10 and 20 to go through configurations where  $T_p = 1.0$  up to 1.3.<sup>6</sup> The higher density central regions in both a) and b), where energies are below the 90 MeV, can result from all the electrons trapped in regions not overlapped by the laser, such as the bubbles subsequent to the initial one following the laser pulse.

### 3.3 Numerical analysis of the Direct Laser Acceleration signatures found in Laser Wakefield Acceleration experiments

As mentioned in the end of Sec. 3.1.1, the single electron analytical model derived in [118] neglected EM fields evolution, as well as the laser pulse finite shape effects and particle interactions. Therefore, to clarify the physical mechanism of DLA in particular, on LWFA schemes and understand the experimental results previously shown, we resort to numerical simulations. For further exploring such a complex scenario, multi dimensional fully relativistic massively parallel particle-in-cell simulations are required. They will allow us to get a deeper insight into the accelerated electrons DLA signatures, i.e. the final bunch ellipticity, fork in the spectra and maximum energies that were detected in the experiments discussed above, see Sec. 3.2. The simulations run in large high-performance computer cluster centers (mainly Fermi [3]. The work presented in this section was done with the state of the art numerical infrastructure OSIRIS [73].

#### 3.3.1 OSIRIS 2D study

References [114, 115], numerically investigated, using the 2D cartesian configuration, the DLA contribution to the LWFA with ionization injection in the quasi-non linear blowout regime. That initial work paved the way to the correctly resolved numerical analysis done in this section. In order to exclude the possibility of DLA energy enhancement effect deriving from spurious numerical heating [141], which is characteristic of numerical simulations where the Yee algorithm [81] is employed and where the laser field was not accurately resolved in a grid influencing the continuous particle movement, extensive resolution simulations scans were performed in this initial 2D study. These simulations indicated that the impact of DLA to the electron overall acceleration process was, in fact, greater for higher levels of the typical plasma bubble, or cavity, length,  $T_p$ . References [114, 115] verified that some of the produced accelerated electrons exhibited higher energies than the estimated values determined for the standard operating non-linear blowout regime in [52, 99] that also suggests DLA being an active and significant accelerating mechanism interplaying in the global process.

#### 3.3.2 OSIRIS 3D simulations setup

We then performed 3D simulations with the numerical code OSIRIS [73] (using 16x1024 cpus for about 50h). The simulations used a moving window, particle tracking and *Ammosov Delone Krai-*

<sup>6</sup>The experimentally analyzed ranges covered  $n_0 = 0.9 \text{ to } 1.5 \times 10^{19} \text{cm}^{-3}$  and  $T_p$  values from 0.8 up to 1.3.

nov ionization model (ADK) ionization models. In order to select trapped electrons and store the information of their trajectory in each time step, needed for the diagnostics (see next chapter) all the simulations were done twice and the total computational cost was of almost 6 million cpu-hours.

Inspired by the experimental setups, the simulations modeled a neutral gas mixture of Helium and Nitrogen, in the proportions of 99.9% : 0.1%, that was ionized by the laser pulse to produce the plasma. The code allowed us to analyze the behavior of the core plasma electrons (from the ionization of  $N^{5+}$  and  $N^{6+}$ ) separately. For that purpose, three simulation designated species of neutral macro particles were created. The helium neutral species had 2x2x2 electron macro particles per cell associated with the first and second level of ionization, each with the density of  $n_{He} = 0.4965n_0$ . There  $n_0$  was set according to the experimental total electron plasma detected. The second species was of Nitrogen neutrals accounting for the first 5 ionization levels and used 2x2x2 electron macro particles per cell with a density level of  $n_{He} = 0.0005n_0$  each. The last species, from which selected trajectories were tracked, represented the final Nitrogen ionization level with also 2x2x2 macro particles per cell with  $n_{He} = 0.0005n_0$ .

The overall neutral gas profile of the three simulated species consisted of an initial ramp of  $100\mu m$  followed by a constant density region, shown in the column of  $L_p$  of the Table 3.1 and a down ramp,  $D_p$  row. For all the simulations, the neutral species were introduced approximately  $1\mu m$  after the laser propagating through a full simulation box that has dimensions  $L_z \times L_x \times L_y = L_z \times L_x^2$  shown in the Table under the column labeled as Box. The laser pulse with  $\lambda_0 = 0.815\mu m$  was focused to a spot size of  $6.74\mu m$  after propagating  $50\mu m$  into the gas and can be seen in the plots of Fig. 3.5 a) to e).

$T_p$	Laser pulse			Helium - Nitrogen profile			Numerical resolution	
	Length	$a_0$	I [W/cm <sup>2</sup> ]	$n_0$ [cm <sup>-3</sup> ]	$L_p$ [ $\mu m$ ]	$D_p$ [ $\mu m$ ]	Grid cells	Box [ $\mu m^3$ ]
0.4	25fs	2.10	$9 \times 10^{18}$	$8.0 \times 10^{18}$	1000	100	$1940 \times 320^2$	$53 \times 54^2$
0.8	45fs	2.10	$9 \times 10^{18}$	$8.0 \times 10^{18}$	1000	100	$1940 \times 320^2$	$53 \times 54^2$
1.0	45fs CP	2.10	$18 \times 10^{18}$	$8.0 \times 10^{18}$	1000	100	$1940 \times 320^2$	$53 \times 54^2$
1.1	45fs	2.03	$8 \times 10^{18}$	$1.43 \times 10^{19}$	430	150	$1566 \times 320^2$	$50 \times 54^2$
1.4	45fs	1.86	$7 \times 10^{18}$	$2.26 \times 10^{19}$	430	150	$1566 \times 320^2$	$43 \times 54^2$

**Table 3.1:** 3D simulation configurations exploring DLA impact in LWFA ordered by the typical bubble length parameter,  $T_p$ . The time step used was computed applying 2.21 to the dimensions of this table. The rows with  $n_0$  over  $8.0 \times 10^{18}$  [cm<sup>-3</sup>] were run with a longitudinally shorter plasma gas density profile because for those cases the expected pump depletion length  $L_{pd}$  is shorter (see Table 3.1). The parameters for the simulation with  $T_p = 1.1$  closely followed the experimental setup used to produce the beams of Fig. 3.4 b).

The run with  $T_p = 0.4$  was configured with a laser pulse shorter than a plasma wavelength thus anticipating small to no contribution of DLA to the general LWFA acceleration process. All other runs used a 45fs laser pulse. The run with  $T_p = 0.8$ , in particular, had no other difference, with respect to

<sup>7</sup>In Table 3.1 the entry with CP indicates that in that particular run the laser had circular clock-wise polarization<sup>8</sup>. The pulse length values represent the FWHM sizes.

the run with  $T_p = 4$ , so that a direct comparison of a simulation with expected **DLA** contribution with the one without can be done. The simulation with  $T_p = 1.0$  shows the effects of circular polarization for which case **DLA** is expected to interfere in both directions perpendicular to the propagation direction. The run with  $T_p = 1.1$  was set to be similar to the experiments yielding Fig. **3.4**. The run with  $T_p = 1.4$  enabled the inspection of the impact of **DLA** in face of a broader range of the  $T_p$  parameter.

Figure **3.5**f) shows the overlap of the longitudinal lineouts of the laser transverse field  $E_x$  initialized at the beginning of each simulation (colored according to their  $T_p$  value of Table **3.1**) and will be used as reference in comparison to the results shown afterwards. Note that the plotted field units are  $m_e c \omega_p e^{-1}$  (independent of the laser frequency  $\omega_0$ ) enabling the direct comparison of the wakefields of the different plasma density setups. Figure **3.5** depicts the plasma wavelength, laser spot size and field of each simulation to serve as a measurement guide for the interpretation of the next figures.

The simulation parameters chosen had the characteristic lengths present in Table **3.2**, a *Rayleigh* length of  $Z_R = 175\mu\text{m}$  and diffraction length of  $L_{\text{Diff}} = 550\mu\text{m}$  (see Sec. **3.1**). To reliably compare the experimental final accelerated electron bunch properties with the numerical results of the core Nitrogen ionized and injected electrons, it is necessary to model their exit of the plasma and further propagation in vacuum. For that reason, the propagation of the accelerated electrons after the plasma ended, in vacuum, for a distance of  $cT_{\text{vac}}$  with the values shown the same table.

$T_p$	$L_{\text{pd}} [\mu\text{m}]$	$L_d [\mu\text{m}]$	$P$ [TW]	$P_c$ [GW]	$cT_{\text{vac}}[\mu\text{m}]$
0.4	695	179	6.4	0.08	100
0.8	1251	179	6.4	0.08	100
1.0	1251	179	13.0	0.08	100
1.1	700	99	6.0	0.14	50
1.4	443	60	5.0	0.23	50

**Table 3.2:** Values of the laser typical pump depletion,  $L_{\text{pd}}$ , dephasing,  $L_d$ , lengths and peak power  $P$  in the interaction with the plasmas, with corresponding critical power  $P_c$  and density  $n_c$ , following the 3D simulation to study **DLA** in the **LWFA** scenarios described in Table **3.1**, also ordered by the typical bubble length parameter,  $T_p$ . Additionally, the final accelerated electrons simulated vacuum propagation distance,  $cT_{\text{vac}}$  is shown. See sec. **3.1** for more information on these parameters.

### 3.3.3 OSIRIS 3D simulations results

The Helium and Nitrogen ionized plasma as well as the on-axis transverse electric field (parallel to the polarization direction) evolution throughout the laser propagation can be seen for each simulation scenario of Table **3.1** in Figures **3.6**, **3.7**, **3.8**, **3.9** and **3.10**. All figures show the same zoom of the simulation box that was used on the plots of Fig. **3.5**. The plots were taken approximately at the end of the plasma density up ramp (labeled as a)), after half (b) and all of the flat profile part,  $D_p$ , of the runs with  $T_p = 1.1$  and 1.4 (c) and at the end of the flat part of the other runs (d). The density color scales are given in terms of the total electron background density for each run (usually OSIRIS

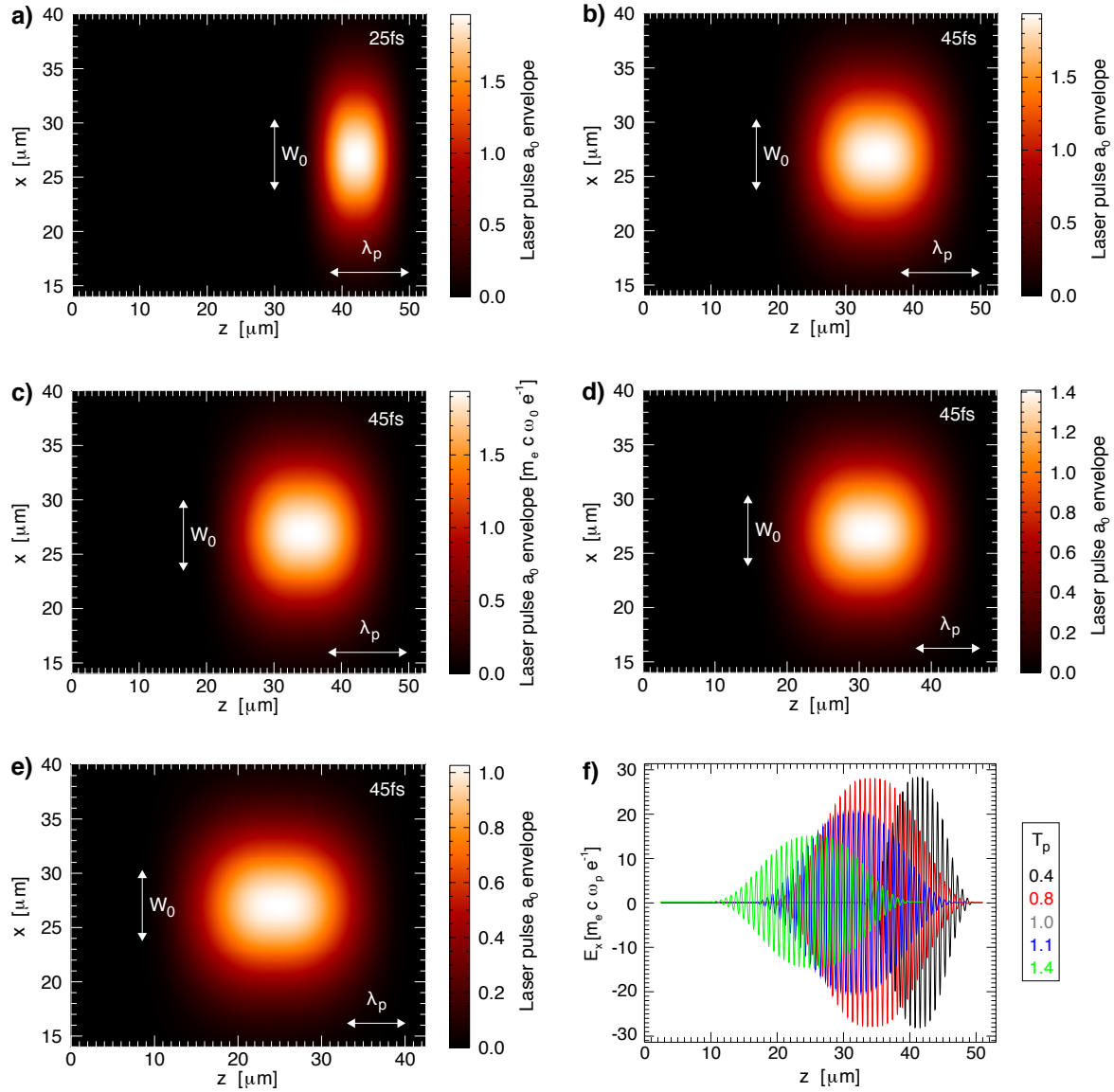


**Figure 3.5:** Transverse zoom of the envelope of the simulated laser pulse normalized potential  $a_0 \approx 8.5 \times \lambda [\mu\text{m}] \sqrt{I [10^{20} \text{W/cm}^2]}$  (red color scale), at the beginning of the simulation, for the different scenarios present in Table 3.1: a), b), c), d) and e) corresponding to  $T_p = 0.4, 0.8, 1.0, 1.1$  and  $1.4$ , respectively. Plot f) shows the initial on-axis transverse field (in the direction of polarization for the linear polarized pulses) for the same cases, normalized with the plasma frequency  $\omega_p$ . Colors indicated in the label box in the left.

outputs densities with  $e\omega_p^3/c^3$ ).

The two configurations with shorter pump depletion lengths  $L_{pd}$  used shorter neutral gas jet (hence plasma) density profiles and had  $T_p = 1.1$  and  $1.4$  in which **DLA** is expected to participate in the acceleration of electrons within more than the first plasma wake bubble. The use of the experiment like length of the gas jet profile would have been, instead, too computationally demanding (both in computer time and memory) to be performed with our resources. Because of the shorter total acceleration distance the final plot of Fig. **3.9**, c), shows Nitrogen core electrons (from  $N^{5+}$  and  $N^{6+}$  ionization) dispersed over the full transverse box, just like in Fig **3.7** b) and c).

Unlike the previous figures, Fig. **3.10** shows trapping within the first two plasma wake cavities of Helium electrons at the end of the plasma constant density region. For this reason our analysis of the acceleration processes, **LWFA** and **DLA**, for this run will include the final electrons ionized from all 3 simulation species. The longitudinal size of the simulation box was also too small to understand if any electrons would be trapped and accelerated in the third and fourth following cavities.

The integrated core Nitrogen ionized trapped charge, for each simulation run, is shown in Fig. **3.11**. Plot a) corresponds to the short laser pulse configuration and shows that ionization injection occurred only until approximately  $400 \mu\text{m}$ , because after that the density of those electrons remains constant. For the longer pulse, plot b), ionization stopped after about  $900 \mu\text{m}$ . The circular polarization scenario, plot c), showed ionization until the end of the run. As did the simulations with shorter plasma profiles, plots d) and e). In the plots c) to e) of Fig. **3.11** the main bunch, with longitudinal charge density over  $6 \text{ pC}/\mu\text{m}$ , was followed by a tail, reaching over  $2 \text{ pC}/\mu\text{m}$ , of electrons trespassing the first plasma cavity into the subsequent ones. These tails are formed after the plasma density up ramp where they start to be concentrated into a second (and third in the case of plot e) bunches.

When the plasma profiles reach the down ramp part and their density is reduced,  $n_0$ , the plasma wake wavelength,  $\lambda_p$ , and size of the wake cavities increases. As a consequence the electron bunch tails can be dispersed longitudinally, as can be easily seen in Fig. **3.11** plots b) to e). This is not clear in plot a) where most of the beam charge was confined in the first cavity. After the down-ramp there are no trapping nor focusing fields making it easier for electrons with high transverse momentum, and low energies, to escape the beam (and escape the simulation box). Figure **3.11** f) compares the total final charge for the different runs and in it the runs with higher  $T_p = 1.0, 1.1$  and  $1.4$  values, corresponding to plots c) to e), the total measured charge corresponding to those electrons and also to the ones that were trapped and ionized so late in the run that they were not sufficiently accelerated to leave the plasma with the final total charge values.

The final electrons that were accelerated and propagated a distance of  $cT_{vac}$  after the neutral gas ended, see Table **3.2**, formed the 3D bunches plotted in Fig. **3.12** labeled sequentially by the  $T_p$  parameter value of each run.

The integrated, in  $x$  or  $y$ , charge density of those bunches is projected into the  $zx$  and  $zy$  planes. The plots a) and b) which correspond to runs with  $T_p = 0.4$  and  $0.8$  that differed only in the laser pulse length,  $25$  and  $45$  fs, and thus in the absence and presence, respectively, of **DLA** contribution in the acceleration mechanism, clearly show a greater transverse position spread for the case with higher

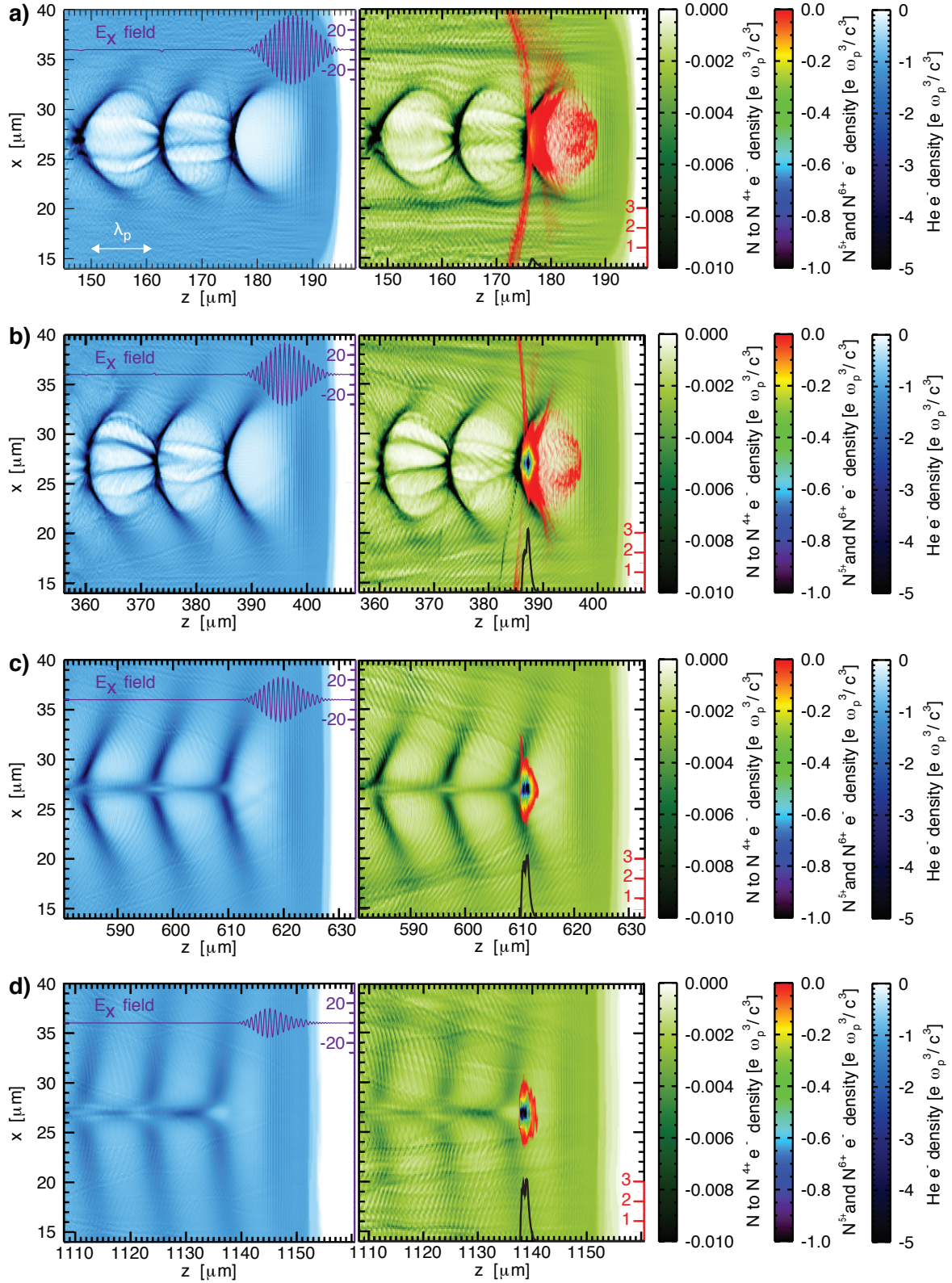


**Figure 3.6:** Evolution of the density of plasma electrons throughout the 3D simulation done with  $T_p = 0.4$ . Left 2D plots show the density of the electrons ionized from He and He<sup>+1</sup> (blue color scale) overlapped with the on-axis lineout of the transverse electric field  $E_x[m_e c \omega_p e^{-1}]$  (purple solid line and axis). Right density plot for the electrons ionized from N up to N<sup>4+</sup> (green scale) and from N<sup>5+</sup> and N<sup>6+</sup> (rainbow color scale). Black solid line and right vertical axis represent the integrated in the transverse directions,  $x$  and  $y$ , on-axis charge of the core electrons, from the ionization of up to N<sup>4+</sup> and N<sup>5+</sup>, N<sup>6+</sup>. 2D plots show the slice at the center of the transverse direction,  $y = 0$  with  $z$  axis representing the propagation direction and the transverse axis,  $x$ , the other transverse direction, parallel to the laser polarization direction. The labels a), b), c) and d) represent simulation times of:  $ct \approx 145, 356, 508$  and  $1108 \mu\text{m}$ .

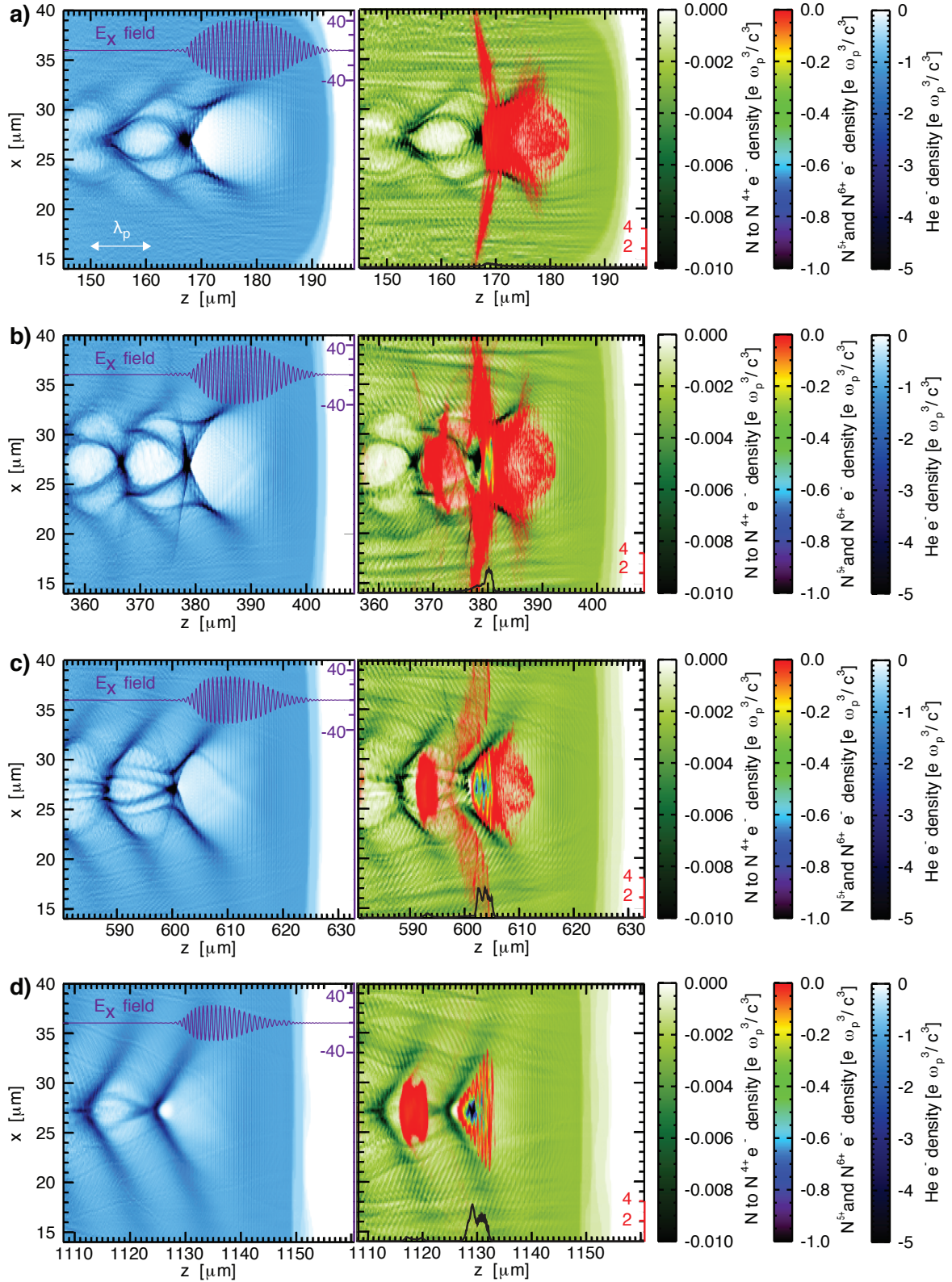


**Figure 3.7:** Evolution of the density of plasma electrons throughout the 3D simulation done with  $T_p = 0.8$ . The laser pulse length for this simulation was 45fs instead of 25fs as in the previous one,  $T_p = 0.4$ . The solid lines, labels and color schemes are identical to Fig. 3.6.

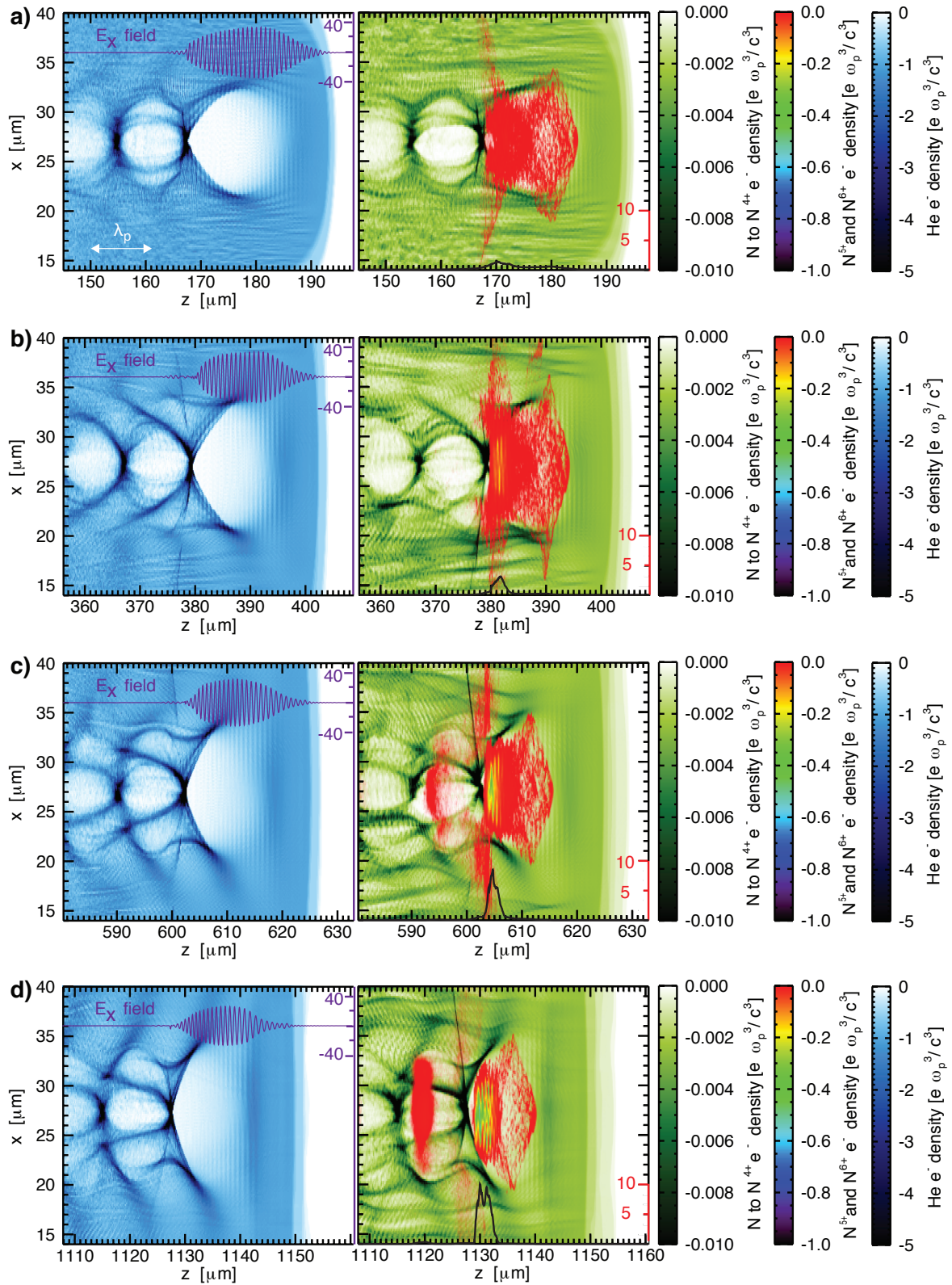


**Figure 3.8:** Evolution of the density of plasma electrons throughout the 3D simulation done with  $T_p = 1.0$ . The laser pulse length for this simulation was 45fs instead of 25fs, as in the one with  $T_p = 0.4$ , and it had circular polarization (clockwise). The laser normalized potential  $a_0$  was kept constant hence the value of the laser intensity and power changed. The labels and color schemes are identical to Fig. 3.6 and the choice of axis was done in accordance with the previous figures.

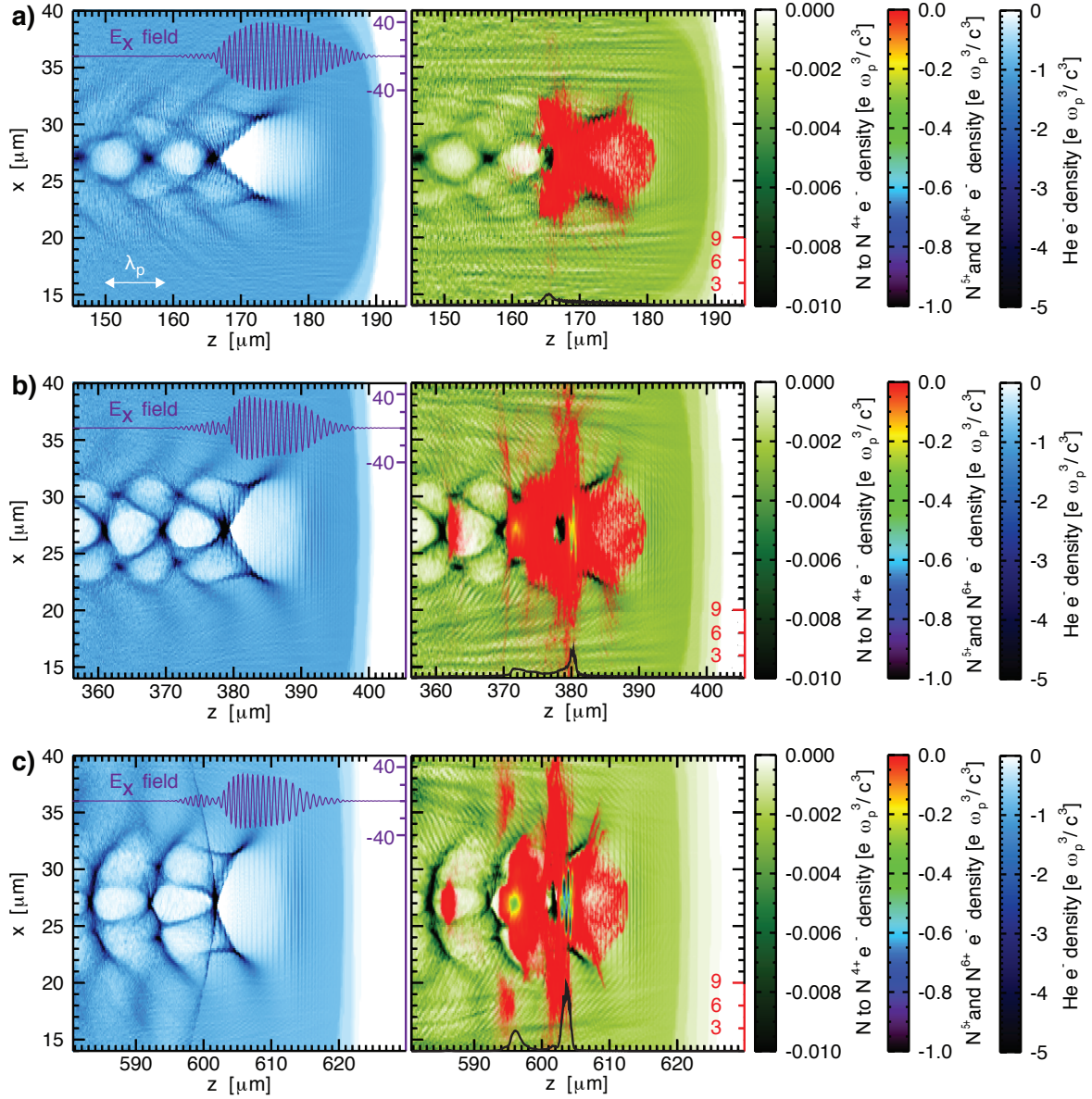


**Figure 3.9:** Evolution of the density of plasma electrons throughout the 3D simulation done with  $T_p = 1.1$ . The laser parameters were similar but the plasma density was increased (180%) significantly and, unlike for the simulations of Figs. 3.6, 3.7 and 3.8 the plasma ended at only  $ct = 780\mu\text{m}$ , therefore only the times  $ct \approx 145, 356$  and  $508\mu\text{m}$  are present. The parameters for this simulation run closely followed the experimental setup used to produce the beams of Fig. 3.4 b).

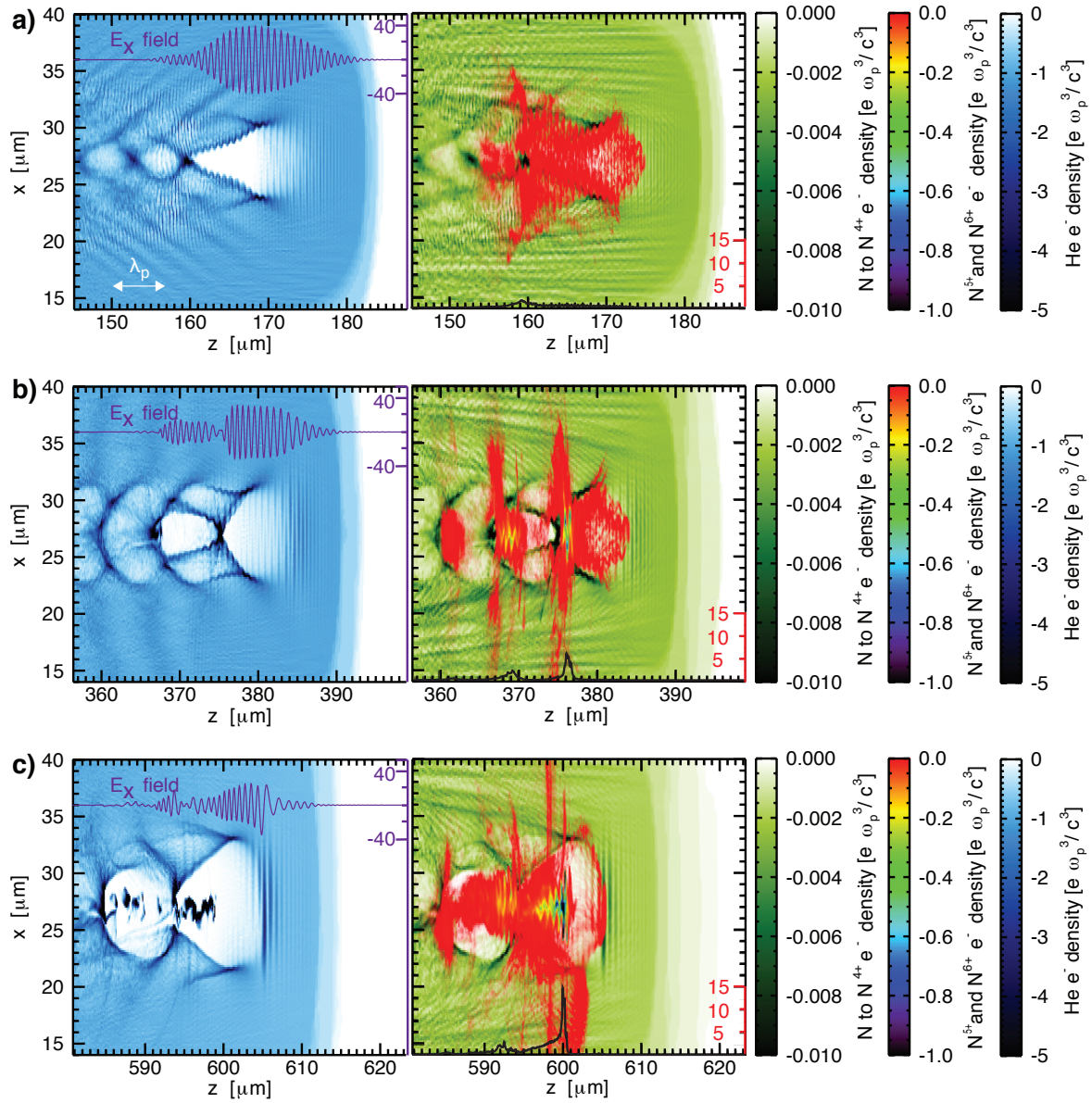


**Figure 3.10:** Evolution of the density of plasma electrons throughout the 3D simulation done with  $T_p = 1.1$ . The laser parameters were similar but the plasma density was increased (280%) significantly and, unlike for the simulations of Figs. 3.6, 3.7 and 3.8 the plasma ended at only  $ct = 773\mu\text{m}$ , therefore only the times  $ct \approx 145, 356$  and  $508\mu\text{m}$  are present.

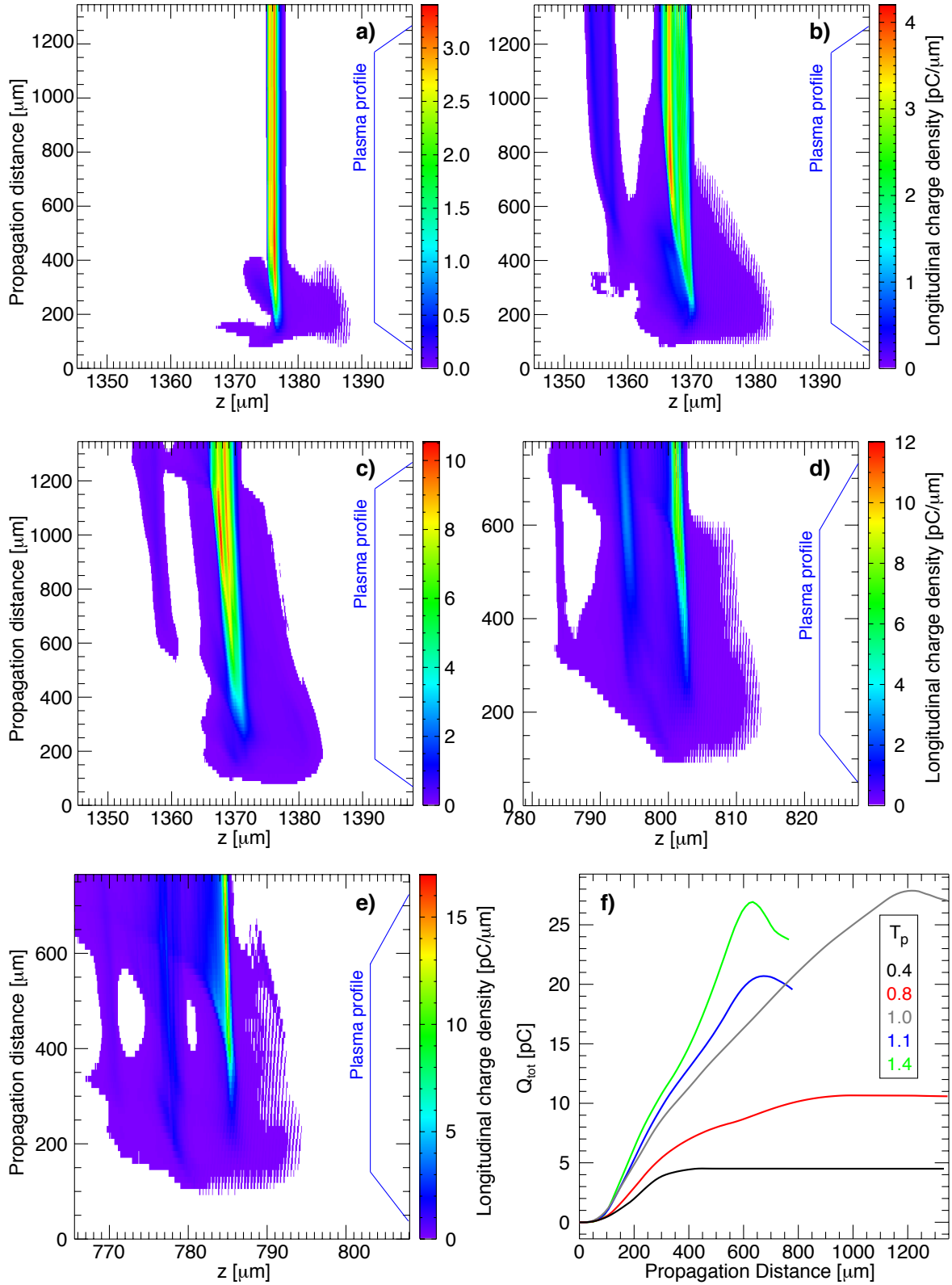


**Figure 3.11:** Evolution of the transversely, in  $x$  and  $y$ , integrated on-axis electron charge originated from the ionization of the  $N^{5+}$  and  $N^{6+}$  ions throughout the propagation distance, with steps corresponding to the time steps in which the simulation results were stored, for all the simulations done, a), b), c), d) and e) ordered by their  $T_p$  value as present in Table 3.1 0.4, 0.8, 1.0, 1.1 and 1.4, respectively. The horizontal axis,  $z$  represents the position relative to the simulation box and is numbered according to the final box location dumped in the simulation. The values were determined from the charge density information that features in the previous plots, Fig. 3.6 to 3.10. The plasma profile is also depicted in the blue solid lines. Plot f) shows the total (integrated also in  $x$ ) charge evolution along the propagation direction.

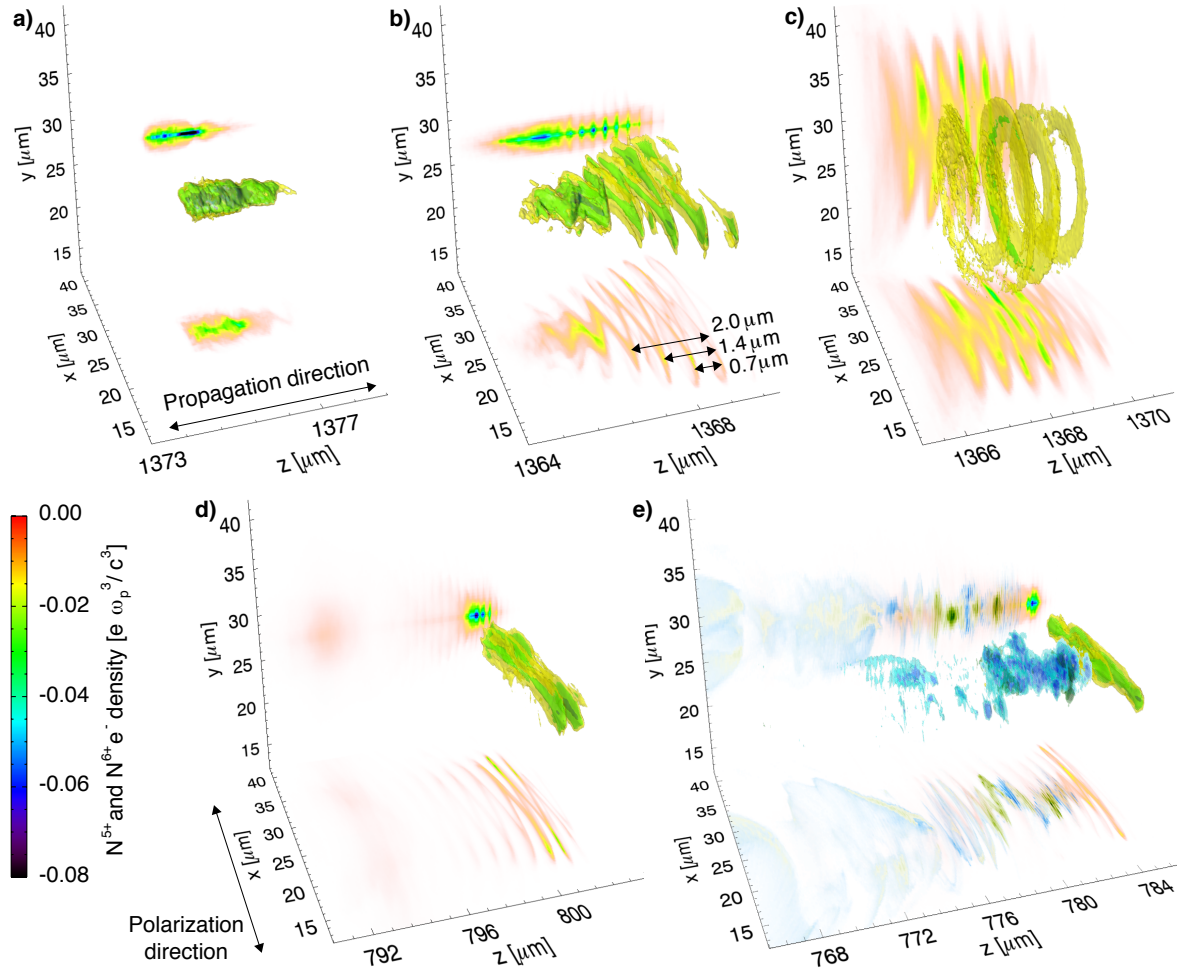


**Figure 3.12:** Accelerated Nitrogen core electron (from  $N^{5+}$  and  $N^{6+}$ ) final density in the 3D simulation box. Labels a), b), c), d) and e) follow the  $t_p$  values of Table 3.1 like in Fig. 3.5. The integrated charge is projected in the z-x and z-y planes of each plot and colored according to the color bar. The isosurfaces were colored according to the grid cell Nitrogen core electron density values (yellow -  $0.045n_0$ ; green -  $0.09n_0$ ; blue -  $0.3n_0$ ). The transverse scale was the same for all the plots. Note that the longitudinal (in z) box width vary for simulations d) and e) for which injection, trapping and DLA occurred also in the second and third plasma wake cavities. The time of the plots was  $ct = 1345\mu\text{m}$  for a), b) and c),  $ct = 779\mu\text{m}$  for d) and  $ct = 767\mu\text{m}$  for e). Plot e) overlaps the electrons from the  $N^{5+}$  and  $N^{6+}$  ionization with those of Helium (density projection and 3D isosurfaces in tones of blue for  $1.0$  and  $2.0n_0$ ) and of the other levels of Nitrogen (projection and isosurfaces in tones of dark green for  $0.005$  and  $0.01n_0$ ).

$T_p$  in the direction of the laser transverse electric field  $E_x$ . Moreover, for plot b) the electron structure is split into sections that are distanced by approximately  $0.7\mu\text{m}$ , they micro bunched, which is of the order of the initial laser wavelength,  $\lambda_0 = 0.815\mu\text{m}$  (measured distances are shown in the plot).

Plot c) represents the final bunch produced with the circular polarized laser and the transverse spread in the two directions  $(x, y)$  perpendicular to the propagation direction  $z$  of equivalent dimensions to that found in plot b). For both plots b) and c) the charge of the second plasma wake trapped and accelerated bunch of electrons was negligible when compared with the first bunch showed in the plots. The final longitudinal charge density at the end of the runs is shown in Fig. 3.11. With circular polarization there is a transverse spread of the electrons away from the propagation axis with a radius that is roughly constant along the propagation distance. Consequently, the effect of DLA through the laser field acceleration and transformation of transverse momentum into longitudinal can have impact all over the beam, which was not the case for the back of the bunch of plot b) where the laser pulse had linear polarization.

Figure 3.12 also shows the final electron beams for the runs with higher plasma densities,  $T_p = 1.1$  and  $1.4$  in which DLA is expected to participate in the acceleration of electrons, d) and e), respectively. In both plots the tail, or secondary electron bunches, with lower integrated density values (orange color in the projections in the two planes) than the first bunch (located in higher  $z$  values), that were mentioned previously for Fig. 3.11 can be seen with a transverse spread along the laser polarization direction equivalent to the first bunch, because the laser encompasses the first two cavities. Plot e) also includes the projected charge density of the electrons ionized from the Helium (blue) and other Nitrogen levels (dark green) that in this run were also trapped and accelerated so would influence the experimental measurements made with a similar laser-plasma setup. These electrons are located in the last plasma wake cavities captured by the simulation box where the laser interaction is less than in the first bubble. It is relevant to note that those trapped electrons have a much narrower transverse spread than the ones located where DLA can have more impact in the electron trajectory and acceleration process.

For all the 3D simulations, files containing the position, momentum, energy and charge information of electron macro particles were created<sup>9</sup>. Because there were over millions of macro particle electrons in the simulation box if we saved the information of all of them into files for each time step. These would require huge storage memory from the supercomputers. It would mean that post-processing of the data of each file would also be quite challenging. Therefore, we did, at each OSIRIS file dumping time step, a random selection of a fraction  $f$ , of the electrons that registered normalized longitudinal momentum above  $\hat{p}_z = \gamma\beta_z = 5$ , which is comparable to the estimated plasma wakefield group velocity  $v_g$  (defined in 3.1.1) relativistic factor  $\gamma_g$ . The values for these parameters can be found in Table 3.3.

<sup>9</sup>These files are commonly designated in the OSIRIS giria as the RAW files.

$T_p$	$e^-$ species	$\gamma_g$	$f$ [%]	$\#N_{>40}$	$g$ [%]	$Q$ [pC]	$Q_{\text{tot}}$ [pC]
0.4	N <sup>5+</sup> and N <sup>6+</sup>	6.8	40	4161162	100	1.80	4.5
0.8	N <sup>5+</sup> and N <sup>6+</sup>	6.8	1.3	286623	91	0.12	10.2
1.0	N <sup>5+</sup> and N <sup>6+</sup>	6.8	1.3	694979	86	0.30	26.8
1.1	N <sup>5+</sup> and N <sup>6+</sup>	5.1	40	4496539	42	3.50	20.8
1.4	N <sup>5+</sup> and N <sup>6+</sup>	4.1	3	381029	63	0.47	24.9
1.4	He and He <sup>+</sup>	4.1	0.07	302	17	0.105	882.4
1.4	N to N <sup>4+</sup>	4.1	0.08	328	19	0.0003	2.0

**Table 3.3:** List of the species of ion macro particles from which the selected electrons present at the end of the runs were ionized,  $e^-$  species for all the simulations, ordered by the  $T_p$  value of the explored configuration like in Table 3.1. The entries below  $f$  represent the percentage of electron macro particles for which position, momentum, energy and charge information was stored. Because the experimental apparatus did not enable accurate measurements below the 40 MeV there was a selection of those electrons with energies above that threshold, which corresponded to a percentage  $g$ , a number of macro particles of  $\#N_{>40}$  with charge  $Q$ . After computing the charge contained in those electrons  $f$  and  $g$  were used to estimate the total charge present in the final accelerated electron bunch  $Q_{\text{tot}}$ . Note that if  $g \times f = 100\%$  then  $Q$  would represent the final total charge as plotted in Fig. 3.11 f) for each run.

Table 3.3 also features the accelerated charge computed from the selected macro-particles of the electrons ionized from the Helium and Nitrogen ion macro particle species, listed under the label  $e^-$  species,  $Q$ , for each simulation and the corresponding estimate on the total charge present in the final electron bunch  $Q_{\text{tot}}$  based on the value of  $f$  at the end of the simulation runs. For this calculation, only electrons that at the end of the run had energies above 40MeV (that were  $\#N_{>40}$  and represented a fraction  $g$  of those present in the file), which was the threshold of the minimum energy correctly detected experimentally, were considered. In the case of the run with  $T_p = 1.4$  also Helium and other Nitrogen electrons were trapped and accelerated, therefore we gathered the macro-particle properties files of those two OSIRIS species and got the values for  $\#N_{>40}$ ,  $g$ ,  $Q$ ,  $Q_{\text{tot}}$  shown in the last two rows of the table.

The values of  $Q_{\text{tot}}$  are more reliable as the parameters  $f$  and  $g$  approach unity and the electron number  $\#N_{>40}$  becomes sufficient for a statistical treatment. Table 3.3 suggests that the final bunch charge,  $Q_{\text{tot}}$ , grows with  $T_p$  for the runs with linear polarization. This is illustrated by the line of Fig. 3.13 that fits the values present on the Table (for the species of electrons that originated from the core of the Nitrogen atoms) with deviations below 20%. It is more accurate to make this fit with the electrons with energies above the plasma wake group velocity than the results present in Fig. 3.11 because those electrons would be the ones leaving the gas cell and being detected experimentally.

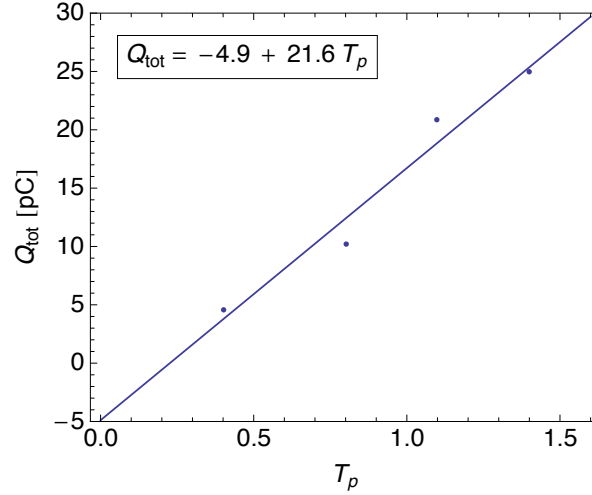


**Figure 3.13:** Plot of the  $Q_{\text{tot}}$  results listed in Table 3.3 for the species  $N^{5+}$  and  $N^{6+}$  and  $T_p = 0.4, 0.8, 1.1$  and  $1.4$  (dots). Solid line represents a linear fit corresponding to the equation shown on the top left box.

To characterize the longitudinal accelerating field that trapped electrons are subject to in the simulated schemes, the on-axis longitudinal electric field was plotted for every run along the time steps dumped to show its evolution, see Fig. 3.14. The dashed lines included in plots a) to e) are guidelines for the final position of the beams as shown in the 3D plots of Fig. 3.12. It is easily seen that these limits match the region of accelerating field for electrons (negative - in blue) before the plasma density profile down ramp section. The plasma wavelengths,  $\lambda_p$  computed for the electron plasma density expected at the flat profile part,  $L_p$ , are shown close to the end of the plasma upramp and are in good agreement with the field wavelength. In the simulations with higher density plasmas, plots d) and e), stronger, more non-linear, in conditions where beam loading is possibly affecting the plasma wave (scenario of the simulation with  $T_p = 1.4$ ), fields are reached and for that reason the resulting field evolution shows more electric field phase variations in respect to the position in the box.

Figure 3.14 f) shows the solid curves of the peak (minimum, since the electron charge is negative) accelerating field within all the box, as the laser pulses propagate through and excite the plasma wakefields. It is interesting to note that for the simulations with lower plasma density and linear polarization, a) and b), the peak field decreased by a factor of approximately 4.5 after propagating  $400\text{-}500\mu\text{m}$  in the plasma. This could be expected from the results of Figs. 3.6 and 3.7 (plots d)) in which the laser pulse exhibits higher pump depletion (lower field values in its front because the laser lost its energy, mostly by ionizing the plasma and exciting stronger wakes in it) and the plasma wake density perturbations seem to vanish, when compared with the results for the following figures. The run with circular polarization (gray line) had a more constant peak accelerating field value which was higher than for the similar setup employing linear polarization (blue line) which could be expected since its pulse power was higher.

The maximum possible energy gain from the longitudinal electric field in all the configurations can be estimated from  $\Delta E_{\text{long}} = \sum_i E_{x\text{max}i} dx$ , where the sum is made over each time step dumped,  $i$ , after the plasma upramp and before the plasma downramp, during  $L_p$ , and  $\delta x$  is the distance between two consecutive time steps dumped,  $cdt$ . The results can be found in Table 3.4 ordered like Table 3.3

$T_p$	$e^-$ species	$\Delta E_{n_{\text{long}}}$	$E_{n_{\text{LWFA}}}$	$\langle E_n \rangle$	$E_{n_{\text{RMS}}}$	$E_{n_{\text{max}}}$	$E_{n_e}$ [%]
0.4	$N^{5+}$ and $N^{6+}$	298	197	137	140	223	25
0.8	$N^{5+}$ and $N^{6+}$	362	197	80	86	165	54
1.0	$N^{5+}$ and $N^{6+}$	1022	197	116	131	287	72
1.1	$N^{5+}$ and $N^{6+}$	320	111	44	53	156	51
1.4	$N^{5+}$ and $N^{6+}$	596	134	63	75	187	67
1.4	He, $\text{He}^+$	596	134	27	36	106	82
1.4	N to $N^{4+}$	596	134	28	36	102	83

**Table 3.4:** Final estimated longitudinal energy gain,  $\Delta E_{n_{\text{long}}}$ , numerically measured average energy,  $\langle E_n \rangle$ , statistical RMS energy,  $E_{n_{\text{RMS}}}$ , both weighted by the electron macro particles charge density value and the  $E_{n_{\text{max}}}$  was the maximum energy of the accelerated electron bunches studied in Table 3.3 without restricting to the electrons with final energies above 40 MeV. The final column shows the relative difference between  $\Delta E_{n_{\text{long}}}$  and  $E_{n_{\text{max}}}$ . Energy values are all in MeV units. This table is ordered in the same manner as Table 3.3.

These values can be compared with the prediction for the typical LWFA blowout regime of operation,  $E_{n_{\text{LWFA}}}$ , computed as the peak accelerating field, through Eq. (2.17), by the plasma flat top region.

It is important to note how the theoretical prediction for the maximum energy (column labeled  $\Delta E_{n_{\text{long}}}$ ) is much lower than the obtained values for the simulations with  $T_p$  over 1, where DLA can have more impact. The mismatch between  $\Delta E_{n_{\text{long}}}$  and the verified  $E_{n_{\text{max}}}$  is of only 25 % for the run where DLA is not supposed to participate in the acceleration of the electrons and is above 50% for all the other simulations and reaches 72% for the scenario with circular laser polarization  $T_p = 1.0$ . The reason for the estimate and verified energies mismatch can be mainly justified by: the electrons not being injected nor trapped in the wake from the start (so the total effective accelerating distance,  $\Delta x$ , is much smaller); the trapped electrons not experiencing the peak accelerating field throughout their acceleration process as they can be trapped at different longitudinal locations and also perform wide betatron oscillations around the propagation axis (where the peak is located). The mismatch is lower when DLA is present because it consists of an additional acceleration mechanism that increases the final energy of the electrons.

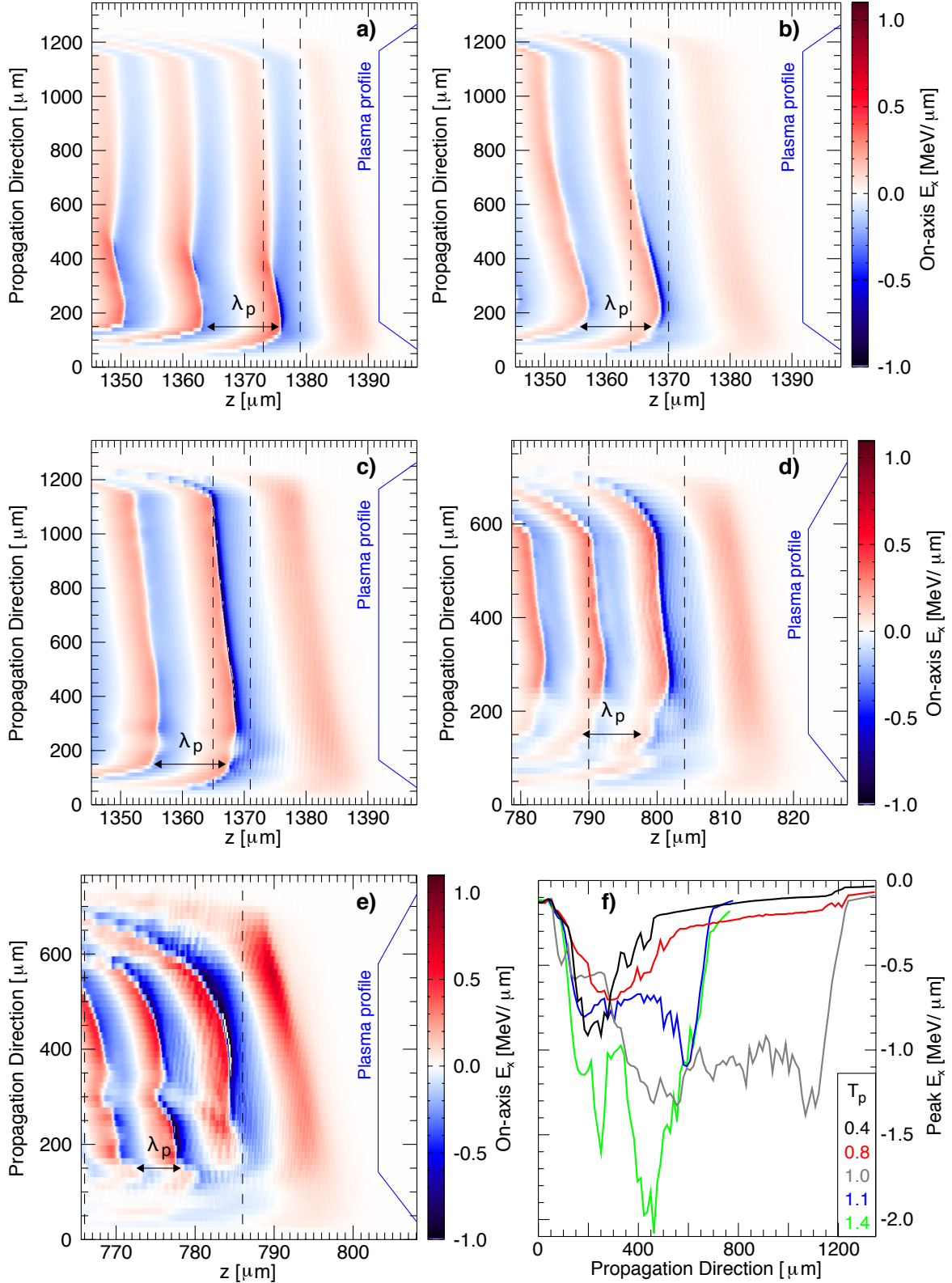


**Figure 3.14:** 2D plots of the numerical on-axis longitudinal electric field values along the propagation distance (color scale indicated in the color bar), i.e. for each time step dumped. Because a moving window was employed, the longitudinal axis corresponds to the longitudinal position relative to the simulation box and the shown values are for the final time step dumped. The dotted vertical lines show the corresponding limits of the 3D boxes used to plot the final beams in Fig. 3.12. Labels a), b), c), d) and e) follow the  $T_p$  values of Table 3.1: 0.4, 0.8, 1.0, 1.1 and 1.4, respectively. Plot f) combines the minimum (negative) longitudinal electric field values over all the simulation box also along the propagation distance. Colors are indicated in the label box to the right. Blue solid lines depicts the gas longitudinal density profile.

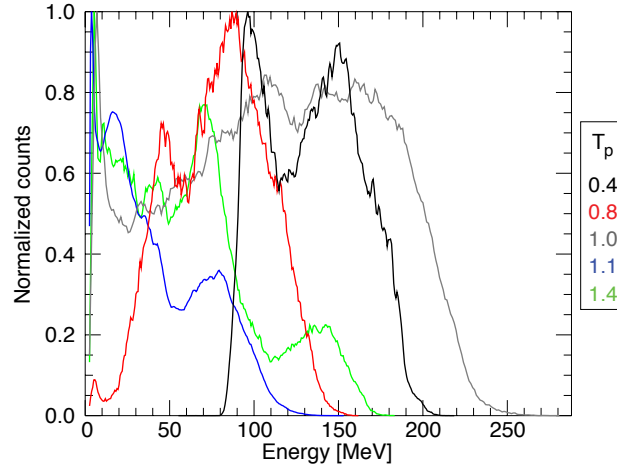


**Figure 3.15:** Energy histogram of 256 energy bins by the number of randomly selected electron macro particles normalized for a better appreciation of the spectrum shape, done for the different numerically explored laser wakefield scenarios present in Table 3.4. Colors follow the label in the right with the configurations  $T_p$  values.

For the simulations and species in Table 3.3, we looked at the final randomly selected electron bunch average energy,  $\langle E_n \rangle$ , RMS energy,  $E_{n_{RMS}}$  and maximum achieved energy,  $E_{n_{max}}$ , which can be seen in Table 3.4. For a better understanding of the electron bunch energy the final histograms can be seen in the plot of Fig. 3.15. The differences between the values of  $\langle E_n \rangle$  and  $E_{n_{RMS}}$  may be justified by the not gaussian like curves of the energy spectra. In the run that differed only in the laser pulse length, with  $T_p = 0.8$  (red line), in contrast to 0.4 (black line), where no DLA effect is predicted, the final electrons had lower  $E_{n_{max}}$  and high concentration of electrons below 80 MeV. Moreover the run with  $T_p = 0.8$  (red) resulted in an energy spectrum with broader peak, i.e. higher concentration of electrons, at the region with highest energies, whilst, the one with 0.4 (black) had the broader peak close to the lower energies. This suggests that when DLA participates in the the acceleration process, the energy of the majority of the electrons is significantly increased.

When the pulse is circularly polarized, Fig. 3.15 (gray line), the peak longitudinal accelerating field is higher and approximately constant throughout the acceleration distance, see Fig. 3.14 c) and  $T_p = 1.0$  gray curve in plot f). The main reason for the uniformity of the field can be the absence of beam loading (the injected and trapped ionized electrons, within the two first bubbles, were not enough to significantly excite their own wakefields). However, the contribution of that field to the electrons final energy is lower than for the runs with similar parameters and linear polarization,  $T_p = 0.8$ , see Fig. 3.16, because the majority of the electrons are away from the propagation axis<sup>10</sup>, see Fig 3.12 plot c), where the longitudinal wakefield peaks. For that reason  $T_p = 1.0$ , exhibits a broad almost uniform spectrum with still a great concentration of electrons at the highest energy levels. This configuration was the one that registered higher energy gain by the electrons and, see Table 3.3, higher estimated total accelerated charge.

When shorter plasmas were employed for the laser with  $T_p = 1.1$  and 1.4, the acceleration distances were also shortened justifying the lower  $E_{n_{max}}$  values. For these cases most of the bunch

<sup>10</sup>The longitudinal field does not strongly depend on the radial distance to the propagation axis in the central part of the bubble. However, for electrons performing wide betatron oscillations the field can be significantly different from the axis to the betatron radius location.

electrons lost energy to the excitation of the wake structure. However, in both cases, there are three very clear humps, the last being at the highest energy portion of the spectra, suggesting different contributions from the acceleration mechanisms for the highest energy electrons of those runs. For the last run, the much lower  $E_{n_{\max}}$  registered for the electrons originated from Helium or from the other Nitrogen levels suggests that only the electrons accelerated in the initial plasma wake cavity, where the impact of [DLA](#) is higher, reach the highest energies. This strongly suggests the presence of [DLA](#) of electrons in this scenario.

For all these simulations, at the end of the plasma we selected 500 random and 20 highest energy macro particle electrons originated from the Nitrogen core that were contained in the first helium plasma wake cavity. We confirmed that these electrons were still present in the simulation box at the last dump time step and we stored the information of the nodes/particle label and iteration at which they were created by ionization of a numerical ion macro particle. With this information we re-ran all the simulations to store the information of the interpolated electric and magnetic field, energy, momentum, position and charge at each time step of each of those electrons along their trajectory<sup>11</sup>. The longitudinal wakefield overall contribution to the acceleration for each of the selected electrons was computed through:

$$W_{\text{long}} = \sum_{j=0} q_j E_{z,j} (z_j - z_{j-1}) \quad (3.6)$$

Where the subscript  $j$  indicates the sum over every time step (numerical iteration). The fraction  $F = W_{\text{long}}/E_{n_{\text{end}}}$ , for all the electrons, with final energy  $E_{n_{\text{end}}}$ , is shown in Fig. [3.16](#) for the different simulations and gives us a hint of the portion of the total energy that the electron gained through longitudinal and not transverse fields, which can be attributed mainly to [LWFA](#). The fraction values above 100% and negative are a consequence of some electrons gaining energy from the longitudinal wakefield and then losing it, either to the transverse wakefields or because of the laser fields, i.e. decelerating. The highest energy electrons of all the runs where [DLA](#) effect is present,  $T_p > 0.4$  have, in comparison with the 550 randomly selected electrons (bulk), lower total longitudinal energy gain. The gap between the maximum energy of the bulk electrons and the minimum energy of the 20 highest energy selected ones ranged from 25 to 80 MeV. That gap was greater when [DLA](#) was present reinforcing the idea that [DLA](#) is responsible for the acceleration of the higher energy electrons in the assisted [LWFA](#) setup. For the run with  $T_p = 0.8$  (red dots), the bulk of the final electron bunch is at the back of the plasma density wake bubble, see Fig. [3.7](#) plot d), subject to the peak accelerating longitudinal field had about 100% energy gain from the wake, whilst the highest energy electrons marked values below 80% and so were also directly accelerated by the laser.

<sup>11</sup>These files are commonly designated in the OSIRIS giria as the TRACK files.

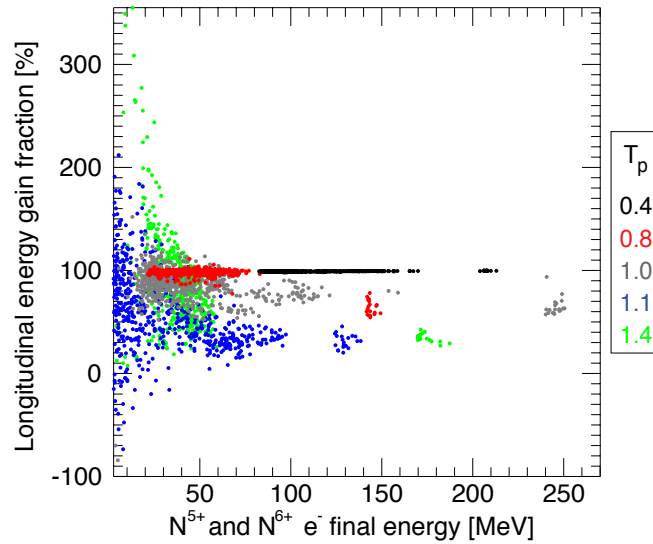


**Figure 3.16:** Plot of the net longitudinal wakefield induced electron energy gain computed with Eq. (3.6) fraction over its final energy and applied to 550 randomly selected and highest energy electrons, originated from the ionization of  $N^{5+}$  and  $N^{6+}$ , that were contained in the first plasma wake bubble at the end of the plasma. Colors indicated in the label box in the right. The values greater than 100% if the electrons lost more energy than they gained by the longitudinal wakefield (mostly due to the laser DLA process and/or the plasma transverse fields).

With similar reasoning the (mainly) DLA contribution along the laser polarization direction, or electric field  $E_x$ , can be roughly estimated by:

$$W_{\text{trans}} = \sum_{j=0} q_j E_{x,j} (x_j - x_{j-1}) \quad (3.7)$$

, shown in plot a) of Fig. 3.17 for the scenarios with linear polarization. For the circularly polarized laser pulse run,  $T_p = 1.0$  we added the discrete integration in the other transverse direction for every electron. Fig. 3.17 b) depicts the fraction  $F' = W_{\text{trans}}/E n_{\text{end}}$

The 20 highest electrons in each run that are also plotted in Fig. 3.17 have the highest transverse energy gain values, which validates the analysis of their longitudinal energy gain fraction from Fig. 3.16. These results indicate that the impact of DLA is higher for higher energy particles. The run with  $T_p = 0.8$  had, overall, less DLA associated transverse energy gain because the bulk of the bunch, see Fig. 3.7 d), was trapped behind the strong laser field region. This is the reason for the tail of the electrons in Fig. 3.12 plot b) being less spread transversely than the front, already bunched, part. Which was not the case for the cases with  $T_p = 1.0, 1.1$  and  $1.4$  (for the first plasma bubble portion of the bunch).

Furthermore, in the case of circular polarization,  $T_p = 1.0$  (gray dots and line), where the electrons can be accelerated by the laser directly in both directions, the highest final energies (and slope/trends) were achieved (when comparing with the same laser-plasma configuration setup that used linear polarization  $T_p = 0.8$ ). For further evidence of the interplay between DLA and LWFA we reproduced the transverse position spectra, equivalent to the experimental results featured in Fig. 3.4, for the simulation setup that reproduced the same  $T_p = 1.1$ , using its  $\#N_{>40}$  electrons information (because the experiment only measured accurately energies above 40MeV), see Table 3.3, in Fig. 3.18<sup>12</sup>.

<sup>12</sup>Note that when in the experiment electron bunches are dispersed in one direction (orthogonal to the propagation direction)

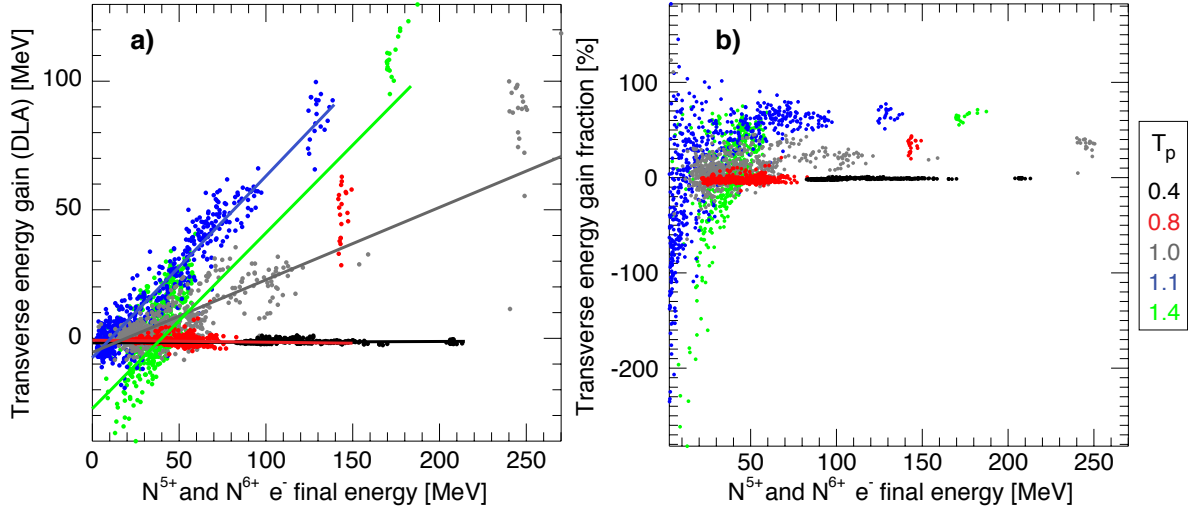


**Figure 3.17:** a) Plot of the transverse wakefield and laser electric field energy transfer throughout the simulations computed with Eq. (3.7) and applied to the same 550 randomly selected and 20 highest energy electrons of Fig 3.16, originated from the ionization of  $N^{5+}$  and  $N^{6+}$ , that were contained in the first plasma wake cavity at the end of the plasma. Colors follow the label in the right with the configurations  $T_p$  values. Solid lines represent a fit to the 550 electrons only with slopes of 0.005, -0.003, 0.265, 0.709 and 0.714 for the simulations with  $T_p = 0.4, 0.8, 1.0, 1.1$  and  $1.4$ , respectively. Plot b) contains the fraction of that value over the final electron energy.

The transverse final positions were determined by free-streaming the electrons from the final time step (neglecting the effects of self-interactions on their trajectory) the  $x, y_{\text{screen}} = x, y_{\text{end}} + p_{x,y}/p_z (z_{\text{screen}} - z_{\text{end}})$  for every electron and then the corresponding charge density was projected over a 256 by 256 grid of Energy versus position values. The virtual detector screen was placed at  $z_{\text{screen}} = 9.2\text{cm}$  after the plasma gas cell and perpendicular to the laser propagation direction. The electron position in the simulation box at the end of the simulation is labeled  $z_{\text{end}}$ . In the experimental results, Fig. 3.4, electrons registered energies up to 140 MeV. This was also the energy range of the electrons according to the numerical results, Fig. 3.18. Both results also showed what we called the "fork"like structure (electrons concentrated at two transverse locations in the laser polarization direction,  $x$ ) for energies above the 90 MeV, plots b. The simulation bunch of electrons did not show an on axis density peak for lower energies, as opposed to the experimental result. This is due to the simulation not covering the electrons that are trapped into the subsequent bubbles of the plasma wake, where the laser does not reach, and hence DLA does not occur. In the direction perpendicular to both the laser polarization and propagation directions,  $y$ , both figures 3.4 a) and 3.18 a) exhibit only a clear central peak which implies that wakefield acceleration was not assisted by DLA in that direction, as was expected. Moreover, Fig. 3.18 a) shows a transverse spread of 0.5 cm corresponding to 75% less than plot b). This agrees with the 50% difference between the directions orthogonal to the laser propagation direction experimental measurements of the HWHM final electrons divergency.

they exhibit their energy in that same direction and their final positions and spread in the other perpendicular direction. The plots of the simulation bunches energy spectra show the red arrows according to the direction the electrons would be "dispersed" in experiment, see Fig. 3.4.

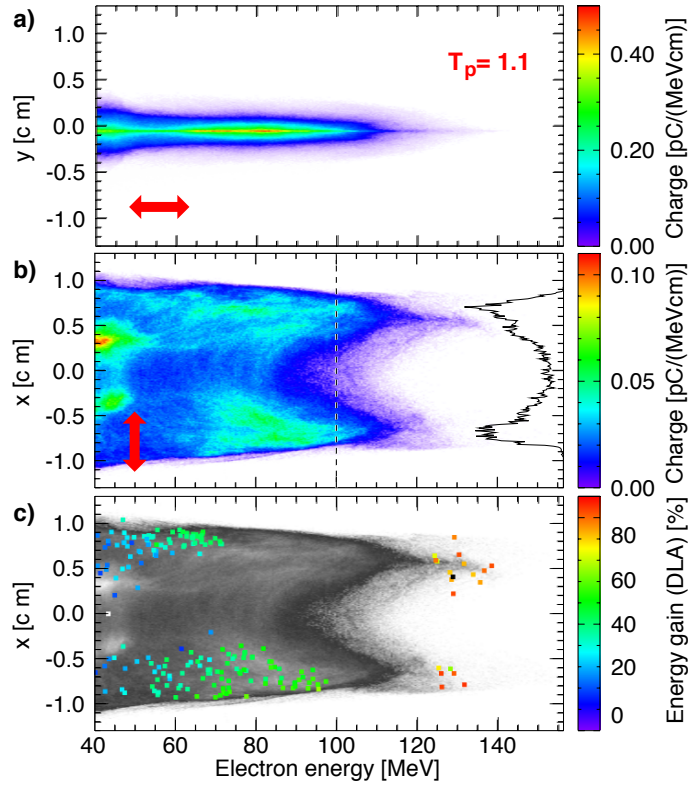


**Figure 3.18:** Plot of the final simulated transverse position orthogonal to the laser propagation direction to correspond to experimental measurement, Fig. 3.4 where electrons were dispersed: a) parallel and b) perpendicular to the laser polarization direction (red arrows). The solid line in b) represents the transverse lineout at 100 MeV (located on the dashed line). In a) and b) the color scale indicate charge density of the Nitrogen core ionized electrons. In plot c) the same density plot as in b) is depicted (gray tones) and overlapped with the 550 selected random (with energies above 40 MeV) and the 20 highest energy electrons color scaled by the fraction of the total energy gain from the transverse  $E_x$  field during their trajectory, Eq. 3.7 over their final energy. This simulation was done with the parameters of the  $T_p = 1.1$  entry in Table 3.1.

Figure 3.18 c) shows the position in the spectra of the 550 randomly selected and the 20 highest energy electrons that were within the first plasma wake bubble before the plasma down ramp part, colored according to the fraction of the transverse energy gain by their final energy that is influenced by DLA. The 20 highest energy electrons that are over the "fork" structure register greater transverse energy contribution, i.e. DLA (reaching 90%) corroborating the experimental findings of see Sec. 3.2.3 that attributed the "fork" on the plots where electrons had been dispersed perpendicularly to the laser polarization direction, to the impact of DLA in the LWFA. There is a mismatch between the regions of higher charge density in Figure 3.18 plots b) and c) (in gray tones) and the distribution of the selected electrons. This is because the electrons from outside of the first plasma wake bubble (where DLA is less important) contributed to the higher concentration regions.

The same analysis done to the scenario with  $T_p = 0.4$ , where DLA effects are not expected because the laser pulse does not overlap the trapped electron bunch, is shown in Fig. 3.19. It shows similar spectra in the two directions orthogonal to the laser propagation direction, plots a) and b), with no visible "fork" like region. The final electron minimum and maximum energy limits are higher than for the other configurations, which is due to the higher longitudinal energy gain, see Fig. 3.16 and no energy loss from the electrons to the plasma wake taking place. This can also be due to the final

bunch being perfectly confined to the first plasma wake bubble region, see Fig. 3.6, which was not the case in the simulations with shorter plasma density profiles nor the one with circular polarization. The transverse total energy gain and loss was less than 3% of the electrons final energy as was to be expected when DLA does not interfere with their trajectories.

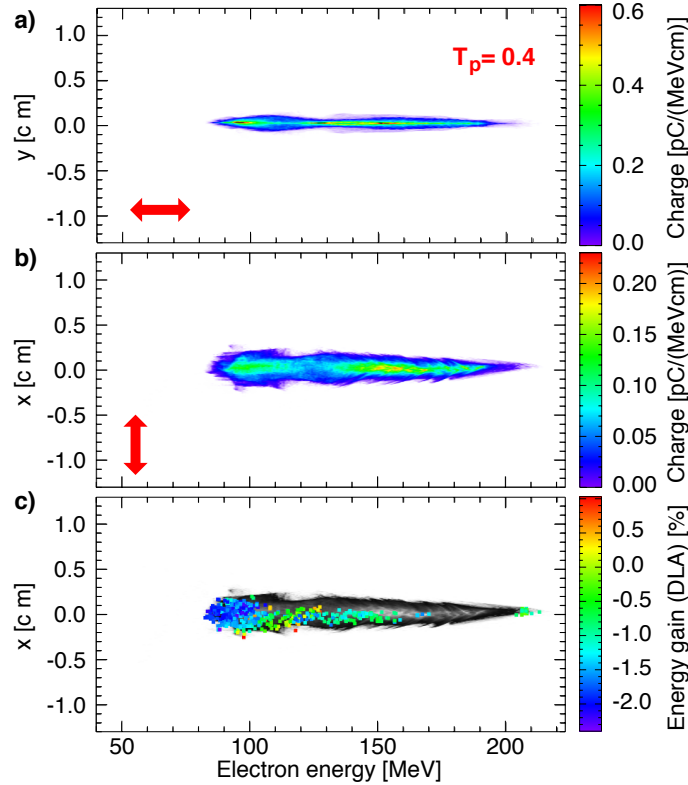


**Figure 3.19:** Plot of the final position energy spread orthogonal to the laser propagation direction to corresponding to electrons being dispersed: a) parallel and b) perpendicular to the laser polarization direction (red arrows) for the simulation with  $T_p = 0.4$ . Color scale indicate charge density of the Nitrogen core ionized electrons. Plot c) shows the 550 randomly selected and 20 highest energy electrons color scaled according to the fraction of the total transverse energy gain by their final energy over the charge density of plot b) (in gray tones).

The run with the same parameters except for a longer laser pulse, that had  $T_p = 0.8$ , showed a clear “fork” for energies also above 90 MeV and the electrons exhibited a central density peak for energies below that, in the direction of the laser polarization, Fig. 3.20 plots b) and c). The selected electrons gained up to 44% of their energy from the transverse electric field, which is dominated by the laser field, but the bulk electron bunch experienced energy loss related to the transverse field. Looking back at the respective wake and bunch electron density evolution, see Fig. 3.7, it is clear that the main (the second peak had negligible charge) final electrons bunch is confined to the plasma wake bubble overlapped by the transverse electric field (due to the laser), which is suitable for DLA to participate in the acceleration of the electrons. Fig. 3.9, for example, unlike Fig. 3.7, had a secondary bunch, where there was at the end no electric field and so those electrons would be accelerated only by the plasma longitudinal wakefield. Moreover, there is significant electron charge outside of the plasma wake cavities contributing to a higher transverse spread regardless of if the electron had been subject to DLA or only LWFA

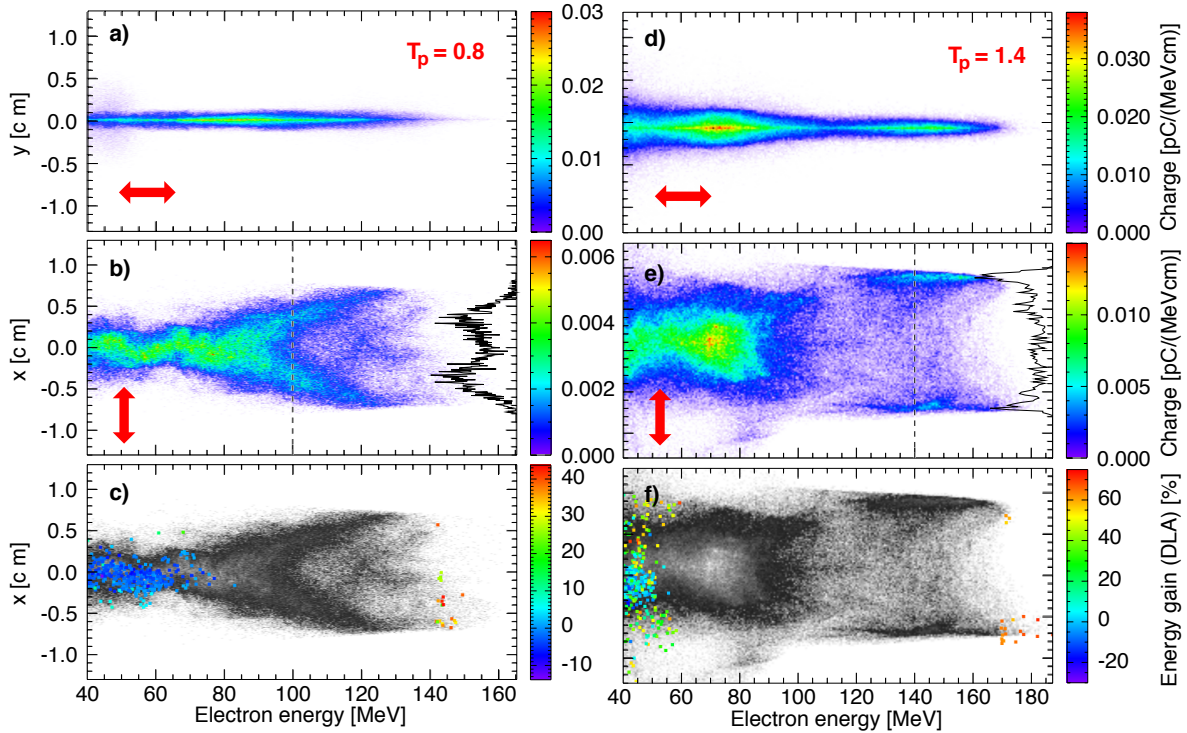


**Figure 3.20:** Plots of the final simulated transverse position orthogonal to the laser propagation direction where electrons were dispersed: a), d) parallel and b), c), e) and f) perpendicular to the laser polarization direction (red arrows), for the runs with  $T_p = 0.8$  and  $1.4$  (red labels) without electrons with final energies below 40 MeV. Solid lines represent the transverse lineout at b) 100 and e) 140 MeV (dashed lines). Plots d) and f) show the 550 randomly selected and 20 highest energy electrons color scaled according to the fraction of the total transverse energy gain by their final energy, over the charge density (in gray tones).

Figure 3.20 plots e) and f) show a clear separation (gap) in energy between the “fork” region, for values above 100 MeV, and the initial central peak. The gap was evident mostly on the simulation with  $T_p = 1.4$ , which had higher maximum energy gain registered for the DLA assisted LWFA and higher peak longitudinal wakefield, see Fig. 3.14. Note that in that run, the selected electrons got up to 75% of their energy from the transverse electric field. In plot f) the energy gap between the regions of higher charge density (bulk) and of the selected electrons is even greater than for Fig. 3.18. The electrons trapped within the first plasma wake cavity seem to be concentrated around the 50 MeV region, indicating that the region between 70-90 MeV results from electrons from the subsequent cavities (where there was no DLA) or that escaped the wakefields.

The previous results are in agreement with the experimental observation of the undispersed electron beams ellipticity (elongation of the beam profile along the laser polarization direction) where the major axis was in the selected polarization direction, see Sec. 3.2.3 and [61]. The simulation with the laser circular polarization yielded the plots of Fig. 3.21 where a large, almost uniform, transverse final spread is present in both directions orthogonal to the laser pulse propagation direction for energies from 80 MeV to 220 MeV. So no “fork” like structure can be seen in this case. This comes from the dispersion of the electron bunch of plot c) of 3.12 where the electrons are concentrated in a spiral shape, quasi symmetric between both transverse directions,  $x, y$  and the energy spectrum (in gray) of Fig 3.15. In this acceleration configuration trapped electrons reached the higher energies than in

those with linear polarization but the minimum energy detected was below what we found for  $T_p = 0.4$ , suggesting greater energy loss by the electron bunch.

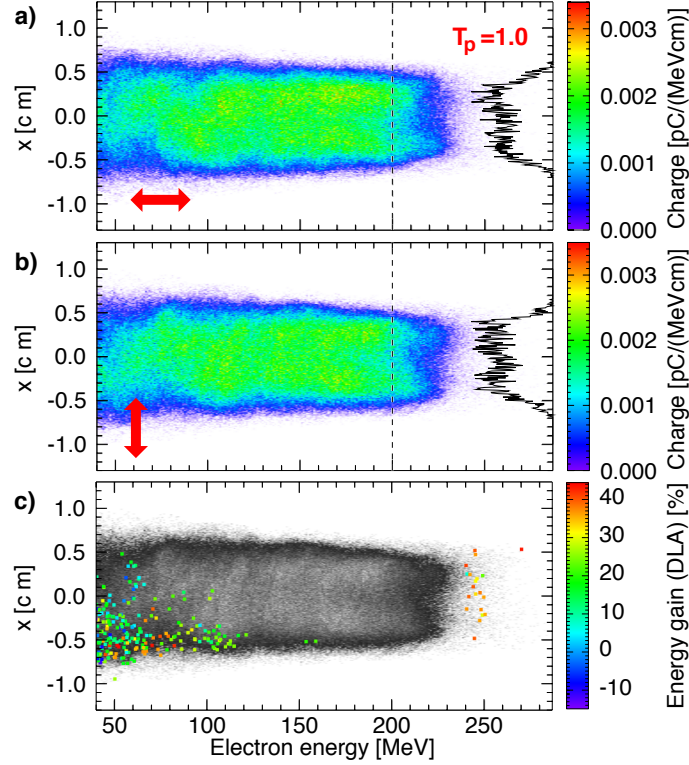


**Figure 3.21:** Plot of the final position energy spread orthogonal to the laser propagation direction to corresponding to electrons being dispersed: a) parallel and b) perpendicular to the laser polarization direction (red arrows) for the simulation with laser pulse circular polarization,  $T_p = 1.0$  without accounting for electrons with final energies below 40 MeV. Solid lines in a) and b) represents the transverse lineout at 200MeV (located on the dashed line). Plot c) shows the 550 randomly selected and 20 highest energy electrons color scaled according to the fraction of the total transverse energy gain (in both directions perpendicular to the laser propagation direction) by their final energy, over the charge density (in gray tones).

Moreover, unlike for previous runs, where higher energy electrons had had greater **DLA** contribution, Fig. 3.21 c) shows that in the circular polarized laser pulse **LWFA** electrons gain up to 45% of their final energy from the transverse field (i.e. **DLA**). That observation is valid for most electrons and not just those with higher final energies, unlike what we observed for the linearly polarized laser setups. This can be explained when looking at plot e) of Fig. 3.22 for which the bulk of the 550 electrons was created right before the neutral gas density down ramp at initial transverse positions with offsets up to  $3 \mu\text{m}$  from the laser pulse propagation axis. Such initial conditions result in **DLA** being present in most of their acceleration process. This was not so for the simulation with similar parameters but linear laser polarization,  $T_p = 0.8$ , see Fig. 3.20 plot c), because, as plot b) of Fig. 3.22 shows, the final electrons created were born close to the axis where **LWFA** is more relevant to their acceleration. It was also not the case for the simulation with the shorter laser pulse. The simulations with higher plasma densities also generated electrons before the plasma down ramp and at transverse positions far from the axis. Therefore, electrons with significant transverse field **DLA** contribution were registered with low final energies, the distinction was clearer than in Fig. 3.21 c), because the plasma length and final energies were much smaller.

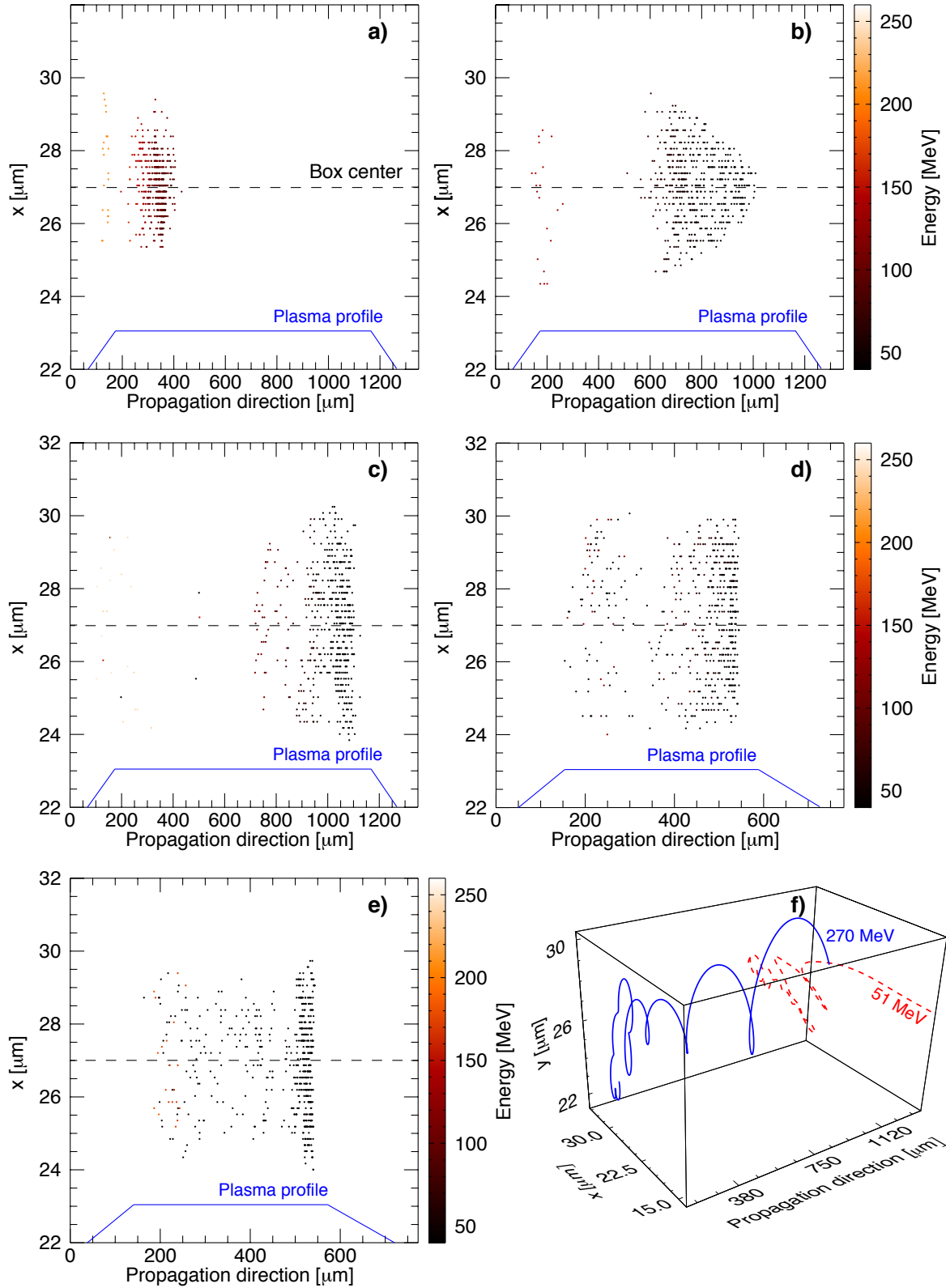


**Figure 3.22:** Initial (ionization) transverse location, parallel to linear laser polarization direction, of the 550 random and 20 highest energy selected electrons for the a), b), c), d) and e) runs with  $T_p = 0.4, 0.8, 1.0, 1.1$  and  $1.4$ , according to Table 3.1, respectively throughout the propagation direction. Color scale corresponds to electron final energy. Blue solid line depicts the neutral gas density profile and the dashed black line the center of the simulation box. Plot f) shows the 3D trajectory of the highest energy of the 20 selected electrons (reaching 270 MeV, blue line) is shown as well as the trajectory of one of the 550 selected electrons with high transverse field, **DLA** associated, contribution to its final energy (reaching 51 MeV, red dashed line).

For a clearer interpretation of the reasoning of the previous paragraph, two 3D trajectories from the simulation run with circular polarization are shown in Fig. 3.22 plot f). One electron (blue line) was ionized after  $140 \mu\text{m}$  at almost the transverse box center,  $x \approx 27 \mu\text{m}$  and quickly described a circular elongated and wide betatron 3D orbit whilst the other one was created already after  $1000 \mu\text{m}$  at  $x \approx 30 \mu\text{m}$ , i. e. already after the laser propagated almost  $859 \mu\text{m}$  into the plasma. Both electrons had high contribution from the transverse electric fields, DLA to their final energies but one reached the highest final energy, 270 MeV (blue line), from the 570 selected ones, and the other had only 51 MeV (red line). The fraction of their final energy that was due to both transverse fields, dominated by the laser fields, was similar, 44% and 38%, and so was the fraction that came from the longitudinal wakefield was 56% and 62%, respectively, so in the plot c) of Fig. 3.21 these electrons would show red color and yet be placed in the low and high energy parts of the transverse final position spectrum.

To illustrate in detail the impact that DLA can have in the LWFA excited with linear polarized laser pulses we followed a part of the trajectory of a trapped and accelerated electron, ionized from the Nitrogen core atom,  $\text{N}^{5+}$  and  $\text{N}^{6+}$ , from the simulation with  $T_p = 0.8$ , black line in Fig. 3.23. In Fig. 3.23 the electron gains energy in the unshaded white regions when its velocity is positive (positive slope of the black curve) and the field it sees is negative or vice-versa, see Eq. (3.7).

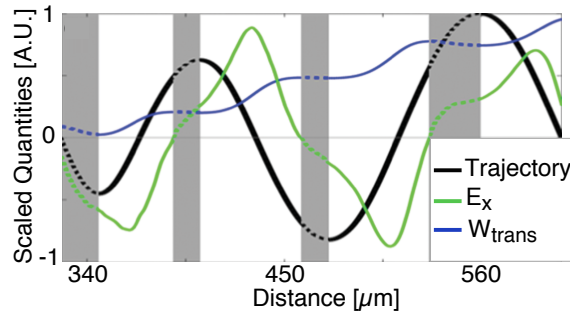


**Figure 3.23:** Single electron (from the 20 highest energy studied) two betatron oscillations trajectory (black solid line) is shown in the laser propagation direction. The transverse electric field on the laser polarization direction,  $E_x$ , sampled by the electron is plotted (green line) as well as the integrated transverse energy gain computed from Eq. (3.7) (blue line). Shaded rectangles (and dashed lines) highlight the regions where the resonance condition, Eq. (3.2), is not verified. All quantities are normalized to their peak value [61, 62].

Considering the resonance condition, Eq. (3.2), in a DLA assisted LWFA that consists, ideally, of the electron going through a laser pulse wavelength per betatron oscillation. The challenge of maintaining the resonance is that the electron energy and the betatron frequency as well as the laser pulse properties vary significantly along the propagation distance. Nevertheless, it is sufficient for that resonance to be verified for longer than half a betatron oscillation for net acceleration of the electron directly by the laser to occur, like in the plot of Fig. 3.23 (white segments need to cover more than half a cycle of the black curve).

### 3.4 X-ray emission from Direct Laser Acceleration in Plasma Wakefield accelerators

In Sec. 2.4 some of the relevant applications of short pulsed hard (critical energy above 30 keV) x-ray probes with low-divergence in the fields of biology, astrophysics, high energy density science and inertial confinement fusion [20] were reviewed. In the DLA assisted LWFA scheme, operating in the nonlinear blowout regime, the trapped electrons perform wide betatron oscillations. Hence it is logical to inquire about the properties of the radiation that they produce and if it carries additional signatures of the presence of the DLA mechanism.

Taking advantage of the trajectory information collected for the analysis of the previous section, the information from the 550 randomly selected and 20 highest final energy electrons contained in the first plasma wake bubble at the end of the run, trajectory, momentum and sampled fields evolution was post-processed by the radiation diagnostic code jRad [70], see Sec. 2.5.2.A. The radiation was determined, according to Eq. (2.19), in a virtual detector placed perpendicularly to the propagation axis. The detector was at a distance of  $z_{\text{det}}$  to the end of the simulations, corresponding to 19 cm from the start of the initialized neutral gas jet (i.e. plasma)<sup>13</sup>. The size and resolution of the detector are presented in the Table 3.5 as well as the energy resolution for the, particle weighted, measurements of the radiated energy spectra. The peak energy position was used to scan the power emitted at an offset in the transverse directions of  $x_{\text{det}}$  and  $y_{\text{det}}$  from the detector center.

$T_p$	$z_{\text{det}}$ [cm]	$(x_{\text{det}}, y_{\text{det}})$ [cm]	$x \times y$ Size [cm <sup>2</sup> ]	Resolution	
				Detector [cells <sup>2</sup> ]	Energy [cells]
0.4	17.7	(0, 0)	1.1 × 1.1	1152 × 1152	9216
0.8	17.7	(0, 0)	3.4 × 1.1	3456 × 1152	9216
1.0	17.7	(-0.38, -0.81)	3.8 × 3.8	1152 × 1152	9216
1.1	18.2	(-0.84, 0)	5.6 × 2.8	2304 × 1152	9216
1.4	18.2	(0.50, 0.05)	4.4 × 2.2	2304 × 1152	9216

**Table 3.5:** Position of the virtual detectors used in the JRAD diagnostic of the radiation of the accelerated electrons in the simulations described in Sec. 3.3.

The radiated energy reaching the virtual detector computed from the trajectories of the 20 electrons for the different simulations are plotted in Fig. 3.24. These electrons showed higher transverse displacements and final energies and DLA contribution, at the end of the runs and, because they were ionized and trapped before the other 550 electrons, they are responsible for emitting more photons and shaping the resulting radiation beam, influencing its final energy and critical frequency (please revisit Sec. 2.4 for the description of the quantities). In the run with  $T_p = 0.4$ , plots a), DLA phenomena

<sup>13</sup>The distance to the virtual detector was chosen to allow for a future experimental implementation of an x-ray diagnostic at approximately that location.

is not expected to influence electron trajectory.

Plot a) of Fig. 3.24 shows an almost symmetric core and halo radiation energy distribution in the virtual detector. It is clear that as the  $T_p$  parameter increases, plots b), d) and e), the core energy (mostly the green region) can be compared to an ellipse with larger axis in  $x$ , which is parallel to the laser polarization direction. This is a consequence of the wider betatron oscillation radius that the 20 highest energy electrons traverse in the laser polarization direction, in comparison with the other direction orthogonal to its propagation direction,  $y$  (see Fig. 3.18 and Figure 3.12). Fig. 3.24 f) the photon energy distribution seems to also reach higher critical energies (corresponding to higher critical frequencies since  $En_{\text{photon}} = \hbar\omega$ ) for the simulations with greater  $T_p$ .

The highest energy electrons from the simulation where the LWFA was achieved with a laser with circular polarization, case of plots c), produce a ring like energy profile in the virtual detector. Moreover, the radiated energy is higher than that generated in the other simulations which can reflect the previous section observations of this scenario having wider radius and more energetic final electron beams. In the linear polarization cases, the energy radiated grows with  $T_p$  just like the expected impact of DLA see Fig. 3.17. In the circular polarization case of plot f), (gray curve) there is still significant relative radiation energy emitted at photon energies beyond 30 KeV suggesting that the DLA assisted LWFA mechanism excited by a circular polarized laser can produce hard x-rays with circular polarization.

The corresponding integrated radiation spectra in each detector direction (following  $y$  or  $x = 0$ ) are shown in Figs. 3.25 and 3.26 respectively. The spectra in the two directions are similar for the run with  $T_p = 0.4$ , plots a). The anisotropy already visible in Fig. 3.24 is also clear in the different directions spectra for the runs of b), d) and e). A triangular spectral shape (of the radiated energy density contours) is easy to identify in plots a) for both figures but difficult for the other plots in Fig. 3.25. This can be due to the presence of the additional acceleration mechanism, DLA, that can interfere with the electrons bubble/blowout typical wakefield betatron oscillations and broaden its radius in the laser polarization direction,  $x$ . The circular polarization spectra are symmetric in  $x$  and  $y$  just like the energy plot c) of Fig. 3.24. The two cuts of the ring-like structure show in the spectra as two high intensity regions that are also not triangular.

The total radiated energy in the virtual detectors caused by the 550 randomly selected energy electrons from each of these simulations is shown in Fig. 3.27 as well as the respective energy spectra. These results show distributions closer to the case of plot a) of Fig. 3.24, without a clear direction orientation nor anisotropy even for plots b), d) and e). In particular, the previously registered offset no longer fits the peak of the energy density verified for the different simulations; the peak energy value is lower (below 20% except for plot a) in which the 20 highest energy electrons properties were comparable to the 550 randomly selected ones); and the energy distribution was less collimated than in Fig. 3.24. Plot c) shows more energy being emitted close to the propagation axis, center of the detector, unlike what was observed before. This can be a consequence of most of the electrons being ionized and trapped so late in the simulation that they radiated mostly before constituting the ring shaped beam and undergoing significant DLA

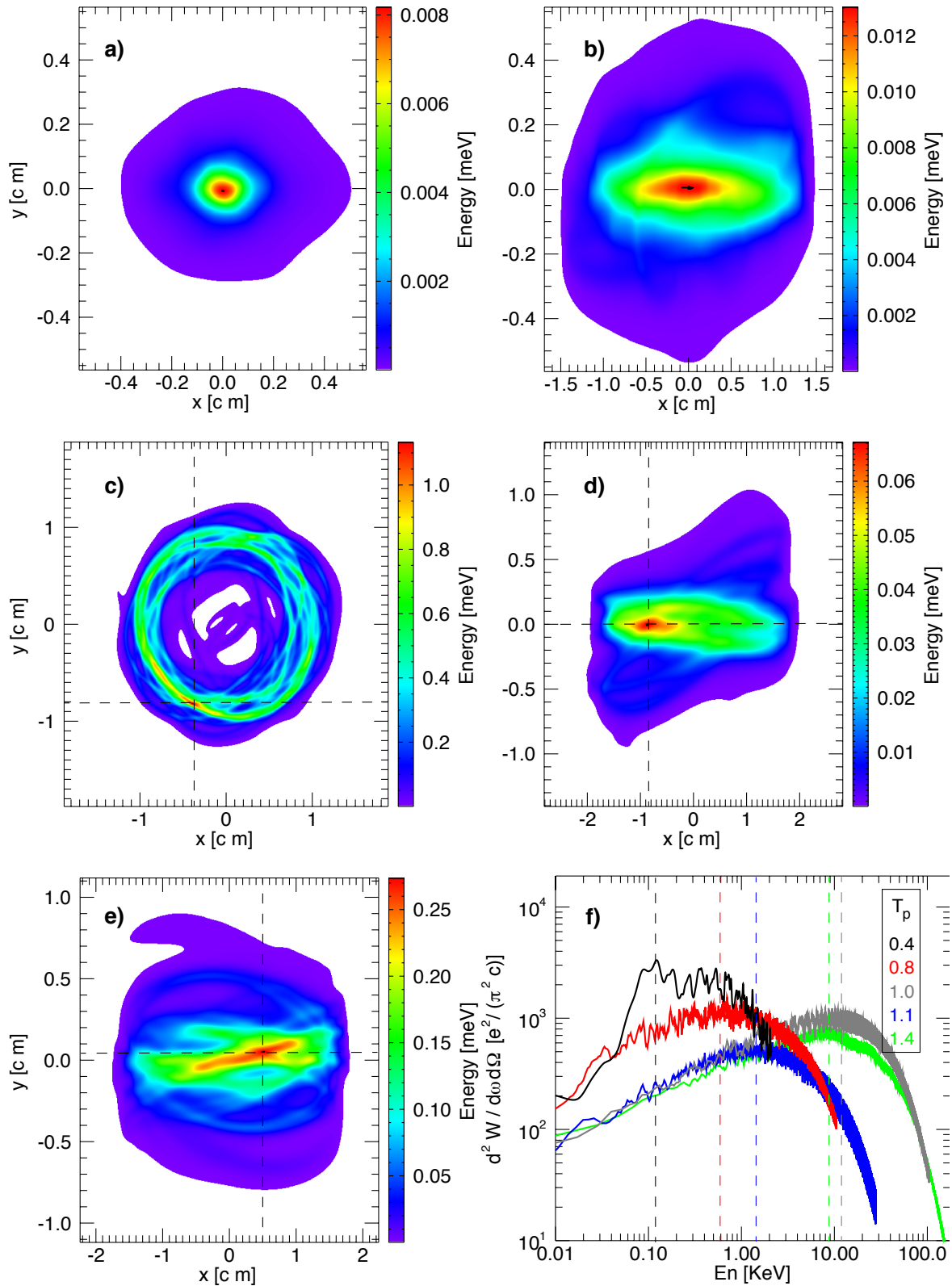


**Figure 3.24:** Plots a) to e) show the computed radiation emitted by the 20 highest final energy selected electrons reaching the virtual detector placed transversely to the laser propagation direction following the position, size and resolutions described in Table 3.5 for the simulations of Sec. 3.3.3 ordered by their  $T_p$  value. The dashed lines in plots c) to e) identify the location of the peak energy, the offset, shown in table 3.5. Plot f) contains the respective energy spectra at the offset positions with colored dashed lines at their critical point.

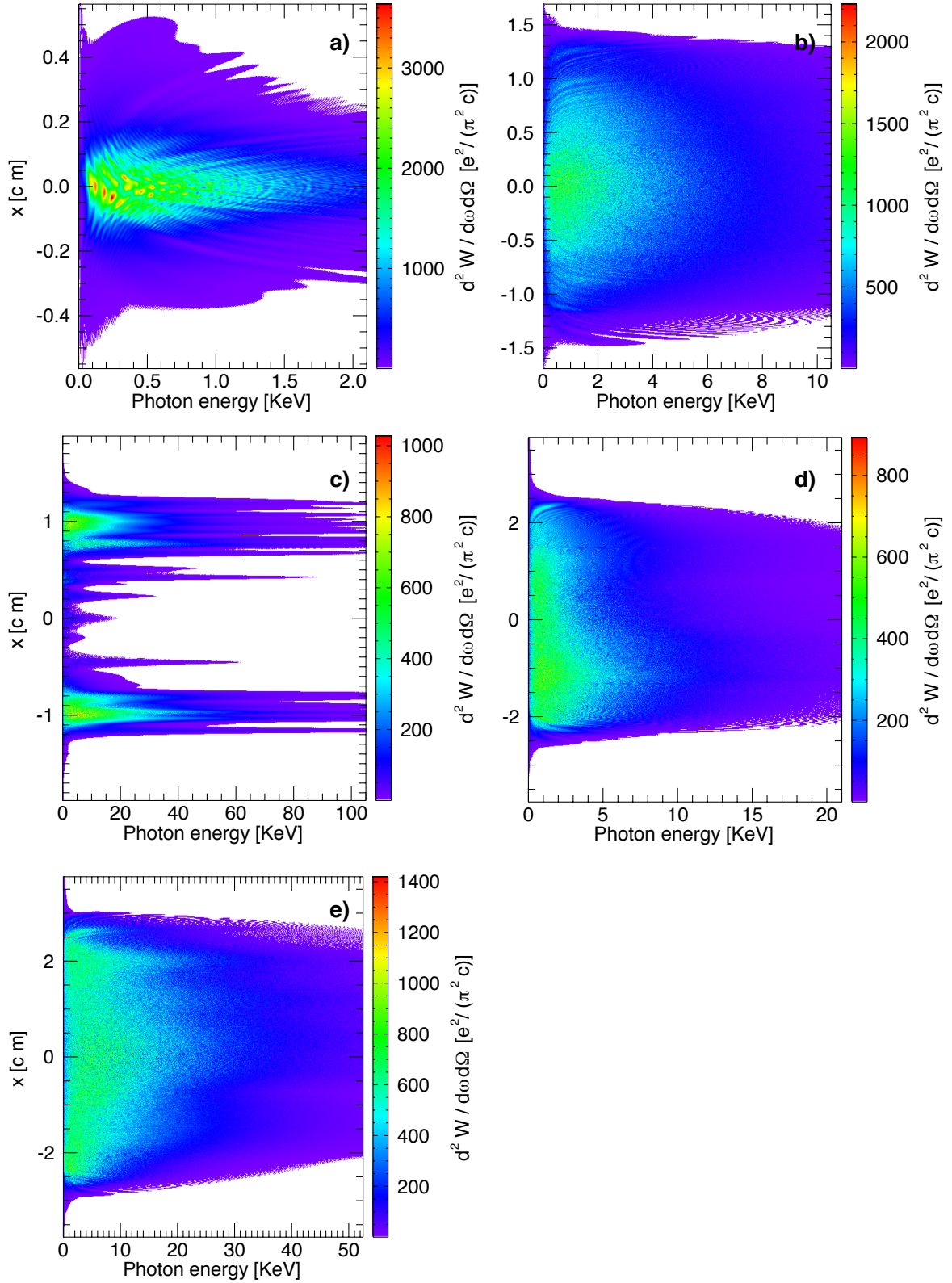


**Figure 3.25:** Plots a) to e) show the computed radiation spectra, energy  $W$  per solid angle,  $\Omega$ , and photon frequency,  $\omega$ , emitted by the 20 highest final energy electrons in the laser polarization direction,  $x$ , following the order of Fig. [3.24](#).

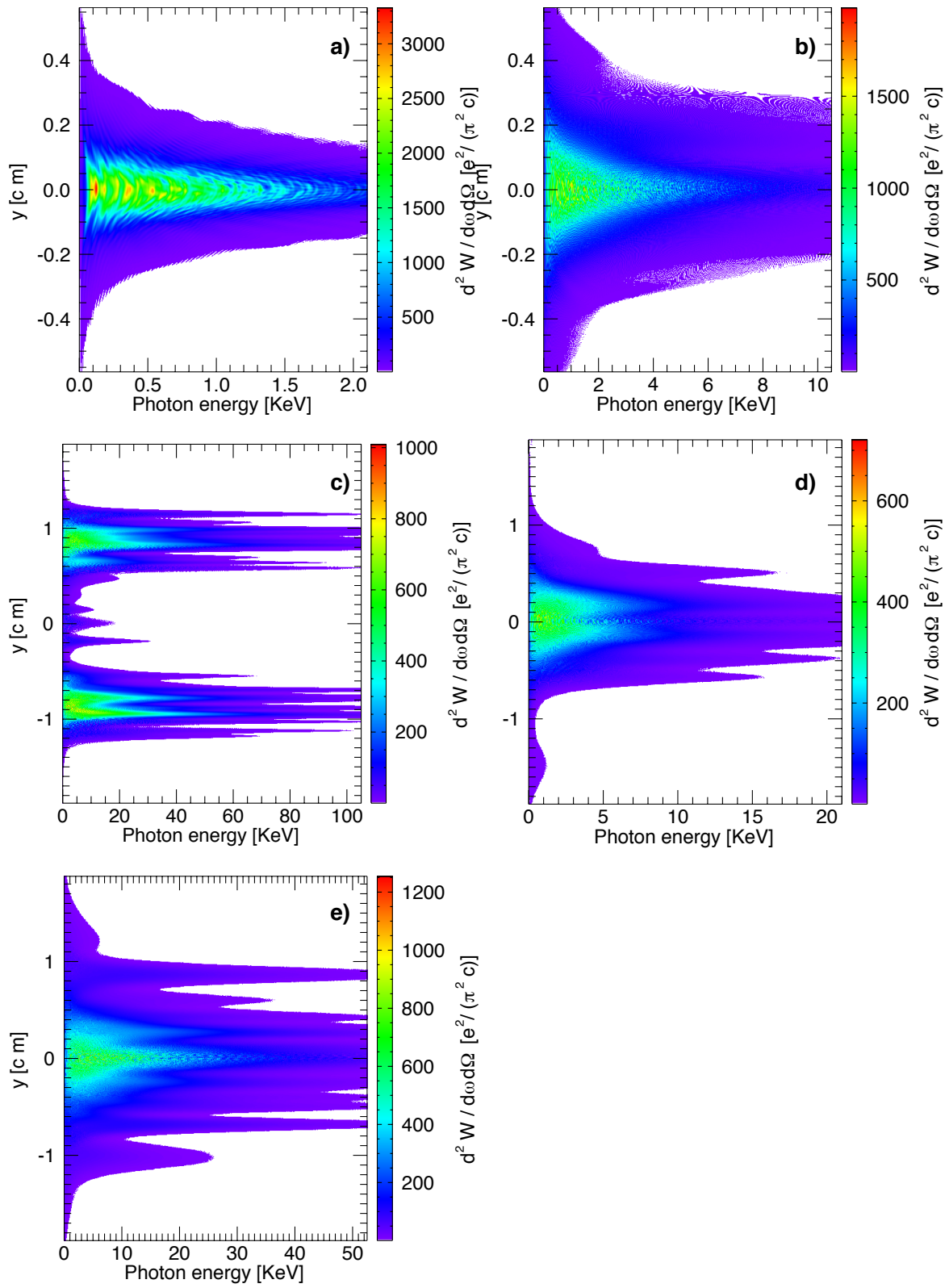


**Figure 3.26:** Plots a) to e) show the same as Fig. 3.25 but in the direction orthogonal to the laser polarization,  $y$ .

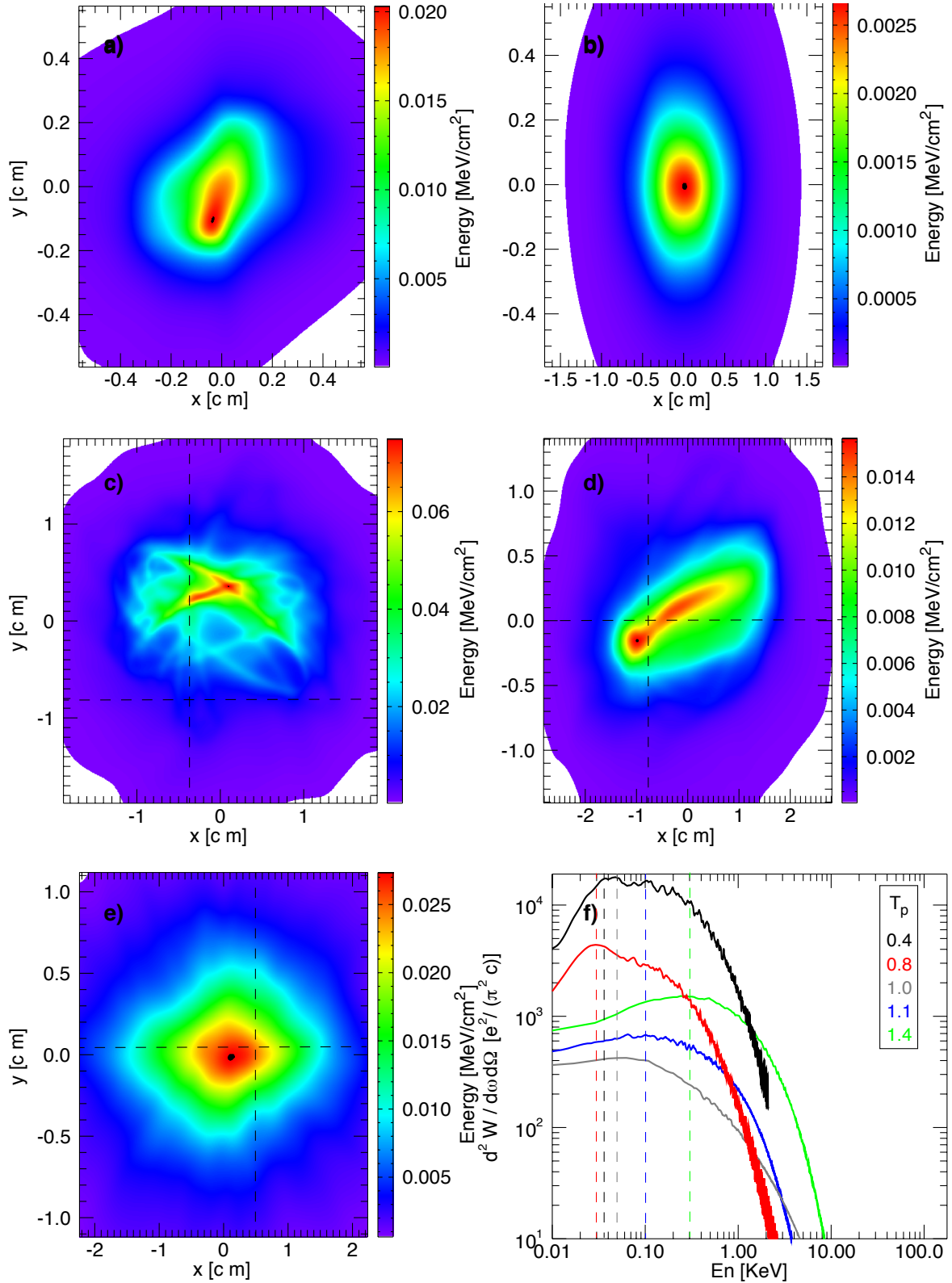


**Figure 3.27:** Plots show the same content as in Fig. 3.24 but computed for the 550 randomly selected and highest final energy electron trajectories. Plot f) also utilized the offset parameters of Fig. 3.24 and so of Table 3.5 to be comparable to it.

The curves present in plot f) of Fig. 3.27 exhibit less noise than in Fig. 3.24. This can be because the selected 20 highest energy electrons were the ones that had greater contribution from DLA contribution and so oscillated according not only to  $\omega_\beta$  but also to the laser frequency  $\omega_0$ . The different curves now have critical energies below 1 KeV and no significant emission beyond the 10 KeV, suggesting that these 550 randomly selected electrons do not generate hard x-ray beams, indicating further evidence of the DLA effect on the radiation emitted by the highest energy electrons.

For a reliable prediction of the radiation output of the different configurations explored, it will be necessary to select electrons from the beam contained in the first plasma wake bubble, based not on their density distribution but on their radial and energy properties, to ensure that those with greater participation on the radiation emission are being modelled. The simulations would have to be re-run then to note the corresponding trajectory, momentum, charge, field information needed to input in jRad.

This preliminary analysis of the emitted radiation already points out clear signatures of the presence of DLA in the LWFA process motivating a future experimental investigation with parallel radiation measurements.

### 3.5 Conclusions and future options

In view of the recent experimental findings of the DLA effect on the electron LWFA by the team [62, 115], we have contributed to the highly computationally expensive, detailed numerical analysis of the overall acceleration process. Our 3D PIC simulations compared scenarios where DLA would not be expected to participate in the electron acceleration with those in which it would and found that, like in the experiment, the electron beams produced showed maximum energies beyond the predicted values for the LWFA operating in the standard blowout regime. The experimental fork like structure found in the portion of the transverse detected position vs energy spectra for the highest energy electrons matched the simulation results and can be explained by the interplay of DLA in the studied schemes. The estimated DLA contribution to the overall final electron energy reached about 80% for the electrons of the fork in the simulation corresponding to the experimental setup discussed in Sec. 3.2.3. The final 3D simulated beam profiles corroborated the correlation between ellipticity and laser polarization direction, which is a sign of the influence of DLA in the electron trajectories as seen in the experiments. Because of the wider betatron oscillations performed in the laser polarization direction by the electrons where DLA dominated the acceleration process, also the radiation emitted can carry signatures of its impact and more detailed investigation of the emitted spectra both experimentally and numerically is timely given the applicability of hard x-ray beams in our society.

# 4

## X-ray production in self modulated laser plasma wakefields

### Contents

---

<b>4.1 Long laser pulse propagation in plasma wakes</b> . . . . .	75
<b>4.2 Numerical study of long laser pulse propagation in plasmas</b> . . . . .	81
<b>4.3 Radiation from long laser plasma wakefield accelerator</b> . . . . .	92
<b>4.4 Experimental investigation of x-ray generation in the long laser wakefield setup</b> . . . . .	92
<b>4.5 Conclusions and future direction</b> . . . . .	95

---

The work of Pukhov et al., in 1999, [118], explained in Sec. 3.1.1, introduced the idea that a relativistic self modulated laser pulse [127], in a Self-Modulated Laser Wakefield Accelerator (SM-LWFA) scheme, i. e. encompassing over several plasma density wake cavities, can directly accelerate electrons, Direct Laser Acceleration of electrons in plasma wakefields (DLA), as well as indirectly, through the resonantly driving plasma wakefields. Due to the technological limitations of that time the laser pulses available were not suitable for the typical and simpler plasma wakefield bubble regime [49–51], see Sec. 2.2 of the Laser Wakefield Acceleration (LWFA) setup. For that reason their study was focused on the SM-LWFA regime that could already be tested experimentally. In it different phenomena, such as self-channeling and focusing, shaped the laser-plasma interaction and interfered with the acceleration mechanism.

In Chapter 3 of this dissertation, we investigated the effects of the DLA process in the bubble regime, where the laser pulse was only long enough to cover the first plasma cavity. That setup allowed to comprehend the main signatures of DLA that were found experimentally [61, 62]. In particular, the characteristic transverse fork-like structure present in the higher final energy electrons spectra; the ellipticity of the final bunch that is elongated in the laser polarization direction; the final energy reaching above the expected maximum value for the standard LWFA operating in the bubble or blowout regime; and the brighter betatron radiation emitted. Chapter 3 therefore provides the groundwork to further investigate the plasma wakefield acceleration mechanism in the SM-LWFA regime, using substantially longer laser pulses.

The SM-LWFA technique became important early on because it relied on long (several plasma skin depths long) laser pulses that were the ones available in the 90s (Nd:Glass and CO<sub>2</sub> class lasers had intensities close to  $I_{rel}$ , Sec. 3.1.1, capable of inducing relativistic electron motion). In the SM-LWFA, long low intensity laser pulses could be used to produce high accelerating gradients in plasmas [25] and even self-trap background plasma electrons [126, 128, 129, 143].

The SM-LWFA allows higher intensity radiation to be produced, in comparison to the standard blowout regime, because the amount of (DLA assisted) wakefield accelerated electrons is greater because they are trapped over a wider region (that encompasses several of the typical bubbles). The DLA higher electron peak energies leads to an increase of the critical emitted photon energy. Moreover, electrons are trapped inside a channel structure, which is formed in the SM-LWFA that can be transversely wider than the typical blowout bubbles leading to a larger betatron radius of oscillation, than in the blowout. The long laser pulse guided in the channel is responsible for the (mainly) DLA acceleration of those electrons. For these reasons, currently, the SM-LWFA is explored to develop light sources with applications in medicine, (for example in the radiology used to diagnose diseases); industry (for example in the radiographic analysis of material properties without destroying its constituents); and possibly  $\gamma$  rays that are employed in the study of well isolated objects; and in condensed matter and high energy density science, radiation is required to reach matter's excited states and to probe exotic scenarios, see Sec. 1.1.1 or [20] for more details.

Recently, a SM-LWFA laser-plasma experiment was installed at Livermore to investigate the radiation produced and acceleration mechanism of plasma wakefields excited by long and high power

laser pulses [144]. I contributed to the effort of numerically benchmarking and understanding the experimental results. This work was done in collaboration with the team of the Laser Plasma Group at UCLA, namely Dr. Nuno Lemos and Dr. Jessica Shaw, and the group at Lawrence Livermore National Laboratory (LLNL), National Ignition Facility (NIF) and Photon Sciences, led by Dr. Felicie Albert et al.. The simulations employed the fully-relativistic Particle-In-Cell (PIC) code OSIRIS in the 2D geometry and the post-processing tool jRad, see Secs. 2.5.1 and 2.5.2.A.

The present chapter is written to follow Chapters 2 and 3, hence it will begin with the extension of the concepts of long laser pulse self-modulation and self-channeling mechanisms that were introduced before, 4.1. The focus of this chapter falls on the numerical analysis of the explored configuration present in Sec. 4.2, and of the radiation produced, Sec. 4.3. In Sec. 4.4 the experimental setup used and main discoveries are discussed.

## 4.1 Long laser pulse propagation in plasma wakes

In the SM-LWFA setup of relevance to this chapter, the front portion of the laser pulse has low intensity and, hence, its evolution can be extrapolated from the case study of the short laser pulse driving plasma wakefields in the linear regime. The propagation of the remainder of the laser pulse will be addressed later in Sec. 4.1.1. In the LWFA process the ponderomotive force, or radiation pressure, acting on a charged particle of a short intense laser pulse, Eq. (2.2), pushes the plasma electrons radially away. The electrons are later pulled back to their initial position by the space-charge of the plasma ions. The generated plasma electron density oscillation, the plasma wake, is characterized by accelerating and focusing fields, called the wakefields. Sections 2.1 and 2.2, 3.1.1, describe the laser driven bubble (and electron driven) blowout nonlinear plasma wake formation process and resolve the respective wakefields. In them, the laser pulse considered is linearly polarized in the  $x$  coordinate of the cartesian system. Moreover, the gas modeled in the scenarios discussed below was considered to be already fully ionized, into a plasma of electrons and ions, before the laser pulses were sent into it. Thus, laser pulse ionization induced defocusing was not accounted for, which is a valid approximation for the long high intensity laser pulses used [145]. The symbols there introduced and present in the List of Symbols at the beginning of this dissertation will be repeated in this chapter if their computing formula and reasoning differs.

In the linear regime, established as the regime driven by a laser pulse with, fast laser oscillation time averaged, normalized vector peak potential intensity  $a_0 \ll 1$ , the wake, and wakefields, correspond to a simple harmonic oscillator at the plasma frequency of  $\omega_p$  and externally injected relativistic particle bunches can be accelerated and focused. Because the wake structure follows the laser phase velocity in the plasma it is possible to write the wake phase velocity as  $v_{ph} \approx v_g = c\sqrt{1 - \frac{\omega_p^2}{\omega_0^2}} \approx c - c\frac{\omega_p^2}{2\omega_0^2}$ . The plasma wake Lorentz relativistic factor associated with its propagation velocity is given by  $\gamma_p = \frac{\omega_0}{\omega_p}$ . For laser frequencies,  $\omega_0 \gg \omega_p$ , a relativistic bunch placed at the peak focusing and accelerating region, of the cylindrically symmetric wake, will begin to defocus and decelerate when it overtakes the wake by  $\lambda_p/4 = \frac{\pi c}{2\omega_p}$  (see red shaded dashed delimited boxes

in Fig. 2.1) which happens after the laser propagated the linear dephasing length of:

$$L_d = \frac{c}{\omega_p} \frac{\pi}{2} \frac{c}{(c - v_{ph})} \approx \frac{\omega_0^2}{\omega_p^2} \frac{\lambda_p}{2} \quad (4.1)$$

The maximum total energy gain of the bunch can then be estimated by  $qE_{z\text{wake}}L_d$ . Along the laser propagation axis it is  $qW_{\parallel}L_d = \frac{\pi^2}{8} a_0^2 \frac{\omega_0^2}{\omega_p^2} m_e c^2 \sim a_0^2 \frac{\omega_0^2}{\omega_p^2} m_e c^2$ , using the peak of Eq. 2.10 for  $L_b = \tau_L = \lambda_p$ . The dephasing effect limits the maximum acceleration distance and hence energy that it can extract from the wake. The linear laser energy pump depletion length,  $L_{pd}$  see Eq. 4.2, that can be defined as the distance for the laser pulse with duration  $\tau_L$  to transfer roughly all of its energy,  $E_L^2 \tau_L$ , into the plasma wake,  $E_{z\text{wake}}^2 L_{pd}$ , is greater than  $L_d$ , 146:

$$L_{pd} \approx \frac{\omega_0^2}{\omega_p^2} \frac{\tau_L}{a_0^2} \quad (4.2)$$

In the bubble scenario, reached when  $a_0 > 2$  48, 52, it is possible to match the laser pulse spot size to the bubble maximum blowout radius  $W_0 \sim r_b \sim 2\sqrt{a_0}c/\omega_p$ , in order to prevent it from expanding inside the plasma. The typical dephasing, diffracting and pump depletion lengths (explained in Sec. 3.1.1), are determined by Eqs. 3.4, 3.1 and 3.3. The peak accelerating wakefield is at the back of the bubble, see Eq. 2.17, and so the maximum energy gain, within the dephasing length, of an accelerated particle bunch follows:  $\frac{4}{3}a_0 \frac{\omega_0^2}{\omega_p^2} m_e c^2$ . These findings allowed the development of scaling laws for both LWFA regimes, but they are no longer valid when a low  $a_0$  laser pulse has a time duration longer than several  $\lambda_p/c$ .

To understand the effects acting on the full size of the long laser pulse, the driven plasma wake perturbations effect on the laser needs to be correctly accounted for. For that reason the relativistic plasma correction is included in the plasma index of refraction, resulting in:  $\eta = \frac{v_g}{c} = \sqrt{1 - \frac{\omega_p^2}{\gamma \omega_0^2}}$ . The index is then dependent on the laser amplitude, frequency and on the plasma density fluctuations and can be approximated by 127, 147:

$$\eta \approx 1 - \frac{1}{2} \frac{n}{n_c \gamma} \approx 1 - \frac{\omega_p^2}{2\omega_0^2} \left( 1 - \frac{\langle a^2 \rangle}{2} + \frac{\delta n}{n} - 2 \frac{\delta \omega_0}{\omega_p} \right) \quad (4.3)$$

where the normalized vector potential term average over the fast laser fields oscillation frequency time is  $\langle a^2 \rangle_{\omega_0} = \langle \left( \frac{a_0}{2} \exp(ik_0\xi) + \text{Complex Conjugate}(\text{CC}) \right)^2 \rangle = \frac{a_0^2}{2}$ , and satisfies the conservation of the classical action, defined as the photon number, i.e. it verifies  $\langle a^2 \rangle W_0^2 \omega_0 L_b = \text{const}$ . The variations of the laser intensity, that scale with  $\Delta \langle a^2 \rangle$ , that occur in laser-plasma instabilities can be due to: longitudinal bunching or shortening, transverse focusing and/or photon acceleration, respectively through  $\Delta \langle a^2 \rangle = - \left( \frac{\Delta L_b}{L_b} + 2 \frac{\Delta W}{W_0} + \frac{\Delta \omega}{\omega_0} \right)$  127. In the coordinate system co-moving with the laser pulse,  $\xi = z - ct$  and  $\tau = t$ , the longitudinal component can be determined as the reduction in the spacing between two initially distant photons  $\Delta L_b = \Delta v_g \Delta t \rightarrow \frac{1}{L_b} \frac{\partial L_b}{\partial \tau} = \frac{\partial v_g}{\partial \xi}$ , during a time interval  $\Delta t$ . This is seen when the rear of the pulse moves faster than its front and results in broadening of the pulse bandwidth. The transverse pulse evolution is due to the variations in  $\delta v_{ph} = \frac{c}{\eta}$  away from the axis of propagation,  $\frac{\partial^2 W}{\partial \tau^2} = - \frac{\delta v_{ph}}{W} c$ . The latter phenomena is caused by the longitudinal perturbations of  $v_{ph}$  and can be computed from  $\frac{1}{\omega} \frac{\partial \omega}{\partial \tau} = - \frac{\partial v_{ph}}{\partial \xi}$ . This is called photon acceleration because

by assuming that the number of photons is constant, action, then the pulse frequency variation affects its group velocity. These processes are responsible for relativistic laser guiding and they allow the understanding of the Laser Raman Forward Scattering (LRFS), Laser Relativistic Self-Phase Modulation (LRSPM), Laser Relativistic Self-Focusing (LRSF) and Laser Envelope Self-Modulation (or laser saussaging) (LESM).

The stimulated LRFS instability was initially studied to model the large amplitude plasma waves and target preheating arising in laser driven inertial confinement fusion experiments [148]. In this instability laser photons are scattered by plasma wake electrons transferring their energy and thus modulating the laser pulse energy. The acceleration of those electrons to high energies results from the high phase velocity of the plasma wave at low plasma densities. The relevant term of Eq. (4.3) is  $\frac{\delta n}{n}$  and the identical contributions of longitudinal bunching and photon acceleration perturbations in  $\Delta\langle a^2 \rangle$ . The ansatz for the plasma response in the linear regime follows the harmonic oscillator,  $n = n_0 + n_1(\xi, \tau) \exp(ik_p \xi) + \text{CC}$  with  $n_1 \ll n_0$  and  $\frac{\partial^2 n_1}{\partial \xi^2} \ll \frac{\partial n_1}{\partial \xi} k_p$ . So the result of the phase and group velocity from Eq. (4.3) without accounting for transverse effects, i.e. with  $\frac{\partial \Delta\langle a^2 \rangle}{\partial \tau} = c \frac{a_0^2 \omega_p^2}{2 \omega_0^2} \frac{\partial}{\partial \xi} \frac{\delta n}{n}$ , implies that the overall change in the envelope can be described as  $\Delta\langle a^2 \rangle = a_1^2 \exp(ik_p \xi) + \text{CC}$  that is modulated at  $\omega_p$ , with  $a_1$  varying slowly with  $\tau$  and  $\xi$ , into a series of micro-pulses due to the plasma fluctuations. Thus Eq. (2.5) in the co-moving frame becomes  $-2k_p c^2 \frac{\partial n_1/n_0}{\partial \xi} = -\frac{a_1^2}{2} c^2 k_p^2$  and straightforwardly leads to the evolution of the LRFS instability according to [74, 138, 149]:

$$\frac{\partial^2 a_1^2}{\partial \xi \partial \tau} = \frac{a_0^2 \omega_p^2}{8 \omega_0^2} k_p \omega_p a_1^2 \equiv \Gamma_{\text{LRFS}}^2 a_1^2 \quad (4.4)$$

The nonlinear growth rate  $\Gamma_{\text{LRFS}}$  describes how the strong initial Electromagnetic (EM) laser wave decays into the plasma wave and two forward Stokes and anti-Stokes EM cascades at  $\omega_0 \pm N\omega_p$  with  $N = 1, 2, 3, \dots$ , respectively, in a four wave resonant process. As the plasma wave increases so does the scattering of the Stokes sidebands and the instability grows. If the plasma is underdense,  $\omega_p \ll \omega_0$ , this instability stops to grow as a consequence of the quick nonlinear plasma wave breaking [129].

When the momentum of the electrons performing a quiver motion in the laser fields becomes relativistic, there is a change in (the effective electron mass and hence in) the  $\eta$  of the plasma seen by the laser and seeding the LRSPM instability. For this the relevant term of Eq. (4.3) is instead the relativistic  $\frac{\langle a^2 \rangle}{2}$  that are generated by the oscillations of  $v_g$  (determined as a function of  $\omega$  from  $\eta$ ), so directly from longitudinal (transverse perturbations are again discarded) bunching and indirectly due to the process of photon acceleration. Analytically the effect is given by  $\frac{\partial \Delta\langle a^2 \rangle}{\partial \tau} = -\frac{\omega_p^2 c}{\omega_0^3} \frac{a_0^2}{2} \frac{\partial \Delta\omega_0}{\partial \xi}$ . The frequency evolution in time can also be computed from  $v_g$  and with Eq. (4.3) yields  $\frac{1}{\omega_0} \frac{\partial \Delta\omega_0}{\partial \tau} = \frac{c}{4 \omega_0^2} \frac{\partial \Delta\langle a^2 \rangle}{\partial \xi}$ . These can be computed from the  $a_1$  term of  $\Delta\langle a^2 \rangle_{\omega_0}$  mentioned before.

In this scenario the phase of the laser pulse is relevant and its envelope variations are modelled according to it. For that reason, the vector potential definition includes an additional phase term,  $a = a_0 \cos(\phi_0) + a_+ \cos(\phi_+) + a_- \cos(\phi_-)$ , where a three wave interaction scenario is modeled with a pump at  $\phi_0 = k_0 z - \omega_0 t$  and two sidebands that make  $\phi_{\pm} = k_{\pm} z - (\omega_{\pm} \pm \omega_0) t$  [138]. For  $k_{\pm} \approx k_p$  then the pulse envelope follows  $\Delta\langle a^2 \rangle_{\omega_0} = \frac{a_1^2}{2} (\exp(ik_p \xi) + \text{CC}) \cos\left(\frac{\omega_- - \omega_+}{2} \tau\right)$  and if we consider the case close to

resonance,  $\omega_{\pm} \approx \omega_0$  and  $a_0 a_{\pm} \approx a_1^2$ , we can expand the modulation of the envelope to give  $\frac{\omega_- - \omega_+}{2} \approx \frac{1}{2} \frac{\partial^2 \omega_0}{\partial k^2} k$ . From the plasma dispersion relation,  $\omega_0^2 = \omega_p^2 + c^2 k^2$  [13] it is then possible to determine the **LRSPM** instability from  $\frac{\partial^2 \Delta \langle a^2 \rangle}{\partial \tau^2} = \left[ \frac{\partial^2 a_1^2}{\partial \tau^2} - \frac{a_1^2}{2} \left( \frac{\omega_- - \omega_+}{2} \right)^2 \right] (\exp(i k_p \xi) + \text{CC}) \cos\left(\frac{\omega_- - \omega_+}{2} \tau\right)$  that using the relations from the previous paragraph leads to [15, 127]:

$$\frac{\partial^2 a_1^2}{\partial \tau^2} = \frac{a_{00}^2 \omega_p^4}{8 \omega_0^4} \omega^2 \left( 1 - \frac{1}{a_{00}^2} \frac{2\omega^2}{\omega_0^2} \right) a_1^2 \equiv \Gamma_{\text{LRSPM}}^2 a_1^2 \quad (4.5)$$

,where  $a_{00}$  is the amplitude of  $a_1$ . Equation (4.5) implies that there is an instability only when the real part of the growth rate is lower than the imaginary part,  $\omega^2 < \frac{\omega_0^2}{2} a_{00}^2$ . The maximum growth rate value is found for  $\omega = \frac{\omega_0}{2} a_{00}$  and is  $\text{Max}(\Gamma_{\text{LRSPM}}) = \frac{a_{00}^2 \omega_p^2}{8 \omega_0^2}$  that corresponds to  $\frac{\omega_0}{\omega_p^2}$  times  $\Gamma_{\text{LRFS}}$ . Without the phase modulation to the pulse envelope contribution (real part of  $\Gamma_{\text{LRSPM}}$ ) the growth rate of the instability would grow with  $\omega^2$ .

The transverse effects so far dismissed have to be considered in studying the **LRSF** phenomena [15, 138, 150, 151]. The relevant term of Eq. (4.3) is again the relativistic  $\langle \frac{a^2}{2} \rangle$ , but this time it influences also  $v_{\text{ph}}$  so that  $\frac{\partial^2 W}{\partial \tau^2} = -\frac{a_0^2 c^2 \omega_p^2}{8 W \omega_0^2}$ . For the standard Gaussian laser pulse, the profile close to its focal position is  $\exp\left(-\frac{2r^2}{W^2}\right)$ , see Sec. 2.1. Where the phase fronts are planar,  $W = W_0 \sqrt{1 + \frac{z^2}{z_R^2}}$  can be approximated to give the transverse spot evolution equation of the **LRSF**:

$$\frac{\partial^2 W}{\partial \tau^2} = -\frac{4c^2}{k_0^2 W_0^3} \left( 1 - \frac{a_0^2}{32} W_0^2 k_p^2 \right) \quad (4.6)$$

The self-focusing takes place if the laser power satisfies  $W_0 a_0 > \frac{\sqrt{32}}{k_p}$ . This leads to the critical power for self-focusing, discussed in Sec. 3.1.1, which can also be written as  $P_c [\text{GW}] \approx 17 \frac{\omega_0^2}{\omega_p^2}$ . At  $P = P_c$  the laser pulse diffraction is exactly canceled and it can be guided and propagate for distances of several *Rayleigh* lengths,  $Z_R$ . If  $P > P_c$  the pulse self-focuses.

When the plasma density transverse oscillations are sufficient to change  $\eta$  the **LESM** or the laser, equivalent to the particle beam sausinging, instability can also occur and it is possible to neglect the **LRSF** effects as long as the spot size evolution due to focusing and the diffraction of the laser are slower than the time for the **LESM** to saturate. This is reasonable when a preformed plasma channel is used or when  $P \approx P_c$ . Taking once again the spot size evolution from Eq. (4.3), but using the plasma density perturbations term instead,  $\frac{\delta n}{n}$ , allows to write  $\frac{\partial^2 W}{\partial \tau^2} = \frac{1}{2} \frac{\omega_p^2 c^2}{\omega_0^2 W} \frac{\delta n}{n}$ . The vector potential envelope is determined by the transverse pulse spot according to  $\frac{\partial^2 \Delta \langle a^2 \rangle}{\partial \tau^2} = -\frac{a_0^2}{W} \frac{\partial W}{\partial \tau^2}$ . The plasma density wake Eq. (2.17), the harmonic oscillator density ansatz and respective field potential vector envelope structure applied in the study of the **LRFS** process, can be combined with the previous relations in the equation of envelope evolution when the laser is sausinging:

$$\frac{\partial^3 a_1^2}{\partial \tau^2 \partial \xi} = -\frac{i a_0^2 \omega_p^2}{8 W^2 \omega_0^2} k_p a_1^2 \equiv i \gamma_{\text{LESM}}^3 a_1^2 \quad (4.7)$$

The **LESM** corresponds to the four wave non-resonant Raman scattering instability found at an angle of  $k_{\perp}/k_0 \approx 1/k_0 W_0$  exceeding  $\frac{\omega_p}{\omega_0}$ , when  $|\frac{\partial^3}{\partial \tau^3}|$  and  $|\Gamma_{\text{LRFS}}^2 \frac{\partial}{\partial \tau}| \ll |\Gamma_{\text{LESM}}^3|$ . The asymptotic solution of the growth rate for the whole finite pulse envelope instabilities, for large  $\tau$ , using the residues complex theorem and the stationary phase methods is  $\Gamma_{\text{LESM}} = \frac{3}{2} (\sqrt{3} - i) \sqrt[3]{\frac{1}{4} \gamma_{\text{LESM}}}$  [127, 138, 152] and the laser intensity variations follow  $\exp\left(\Gamma_{\text{LESM}} \sqrt[3]{\tau^2 \xi}\right)$ . In the resonant case the imaginary contribution

to the growth rate would vanish and the laser intensity envelope and the plasma density wake would be apart by a phase of  $\frac{\pi}{2}$ . In the non-resonant case, the **LESM** one, there is an additional  $\frac{\pi}{6}$  phase difference and the finite size laser pulse is coherently focused in to the lower plasma electron density regions. Its intensity increases and its ponderomotive force expels more electrons from those regions, causing the laser to focus even more leading to the instability. Note that for the Raman scattering instabilities to grow they have to be seeded by, for example, plasma electron density fluctuations (arising from thermal variations) or laser ponderomotive excited wakes, at  $k$  and  $\omega$ .

The various scaling laws present in [127, 138] allow to predict the dominant instability and the necessary seed for given laser-plasma parameters.

#### 4.1.1 Laser pulse relativistic self-channeling

In this Section the **SM-LWFA** regime is explored, in which the front of the laser pulse undergoes **LRSE** as the plasma electron relativistic mass (inertia) increases. Its front then begins to modulate due to the **LRFS** and **LESM** instabilities, until the **EM** pulse fields are contained and compressed inside several electron plasma cavities. Then, as the laser intensity and plasma fields, continuously increase towards the back of the laser pulse, the plasma electron wake transversely breaks down and the plasma ions are repelled by the laser ponderomotive force. As the ions and electrons vanish from the propagation axis, they form a narrow hollow channel in what is called the Laser Relativistic Self-Channeling (**LRSC**). Hollow channels have been researched in view of their applications for particle acceleration and fast ignition (hole boring) of inertial confinement fusion targets since the 90s [117, 133, 134, 153-155]. The ion restoring force that pulls the electrons back to the axis thus vanishes. Therefore, the channel contains mainly just the electrons that were trapped within it. Those trapped plasma electrons can be accelerated through **DLA**, see Chapter 3. The **SM-LWFA** scheme explored in this chapter is illustrated in Fig. 4.1 where the long pulse electric field (in red) propagates (in the red arrow direction) through the plasma ions and generates a clear depression in their density (in gray).

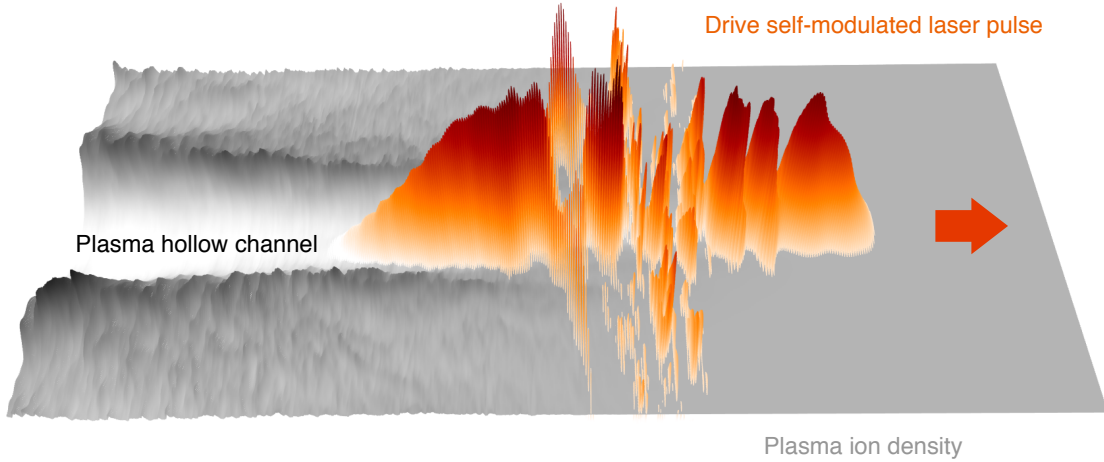


**Figure 4.1:** 3D visualization of a 2D simulation of a plasma based wakefield acceleration scheme where the front of a long laser pulse electric field is modulated (red separate peak structures) and focused until its intensity is enough for wavebreaking and then for it to self-channel through the electron and ion plasma (density in gray).

The channel has the effect of decreasing the local refractive index leading to further focusing of the laser pulse. The focused laser intensity then alters the refractive index and so the **LRSC** mechanism is an instability. It saturates when the laser back becomes a stable paraxial mode propagating, being guided and confined within the channel, along the axis. To describe it, the laser pulse length is considered to be much greater than the plasma and the laser wavelengths,  $c\tau_L \gg \lambda_p, \lambda_0$ .

We start the analysis from the plasma electron and ion (that are henceforth represented by the subscript index  $i$ ) *Poisson* equation that is written as  $\nabla^2\Phi = -4\pi q(-n + n_i)$ . Inside the channel the light plasma electrons are then assumed to be in a steady state in which their potential energy balances the kinetic motion due to the ponderomotive effects,  $\gamma - 1 = +\frac{q\Phi}{m_e c^2}$ , therefore  $\nabla(\gamma - \phi) = 0$ , with the normalized scalar potential  $\phi \equiv \frac{q\Phi}{m_e c^2}$ . The normalized relativistic plasma electron density,  $n_{er} \equiv \frac{n}{\gamma n_0}$ , can then be computed as a function of the ion channel density,  $n_{i1} \equiv \frac{n_i}{n_0}$ , and electron energy from *Poisson's* equation,  $n_{er} = \frac{n_{i1} + \nabla_{\perp}^2 \gamma / k_p^2}{\gamma}$  (or zero in case that equation yields an unphysical negative particle density). Note that the mobile ions are not relativistic,  $\gamma_i \approx 1$  and so their density does not need the relativistic correction. From the *Lorentz* equation of motion for the plasma electrons in the laboratory reference frame:

$$\frac{\partial \vec{p}}{\partial \tau} + \frac{1}{2\gamma} \nabla \frac{\vec{p}^2}{m_e c} - \frac{\vec{p}}{\gamma} \times \nabla \times \vec{p} = q \left( \vec{E} + \frac{\vec{p}}{\gamma c} \times \vec{B} \right) = q \left( -\nabla\Phi + \frac{\vec{v}}{c} \times \nabla \times \vec{A} \right) \quad (4.8)$$

which can be simplified introducing the analytical definition of the electron relativistic momentum,  $\vec{p} = \gamma m_e v = m_e \sqrt{\gamma^2 - 1} c$ , into the relation of  $\nabla(\phi - \gamma) = \frac{1}{m_e c} \left( \frac{\partial}{\partial t} \left( \vec{p} - \frac{q\vec{A}}{c} \right) - \vec{v} \times \nabla \times \left( \vec{p} - \frac{q\vec{A}}{c} \right) \right) = 0$  leading to the approximation valid for long pulses of  $\vec{p} = \frac{q\vec{A}}{c}$ .

For the not relativistic ions,  $\frac{\vec{v}_i}{c} \rightarrow 0$  and so they do not gain longitudinal momentum from the magnetic field nor, for a long laser pulse, from the longitudinal ponderomotive force, which is negligible,  $\frac{\partial A^2}{\partial z} \rightarrow 0$ . So the plasma ions only move transversely to the propagation axis, as a consequence,  $\frac{\partial}{\partial z} \rightarrow 0$  and  $\vec{v}_i \times \nabla \times \vec{v}_i \rightarrow 0$ . In this case the co-moving frame ion *Lorentz* equation of motion is given

by:

$$m_i \frac{\partial \vec{v}_i}{\partial \tau} + m_i \frac{1}{2} \nabla_{\perp} \vec{v}_i^2 = q_i \vec{E}_{\perp} = -q_i \nabla_{\perp} \Phi = \frac{-q_i}{q} m_e c^2 \nabla_{\perp} \gamma \quad (4.9)$$

The ion continuity equation is just  $\frac{\partial n_i}{\partial \tau} + \nabla_{\perp} \cdot (n_i \vec{v}_i) = 0$ . Because the heavy ions move on a slow time scale compared to the electrons it is reasonable to assume that their canonical momentum  $P_H = m_i v_i + \frac{q_i \vec{A}}{c}$  is constant, which enables the trivial solution of:  $v_i = -\frac{q_i \vec{A}}{m_i c}$ .

The laser pulse vector potential evolution can thus be derived from the combination of the other *Maxwell* equations in the *Coulomb* gauge,  $\nabla \cdot \vec{A} = 0$ , and in the reference frame co-moving with the pulse:

$$\nabla_{\perp}^2 \vec{A} + \frac{\partial^2 \vec{A}}{\partial \xi^2} - \frac{1}{c^2} \frac{\partial^2 \vec{A}}{\partial \tau^2} + 2c \frac{\partial^2 \vec{A}}{\partial \tau \partial \xi} = \frac{1}{c} \nabla \frac{\partial \Phi}{\partial \tau} - \frac{4\pi}{c} \vec{J}_e \Leftrightarrow \nabla_{\perp}^2 \vec{A} + 2ik \frac{\partial \vec{A}}{\partial \xi} \approx \frac{4\pi}{c^2} \left( \frac{q^2 n_e}{\gamma m_e c} + \frac{q_i^2 n_i}{m_i c} \right) \vec{A} \quad (4.10)$$

where the plasma dispersion relation and the low frequency dependence of  $\Phi$  were employed.

The scaling laws for this phenomena include the transverse ion acceleration taken from the approximate laser ponderomotive force which leads to the velocity  $v_i(\tau) = \frac{m_e c^2 a_0^2}{4\gamma m_i} \frac{\tau}{W}$ . It is then possible to get the time after which the ions were completely expelled from the beam, radially corresponding to a size of  $2W$ ,  $c \tau_{ic} = 2\sqrt{\frac{\gamma m_i}{m_e a_0^2}} W$ . The ion velocity results in  $v_{ic} = \frac{c a_0}{2\sqrt{\gamma} \frac{m_i}{m_e}}$ . The channel continues to expand, as the ions keep moving away from the axis, even after the laser has passed by, at which point the plasma electrons, that had already returned close to the propagation axis, are responsible for restoring the initial plasma electrostatic and thermal equilibria.

In the hollow channel the laser pulse field loses energy, which leads to the longitudinal difference in its intensity value due to the ion radial motion from the axis towards  $W$  in a time  $\frac{W}{v_i}$ , i. e.  $\frac{\partial I}{\partial z} = \frac{\pi m_e^2 c^5}{2q^2 \lambda_0^2} \frac{\partial a_0^2}{\partial z} = -\frac{1}{2} m_i v_i^2 n_i \frac{v_i}{W}$ , resulting in the equation:

$$\frac{\partial a_0^2}{\partial z} = -\frac{1}{8\gamma^{3/2} W} \frac{n_i}{n_c} \sqrt{\frac{m_e}{m_i}} a_0^3 \equiv \Gamma_{\text{RSC}} a_0^2 \quad (4.11)$$

that shows that the growth rate of the **RSC!** (**RSC!**) in this scenario,  $\Gamma_{\text{RSC}}$ , depends on the ion mass, laser properties and plasma density. The distance before absorption is greater than the critical limit of the diffraction length,  $\frac{n_e}{n_i} k_p$  [154]. For a more rigorous deduction the reader is referred to, for example, reference [156] and to [157] for recent related findings.

## 4.2 Numerical study of long laser pulse propagation in plasmas

With the previous analysis of the physical phenomena present in the explored **SM-LWFA** scheme, it is possible to understand the results of the numerical simulations performed with the 2D-cartesian  $(z, x)$  **PIC** code OSIRIS with a  $30000 \times 1024$  cells grid, corresponding to the size of  $500 \times 150 \mu\text{m}^2$ , belonging to the window traveling at  $c$ , that was computed every time step interval of  $\Delta t = 0.00965013$  and for which the data was stored after every  $260 \times \Delta t$ . The simulation was performed twice, once to select a set of 512 macro-particles throughout the simulation, and then to determine and store their

<sup>1</sup>The simulation was processed in 400 by 8 cores at the BlueWaters supercomputer [5] taking  $\sim 48$ h. Jrad runs were done at the Hoffman2 machine at University of California Los Angeles (UCLA) [2] with 7 split sets of particles taking a total of 36h each.

field, momentum and position information for each time step. The radiation associated with selected trapped and accelerated electrons trajectories was determined with the post-processing code jRad.

The simulation box contained the two mobile macroparticle species of Helium, electrons and ions with  $\frac{q_{\text{part}}}{m_{\text{part}}} \frac{m_e}{|q_e|} = -1$  and  $+1836.152$  (charge to mass ratios normalized to positron), respectively, with  $4 \times 4$  particles per cell each and evaluated with cubic interpolation. The simulation used normalized parameters, but the system was conceived to reproduce a pre-fully-ionized Helium gas jet with homogeneous density of  $1.0 \times 10^{19} \text{cm}^{-3}$  with a linear up-ramp of  $200 \mu\text{m}$  (starting right after the simulation box  $500 \mu\text{m}$ ), and a downramp of the same length, after a constant density region of about  $3000 \mu\text{m}$  in the propagation direction,  $z$ . The wavebreaking field limit for this plasma is  $E_{\text{WB}} = \frac{k_p m_e c^2}{|q|} = 3.0$  GV/cm. From all the plasma electron macro-particles,  $4 \times 4$  initially created in each grid cell, 20% were randomly chosen from those that had  $p_{\text{OSIRIS},z} = p_1 = \gamma \frac{v_z}{c} > 5$  at each time step to show their momentum, energy and spatial information.

The laser parameters used were inspired by the experimental setups that were tested at the TITAN infrastructure operating in the LLNL laboratory in California, USA [144]. The wavelength was  $\lambda_0 = 1.053 \mu\text{m}$  and the 700 fs Full Width Half Maximum measurement (FWHM) long pulse was focused into a spot size of  $W_0 = 15 \mu\text{m}$  (FWHM of the electric field) after propagating  $100 \mu\text{m}$  in the plasma. The pulse Rayleigh length is  $Z_R \approx 670 \mu\text{m}$ , the diffraction length is  $L_{\text{Diff}} = \pi Z_R \approx 2100$ , the plasma dephasing and the laser pump depletion lengths are  $L_d \approx 320 \mu\text{m}$  and  $L_{\text{pd}} \approx 21200 \mu\text{m}$ , as determined in the previous chapter. The resolution was of about 63 cells per  $\lambda_0$  longitudinally and 102 per  $W_0$  transversely. The chosen laser polarization was linear and in the simulated direction  $x$ . The normalized vector potential was  $a_0 = 2$ . This simulation complemented a previous study done with  $a_0 = 1.5$  and 3 [59]. The plasma wake group velocity is  $v_g = 0.995c$  associated with the relativistic factor of 10. In our code we analyzed only the electrons with longitudinal momentum above 10 and so captured only the trapped electrons.

The laser  $W_0$  does not match the predicted standard blowout radius of  $r_b = 2\sqrt{a_0} k_p \approx 4.75 \mu\text{m}$  (or  $2 \times r_b \approx 9.51 \mu\text{m}$ ) at its focal point. But, because its peak power is given by:  $P(W_0)[W] = 10^7 \frac{a_0^2 m_e^2 c^5 \pi^2 W_0^2}{4q^2 \lambda_0^2} \approx 17.4$  TW that is above the critical power for self-focusing,  $P_c = 1.7$  TW (corresponding to a critical plasma density of about  $1.0 \times 10^{21} \text{cm}^{-3}$  above the experiment one), its spot size decreases according to Eq. (4.6), increasing its intensity, when it propagates through the plasma for many  $Z_R$ .

Looking at the values for the maximum growth rates of the: LRSPM, LRFS, LESM,  $\Gamma_{\text{LRSPM}} \approx 8.9$  ps<sup>-1</sup>, of  $\Gamma_{\text{LRFS}} \approx 0.7 \sqrt{\frac{1}{\text{ps} \mu\text{m}}}$  and of  $\Gamma_{\text{LESM}} \approx 0.02 \frac{1}{\sqrt[3]{\text{ps}^2 \mu\text{m}}}$  and considering that our scheme evolves at the ps and  $\mu\text{m}$  scales leads us to believe that the laser envelope transverse modulations will not be as relevant as the combination of LRSPM and LRFS.

Since the simulation was run in the 2D cartesian geometry it is not straightforward to distinguish the Raman scattered instabilities in the different angles relative to the laser pulse propagation direction. Therefore, both LRSPM and LRFS interplay in this SM-LWFA numerical scenario. A full 3D simulation would yield more conclusive information regarding the competition between the instabilities but it was at the time of this dissertation's work too computationally demanding to be performed.

Figure 4.2 a) and b) show the density of the electrons (blue) and ions (gray scale) of the plasma. Plot b) already exhibits initial signs of the ion motion in its density perturbation (lighter gray regions). Plot c) shows the transverse electric field that mainly corresponds to the laser field. The front of the laser pulse, in the right side of c), has focused into a width close to the matched value that is below its original spot size,  $W_0$  (indicated for reference in the plot). The central portion of the laser (field), within the vertical black lines, shows signs transverse nonlinearities both in the laser and the wake (away from the axis). These non-linearities arise because of plasma wave breaking, electrons overshooting across the propagation axis, Fig. 4.2 a). The back of the pulse is still intact as the plasma density is still low in the upramp. Plot d) indicates that some plasma electrons behind the front part are already being accelerated. The electrons closest to the laser front show a peak momentum modulation that is associated with them being trapped at the back of the wake bubbles, i.e. regions of almost spherical shape where the plasma density is negligible when compared to the initial background equilibrium plasma density (white regions in a). At this point,  $ct \approx 487 \mu\text{m}$ , the trapped electrons were transversely confined within  $x \in [65, 85] \mu\text{m}$ , which corresponds to the plasma bubbles regions, and had energies up to 15 MeV, Fig. 4.2 d).

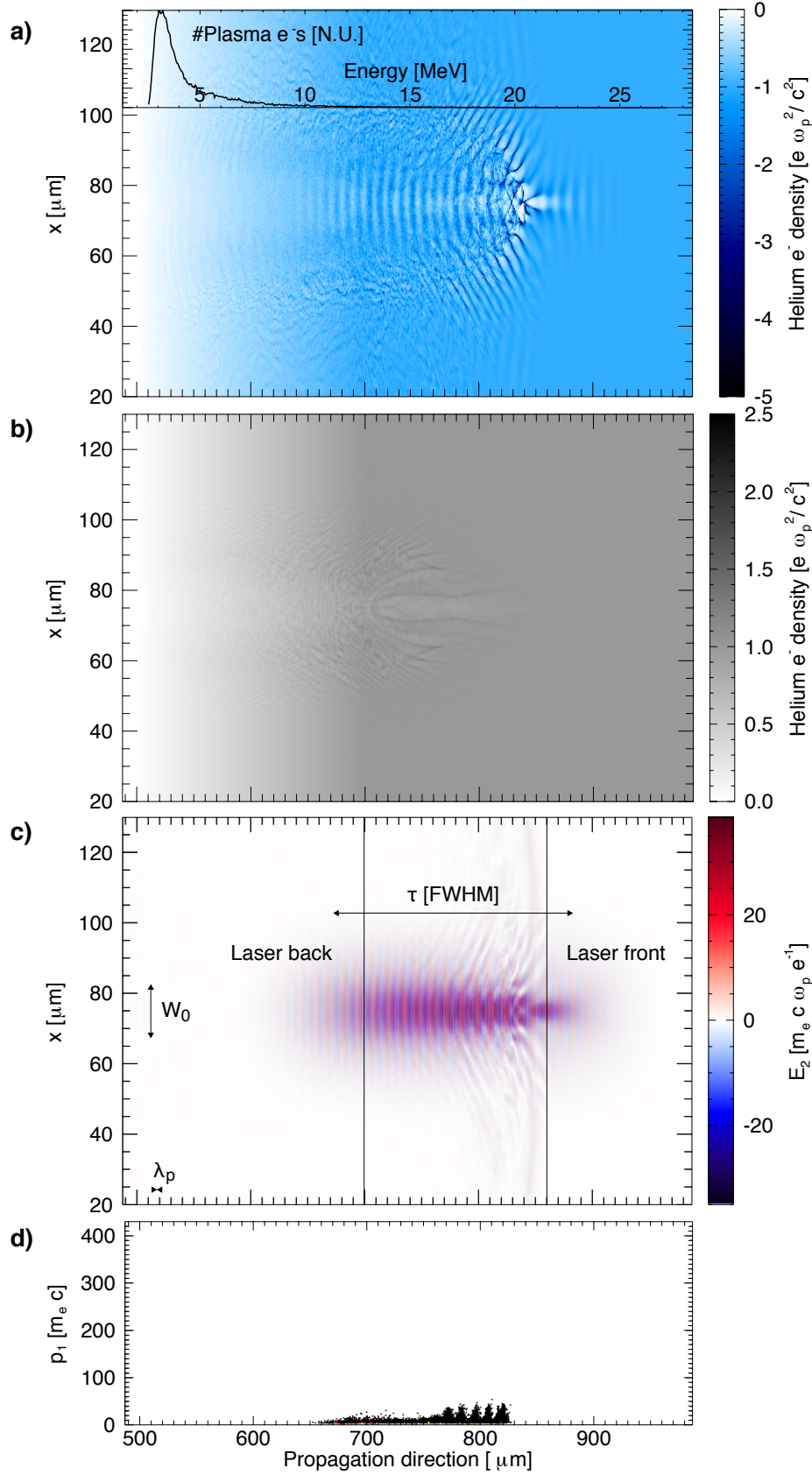


**Figure 4.2:** 2D plots of the electron (a) and ion (b) density at the simulation time  $ct \approx 487 \mu\text{m}$ . In a) the density plot is overlapped by the line depicting the energy histogram of the 20% accelerated electron macro particles. Plot c) shows the laser transverse electric field (c), the laser propagates to the right, with the arrows referencing the spot and duration values. The vertical lines delimit the laser front that undergoes LRFS and/or LESM (right portion); the central region where the plasma electrons have experienced wavebreaking and the density becomes nonlinear and the ions start to be expelled; and the final part in which the laser is modulated, bunched, at  $\lambda_p$ . The final plot contains the longitudinal phase space,  $p_1$  vs  $\xi$ , of the 20% selected electrons.

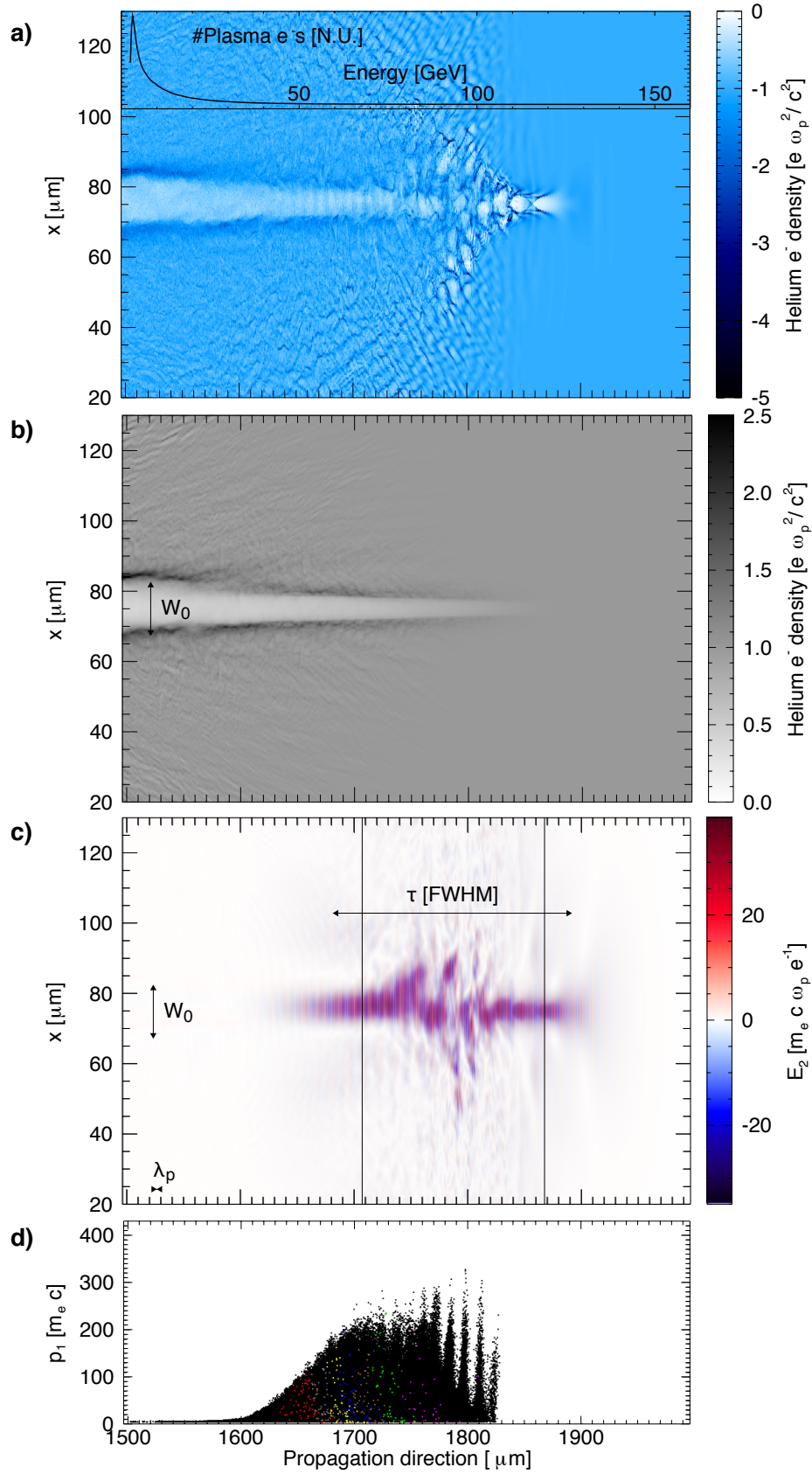


**Figure 4.3:** Plots a) to d) show the results as indicated by the label of Fig. 4.2 but at  $ct \approx 1495\mu\text{m}$ . With the exception of plot d) where the 512 electrons selected for the radiation analysis are also present (colored according to Table 4.1)

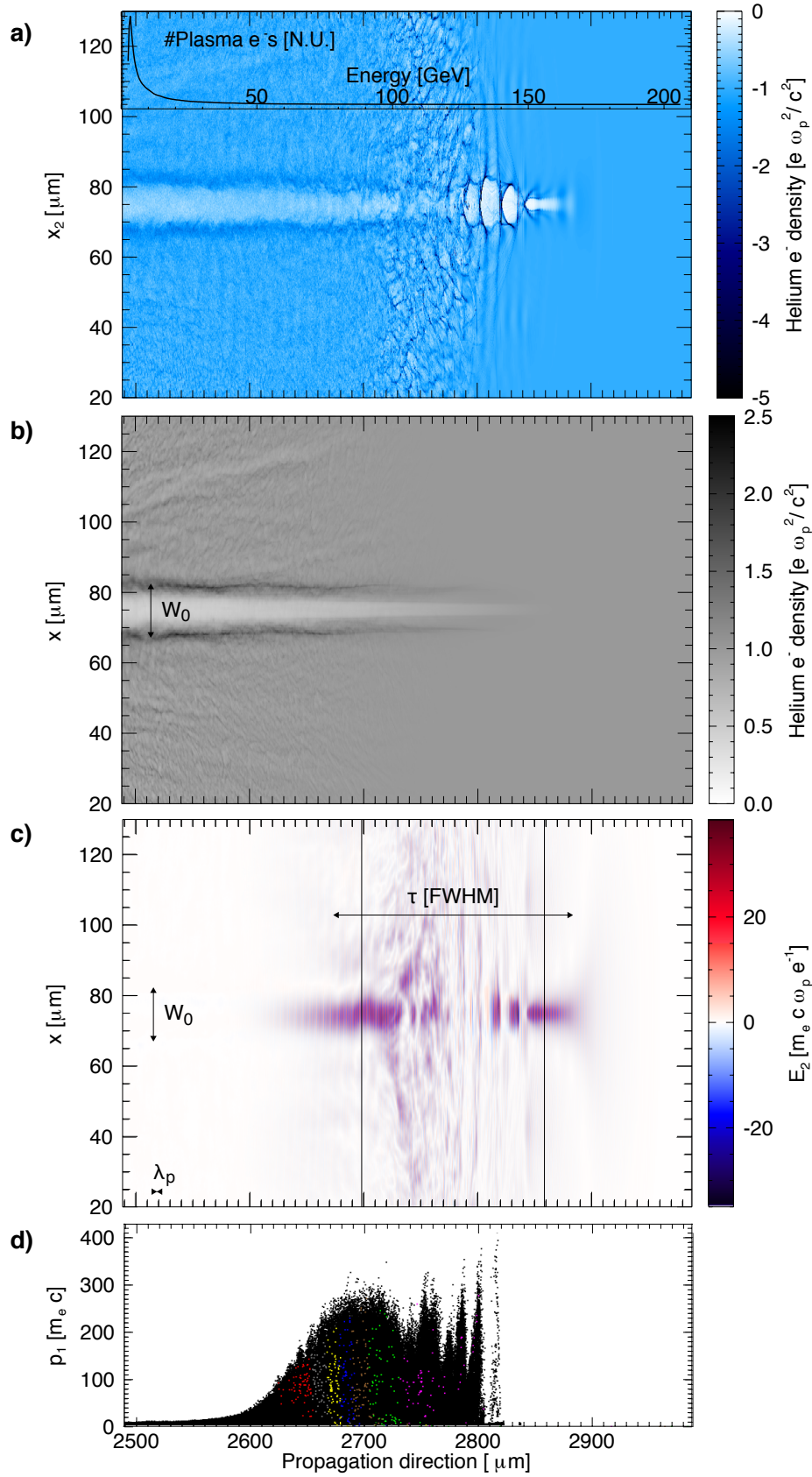


**Figure 4.4:** Plots a) to d) show the results as indicated by the label of Fig. 4.3 but at  $ct \approx 2486 \mu\text{m}$ .

Figures 4.3 and 4.4 contain the equivalent data but taken at  $ct \approx 1000$  and  $2000 \mu\text{m}$ . In them the depleted channel, with width close to  $W_0$ , behind the laser pulse, both in the plasma electron a) and

ion b) density plots, becomes evident. Moreover, also the back of the laser segments of the electric field, c), has self-focused. The central part, in Fig. 4.3, exhibits an initial modulation of the laser and then becomes highly nonlinear showing fingers that correspond to longitudinal laser segments with centroids transversely displaced of the propagation axis. This hosing like phenomena<sup>2</sup> is associated with transverse changes to the refractive index and the plasma density wake disruption, with bubbles being generated away from the axis. In Fig. 4.4 the central part of the laser field, where the disruption occurred, was depleted and/or diffracted away from the plasma whilst the front was modulated and compressed within the front plasma bubble structures. The accelerated electrons reach energies beyond 200 MeV that is beneath the value estimated because there were no electrons trapped for all the  $2000\mu\text{m}$  and most lost energy to the plasma. Their momentum spectra showed individual narrow spikes in the highly nonlinear section (at the back of each bubble) in the front region of the laser pulse. Whilst inside the channel the spectra is gaussian like. This is due to the different acceleration mechanisms that are characteristic to both regions. There is no significant trapping and acceleration of electrons at the laser front portion, the more linear LWFA part.

To better understand how the trapped and accelerated electrons propagate and radiate in the SM-LWFA, some of them (represented by the different colours of Fig. 4.4) were selected randomly (and categorized within several longitudinal regions), see Table 4.1 and Fig. 4.5. Together those electrons reproduce the trapped electron density distribution, but not their final energy spectrum. This means that the output radiation from all the trapped and accelerated electrons can not be extrapolated directly from the radiation emitted by these selected electrons. Nevertheless, they will allow us to study the key radiation features of electrons accelerated in the different parts of the long laser pulse wake and channel.

To see how the self-focusing affected the peak on-axis laser pulse  $a_0$ , Fig. 4.5 a) shows its evolution along the simulation. The front of the laser  $a_0$  intensifies as it self-focuses. The focusing starts to be evident after  $500\mu\text{m}$ , after which also the modulation at a wavelength close to  $\lambda_p$  of the pulse between  $\xi = 320$  and  $380\mu\text{m}$  is visible, saturating when the splitting occurs,  $ct > 1800\mu\text{m}$ . It is interesting to note how the laser group velocity evolves in time ( $\frac{v_g}{c}$  can be measured as  $\frac{\Delta\xi}{c\Delta t}$  following an individual bunched segment of the pulse): first it corresponds to  $c$  and then it is transformed to  $\approx 0.3c$  at the laser back. The nonlinear effects on the central portion of the pulse, associated with its centroid variations about the axis, are noticeable after  $1200\mu\text{m}$  of its propagation in the plasma, i.e. after  $500\mu\text{m}$  into the plasma flat top profile section.

Figure 4.5 b) shows the plasma electron charge density before the plasma downramp is reached by the laser front (blue). That black square defines the spatial limits imposed over the 20% randomly selected macro electrons to then randomly pick 512 representative ones. Those 512 electrons were followed in the re-run of the simulation and their charge, time, trajectory, momentum, energy, and sampled fields information for every simulation time step,  $\Delta t$ , was analyzed.

<sup>2</sup>More detailed information on the Hosing instability is presented in Chapter 6

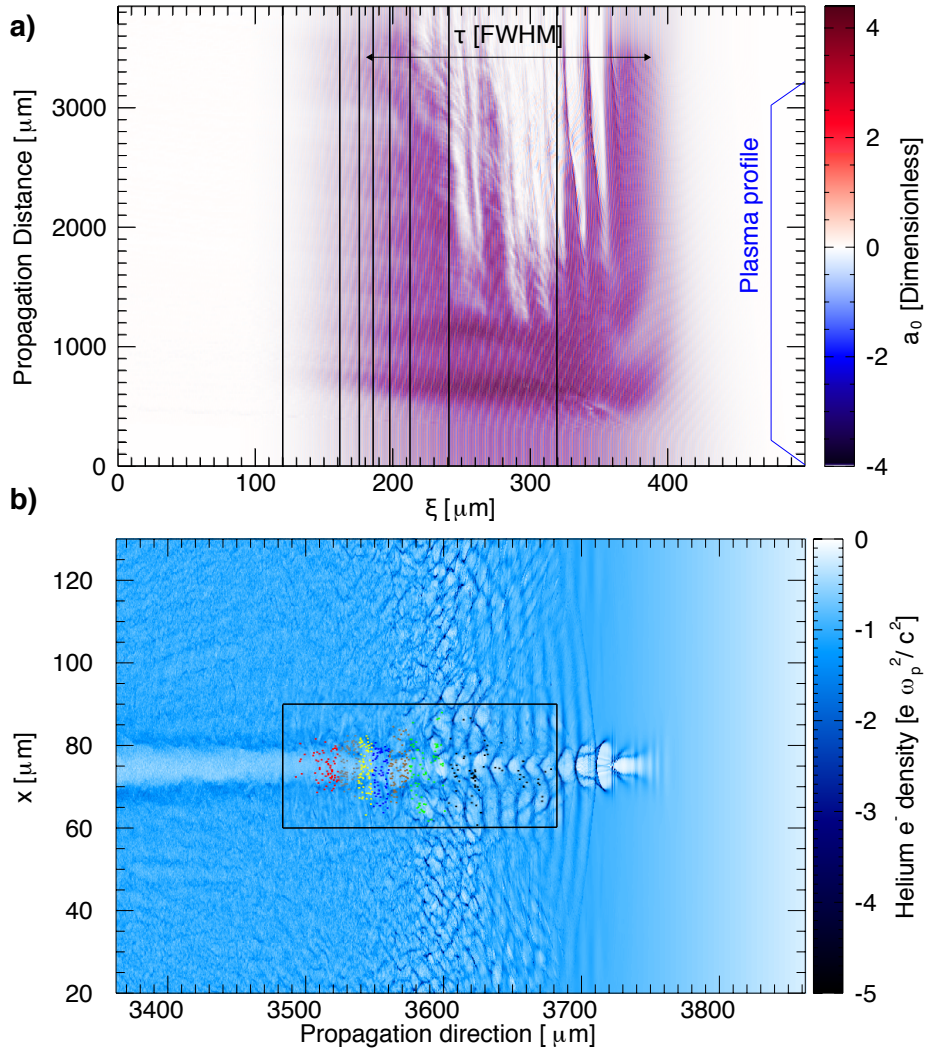


**Figure 4.5:** a) Sequence of the on-axis  $a_0$  information for each time step (listed as propagation distance  $ct$ ) versus the simulation box relative position,  $\xi = z - ct$ . Blue lines illustrate the plasma longitudinal profile as seen from the laser front (or at  $\xi = 500\mu\text{m}$ ) and the solid vertical lines show the limits of the trapped and accelerated 512 electrons selection regions. Plot b) includes the 2D plasma electron density plot at  $ct \approx 3360\mu\text{m}$  with the box delimiting the range and the coloured dots showing the 512 picked electrons according to Table 4.1

The different colors of the dots in Fig. 4.5 b) represent the electrons within the different sections that were defined for the radiation analysis. The vertical solid lines in Fig. 4.5 a) are the corresponding limits for each of those sections and help guide the eye in order to understand that, for example, the final two portions (referred to as a) and b) in Table 4.1) will have the lowest DLA contribution because there the  $a_0$  value is lower than in the other sections.

Figure 4.6 shows in a) the evolution of the on-axis accelerating field. At the laser front the plasma wakefields are present and become more intense as the laser self-focuses and depletes more plasma electrons. In the central region there are clear wakefields after the laser pulse was split and the self-modulation saturated. These fields have a constant peak value for less than  $2000\mu\text{m}$  allowing to estimate maximum total energy gained in this system from  $\Delta E_n \approx 2E_{\text{WB}}[MV/cm]0.2[cm] = 600\text{ MV}$  as 600 MeV.

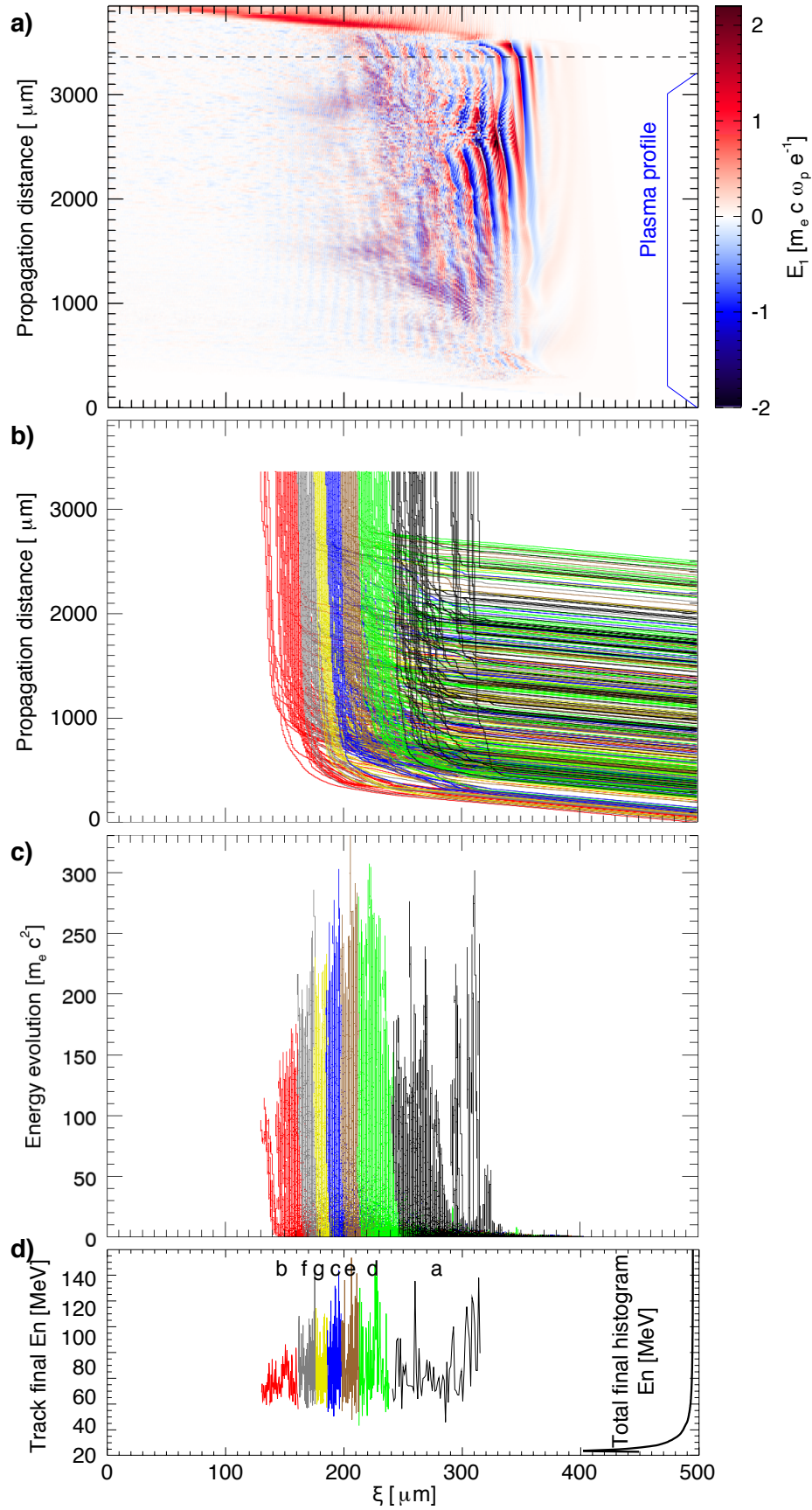


**Figure 4.6:** The on-axis longitudinal electric field value is plotted in a) as a function of  $\xi$ . It includes blue lines depicting the plasma profile as in Fig. 4.5 and a dashed horizontal line at simulation the point where the 512 electrons were picked. Plots b) and c) show those electrons trajectories along the propagation distance ( $ct$ ) and their energy evolution. Plot d) contains the final energy vs  $\xi$  and a solid black line showing the normalized histogram of all the 20% randomly selected electrons at that time (energies featuring in the vertical axis). The colours follow Table 4.1

Identification	a)	b)	c)	d)	e)	f)	g)
Nr tracks	67	70	73	74	75	76	77
Color	Black/Purple	Red	Blue	Green	Brown	Gray	Yellow
$\xi_i$ [ $\mu\text{m}$ ]	240	120	185.8	212.99	197.7	161	175.5
$\xi_f$ [ $\mu\text{m}$ ]	320	161	197.7	240	212.99	175.5	185.8

**Table 4.1:** Determination of the longitudinal space interval selection,  $[\xi_a, \xi_b]$ , relative to the simulation box for each of the groups of the 512 picked macro-particle electrons, which detailed information was stored for every time step ordered by the number of electrons they contain. The colours chosen for a) are two for better visualization in the next figures.

The nonlinearities within the laser central portion (where the plasma wake is disrupted) are visible in Fig. 4.6. The back of the laser shows fields with much lower intensity. As a consequence, all the longitudinal momentum gained by the electrons, see plots d) of figures Fig. 4.2 to 4.4, is due to the laser field, DLA. It then becomes relevant to investigate the DLA overall contribution in the acceleration of the 512 selected electrons, in similar fashion to what was done in Sec. 3.3.3, see Fig. 4.7. Figure 4.7 b) shows the 512 picked electrons trajectories relative to the simulation box longitudinal position along the propagation distance. It shows electrons being trapped from  $ct \sim 500$  up to  $\sim 2800\mu\text{m}$  and no significant motion in  $\xi$  after that. The fact that electrons are trapped in such a wide interval of the propagation distance in the plasma implies that different electrons will be accelerated over very different distances, leading to a broad range of final energies, as can be seen in plots c) and d), where the energy evolution and the final values for each electron are shown. Plot d) also includes the energy spectrum of the 20% selected electrons, corresponding to 2700000 macro-particles, from all the simulation box that allows to place the 512 selected electrons already in the spectrum tail (which is the more important part to analyse the effects of DLA and betatron radiation).

Figure 4.7 shows the fraction of the total energy transferred from the transverse electric field, in the laser pulse polarization direction, computed from Eq. (3.7) over their final energy. The values above 100% result from cases in which the electrons gained energy from DLA but lost it (mostly through the electric field perpendicular to both the longitudinal and laser polarization directions). Most electrons gained over 50% of their energy from the transverse laser field. The fraction value was greater for higher energy electrons, which is in agreement with our conclusions in Sec. 3.5. The electrons in a), from Table 4.1, with higher energies gained about 20% of energy from the field or over 140% which can be explained if some of them were trapped in the plasma wake and bubbles in the accelerating regions of the laser front, visible in Fig. 4.6 a), while others were trapped off-axis, where the longitudinal wakefields have higher intensities, performing betatron oscillations as explained in the previous chapter while being subject to DLA.

The spectrum of the Fast Fourier Transform algorithm (FFT) of the laser field intensity (roughly given by the simulated transverse electric field) as a function of the transverse  $k(x)$  is plotted in Fig. 4.8 for the two times studied in Figs. 4.2 to 4.4 at the longitudinal  $k(z) = k_0 = 10k_p$  position.

The spectrum becomes broader than ten as the laser propagates through the plasma, indicating the presence of transverse waves at different frequencies, consequence of the **LRSPM** instability side *Raman* scattered light.

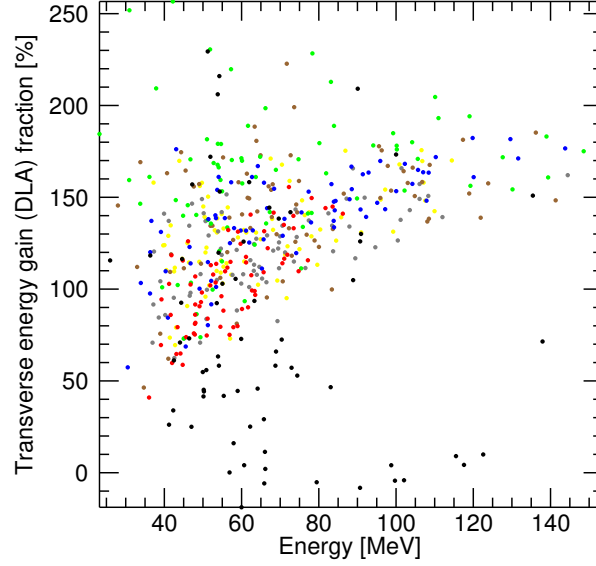


**Figure 4.7:** Ratio of the transverse electric field work, determined by Eq. (3.7), of the 512 electrons, picked and coloured as stated in Table 4.1 over their final energy at  $ct \approx 3360\mu\text{m}$  plotted against that energy. The values reach over 100% because trapped and accelerated electrons loose gained energy to the plasma.

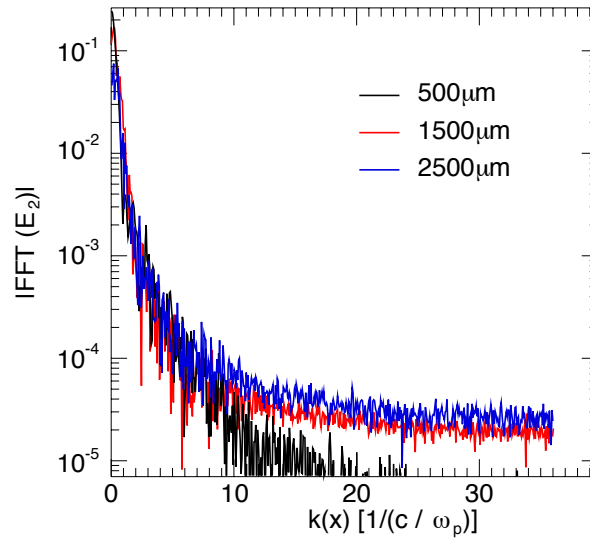


**Figure 4.8:**  $k_x = \frac{k(x)}{k_p}$  transverse space spectra of the **IFFT** of the transverse electric field (mainly the laser pulse) at the normalized  $k_z = \frac{k(z)}{k_p} = \frac{\omega_0}{\omega_p} \approx 10$ , after the simulation propagation distances of  $ct \approx 487, 1495$  and  $2486\mu\text{m}$  in black, red and blue, respectively.

### 4.3 Radiation from long laser plasma wakefield accelerator

The 512 selected electrons trajectory, charge, momentum, sampled field and energy information was used to input the jRad [70] post-processing diagnostic tool [70-72], see Sec. 2.5.2.A, to compute the radiation, using Eq. (2.19), like in Sec. 3.4.

The 2D vertical ( $x$  and  $y$ ) virtual detector was placed at about  $z = 13.4\text{mm}$  away from the end of the simulated plasma. The resolution of the detector was of  $6912 \times 1152$  cells ranging between  $x \in [-0.2, 0.2]$  and  $y \in [-0.034, 0.034]\mu\text{m}$ . For each of the groups of electrons, labeled as in Table 4.1, the resulting radiation energy density reaching the detectors is present in Fig. 4.9. The radiation is spread through a broader region in the laser polarization direction,  $x$ , which is an indication that DLA took place in the acceleration process, than in the orthogonal one,  $y$ . This asymmetry is also a consequence of the 2D cartesian configuration of the run that fixes the particles trajectory in the  $y$  direction at 0. The result for the electrons inside the channel behind the transverse nonlinearities, is similar in  $x$  range and intensity (when wighted against  $a_0$ ), plots f) and g).

Plots c),e) and d) are also identical, but possess higher peak radiation energy than the others. The radiation in c), e) and d) seems to be emitted in an angle to the centre of the detector unlike for f) and g), where the peak of the radiation energy lies close to  $(x, y) = (0, 0)$ . The radiation in the detector of plot a) is less intense and spread in a narrower region having a less ellipsoidal like shape. This suggests less DLA participation in the trajectory of the electrons that is consistent with Fig. 4.7 (black dots), i.e. lower energy values and radial displacements.

The electrons inside the plasma channel and at the back of the laser where the  $a_0$  value is lower (and so is the expected DLA energy gain), plot b), lead to much lower radiated energy density with similar ellipticity as plots f) and g), see Fig. 4.5.

The spectra of the total emitted radiation is shown in Fig. 4.10 a) for the laser polarization direction,  $x$ , and b) for the orthogonal one,  $y$  with a energy resolution of 1152 cells. The radiation in  $x$  has the not triangular broad shape identified in Sec. 3.4 in the simulation setups where DLA was expected to have considerable impact in the electron trajectory and their final energy. For a more precise evaluation of the photon energy spectra, Fig. 4.11 shows that this far into the simulation the total radiation emitted has energies up to 23 keV which nears the characteristic energy of hard x-rays.

### 4.4 Experimental investigation of x-ray generation in the long laser wakefield setup

The laser-plasma system explored in this sections was simulated before with different power, in particular with  $a_0 = 1.5$  and  $a_0 = 3$ , [59]. Both simulations compared in [59] showed laser self-focusing and self-channeling. For the simulation with the greater  $a_0$ , the acceleration of the electrons inside the channel at the back of the laser, results mainly from DLA and not the plasma wake. The explored scenario resulted in the excitation of nonlinear amplitude plasma density perturbations (as opposed to linear periodic oscillations). The wake is disrupted and prevents most of the laser to undergo self-modulation and resonantly excite plasma wakefields (as opposed to the more linear regime of

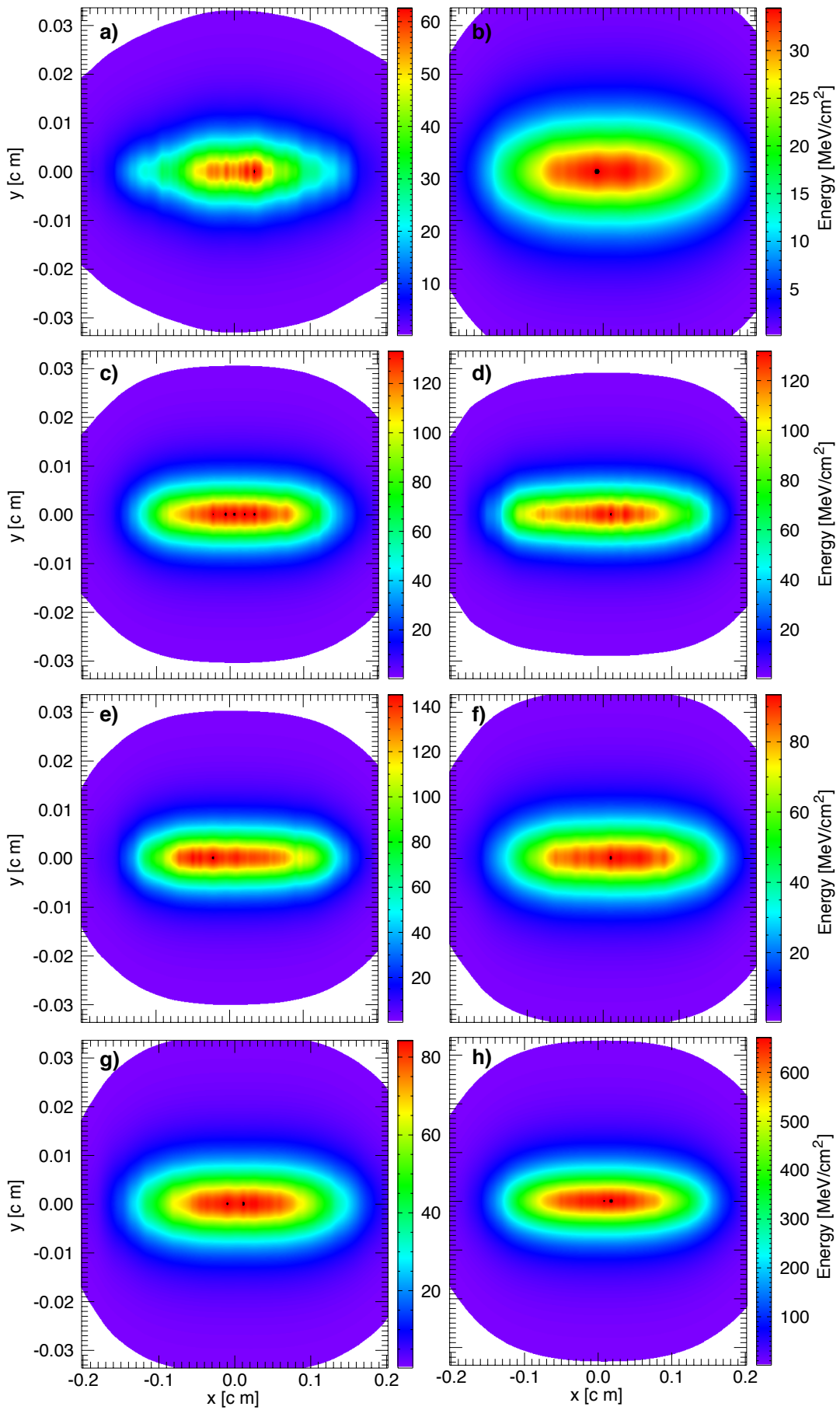


**Figure 4.9:** Computed radiation energy reaching the virtual detector that was emitted by the 512 picked electrons labeled according to Table 4.1. Plot h) shows the total of plots a) to g).

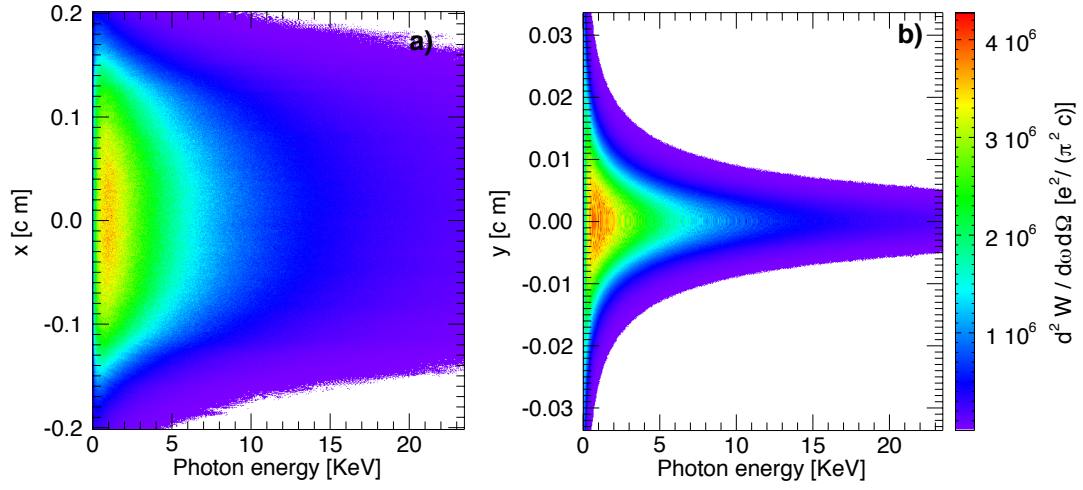


**Figure 4.10:** Computed radiation spectra at the virtual detector emitted by all the 512 picked electrons in the laser polarization direction,  $x$ , and in the orthogonal one,  $y$ .

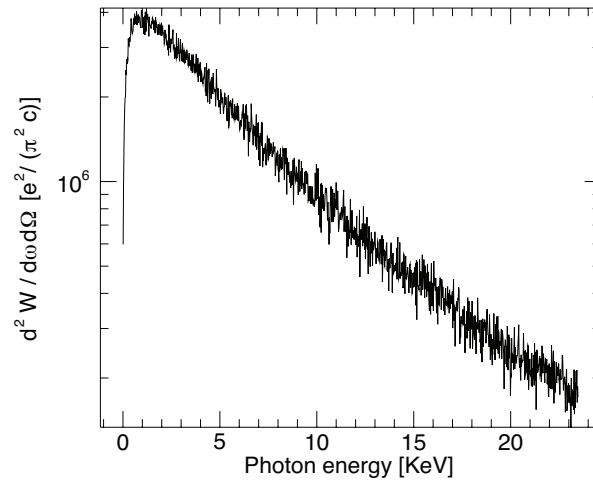


**Figure 4.11:** Computed radiation spectra at the centre of the virtual detector emitted by all the 512 electrons.

$a_0 = 1.5$ ). The maximum photon energy registered was ten times higher for the higher  $a_0$ , reaching over 100 keV, and its spectra in the laser polarisation direction was no longer characterized by a triangular like shape. Two different sets of critical energy were found for the simulations, the set with 1.4 keV + 0.3 keV and the one with 45 keV + 13 keV, for the higher  $a_0$ . The results shown in the previous section of this dissertation, for the simulation with  $a_0 = 2$ , are much closer to the highly nonlinear,  $a_0 = 3$ , regime.

The different simulations were inspired by the experimental setup available at [LLNL](#) that corresponded to  $a_0 \in [1, 3]$  [\[144\]](#). The experiment took place in the Jupiter Laser Facility of [LLNL](#) and used the Titan Nd:glass laser system that provides about 1ps long pulses at a wavelength of  $1.052\mu\text{m}$ , focused to a  $30\mu\text{m}$  spot. The setup included a Helium (with/out Nitrogen impurities) 3mm gas jet that was completely ionized by the laser pulse. The light exiting the gas jet is then reflected by a glass wedge. An optical imaging spectrograph was used to capture that reflected light. The accelerated electrons propagate through a whole in the glass wedge and are sent through a magnet spectrometer. The signal radiation from the latter spectrometer is captured by either a stacked-image-plate (that allows to determine x-ray yield) or a 15 filter wedges arranged as Ross pairs in a wheel to study the photon energy.

After analyzing the experimental data it was clear that the underlying acceleration and radiation processes were better modeled by the simulation that considered the highest laser power,  $a_0 = 3$ . The electron energy measurements registered up to 300 MeV, the critical radiation energies ranged from 10 to 20 keV and the outgoing laser spectra showing two clear peaks attributed to the *Raman* anti-stokes satellites.

## 4.5 Conclusions and future direction

In this chapter the 2D SLAB OSIRIS simulation reproducing the experimental [SM-LWFA](#) setup used at [NIF](#) in the [LLNL](#) were discussed. The goal is to determine the x-ray production of that numerical configuration. In that setup a long laser pulse is sent through the plasma and its behavior, associated to the plasma density that it affects, was analyzed in three separate regions. The laser front, where the [LRSE](#) effect was predominant, allowed an initially not matched laser pulse to go through many *Rayleigh* lengths through the plasma with focused intensity. This allows the ponderomotive force of the laser front to drive plasma wakes with stronger fields and [LRFS](#) and low angle [LRSPM](#) instabilities to take place. Quickly, the wakefields become nonlinear and there is wave breaking as the electrons cross, or overshoot through the laser propagation axis. This is changing the local plasma refractive index having great impact in the laser transverse pulse profile. The nonlinearities are responsible for inducing a hosing like phenomena in the buckets of photons that are later dispersed. Behind the central part of the laser, where the intensity starts to diminish the fields do not become as nonlinear, but due to the collective plasma wakefields and laser ponderomotive force effects, the laser generates a channel depleted of both electrons and ions at its back, [LRSC](#).

In the resulting channel the main electron acceleration process is [DLA](#) and this is visible in the

higher energy gained by the electrons and in the radiation sample that was emitted by a random selection of 512 electrons and captured in a virtual detector, being determined by use of the post-processing jRad tool. There was significant asymmetry elongation in the laser polarization direction (attributed to [DLA](#) and to the trajectories of the electrons being in 2D) of the measured radiation energy density from the channel electrons, with photon energies reaching beyond 23 keV. The spectra in the laser polarization direction is shaped just like the [DLA](#) assisted scenarios explored in Chapter [3](#). The fit of the observed spectra to synchrotron radiation emitted at two critical photon energies remains to be done, as well as the end of the second simulation where the particle spatial, momentum and sampled field information of 512 electrons was stored.

Our results provided insight over the  $a_0$  influence on the radiation produced in the experiment with identical parameters to the simulated ones. This allowed us to, afterwards, pick a previously run simulation done for a laser of  $a_0 = 3$  [\[59\]](#), to model the experimental findings published in [\[144\]](#). In addition to the extra plasma and laser technological requirements that using a greater  $a_0$  to create hard x-rays with higher critical energies brings, the challenge of controlling the laser pulse and plasma near or complete hollow channel during the nonlinear phenomena increases. We plan to further investigate the present findings with a full 3D OSIRIS simulation.

# 5

## Positron beam based Plasma Wakefield Acceleration in a self-driven Plasma Hollow Channel

### Contents

---

<b>5.1 Analytical model for self-driven hollow channel wakefields</b> . . . . .	100
<b>5.2 Simulations of the positron self-channeling accelerator</b> . . . . .	105
<b>5.3 Concluding remarks</b> . . . . .	112

---

More compact, efficient and economic next generation accelerators are required for future linear lepton colliders. Those will allow scientists to study physics beyond the energy frontier, beyond the known particles of the Standard Model and the dark matter, that represents over 20% of the matter in our universe. The introduction to this dissertation began by a brief historical overview of worldwide particle accelerator science, with emphasis on the 20 century breakthrough reached with the invention of the Plasma Wakefield Accelerator technique, in which the plasma state of matter has the potential to support electric fields 1000 times stronger than standard devices, limited by their constituents material breakdown, could accelerate particles passing through the full length of the plasma [14].

When that accelerator operates in the linear regime (see Sec. 2.1) and a drive laser pulse (Laser Wakefield Acceleration (LWFA)), with normalized vector potential  $a_0 \ll 1$ , is sent into the plasma, the plasma density oscillations are denominated the wake. They are associated to fields, called the wakefields with maximum acceleration gradient, experienced by electrons or positrons, of charge  $|q|$  and mass  $m_e$ , given by<sup>1</sup>  $Max(W_{||}) = \frac{\pi m_e c^2 k_p a_0^2}{8q}$  that for typical plasma densities,  $10^{16} - 10^{18} \text{ cm}^{-3}$ , achieves about 4 – 40 MV/m for  $a_0 = 0.01$ .

If instead a lepton (electron or positron) drive beam, (Plasma based Wakefield Acceleration (PWFA)), with peak charge density  $q_b n_{b0} \ll \frac{2}{\pi} q n_0$  and normalized spot size of  $\sigma_r \ll 1$ , is used to perturb the plasma and generate the wakefields with associated accelerating gradients up to  $Max(W_{||}) = 2\pi^2 q_b n_{b0} \sigma_r (0.058 - \ln(\sigma_r))$ , which for realistic lepton drive beam parameters close to  $\sigma_r \sim 0.01$  and  $n_{b0} \sim 0.01 n_0$  lead to a range of 0.7 – 7 GV/m, can be used to accelerate both electrons and positrons in similar fashion.

When the so called bubble or blowout [49, 52] regime is reached the plasma wake follows the structures illustrated in [2.3], plot a). In such a case the peak accelerating field is at the back of the first plasma electron density cavity. That cavity can be approximated by a spherical bubble of radius  $r_b \approx 2\sqrt{a_0} k_p$  or  $2k_p$  if a laser of  $a_0 \sim 2$  or electron beams are used to drive the wakefields, respectively. The accelerating gradient generated reaches  $Max(W_{||}) = \frac{m_e \omega_p^2}{2|q|} r_b$  that corresponds to 1 – 14 TV/m. Plasma wakefield accelerators operating in this nonlinear regimes are promising candidates for the acceleration of high charge electron beams in short distances, which is ideal for future colliders. However, in the bubble nonlinear scheme the region where positrons can be placed and be simultaneously accelerated and focused is very narrow. Therefore the task of accelerating positrons in them is very challenging.

A drive positron beams can not be used to produce the same plasma bubble wakes. It will, instead, excite the plasma wakefield suck-in regime [63, 2.3] plot b), see Sec. 2.3. Where the plasma density exhibits ring like structures instead of bubbles. This regime is associated with weaker wakefields than the electron beam driven ones, making it ineffective. It is therefore important to develop the current plasma wakefield technique and investigate alternative competitive configurations for the acceleration of positron beams up to extremely high energies with a reduced price and physical space cost.

Research has focused its recent efforts in the pursuit of plasma wakefield positron acceleration in cylindrical, near or completely hollow channels [44, 158-161]. Because they allow realistic positron

<sup>1</sup>The repetition of the expression for the symbols that were determined in previous chapters will, preferably, be avoided in this one.

beams to accelerate within high accelerating gradients and minimal transverse wakefields, maintaining their emittance. Without requiring unrealistic short positron beams the total positron charge effectively accelerated can also be larger. One of the main setbacks of those preformed hollow channels was the presence of neutral particles inside them (mainly from the gas that gives rise to the plasma when ionized) that can give rise to secondary ionization or unwanted neutral particle collisions with the beam. It was recently shown that the ponderomotive force of Orbital Angular Momentum laser beams (OAMs) can generate doughnut like shaped plasma electron low density wakes that confine the high electron density regions close to the propagation axis where positron beams can accelerate [162-164].

In 2014 we proposed a novel plasma based positron driven setup that induces the generation of the ion and electron hollow channel in an initially homogenous plasma, the Positron self-driven Hollow Plasma Channel Wakefield Acceleration (PHPCWA) scheme, in similar fashion as in the laser pulse self-channeling effect, Laser Relativistic Self-Channeling (LRSC), that was described in Sec. 4.1.1 [165, 166]. In it a tightly focused, i.e. with a transverse size much narrower than the plasma skin depth, relativistic positron beam is sent into a fully ionized uniform plasma of electrons and ions. The beam space charge is sufficient to suck-in the plasma electrons, its narrow width preventing return current effects to completely neutralize it [167], and repelling the plasma ions. After the beam passes through the electrons are quickly blownout by their own space charge, initiating a plasma nonlinear wake structure, while the slower ions continue to free-stream away from the propagation axis forming a depleted cone like channel behind the beam. A trailing high charge positron beam, henceforth called the witness beam, of length up to  $\frac{\lambda_p}{2}$  can be injected after the drive beam and be accelerated by the electron wake while not sampling any defocusing force within the channel where the plasma transverse wakefields vanish.

The ultimate goal of this technique is to accelerate a trailing positron beam within the plasma hollow channel. The hollow channel quickly becomes a stable structure co-moving with the beam. Therefore, the acceleration is mainly governed by the same physics as the positron acceleration within pre-formed plasma hollow channels. For that reason the present chapter starts with a short derivation of the linear acceleration of charged particles mechanism inside pre-formed plasma hollow channels. It also includes the calculation of the positron beam properties needed for the self-channeling process to be successful, Sec. 5.1. The OSIRIS fully relativistic 3D, 2D and Quasi-3D Particle-In-Cell (PIC) infrastructures developed by the teams at Instituto Superior Técnico - Universidade de Lisboa (IST) and at University of California Los Angeles (UCLA) [73, 78, 80], and the numerical code QuickPIC created by the latter [93, 94], were used to model and benchmark the theory for the channel formation and positron acceleration in the proposed scenario as well as to investigate its accelerating capabilities. For more detailed information on the codes please revisit Sec. 2.5. In Sec. 5.2, the most significant numerical results are discussed. Section 5.3 features the main conclusions.

## 5.1 Analytical model for self-driven hollow channel wakefields

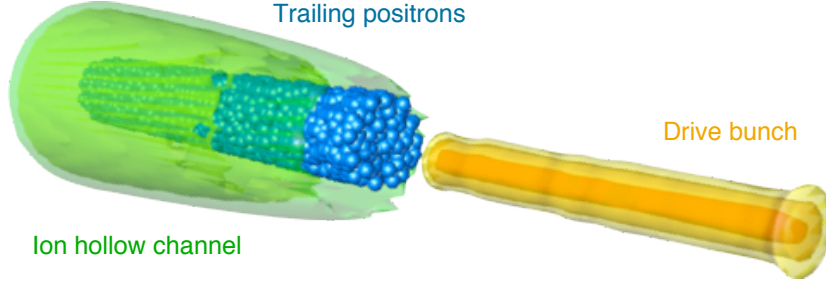


**Figure 5.1:** Illustration of the tightly focused positron drive bunch (in yellow) self-driven plasma ions hollow channel (delimited by the green isosurfaces) for ideal acceleration of trailing positrons (blue spheres).

Figure 5.1 a) illustrates the PHPCWA process with the drive and witness trailing positron bunches and the resulting plasma hollow channel. In the section below the perturbation theory for particle acceleration inside a pre-formed plasma is reviewed. In the cylindrically symmetric completely hollow channel with a surface, at  $r_b \approx r_c$ , linear plasma waves are excited as explained in [44]. The acceleration process inside the stable self-generated hollow channel is similar to the one explored with the pre-formed channel.

### 5.1.1 Particle acceleration inside pre-formed plasma hollow channels

The longitudinal accelerating field piecewise solutions inside the plasma, i.e. outside of the channel, were derived in chapter 2, Sec. 2.1, from Eqs. 2.3 and 2.4,  $G_{z,\text{wake}} = c_0 \frac{K_0(k_p r)}{K_0(k_p r_c)} K_0(k_p r)$ . There  $K_0$  is the modified *Bessel* function of zeroth order and second kind. From those equations it is possible to determine that  $G_{r,\text{wake}} = -\frac{ik}{k_p} \frac{K_1(k_p r)}{K_0(k_p r)} G_{z,\text{wake}}$ , where the first order *Bessel* function was used.

Similarly, from 2.3 and 2.4, inside the hollow channel the field corresponds to that of a harmonic oscillator with *Green* function solutions of the form  $G_{z,\text{channel}} = A \exp(-i(\omega t - kz)) + B \exp(i(\omega t - kz))$  with the dispersion relation  $\omega^2 = c^2 k_{\parallel}^2 + c^2 k_{\perp}^2$ .

In the analysis of chapter 2 it was seen that the transverse electric field is related to the longitudinal field through:  $G_{r,\text{channel}} = \frac{ikr}{2} G_{z,\text{channel}}$ . Moreover, there are no particles to generate currents, and induce magnetic fields, therefore, close to the axis the transverse focusing field vanishes,  $W_{\perp}(r \rightarrow 0) \rightarrow 0$ .

From *Gauss's* law  $\nabla \cdot \epsilon \vec{E} \rightarrow 0$ , where  $\epsilon$  is defined as  $1 - \frac{\omega_p^2}{\omega^2}$  in the plasma and 1 in vacuum. Thus, the channel, that is completely depleted of charged particles, will only sustain transverse modes. Outside of the channel, the continuity of  $\nabla \times \vec{E}$  implies that also only transverse modes are excited. Hence, both  $E_z$  and  $\epsilon E_r$ , have to be continuous at the boundary  $r = r_c$  leading to the excited mode wave frequency:

$$\omega^2 = \omega_p^2 / \left( 1 + k_p r_c \frac{K_0(k_p r_c)}{2K_1(k_p r_c)} \right). \quad (5.1)$$

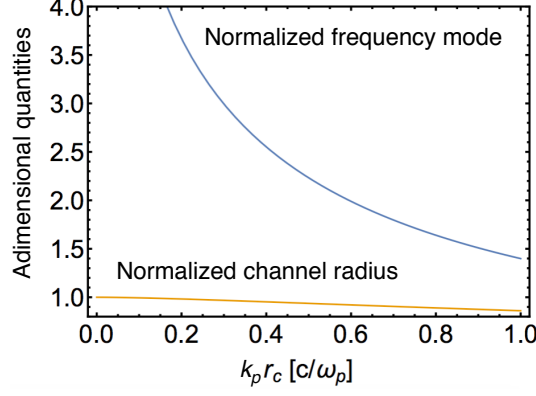


**Figure 5.2:** Plot of the normalised excited frequency mode (in blue) and of the channel radius (yellow) as functions of the normalized plasma hollow channel radius.

The parameter  $\frac{\omega}{\omega_p}$ , also referenced as the normalized excited frequency mode, then depends on the normalized channel radius,  $\frac{K_0(k_p r_c)}{2K_1(k_p r_c)}$ . Both quantities are represented as functions of the normalized plasma hollow channel radius,  $k_p r_c$ , in Fig. 5.2. The figure shows that both  $\frac{\omega}{\omega_p}$  (blue) and  $\frac{K_0(k_p r_c)}{2K_1(k_p r_c)}$  decrease with the channel radius, starting from an unlimited value and 1, respectively, that corresponds to the limit of no channel, i.e. of an uniform plasma,  $r_c \rightarrow 0$ .

To introduce the drive laser ponderomotive force,  $\frac{\omega_p^2 m_e}{2q} \nabla \langle a_0^2 \rangle$ , or particle beam space charge effects,  $-\nabla (4\pi n_b q_b + 4\pi n_1 q)$ , in the right side of equations 2.3 and 2.4 with the respective *Green* functions consider its general form as  $\nabla f$  with *Fourier* solution in the reference frame co-moving with the plasma wake of  $F(k, r) = \int_{-\infty}^{\infty} f(\xi, r) \exp(-ik\xi) d\xi$ . The field configuration in the channel then becomes constant  $E_{z, \text{channel}} = c_1$ . The continuity of  $E_z$  and now of  $\epsilon \left( \frac{\partial F}{\partial r} E_r \right)$  yields the field created by the drive beam force  $E_z(r, k) = \frac{-ik k_\omega^2}{k^2 - k_\omega^2} F(r_c, k) \frac{c^2}{\omega_p^2}$ , where the channel dispersion relation makes  $k_\omega^2 = k_p^2 / \left( 1 + k_p r_c \frac{K_0(k_p r_c)}{2K_1(k_p r_c)} \right)$ . Returning to the real space, still with cylindrical geometry, the accelerating gradient that the trailing charged particles experience inside the channel is then given by:

$$E_z(r, \xi) = k_\omega^2 \frac{c^2}{\omega_p^2} \int_{-\infty}^{\xi} \cos(k_\omega \xi') f(r_c, \xi - \xi') d\xi'. \quad (5.2)$$

The lines of Fig. 5.2, imply that the frequency mode,  $\omega$ , decreases for higher plasma channel radius. Consequently the field, which is proportional to  $k_\omega$  and scales with the radius just like the frequency mode, also decreases. Given that the electron surface wake is linear inside the hollow channel there will be no electrons,  $n = n_0 + n_1 = 0$  and so a low density drive bunch will have  $f \approx 4\pi n_b q_b$ . For the linear parameters mentioned in the previous section and for a reasonable channel radius of about  $r_c k_p \approx 1$  the maximum gradient reached on-axis at  $\xi = \frac{\pi k_p}{2k_\omega}$  has the values of 8 – 80 GV/m for the typical plasma density (outside of the plasma where the plasma is in electrostatic equilibrium) range. For a low intensity (also long) laser pulse,  $f = \frac{\omega_p^2 m_e}{4q} a_0^2$ , exciting gradients between 9 – 90 MV/m. In the previous rough estimates, the beam was assumed, for simplicity, to be longitudinally uniform. This can be interpreted as the hollow channel providing a setup where the accelerating fields identical to the linear **LWFA** and **PWFA** scenarios are achievable and the transverse forces vanish close to the axis motivating the use of hollow channels for the acceleration of positrons in the linear and potentially

also in the nonlinear regimes. In fact, Pukhov et al., recently studied the nonlinear regime driven by a laser pulse propagating in a pre-formed near hollow plasma channel [160]. The novel PHPCWA configuration has the main distinction that the channel is generated directly by the positron bunch, precluding neutral particles from remaining on-axis and enabling a simpler, possibly more compact and successful, overall accelerator infrastructure to provide the same final results.

### 5.1.2 Hollow channel formation by tightly focused positron bunches

The analytical model described in this section, where the self-generated hollow channel is studied, assumes that the positron drive bunch is cylindrically symmetric and longitudinally uniform. These are valid assumptions when the positron bunch is longer than the typical skin-depth associated with the ion motion,  $L_b \gg \frac{c}{\omega_{pi}} \equiv \sqrt{\frac{m_i c^2}{4\pi \mathcal{Z}^2 q^2 n_0}}$ . The symbol  $\mathcal{Z}$  standing for the ion atomic number, i.e. ionization level. Moreover, the present model considers that the bunch spot size is narrow,  $\sigma_r k_p < 1$ , so that the excited plasma electron return current is insufficient to significantly neutralize its space charge or to perturb its shape and evolution [167]. The beam density is then given by:  $n_b \exp\left(-\frac{r^2}{2\sigma_r^2}\right)$ .

The plasma ions are characterized by a heavy mass  $m_i$  and so not relativistic (reason for neglecting the impact of the magnetic field in their trajectory) velocity  $\vec{v}_i$ , the charge  $q_i = \mathcal{Z}|q|$ , are repelled by the positron drive bunch according to the *Lorentz* force that is expressed as  $m_i \frac{d\vec{v}_i}{dt} = q_i \vec{E}$ . Here the radial repelling field can be determined from *Gauss's* law given by  $E_r = 4\pi|q|/r \int_0^r n_b r dr$ .

For the typical positron bunch configuration, the Gaussian transverse profile is defined by the radial standard variation of the positrons  $\sigma_r$  and the electric field follows:  $E_r = 4\pi|q|n_b \frac{\sigma_r^2}{r} \left(1 - \exp\left(-\frac{r^2}{2\sigma_r^2}\right)\right)$ . Close to the axis,  $r \ll \sigma_b$ , the *Taylor* expansion of the field exponential component can be truncated at the 3rd order to write  $\exp\left(-\frac{r^2}{2\sigma_r^2}\right) \frac{1}{r} \sim \frac{1}{r} - \frac{r}{2\sigma_r^2} + \frac{r^3}{4\sigma_r^4} - \mathcal{O}(r^{5/8}\sigma_r^4)$  (for narrow positron bunches each higher order term contributes less to the final result so need only be included if a more rigorous analysis is required).

Going into the co-moving frame coordinate system, with  $\xi = z - ct$  and  $\tau = t$ , the simplified equation for the ion transverse motion close to the positron drive bunch propagation axis is:

$$\frac{\partial^2 r}{\partial \xi^2} \approx \frac{2\pi|q|^2 \mathcal{Z} n_b}{m_i c^2} \left(r - \frac{r^3}{2\sigma_r^2}\right) \equiv k_i^2 r - \frac{k_i^2 r^3}{2\sigma_r^2}. \quad (5.3)$$

For simplicity, we consider that  $\frac{r^2}{2\sigma_r^2} \ll 1$ , which allows to neglect the last term of the right end side of Eq. [5.3]. That approximation is valid for positrons that are being accelerated within the central region of the plasma hollow channel. In such case the solution is simply  $r = r_0 \exp k_i(\xi - \xi_b)$  and the ion ring gets exponentially wider as the beam propagates<sup>2</sup>.

Imposing that there is no sheath crossing of the ion ring trajectories, the total ion charge in the plasma is conserved and the density respects the continuity equation. Hence,  $\int n_0 r_0 dr_0 = \int n_i r dr$ , where  $n_i$  is the ion density inside the hollow channel generated within the initially uniform plasma with

<sup>2</sup>Note that equation [5.3] is similar to the *Duffing's* equation. The *Duffing* equation describes a damped and driven simple harmonic oscillator when the term of first order in  $r$  is of the same sign as the second derivative term. Otherwise it models an exponential growth/decrease. If the equation was an oscillator it could be solved by means of the *Poincaré-Lindstedt* [168] perturbation method resulting in the formula for the radial displacement of the ions that are initially close to the longitudinal axis:  $r(\xi) = r^{(1)}(\xi) + r^{(2)}(\xi)$  with  $r^{(1)}(\xi) = r_0 \cosh(k_i(\xi - \xi_b))$  and  $r^{(2)}(\xi) = -\frac{r_0^3}{64\sigma_r^2} (\cosh(3k_i(\xi - \xi_b)) - \cosh(k_i(\xi - \xi_b)))$ , in which  $\xi_b$  represents the position of the front of the positron drive bunch.

electrostatic equilibrium density of  $n_0$ . Therefore, from computing the integrals of the result on the previous paragraph, the density of a plasma ion ring sheath starting from  $r_0$  in the channel becomes  $n_i = n_0 r_0^2 / r^2$  as the ring expands<sup>3</sup>.

After the positron bunch passes through the plasma ions, i.e. for  $\xi < \xi_f$ , where  $\xi_f = \xi_b - L_b$ , there will be no significant restoring electric force from the electrons capable of attracting the heavy ions back to the propagation axis. Instead the ions will approximately have a free-stream like motion behind the bunch, giving the hollow plasma channel the conical unique shape. Their final trajectory takes the form:  $r_f(\xi) = r(\xi_f) + \frac{\partial r}{\partial \xi} |_{\xi_f} (\xi - \xi_f)$ .

The plasma ion channel can be recognised as hollow when the requirement that  $n_i \ll n_0$  inside it is verified. To first order of approximation that inequality is equivalent to stating that  $r$  or  $r(\xi_f) \gg r_0$  which can be enunciated as  $k_i(\xi - \xi_b) \approx k_i L_b \gg 1$ , leading to, from the definition of  $k_i$  stated in Eq. (5.3), the condition for hollow channel formation in the PHPCWA:

$$n_b \gg n_0 \frac{2}{Z} \left( \frac{1}{k_p L_b} \right)^2 \frac{m_i}{m_e}. \quad (5.4)$$

After some algebra Eq. (5.4) can be converted into the engineering formula for the condition on the total number of positrons in a bi-gaussian bunch, i.e. with the following longitudinal dependence  $\exp\left(\frac{-(\xi - \xi_b)^2}{2\sigma_z^2}\right)$ , yielding:

$$N_b \gg 6.52 \times 10^9 \mathcal{A} / Z (\sigma_r [\mu\text{m}])^2 / \sigma_z [100\mu\text{m}], \quad (5.5)$$

where  $\mathcal{A}$  is the atomic mass of the plasma ions.

Sending a tightly focused positron bunch through an homogenous plasma will thus generate an ion hollow channel provided that Eq. (5.4) is satisfied. Plasma electrons, on the other hand, are attracted to the bunch axis, quickly sucked-in, see in Sec. 2.3, where the electrons arising from different initial radial positions  $r_0$ , traveled during different time periods before collapsing on (and crossing) the longitudinal axis, consequently, phase mixing occurs and the maximum accelerating gradient is much lower than the one for equivalent plasma-electron bunch parameters in the PWFA blowout nonlinear regime. Behind the drive bunch the electrons form an oscillatory, bubble-like wake structure that is as nonlinear as the channel is deeper and wider. A possible analytical analysis for electron sheath crossing is complex so we made use of numerical observations from 3D and 2D simulations done with the fully relativistic Particle-in-cell code OSIRIS [73] to understand their behaviour in the channel and the wakefields they generate, which will be discussed in the next sections.

<sup>3</sup>For the oscillator like solution this would be:  $n_i = n_0 r_0^2 / (r^{(1)} + r^{(2)})(r^{(1)} + 3r^{(2)})$ .

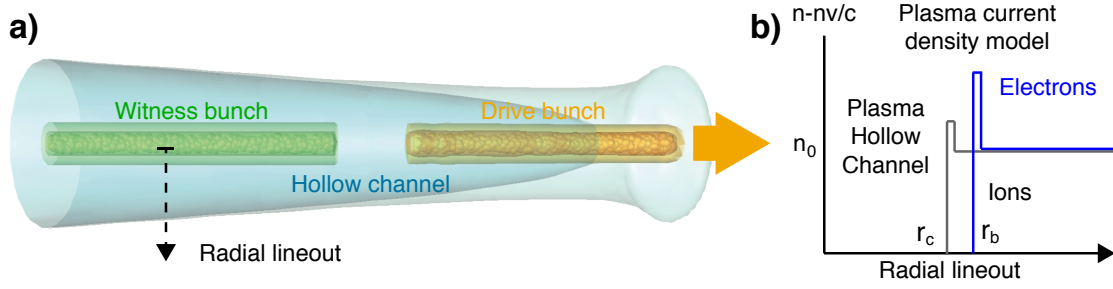


**Figure 5.3:** a) 3D sketch of the hollow channel wakefield accelerator where a drive positron bunch (orange tones) propagates into the plasma of electrons and ions forming a hollow channel (limited by the blue ion density isosurfaces). b) radial lineout, taken at the middle of the witness bunch (dashed arrow), of the electron wake current density (blue), like Fig. 2.2 and the plasma ions (gray line) existing outside of the hollow channel ( $r < r_c$ ).

Figure 5.3 a) contains the illustration of the PHPCWA setup resulting from a 3D simulation. Plot b) is equivalent to the plot b) of Fig. 2.2 and depicts the step-like function used to roughly describe the radial profile of the plasma ions (gray lines) and electrons (blue) in the first electron density bubble excited behind the drive positron bunch, in the model investigated below.

In the remainder of this section and the following one the electric fields are normalized to the cold plasma wave breaking limit  $E_0 = \frac{m_e c^2 k_p}{|q|}$ , the densities to the plasma equilibrium background density,  $n_0$ , and the distances to the electron skin depth  $\frac{1}{k_p}$ .

In order to determine the wakefields we focus our study in scenarios where the ion channel radius,  $r_c$ , for which  $n_i \approx 0$ , is shorter than the electron bubble radius,  $r_b$ , after which  $n_i = n = n_0$ , which is the case for realistic dense bunch-plasma configuration. According to the nonlinear wakefield theory of Lu et al., [48, 99] see Sec. 2.2 the electric potential from where the longitudinal accelerating field can be computed  $E_z$  is given by:  $\psi(r_b) = -\log(r_b)a(r_b)$ , where the definition  $a(r_b) = \int_0^{r_b} r' n_i(r') dr'$ , in the central region of the bubble for which  $\frac{\partial a(r_b)}{\partial \xi} \approx 0$ , was employed.

Therefore, the accelerating field can be written as  $E_z = \frac{\partial \psi}{\partial \xi} = -a(r_b) \frac{\partial \log(r_b)}{\partial r_b} \frac{\partial r_b}{\partial \xi} = -\frac{\xi}{r_b} a(r_b)$  taking  $r_b^2 = r^2 + \xi^2$ . Inside both the electron depleted bubble and the ion depleted hollow channel and behind the bunch, due to the complete absence of charged particles, the transverse forces ought to be negligible. These results are in agreement with the findings of Pukhov et al. [160] where the electron wake and the fields were excited by the laser in a pre-formed nearly hollow plasma channel.

Considering the piece-wise profile for the plasma ions like:  $n_i(r) \approx 0, r < r_c \vee n_i(r) \approx n_0, r > r_c$ , drawn in Fig. 5.3, then the previous expression becomes  $E_z \approx -\xi \frac{1}{2} (1 - r_c^2/r_b^2)$ . When the ion hollow channel becomes narrower and weaker and a uniform plasma profile is approached,  $r_c \rightarrow 0$ , the typical slope for the standard nonlinear blowout regime,  $\partial E_z / \partial \xi = -1/2$ , is recovered. Inside a deep wide hollow channel, when  $r_c$  is considerable, the accelerating gradient is lower.

A more complete analysis of the overall complex acceleration and hollow channel formation processes is very demanding and so we resorted to numerical simulations to gain deeper insight, and corroborate the predictions of the simplified model discussed this far, into the PHPCWA mechanism.

## 5.2 Simulations of the positron self-channeling accelerator

### 5.2.1 Limits of the linear theory for positron acceleration inside a pre-formed channel

Starting from the linear theory, described in the previous section, for the longitudinal fields due to pre-formed hollow channels surface linear plasma waves excited by charged particle bunches, we aimed to understand the limit at which the wave breaks for both positron and electron drive bunches.

It was too computationally demanding to make a parameter scan with 3D simulations so instead, we recurred mostly to the 2D, Quasi-3D OSIRIS and the 3D QuickPIC frameworks to do it. For simplicity of the analysis, a pre-formed plasma was used and the ions were initialized as an immobile background uniform positive charge density. The electron and positron drive and witness bunches and plasma parameters were  $n_0 = 10^{17} \text{cm}^{-3}$ ,  $r_c = 40 \mu\text{m}$  ( $\frac{2.4}{k_p}$ ),  $E_{WB} = \frac{m_e c \omega_p}{e} = 30 \text{GV/m}$  and  $\sigma_r = 10 \mu\text{m}$ ,  $\sigma_z = 20 \mu\text{m}$  and charge current normalized value of  $\frac{I_b}{I_A}$  was scanned from 0.0001 to 2, i.e.,  $\frac{n_b}{n_0} = 0.0015$  to 30, where  $I_A = \frac{m_e c^3 \beta_A \gamma_A}{q} \approx \frac{m_e c^3}{q}$ , the symbols  $\beta_A$  and  $\gamma_A$  represent the Álfven speed and corresponding relativistic *Lorentz* factor, respectively.

The results obtained showed that the linear wakefield theory detailed in Sec. 5.1.1, breakdowns when the space charge of the drive beam is such that it overcomes the restoring force that the ions generate on the plasma electrons towards the outside of the channel, making plasma electrons to cross the axis and phase mixing to occur. Relativistic electrons and positrons driven wakes reached the breakdown limit for charge currents ratio of  $\frac{I_b}{I_A} = 0.1$  and 0.2, respectively.

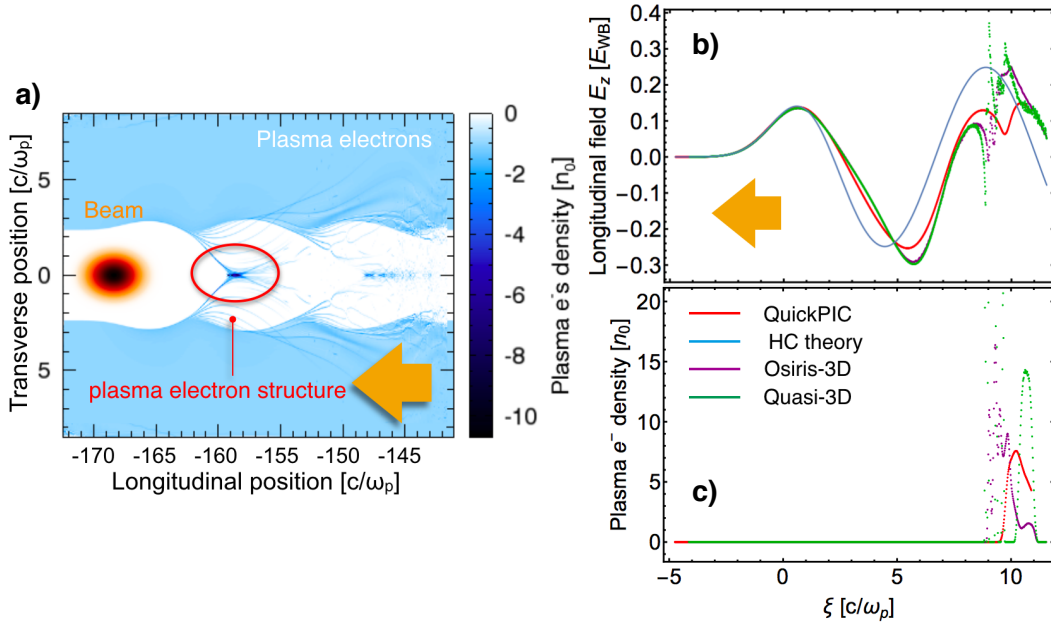


**Figure 5.4:** a) 2D QuickPIC output plot of the plasma electron density perturbed by a drive electron beam propagating towards the left side of the box in a plasma hollow channel b) Longitudinal on-axis accelerating wakefield of that scenario simulated with QuickPIC (red) and 3D (purple) and Quasi-3D (green) OSIRIS codes over the theoretical value according to Eq. (5.2) (blue line). Plot c) shows the on-axis electron density for the same runs. The arrows indicate that in this setup the beam propagation direction was to the left.

To illustrate one of the simulated configurations where breakdown occurred, Figure 5.4 a) has the

2D plot of the plasma electron density showing the creation of an on-axis high density co-moving structure that follows the drive beam, as the electrons that are being attracted to the hollow channel surface plasma ions cross the axis in different regions. Plot b) exhibits the on-axis electric accelerating (and decelerating) field driven in the hollow channel using the different codes in comparison to the linear theory for a bunch number of electrons of  $N_b = 10^7$  and so  $\frac{n_b}{n_0} = 0.003$ . Plot c) further proves that at  $\xi \approx \lambda_p$  behind the drive electron bunch the plasma electrons from the channel cross the propagation axis with extremely high concentrations and at different  $\xi$  positions. For the runs with the positron drive bunch this density spike and phase mixing was verified even for lower bunch densities, because the positrons already start by attracting the electrons to the axis.

Although the breakdown of the linear theory is found for bunches that would still create a linear plasma wake in the typical **PWFA** setup, i.e. despite the wakefields being rather low, the electron co-moving density structure, in the electron driven wake, can be used for focusing the trailing positron bunch. These preliminary results suggest that a trailing positron bunch placed in the region of the structure could be accelerated evenly (leading to a mono-energetic final positron bunch) while being focused by the plasma electrons, more details on this are presented in Chapter **5.2.3.A**. An electron bunch, however, would be defocused. More work is needed to confirm this potentiality of the plasma hollow channel configuration.

## 5.2.2 Positron self-driven plasma hollow channel numerical results

To illustrate the described acceleration mechanism we performed 3D simulations with OSIRIS using the cartesian coordinate system:  $x_1 \times x_2 \times x_3$ , where the indexes 1, 2, 3 indicate the drive bunch propagation ( $z$  as labeled in the previous sections) and transverse directions ( $x, y$ ), respectively. The simulations employed the moving window to follow the relativistic bunch at  $c$ , with normalized grid dimensions of  $15 \times 21 \times 21 \frac{1}{k_p^3}$  filled with  $225 \times 1600 \times 1600$  ( $4.6 \times 10^8$ ) cells, in the longitudinal and transverse directions, respectively. Each cell containing 1 macro particle of the plasma electrons and another of the plasma ions (protons,  $\mathcal{A} = \mathcal{Z} = 1$ ).

The **PHPCWA** configuration used is depicted in Fig. **5.5** a), where a tightly focused cylindrical positron drive bunch (in red) with flat top longitudinal density profile of  $n_b = 200n_0$ , for a length of  $\sigma_1 = 2\pi/k_p \approx \lambda_p$ , and gaussian transverse profile set to have  $\sigma_2 = \sigma_3 = 0.1/k_p$ , goes through an uniform cold plasma of protons (blue) and electrons with density  $n_0$  and length  $1320/k_p$  forming the hollow channel within which a positron trailing witness test bunch of positrons (green), with simulation macro particle density  $n_w = 0.00001n_0$ , is accelerated. The slice of the ion density (blue) and hollow channel (white) at the edge of the simulation box are shown in Fig. **5.5** b).

In Fig. **5.5** c) the solid lines show that the ion radial motion model (green solid line) described above is in good agreement with the simulated results (blue solid line). For this computation the net positive charge acting on the plasma ions was considered to be the average drive positron bunch minus the average negative plasma electron densities evaluated close to the front of the bunch, taken from the simulation results.

The electron density is shown in Fig. **5.6** a) (grey) along with it's lineout (black solid line) and of the

ion density (blue solid line) in the central region of the bubble (dashed line). Inspecting both solid lines allows us to confirm that  $r_b k_p \approx 1.05 > r_c k_p \approx 0.48$  and to determine the slope of the accelerating field given by our model as  $0.4E_0 k_p$  that is shown (green solid line) in Fig. 5.6 b). For the witness bunch positioned according to Fig. 5.5 the estimated peak accelerating field that it will be subject to is then  $0.8E_0$  (considering the center of the bubble at  $\xi k_p = 292$  and the head of the bunch at  $\xi k_p = 294$ ) that corresponds to an accelerating gradient of 7.7 GeV/m for a plasma density of  $10^{16} \text{cm}^{-3}$ . The 2D plot of the accelerating field is also shown in plot b) along with its on-axis lineout (solid black line) that is in good agreement with our model's prediction. The transverse wakefield inside the hollow channel can be seen in plot c) where negligible fields showing a sign reversal. In comparison to the defocusing (for positrons) transverse wakefields found inside the electron beam driven regime bubble. The slightly focusing fields result from a few electrons shooting through the hollow channel. Those focusing fields were not predicted by our model but make this scheme even more appealing for positron bunch acceleration.

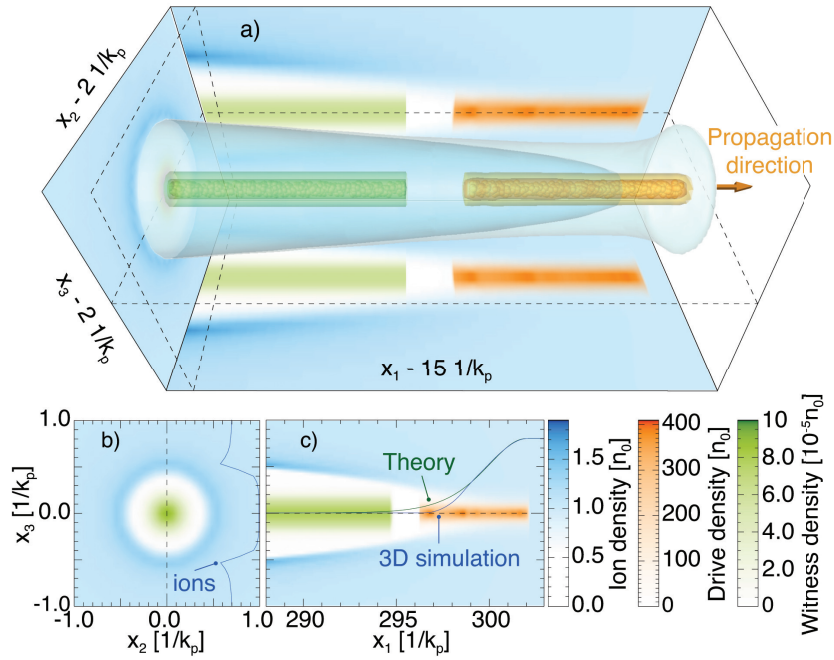


**Figure 5.5:** (a) Scheme of the positron drive bunch (red - to the right) going through the plasma (ions in blue) forming the hollow channel region (white) where a witness positron bunch (green) is accelerated. The arrow indicates the propagation direction. (b) Transverse slice showing the ion (blue) and witness bunch (green) densities superimposed by the lineout of the ion density (blue solid line). (c) Longitudinal slice showing the ion (blue), drive (red) and witness (green) bunches superimposed by the ion density curves from the on-axis lineout of the simulation (blue solid line) and predicted according to our model (green solid line).

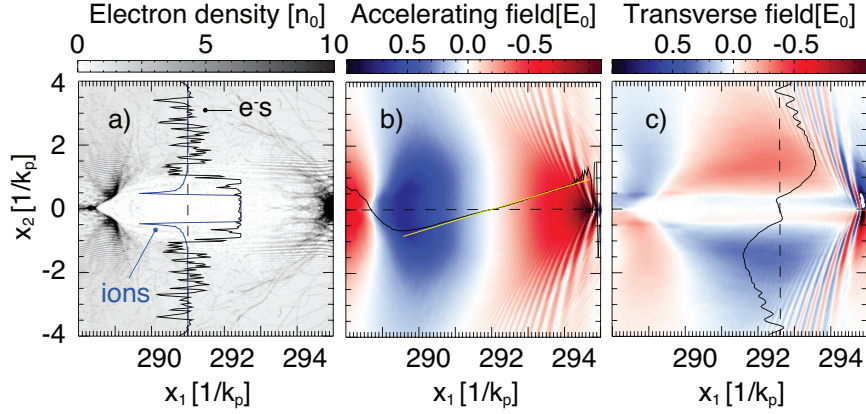


**Figure 5.6:** a) Slice and lineout (black solid line) of electron density showing also the lineout of the ion density (blue solid line). b) Accelerating and c) transverse wakefields plot superimposed by the respective b) longitudinal on-axis and c) transverse lineouts. The wakefield lineouts taken at the bunch axis (a) and in the back of the focusing region (b) are shown (black solid lines). All plots a), b) and c) are zoomed in the region of the hollow channel behind the drive bunch.

Furthermore, our simulations show a stable drive beam propagation into the plasma associated with a stable wake generation and mainly constant accelerating field. This was verified for propagation distances longer than twice the blowout regime betatron wavelength [57]  $\lambda_b = \sqrt{(2\gamma)}2\pi/k_p$ . Hence the simulation trailing bunch after  $2\lambda_b$  (at  $\Delta tck_p \simeq 1320$ ), shown in Fig. 5.7, was accelerated by a rather constant wakefield along the propagation direction, but that was different for each longitudinal slice of the trailing bunch, Fig. 5.6 b). Taking into account the estimated peak accelerating field,  $0.8E_0$ , the predicted energy gain over the acceleration distance of  $1320/k_p$  is of  $0.8 * 1320m_e c^2 \approx 1060m_e c^2$  as can be seen in Fig. 5.7 a) (blue line). This result is well inside the statistical standard deviation (orange shaded region) of the simulation average witness bunch energy variation (green line). In Fig. 5.7 b) the final bunch energy spectrum exhibits a long tail that can be avoided if beam-loading would take place in the acceleration process, i.e., if higher witness bunch initial charge had been used. In the last plot, c), the slice of the plasma ion (blue), drive (red) and witness (green) bunches final density are shown. Note that the witness bunch density increased significantly, comparing to its initial value, but mainly in the region close to the drive bunch where the transverse fields are more intense (see Fig. 5.6 c)). We are currently researching the impact of the highly nonlinear initial fields that arise behind the drive beam, before the ion channel is completely depleted, that prevent the rest of the witness bunch from also being focused in the channel. They can be attributed either to the very high fields and currents established inside the focused drive beam or to very low resolution and particle in cell number that were possible to use in this extremely computationally consuming simulation; or to the unphysical rise time of the longitudinal positron drive bunch profile.

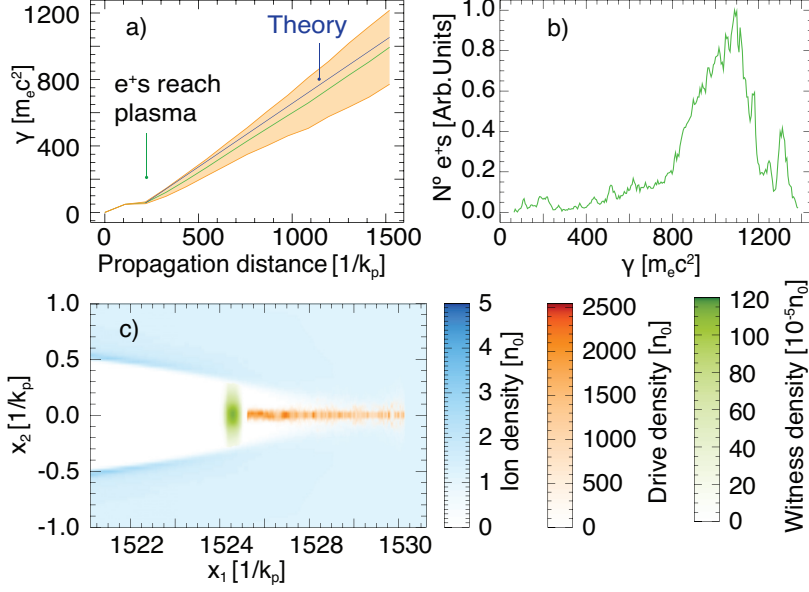


**Figure 5.7:** a) Plot of the average (over more than 30000 particles) witness bunch evolution gain (green line) and corresponding standard deviation region (shaded orange region) overlapped by the theoretical prediction (blue line). b) Final witness bunch spectrum (at  $tck_p \simeq 1520$ ). c) Respective drive (red) and witness (green) bunch densities inside the hollow channel (ion density in blue) in a transverse slice of the 3D simulation.

Additional 2D slab, quasi-3D and cylindrical simulations have been performed in order to analyse the impact of the bunch rise and fall times in the formation of the hollow channel. The bunch longitudinal profiles studied followed the expressions:  $\exp\left(-\frac{\xi-\xi_b}{2\sigma_{z1}^2}\right)$ ,  $\xi > \xi_b$  and  $\exp\left(-\frac{\xi-\xi_b}{2\sigma_{z2}^2}\right)$ ,  $\xi < \xi_b$  for the values of rise time of  $\sigma_{z1}k_p = 0, 0.2, 0.4$  and fall time of  $\sigma_{z2}k_p = 0, 1.75, 3.5$ . We found that, when  $\sigma_{z2}$  is higher than a threshold, for our simulations indicated it was  $2/k_p$ , the trajectory of the electrons intersects the bunch axis in a wide range of  $\xi$ , which led to the vanishing of a clear accelerating structure of the wakefields. On the other hand, we also found that the hollow channel structure is achieved in agreement with our model provided  $\sigma_{z1}k_p \ll 1$ , which represents a rise time that table top accelerators, for example the FACET facility at National Accelerator Laboratory in California (SLAC), can already provide. Additional 3D simulations are needed for the development of more accurate bunch-plasma parameters scaling laws.

Simulations done with laser beams, with normalised vector potentials of  $a_0 = 50$  focused down to  $W_0k_p = 0.1$ , showed plasma electrons and ions excited by the driver beam being repelled, thus generating both the bubble and hollow channel structures. These results still need to undergo a more rigorous analysis. Recurring to the same reasoning as the one we applied previously, when describing our model, we can consider the Lorentz force acting on the ions due to the laser as the ponderomotive force  $\frac{d\vec{p}}{dt} = -\frac{q^2}{2m_i^2}\nabla(\vec{A}^2)$ , where  $\vec{A}$  is the laser vector potential and the other parameters are as introduced previously. The transverse equation of motion can then be transformed, as in the case of a positron drive bunch, to yield:

$$\frac{\partial^2 r}{\partial \xi^2} = \left(2 \frac{a_0}{W_0} \frac{m_e}{m_i}\right)^2 \exp^2\left(-\frac{\tau^2}{\sigma_\tau^2} - \frac{r^2}{W_0^2}\right) r, \quad (5.6)$$

leading to a typical  $k_i = \frac{2a_0m_e}{m_iW_0}$ , where a gaussian profile for the laser was assumed  $A(r, \tau) = A \exp(-\tau^2/\sigma_\tau^2 - r^2/W_0^2)$ , with  $\tau$  duration and  $W_0$  spot size, normalised according to  $a_0 = qA/m_e c =$

$\sqrt{2e^2\lambda_0^2 I/\pi m_e^2 c^5}$  with laser wavelength  $\lambda_0$  and intensity  $I$ . Note that this equation is similar to the one for the positron bunch, Eq. (5.3). As a consequence, conditions for the hollow channel formation in the laser wakefield setup can be described as:  $k_i \xi \approx k_i Z_R \gg 1$  which means  $a_0 \gg m_i \lambda_0 / (2m_e \pi W_0)$ , for the laser spot size  $Z_R = \pi W_0 / \lambda_0$ . The corresponding engineering formula being:  $I [10^{19} \text{W/cm}^2] \gg 1.17 / W_0 [\mu\text{m}]$ , which indicates that table top laser devices could be used to accelerate positrons in our self-driven hollow channel scheme.

The use of a long tightly focused electron drive beam is fundamentally different from both cases explored this far for it radially repels the plasma electrons while attracting the plasma ions leading to their collapse later on and producing the opposite effect as that desired for positron acceleration. If the structure formed would consist of an efficient or optimal scenario for electron acceleration is the object of a future study.

## 5.2.3 Preliminary results and future research directions

### 5.2.3.A Beam loading in hollow channel linear to nonlinear electron wakes

After showing that the channel can be formed and that it processes accelerating fields and transverse fields suitable for positron acceleration, the potential of the PHPCWA mechanism needs the assessment of the maximum positron witness bunch charge that can be injected into it without jeopardizing the control over the channel and acceleration process. The space charge of the trailing witness bunch has its own electric field. When the charge of the bunch is high enough, that field becomes comparable and has significant impact in the plasma wakefields, which were excited by the drive bunch, to which it is super-positioned. By tuning the trailing bunch charge and position, relative to the plasma wake or drive beam, it is possible to balance the bunch fields with the plasma wakefields. Ideally, the balance is chosen so that the total accelerating field that the bunch experiences is uniform along its full length. When this happens the trailing bunch has beam-loaded the plasma wake [158]. In the case of our plasma hollow channel technique the positron trailing bunch can beam-load the wake and so have no energy spread at the end of the acceleration process, as well as no damage to its quality (transverse profile).

In this section we will again recall that the witness bunch, in the self-driven PHPCWA configuration, travels inside the channel structure. The latter is stable enough for its dynamics to be similar to that of a pre-formed channel. For that reason, we now focus on the theoretical approach done for the simpler case, the pre-formed channel setup to understand the witness bunch beam loading effect.

To study the beam loading effect we performed several simulations with the QuickPIC code based in the setup analyzed in [158], in which, the key distinctions are that the drive beam would excite the plasma wake for the trailing beam that was shaped longitudinally like a triangle to beam load. We show the simulation results for the case where the plasma was composed of an immobile ion background with density  $n_0 = 10^{17} \text{cm}^{-3}$ , a completely hollow channel of radius  $r_c = 25 \mu\text{m}$  (i.e.  $2.4 \frac{1}{k_p}$ ), yielding a  $E_{WB}$  of 30 GV/m. The drive and witness bunch were composed of electrons (Fig. 5.8 plot a)) in one run and of positrons in the other (plot b). The drive bunch had  $N_b = 2.8 \times 10^9$ ,  $\sigma_r = 20 \mu\text{m}$ ,  $\sigma_z = 17 \mu\text{m}$  and  $\frac{I_b}{I_A} = 0.35$ ,  $\frac{n_b}{n_0} = 0.53$ . The witness was set as  $N_b = 1.4 \times 10^9$ ,  $\sigma_r = 4.2 \mu\text{m}$ ,  $\sigma_z = 44 \mu\text{m}$ ,  $\frac{I_b}{I_A} = 5.5$

and  $\frac{n_b}{n_0} = 8.25$  and its visible in the bunches density on-axis lineouts (in blue).

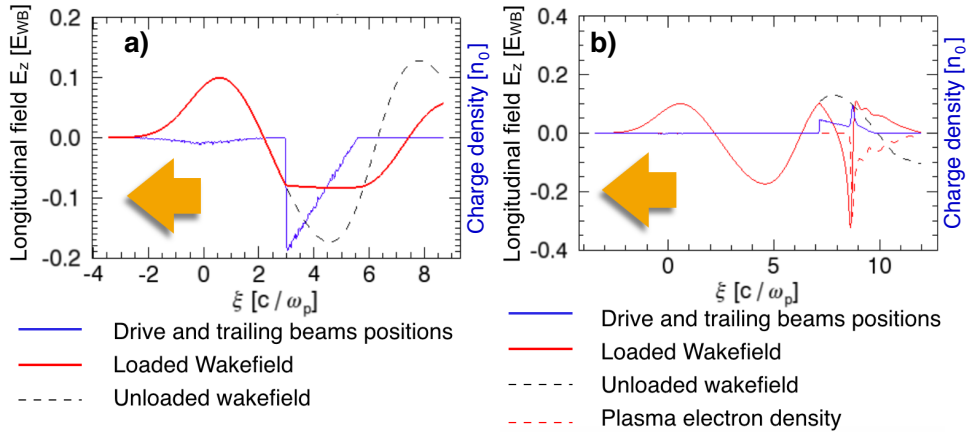


**Figure 5.8:** Plots of the 3D QuickPIC simulations lineout over the propagation axis of the two electron, a), and positron, b), bunches exciting and loading the plasma wake excited in a pre-formed hollow plasma channel (blue lines). Also showing (red lines) the longitudinal accelerating loaded electric field and the field of the drive bunch propagating alone (gray dashed lines). Plot b) also includes the lineout of the plasma electrons (red dashed line).

In Fig. 5.8 a) the on-axis accelerating wakefield (red) driven by the electron drive bunch (charge density in blue) and beam loaded by the electron witness bunch is shown. In Fig. 5.8 b) the witness bunch is a positron bunch and is accelerated in the subsequent bubble of the wake, where it is positioned (blue). In b) the plasma electron density is also plotted (red dashed lines) and it shows a concentration peak that is responsible for the local longitudinal field drop (and sign reversal). This suggests that the maximum positron charge that can be successfully accelerated in a flat field to produce a final mono-energetic bunch, i.e. loading the wake, is lower than the maximum possible electron charge set to trail an electron drive bunch. This is because the high density space charge of the positrons strongly attracts the electrons from the channel surface leading to the quick break of the wake and the formation of the electron structure. The same notion was considered in the numerical analysis of the linear plasma channel wakefield theory, mentioned in the beginning of this chapter. The discrepancy between the electron and positron beam loading processes made us re-derive the properties of the positron witness beam charge for beam loading to occur in the PHPCWA setup. This preliminary results need to be further investigated and explained with an analytical model.

We are currently investigating the potential use of the self-formed channel PHPCWA scheme where the electron density wake is nonlinear and similar to the bubble nonlinear PWFA standard operating regime. Consequently, the plasma electrons only cross the axis behind the bubble and a trailing bunch positioned right behind the tightly focused drive positron bunch can contain high charge before shortening the bubble length in a way that the electrons start crossing the axis within the witness positron bunch, preventing it from beam loading efficiently.

### 5.2.3.B Field mode excitation in the hollow channel by propagating azimuthal modes 0 and 1 electron beam

One remaining question in the beam driven plasma wakefield accelerators that utilize hollow channels is how much impact the typical experimental misalignments have on the outcome. In this section we aim to discuss the effects of a slight asymmetry in the beam shape. Asymmetries in the hollow channel structure or a displacement of the propagation axis of the beam and channel will not take place in the self-driven proposed scenario. In fact, that is one of its important advantages in comparison to the used hollow channel accelerating techniques.

Taking advantage of the Quasi-3D and 3D OSIRIS numerical infrastructures, and the postprocessing tool developed by Thamine Dalichaouch et al. at [UCLA](#) to decompose the 3D run output fields into their first azimuthal  $n$ th harmonic components,  $E(r, \xi\phi) = E(r, \xi) \sim_{n=0}^{\infty} \exp(in\phi)$ , it was possible to study the effect of small transverse bunch initial profile assymetries in the plasma wakefields it generates inside a pre-formed plasma hollow channel structure.

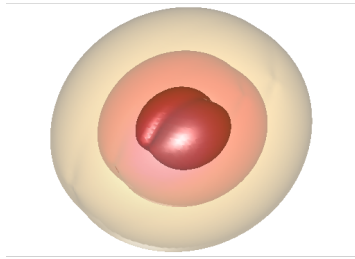


**Figure 5.9:** 3D illustration of the particle density profile composed of the azimuthal modes 0 and 1 in the proportions of 90:10. Darker isosurfaces represent higher electron density.

The simulations modeled the drive electron beam profile, depicted in Fig. [5.9](#), as in the previous sections, but with an additional dependence in  $\phi$  given by the combination of the zeroth and first modes,  $n_b = n_b f(r, \xi) (0.9 + 0.1 \times \exp(i\phi))$ . The number of electrons was changed to excite linear to nonlinear wakes with peak accelerating fields ranging from  $10^{-5}$  to  $0.1 \times E_{WB}$ . The results showed that even after there is phase-mixing and generation of the plasma electron high density trailing structure, the superposition of the decomposed modes is still valid and the excited higher order field modes, for example, 1 to 3, have peak intensities below 1% and 2% of that of the field of mode 0, in the linear and nonlinear runs, respectively.

This preliminary results suggest that the propagation of a beam with only minor asymmetries in the hollow channel will not have significant consequences as the effects on the field will be negligible. This would not be the case if the impact of higher order modes would be greater.

## 5.3 Concluding remarks

We have studied the limits of the linear wakefield excitation theory for positron and electron drive bunches propagating in completely depleted hollow plasma hollow channels that breaks when the

bunch space charge force is sufficient to make the plasma electrons cross the propagation axis. They tend to form a high density long electron co-moving structure that can be used for focusing of trailing positron bunches. The limit is sensitive to the beam current and channel radius, because they both affect the strength of the electron plasma excited fields and is lower for the positively charged drive bunch that attracts the plasma electrons before repelling them away, as the electron bunch does.

A novel positron bunch plasma wakefield configuration was proposed [165] where ion motion was relevant, in which a tightly focused positron bunch excites a pre-ionized uniform cold plasma generating an ion hollow channel and an electron wake associated to high accelerating and vanishing transverse wakefields that are suitable for positron acceleration. We developed an analytical model for this scheme. It was illustrated through a 3D simulation done with the particle in cell code OSIRIS, showing the possibility of attaining and sustaining for more than twice the bunch corresponding betatron distance creating 7.7 GeV/m accelerating gradients inside the hollow channel. 2D simulations were explored to show the robustness of the scheme for bunch fall time profiles no longer than twice the plasma skin depth. Furthermore, the applicability of the technique with laser drive beams instead of the positron bunch was discussed. Additional simulations are still needed to completely understand the nonlinearities of the fields right behind the drive beam that initially disrupt the positron test-particle bunch in the analyzed 3D simulation, with focus in the numerical resolution and return current role in seeding them. A proof-of-principle experiment will be possible with the state-of-the-art laser-positron beam-gas chambers technology, for example available in the SLAC FACET facility provided that the positron bunch is subject to transverse focusing before reaching the uniform plasma.

Trailing bunches beam loading is found to be limited by the breaking of the plasma surface wave and the creation of the electron co-moving structure in the witness bunch. Positron witness bunches are allowed lower total charge than electron bunches if they are to load the accelerating wakefield and produce a final monoenergetic high energy bunch that may be useful for future linear colliders.

Final remarks about the propagation of bunches inside the channels with not perfectly axis symmetric profiles showed that the main field components are (not) still axis symmetric in the linear(nonlinear) pre-formed plasma hollow channel wakefield regimes.



# 6

## Proof-of-principle experiment and numerical investigation of the self-modulation of long lepton beams

### Contents

---

<b>6.1 Self-modulation instability of long particle bunches propagating in plasmas</b> . . .	117
<b>6.2 Experimental setup of the self-modulation of lepton bunches at SLAC - FACET experiment E-209</b> . . . . .	119
<b>6.3 Numerical simulations of the positron acceleration</b> . . . . .	121
<b>6.4 Conclusions</b> . . . . .	129

---

In the previous chapters of this dissertation diverse plasma based wakefield accelerator processes were investigated aiming at the production of more energetic electron beams, hard x-rays and ideal positron bunches for the next-generation linear collider science. This particular chapter, was driven by an additional motivation. Recently the use of short (shorter than  $\lambda_{pe}$ ) dense proton bunches to drive plasma electron density oscillations, wake, in the highly non-linear regime was proposed in the so called Proton Driven Plasma Wakefield Acceleration (PDPWFA). Numerical simulations indicated that high energy proton beams are good candidates for the acceleration, with energy gain beyond 620GeV in a 450m plasma, of a 2.4nC electron bunch [169]. High energy, in the TeV scale, relativistic proton beam sources are already available at the European Organization for Nuclear Research (CERN) Large Hadron Collider (LHC) and Super Proton Synchrotron (SPS) facilities. However, the length of the bunches is much larger than the electron plasma wake wavelength  $\lambda_p$  and compressing them to fit the requirements of the scheme proposed in [169] is challenging. Injecting only a small portion of the beam at the time into the plasma represents significant waste of charge and energy making the whole accelerator concept inefficient and unattractive as an alternative to standard accelerating systems.

Nevertheless, a technique where the entire proton beams provided at CERN undergo the self-modulation instability allows for successful energy transfer from the proton beam to the plasma wake associated Electromagnetic (EM) fields, named the wakefields [38, 170-174]. The wakefields are in turn responsible to accelerate a trailing externally injected witness electron bunch. Moreover, such bunch can have sufficient charge for it to excite its own wake and wakefields in the plasma. By adjusting the electron bunch charge, the accelerating field resulting from the superposition of both wakefields, from the proton and electron bunch, can be made uniform over the full length of the electron beam. Consequently, all electrons from the beam will be accelerated equally and the beam energy spread maintained throughout the acceleration process.

The proton beam self-modulation plasma wakefield acceleration technique is possible to apply with current state-of-the-art lasers and plasmas. In fact, its potential recently led to the proposal and development of the proof-of-principle experiment called Proton Driven Plasma Wakefield Acceleration Experiment (AWAKE) [41, 42] at CERN. AWAKE had its first self-modulated proton plasma wake generation, corroborating the self-modulation wake principle, already in 2016.

The beam self-modulation instability occurs when the plasma background electrostatic equilibrium density is greater than the beam one,  $n_0 > n_b$  and its front generates a linear plasma wake (i.e. with periodic sinusoidal density oscillations) with linear transverse focusing and defocusing wakefields. For beams longer than  $\lambda_p$  those initial linear wakefields are responsible for starting to split the beam into a train of beamlets, distant by  $\approx \lambda_p$ . The direct consequence of the PDPWFA occurring in the self-modulation regime is allowing the beam to resonantly excite the plasma wakefields up to the values reached in the ideal standard nonlinear blowout and bubble regimes [48-52].

By the time I did the work reviewed in this chapter, much progress had already been done in comprehending the self-modulation phenomenon of a few  $\lambda_p$  periods long bunches [38]. In particular, [175] had numerically shown that lepton, i.e. electron and positron, long beams resembling those that were at the time already available at the National Accelerator Laboratory in California (SLAC) Facility

for Advanced Accelerator Experimental Tests (FACET) facility could be used to study the key physics of the self-modulated plasma wakefield accelerator, Self-Modulated Particle beam driven Wakefield Accelerator (SM-PWFA). Therefore, because it was only later that the AWAKE experiment was planned, the first insight of the long particle beam self-modulation mechanism in the plasma accelerator came from the E-209 experiment [39, 175-181] that started in 2013. In the E-209 experiment the self-modulation instability signature was determined with the analysis of the final lepton bunch energy gained and energy lost, the formation and diagnostic of a transverse halo composed by the displaced (defocused) leptons around the central region and by observing the radial modulation period through Coherent Transition Radiation (CTR) interferometry [66, 182].

It is worth mentioning that as part of my PhD program I had the opportunity to participate in the E-209 experiment that took place in the SLAC FACET facility, for which the results are well documented in the previously referenced work and so will not be greatly expanded in this chapter, that led to an enhanced understanding of not only this experiment but also the technologies available for future experimental possibilities and proposals. I also contributed to the numerical investigation of the lepton self-modulation using the Particle-In-Cell (PIC) code OSIRIS [73].

In this chapter a brief introduction to the overall SM-PWFA process is included, Sec. 6.1. The main numerical settings and findings are discussed in Sec. 6.3. The SLAC FACET E-209 experimental layout and results feature in Sec. 6.2. Finally the overall remarks and future orientation of this work, including the AWAKE recent breakthroughs, are summarized in Sec. 6.4.

## 6.1 Self-modulation instability of long particle bunches propagating in plasmas

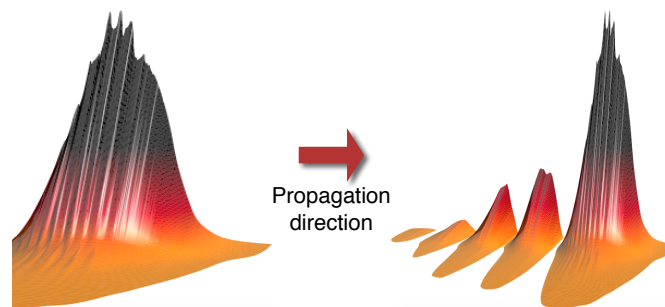


**Figure 6.1:** 3D plots of the initial long drive bunch and the density spikes corresponding to the different beamlets that were generated through the self-modulation instability.

In the radial self-modulation instability the plasma wakefields act to focus and defocus periodic regions of the long particle bunches. As a feedback the resulting bunch charge density then resonantly increases those wakefields. The instability grows until the bunch is completely divided into a train of beamlets, see Fig. 6.1, that is when it saturates. According to [171], the growth rate of the self-modulation instability in the linear plasma wakefield accelerator setup, in the co-moving reference frame is given by:

$$\Gamma_{SMI} \approx \frac{3\sqrt{3}}{4} \left( \frac{n_b}{n_0} (k_p \xi) (k_\beta z)^2 \right)^{1/3}, \quad (6.1)$$

where  $k_\beta = \frac{\omega_p}{c\sqrt{2}\gamma_0} \sqrt{\frac{m_e}{m_b}}$ . Equation 6.1 suggests that SLAC positron and electron bunches will be modulated at identical time scales, whilst the AWAKE heavier protons will take more time to develop the instability. Moreover in parallel to the modulation of the bunch density longitudinal profile the wake phase velocity changes according to  $v_{ph} = v_b \left( 1 - \frac{1}{2} \left( \frac{\xi}{ct} \right)^{1/3} \left( \frac{n_b m}{2n m_b \gamma_0} \right) \right)$  that is independent of the beam charge. The wake phase velocity decreases for beam density close to or higher than the plasma background density.

The previous properties mean that in the linear regime the self-modulation is independent of the sign of the charge of the bunch. In [175], however, the comparison between the SM-PWFA schemes driven by dense electron and positron bunches, with identical properties except for the sign, showed different results for the case when the resonantly increasing wakefields reach nonlinear values before the instability saturated. In fact, it showed lower final accelerating gradients and quicker saturation of the instability for the long drive positron bunch. This is because closer to the nonlinear regime the plasma electrons form bubbles that focus the positron beamlets in narrower regions than the electron beamlets, implying that a greater portion of the positron bunch is lost in the modulation process. It was then clear that a full understanding of the differences due to the sign of the beam charge in the self-modulation technique, in mildly to nonlinear regimes, was needed. The SLAC/FACET E-209 experiment and respective simulation investigations were done aiming to explore just that, before the CERN/AWAKE experiment, using the positively charged proton bunch, would be built.

Moreover, [38] showed that in the SM-PWFA the self-modulation instability competes with the hosing instability, with both growing from noise. Hosing occurs when the transverse centroid of a certain portion of the beam becomes slightly off-axis, say at  $x_{bi} = x_{off1}$ , relative to the whole plasma bubble,  $r_{pi} = 0$ . The feedback of the plasma is to try to re-focus the beam back to the main axis, at  $x_{bf} = 0$ . But, while off the axis, the beam is exciting the plasma section from that region, you may think of it as a ring of plasma electrons, also off of the main axis, to  $x_{pf} = x_{off2}$ . Therefore, the on axis beam,  $r_{bf}$ , will still be off-centered with respect to the off axis plasma ring,  $x_{pf}$ . The transverse displacement between that portion of the beam and the ring of the bubble electrons grows continuously disrupting most of the beam. It is then straightforward that if hosing occurs before the self-modulation saturates, then the beam charge becomes unable to resonantly excite the plasma wakefields required for acceleration.

An ideal self-modulated scenario then needs an initial seeding of the self-modulation instability so that it saturates faster than hosing can disrupt the beam. Through numerical simulations inspired from the SLAC/FACET like parameters [175, 176] different beam longitudinal and transverse profiles, and in particular front shapes connected to its rise times, were studied. The effective seeding of the self-modulation was found when the front of the drive long particle bunch has a longitudinal sharp rise time. In Fig. 6.2 you can see the illustration of the case with competing instabilities, a), and the one where hosing is mitigated by successfully seeding self-modulation, b).

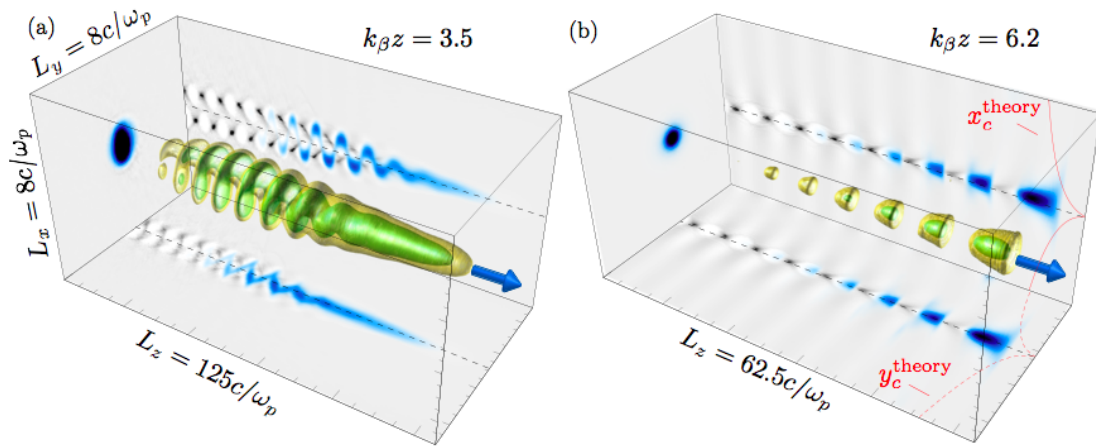


**Figure 6.2:** 3D plots from the simulations, showing the cork screw like shaped beam resulting from the leveled competition of the self-modulation and hosing instabilities a), and showing the completely self-modulated, axis symmetric, final bunch resulting from a similar setup as in a) but with a sharp bunch front [176].

During the runs of the E-209 experiment, the **SLAC FACET** facility delivered lepton beams with shapes that were not sharp enough to facilitate the complete elimination of the possibility of the growth of the competing hosing instability.

Moreover, numerical studies were also employed to the investigation of the effect of the plasma profile in electron beams up to  $10\lambda_p$  long, that undergo the self-modulation instability. The focus of the studies was in scenarios where the plasma cylindrical radial size was narrower or of the same order as the beam radius and where the transverse plasma profile was not homogeneous. In [174], it was shown that narrow, finite, plasmas led to stronger focusing fields being excited, which, in turn, resulted in higher growth rates of the instability.

## 6.2 Experimental setup of the self-modulation of lepton bunches at SLAC - FACET experiment E-209

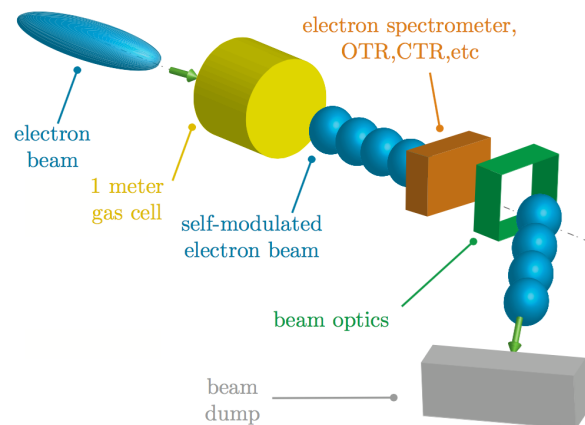


**Figure 6.3:** 3D sketch of the experimental configuration used at **SLAC**'s FACET facility in the E-209 plasma (yellow cylinder) wakefield drive lepton bunch (blue oval shape) undergoing self-modulation instability (resulting in the train of blue spheres) investigation.

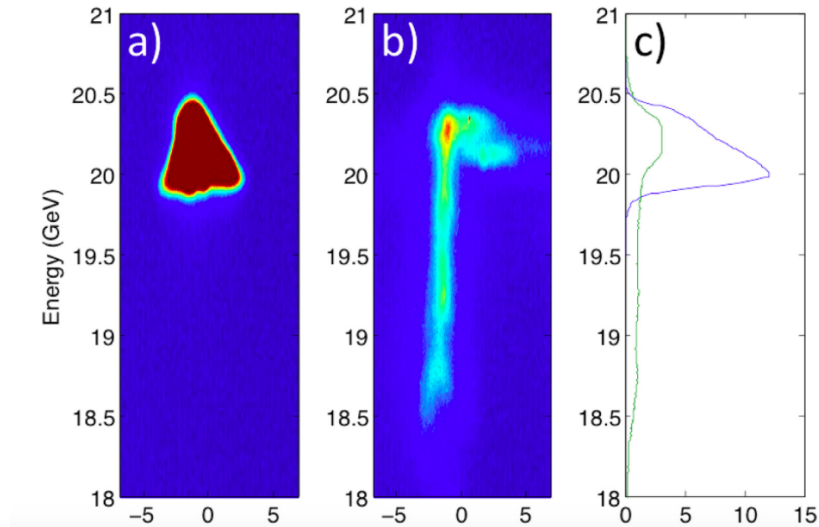


**Figure 6.4:** Experimental spectrum of the bunch electrons dispersed by a magnet, in one of the transverse directions, according to their energy (transverse axis) in two shots: a) without plasma, i.e. without the laser pulse to pre-ionize the plasma being sent into the chamber, and b) with the plasma. c) shows the respective integrated value for the two scenarios, without plasma (green line) and with (blue). These results were presented in [181].

The E-209 experiment held at the SLAC FACET facility was conceived to test the fundamental physical principles of the self-modulation instability. Its design [175, 178], sketched in Fig. 6.3, included a laser system focused at the entrance of the Argon (or in the experimental runs of 2014 Hydrogen) chambers to pre-ionize a long plasma cylindrical channel, that was inspected through scans of the ion recombination emitted light.

After the long particle bunch, of electrons or positrons, was injected into the plasma, its self-modulation was measured through three diagnostics. In the first one, the bunch final energy was determined with an imaging magnetic spectrometer, aiming to show the gain of accelerated electrons and the loss of those that contributed to the wake formation, see Fig. 6.4 for an example of the results obtained. The tail of electrons that lost up to 2 GeV of their initial energy, which would occur when exciting the plasma wake, is evident when the the electron bunch does pass through a plasma.

In the second diagnostic Optical Transition Radiation signals were captured in two interaction points, close to where the bunch reached the plasma gas chamber and after it. They were done in order to determine the shape of the transverse halo cloud formed around the final bunch by the defocused particles, that originated from the portions of the beam in the defocusing regions of the plasma wakefields, Fig. 6.5 includes some of the most clear results. It is clear that the beam profile does not change significantly in the absence of the ionized plasma in its trajectory. However when the plasma is present by the laser, the figures show a clear halo and a more confined higher density region, which is due to the transverse focusing of the modulated bunchlets by the wakefields.

The last diagnostic used consisted of an interferometry pyro camera measurements of the CTR produced by the bunch as it passes through a titanium foil. The radiation emitted is auto-correlated and because it scales with the charge of the beam (squared since the measurement is coherent and made on the radiation intensity) it carries the information on its final modulated longitudinal profile. The Fast Fourier Transform algorithm (FFT) of that signal was expected to highlight the longitudinal

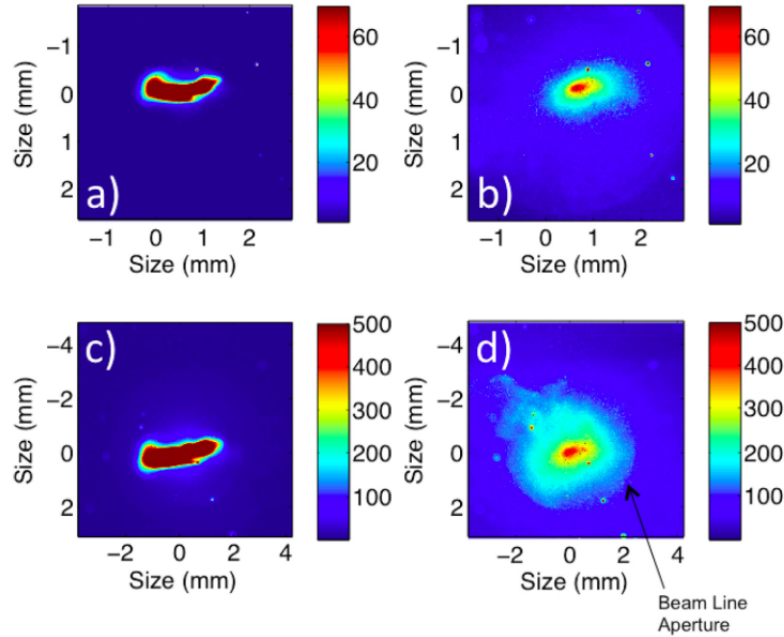


**Figure 6.5:** Plots of the experimental results from shots where the plasma was not ionized by the laser, a) and c) and when it was, b) and d) for two positions in the electron bunch propagation direction: close to the gas chamber entrance, a) and b) and afterwards, c) and d). These results can also be found in [181].

periodicity of the electron bunchlets, through peaks spaced by  $\approx \lambda_p$  harmonics. In Fig. 6.6 one of the signals with strongest peaks achieved is plotted. In b), in the FFT of the electron beam signal when the plasma was pre-ionized different peaks can be spotted that were close to the plasma wake wavelength,  $\lambda_p = 118\mu\text{m}$ .

In the next section the comparison between the electron and positron bunch will discuss the experimental results for the runs with positron bunches. Those runs yielded less clear and consistent signals, for this reason not included here, than the ones performed with electron bunches.

Despite the fact that the realistic bunch shape that allowed hosing instability to occur and thus precluded stronger self-modulation evidence in the results and also the technological challenges of the gas chamber and laser system used, the experimental results, corroborated by the simulation work presented in the next section, were sufficient to drive our community towards the development of the AWAKE long self-modulated proton driven plasma wakefield acceleration of electrons experiment held at CERN.

### 6.3 Numerical simulations of the positron acceleration

The goal of the first set of simulations was to model the first run (2013) of the SLAC FACET E-209 experiment. They were performed in 2D-cylindrical coordinates using a computational box of  $940 \times 380\mu\text{m}^2$  divided into  $1010 \times 425$  cells with  $2 \times 2$  plasma and bunch particles per cell. A 20GeV electron bunch with  $1.9 \times 10^{10}$  particles was considered.

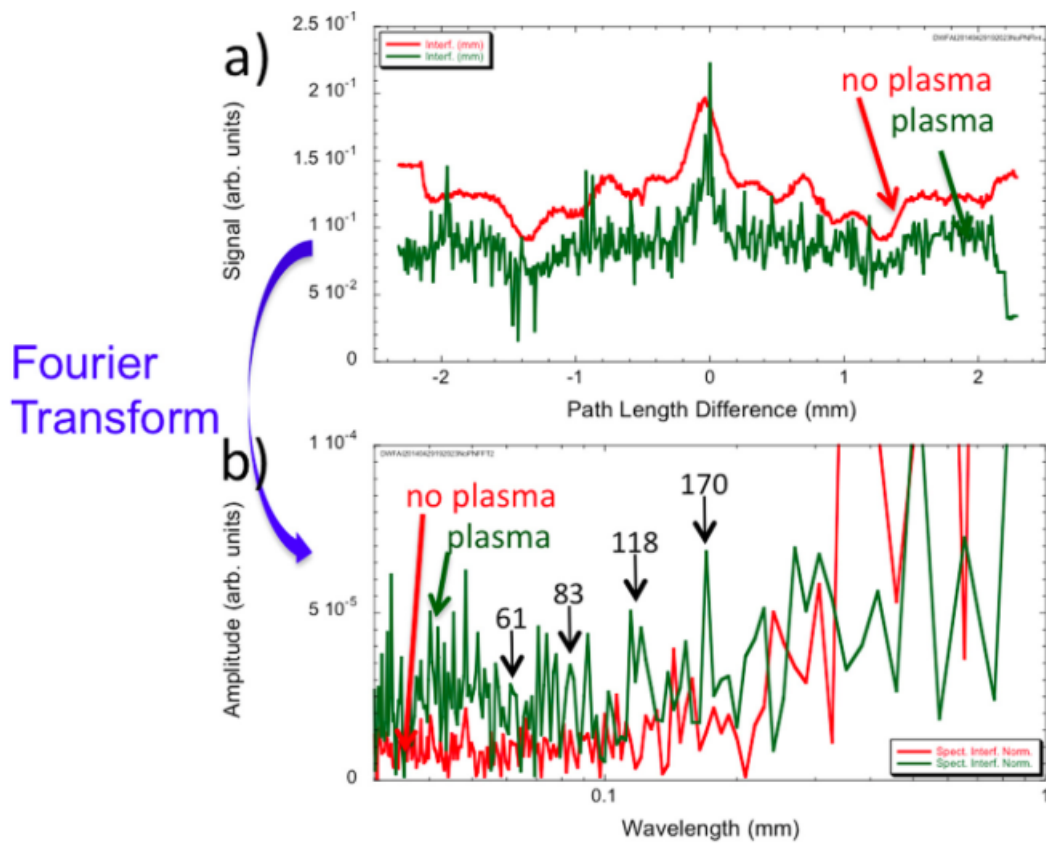


**Figure 6.6:** Experimental a) signal captured through the CTR technique for shots where the plasma was not ionized (red line) and when it was (green line). b) FFT of the signals in a) with evidence of the electron bunch longitudinal modulation, at different wavelengths, in the case where it goes through a plasma [181].

### 6.3.1 Long lepton beams and plasma configuration

The longitudinal electron bunch profile, shown in Fig. 6.7, closely followed the experimental profile and was described by:

$$\frac{n_b}{n_{b0}} = \left[ 2 \exp\left(-\frac{(z - z_1)^2}{2\sigma_{z1}^2}\right) + \exp\left(-\frac{(z - z_2)^2}{2\sigma_{z2}^2}\right) \right] \exp\left(-\frac{r^2}{2\sigma_r^2}\right) \quad (6.2)$$

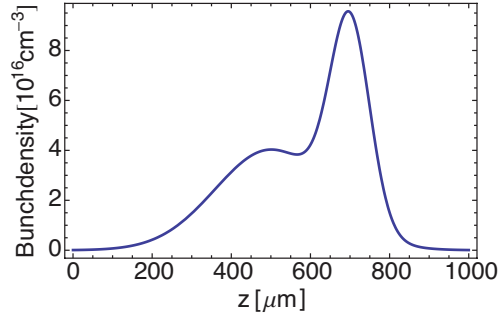


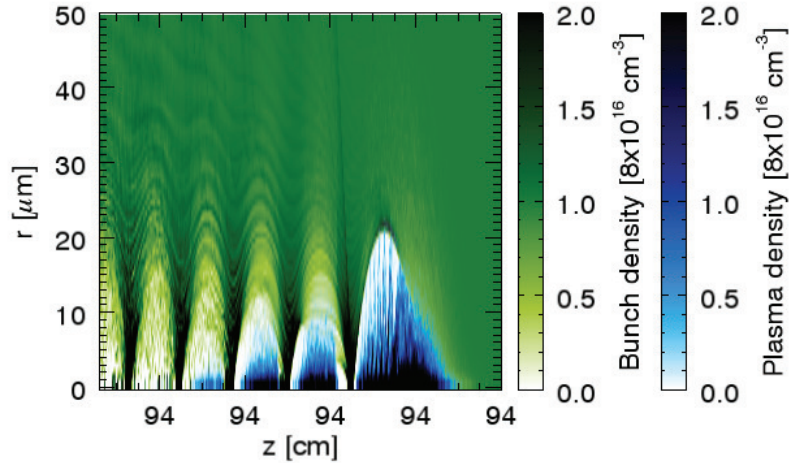
Figure 6.7: Initial electron bunch profile as given by Eq. 6.2

Table 6.1: Values of the parameters of the profile specified in Eq. 6.2 used in the simulation.

$\sigma_{z1}$	$\sigma_{z2}$	$\sigma_r$	$z_1$	$z_2$
$50\mu\text{m}$	$140\mu\text{m}$	$30\mu\text{m}$	$700\mu\text{m}$	$500\mu\text{m}$
$2.7\lambda_{pe}$	$7.5\lambda_{pe}$	$1.5\lambda_{pe}$	$37.2\lambda_{pe}$	$26.6\lambda_{pe}$

The parameters explored in these simulations can be found in Table 6.1. The peak bunch density used in the simulations is  $n_{b0} = 6.4 \times 10^{15} \text{cm}^{-3}$ , which is much lower than the initial uniform background electron plasma density  $n_{p0} = 8 \times 10^{16} \approx 12.5 n_{b0}$ . The plasma wavelength is  $118\mu\text{m}$ . The bunch total length is of about  $500 - 600\mu\text{m} \approx 4\lambda_{pe} - 5\lambda_{pe}$ , thus it is sufficient for self-modulation to occur. The simulated plasma total length is 1m.

The simulations used a moving window traveling at the speed of light,  $c$ , moving in the direction of the beam. Figure 6.8 shows the self-modulated electron (blue) and plasma (green) density at the end of the simulation. The direction of propagation is to the right of the plot. The wake bubbles can be seen in Fig. 6.8 as well as the four self-modulated bunches that fit inside those bubbles.



**Figure 6.8:** Final electron bunch (blue) and plasma densities (green). Color scales represent densities normalized to  $n_0$ .

From this result, the plots shown in Fig. 6.6 can be better understood. Simulations show that portions of the bunch propagating in the defocusing field regions are pushed away from the propagation axis, leading to the formation of the observed halo. The portions that remain in the focusing regions, bunchlets, are focused towards the axis, reaching almost twice the initial concentration value, while the overall bunch propagated in the plasma. In other words the bunch does become self-modulated through the SMI into a train of narrow bunchlets.

The evolution of the accelerating wakefield as a function of the propagation distance can be found in Fig. 6.9. It follows the curves found in SMI numerical studies [39, 175, 177–179]. The SMI grows and saturates over the first  $\approx 5$  cm of the electron bunch propagation in the plasma, reaching maximum accelerating field values close to 20 GeV. After the saturation of the SMI the fields decrease slightly by  $\approx 5$  GV/m and remain approximately constant ( $15 \pm 2$  GV/m) during the remainder of the propagation in the 1 m long plasma.

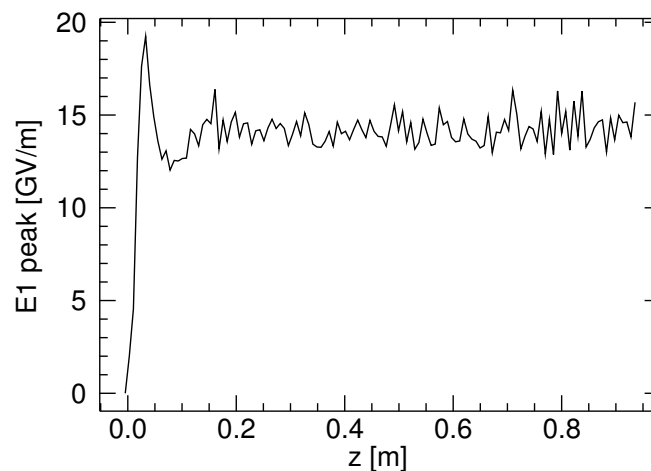


**Figure 6.9:** Evolution of the accelerating wakefield as a function of the propagation distance near the axis at  $r = 0.75 \mu\text{m}$ .

Note that the wave breaking field is  $E_0 = m_e c \omega_{pe} / e \approx 27 \text{GV/m}$ . Thus, wake excitation in this simulation occurred in the mildly non linear regime when the accelerating peak field almost reaches the wave breaking limit. Although the initial bunch had a charge density many times lower than the plasma background density after it underwent self-modulation and transformed into the train of beamlets, it resonantly excited higher accelerating wakefields. This is how long low density bunches can excite plasma wakes with high acceleration gradients almost in the nonlinear regime.

The final electron bunch energy spectrum is shown in Fig. 6.10. The two peaks that can be seen in the spectrum are the initial bunch energy 20GeV and the final energy of most of the decelerated particles at 16GeV. The energy gain/loss by the beam electrons ( $\approx 5 \text{GeV}$ ) is lower than what could be expected from Fig. 6.9 which indicates maximum wakefields that would lead to acceleration in the order of the 15GeV/m. This is because the bunch particles do not propagate solely nor constantly in the regions of maximum accelerating wakefields [174]. Do note that the experimental proof, shown in the previous section, indicated a energy loss of up to only 2GeV which is even lower than this result, possibly because 2D-cylindrical simulations do not account for the occurrence of the competing hosing instability.

Simulations with the same parameters, but with positron bunches, lead to accelerating wakefields with similar evolution but with half the accelerating field amplitudes. The final modulated bunches are shorter and narrower (see Fig. 6.11), which indicates that the experimental analysis of the positron bunch self-modulation can be more challenging than the first run of the E-209. The energy spectrum ranges from the 17 to 22 GeV with a central peak-like region at 19.6GeV.

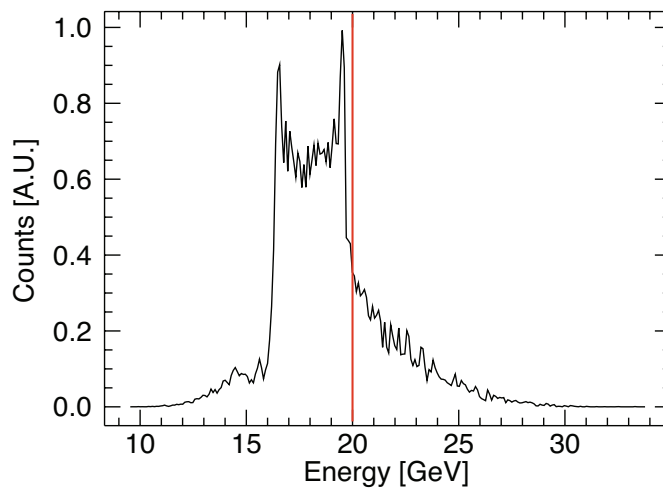


**Figure 6.10:** Energy spectrum showing the energy variation after the propagation in the plasma relative to the initial 20GeV of the initial electron bunch.

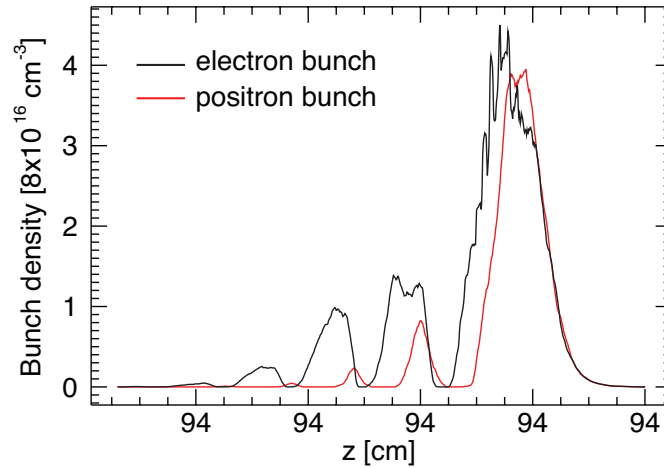


**Figure 6.11:** Comparison of the final self-modulated electron (black) and positron (red) bunches.

The subsequent experimental run was done with a different plasma chamber but, most importantly, a different lepton bunch longitudinal profile, similar to that depicted by Fig. 6.12. Because the bunch profile is a crucial parameter in the mitigation of hosing a new simulation was performed and analyzed for both an electron and a positron bunch. The different simulation scenario sent 20 GeV lepton bunches with  $\sigma_r = 40\mu\text{m}$  and beam normalized emittance ranging from 3-30 mm.mrad to a, not fully ionized, pre-formed  $\text{Ar}^{18+}$  plasma with density  $n_0 = 8 \times 10^{16}$  ( $E_{WB} = 27\text{GV/m}$ ).

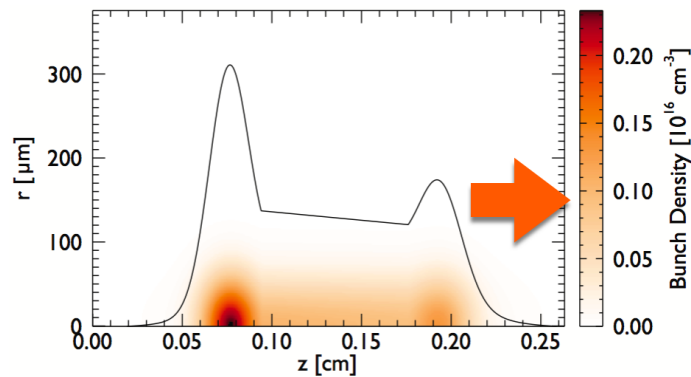


**Figure 6.12:** 2D Radial and longitudinal density profile of the lepton bunch available at the SLAC E-209 experiment, propagating in the direction of the red arrow, the opposite direction as the one of Fig. 6.7. Black solid line represents the on-axis ( $r = 0$ ) profile.

The qualitative results found were critically different because the initialized bunch rise time was much longer than in the previous analysis and the bulk of the charge was now in the modulated, i.e. focused and defocused, instead of front, part of the bunch. For this reason the accelerating wakefields saturated below 3 GV/m. The use of a sharp rise time cutting through the correct front part of the bunch would enable fields to saturate at about 12 GV/m and energy gain and loss of up to 1.5 GeV by the bunch particles. Although in a more linear regime, in this setup the electron and positron final completely modulated bunches differed in total charge by up to 36% and the greater difference in the trailing beamlets that almost vanish, in the run with the positron bunch, see Fig 6.13. These results

can explain why in the experiment the diagnostics for the runs where the positron bunches were sent into the plasma were less clear than for those with electron bunches.

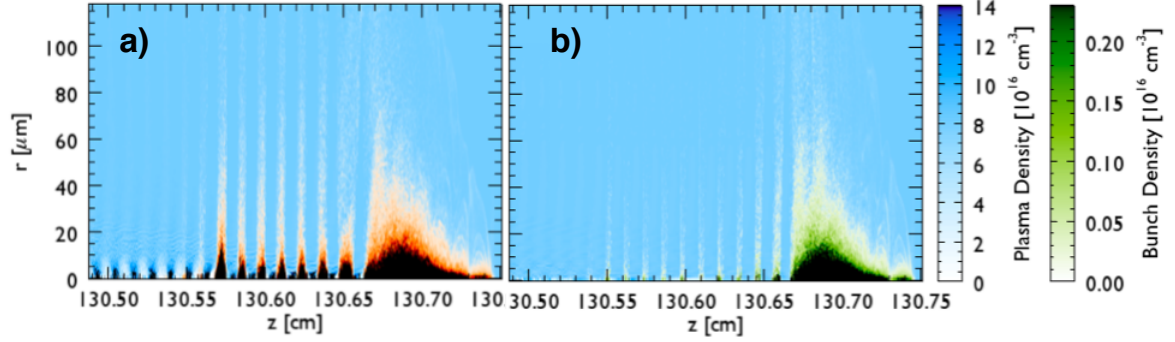


**Figure 6.13:** Density plot of the self-modulated electron bunch (red - a) and positron bunch (green - b) and plasma wake density fluctuations (blue).

To have a better insight over the expected experimental **CTR** diagnostic results for this run, the Poynting flux of the final lepton bunch leaving the simulation box signals produced by the electrons, positrons and sharp rise time ideal electron profile bunch are plotted in Fig. 6.14. It suggests that capturing the modulated beamlets longitudinal frequency for the positron bunch (that nearly vanished) will be challenging.

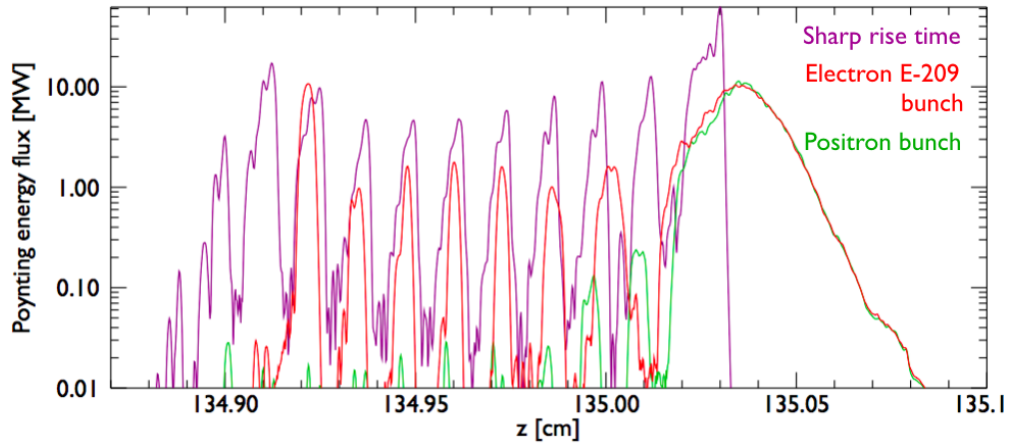


**Figure 6.14:** Poynting flux over radially integrated the final self-modulated E-209 inspired electron (red), positron (green) and sharp rise time electron (purple) bunches in Logarithmic scale.

In the context of determining the charge sign impact on the self-modulation of the beams propagating in plasmas, it is relevant to mention that the scenarios explored in [174], i.e.  $\sim 10\lambda_p$  electron beams propagating in radially finite plasma profiles, were simulated also with the **PIC** code OSIRIS also for positron bunches, in 2D-cylindrical geometry. The conclusions drawn in [174] regarding the higher growth rate of the self-modulation instability being found for narrower plasmas were found also for positron beams.

For simplicity, only two sets of the simulated scenarios will be discussed here. The first configuration used a plasma with  $n_0 = 4.85 \times 10^{15} \text{ cm}^{-3}$  and a transverse flat top profile ending in the radial position of  $R_p = 180\mu$  or  $500\mu\text{m}$ . The electron and positron 58.3MeV bunches had densi-

ties of  $n_{b0} = 7.2 \times 10^{13} \text{cm}^{-3}$  which translated into  $n_{b0} \approx 0.015n_0$ , longitudinal profiles of lengths  $960 \mu\text{m}$ , gaussian transverse profiles with standard deviation  $120 \mu\text{m}$  and normalized emittances of  $13 \text{mm-mrad}$ . The peak of the accelerating wakefields found for those electron and positron bunches scenarios, taken from a longitudinal lineout at a radius of  $r = 19 \mu\text{m}$  at each time step, runs evolved according to Fig. 6.15.

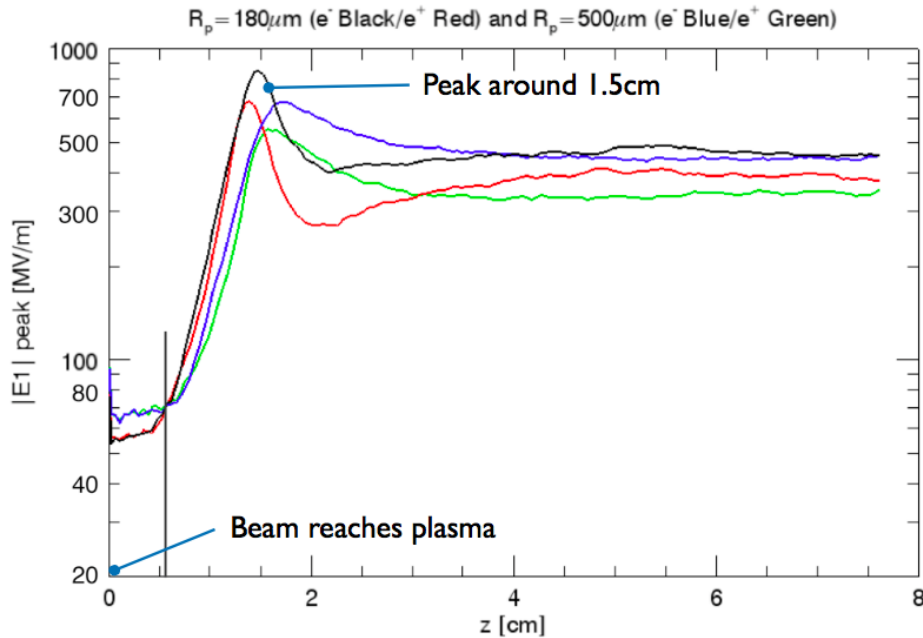


**Figure 6.15:** Evolution of the longitudinal wakefield of electron and positron bunches excited in plasmas with transverse flat top densities up to  $R_p = 180 \mu\text{m}$  (electrons black / positrons red) and  $500 \mu\text{m}$  (electrons blue / positrons green) along the propagation direction. The black/red solid lines correspond to a less linear case of the plasma wakefield self-modulation regime, with  $n_{b0} \approx 0.015n_0$ . Refer to main text for the other parameters of these simulations.

The differences pointed out in the analysis carried out this far hold true also for narrower plasmas, as can be seen in Fig. 6.15. The accelerating field reached higher values for the electron beams. In the case of the narrower plasma (black/red solid lines) the fields excited show higher peaks, saturate before and still evolve, after the peak, for a longer acceleration distance, than in the other one (blue/green lines). The same lineouts were also taken further away from the propagation axis to prove transverse consistency of the results. At a radius of  $r = 19 \mu\text{m}$ , showed lower field values but very similar comparison between electron and positron bunches and the two plasma profiles, see Fig. 6.16.

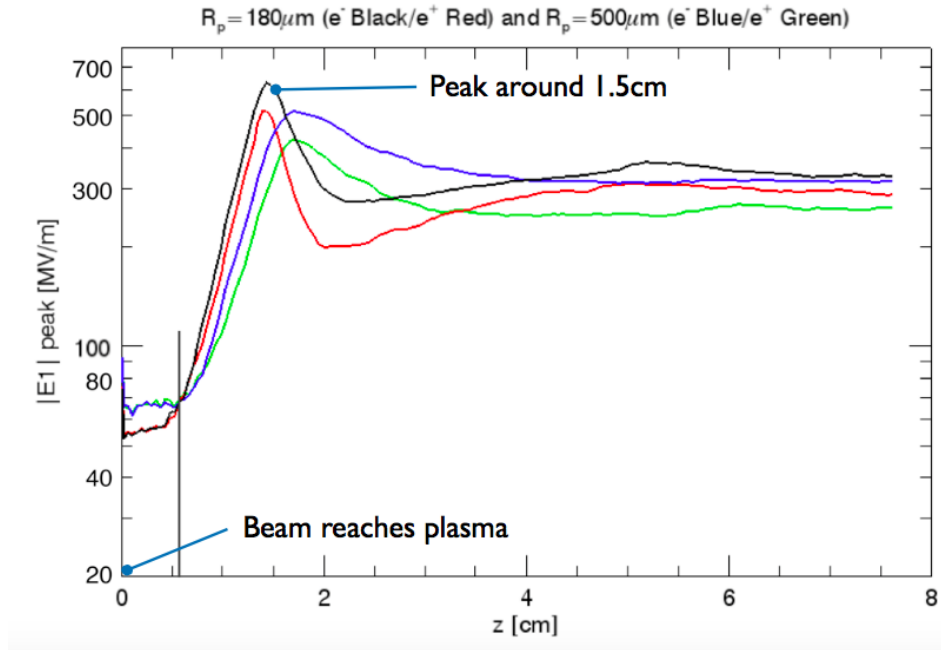


Figure 6.16: Same plot as in Fig. 6.15 but taken at  $r = 19 \mu\text{m}$  away from the axis.

## 6.4 Conclusions

The work on this chapter has shown that the electron beam configuration (length higher than 4-5 plasma wavelengths) used in the E-209 experiment at SLAC undergoes the self-modulation instability with a saturated state in the mildly non linear plasma wakefield acceleration regime. We found that within the first 5 cm of propagation, the SMI leads to a train of four self-modulated bunches separated by  $\lambda_p$  that resonantly drive GV/m wakefields. The self-modulation saturates the bunch propagated 5cm leading to stable accelerating wakefields about 3GV/m. The final bunch electrons energy spectrum showed energy gain and loss with up to 1.5 GeV tails. The same setup depletes most of the positron bunch. The signatures of the instability would have been clearer if the bunch had a sharp rise time longitudinal profile.



# 7

## **Conclusions and Future Work**

The present dissertation includes the most relevant numerical and experimental investigation results of the work that I carried out during the period of my PhD course.

Firstly, the effect of direct laser acceleration inside a plasma bubble with uniform background ions and void of plasma electrons for different laser pulse configurations was studied, for different laser configurations, through OSIRIS 3D simulations and experiments that were done at University of California Los Angeles (UCLA). The numerical study showed signatures of the accelerating process, in which the transverse field of the laser gives transverse momentum to trapped relativistic electrons and is transformed into longitudinal energy gain by the magnetic field. Mainly the final accelerated electrons ellipsoidal transverse profile, the higher energies than in the standard bubble nonlinear regime attained, the creation of a fork profile in the highest energy part of their transverse spectra in the laser polarization direction and in the energy and spectrum of the radiation emitted. These were used to corroborate the experimental results and attest the participation of the direct laser acceleration mechanism in the explored setup. The most important next step in this investigation is to confirm the hypothesis that the central peak in the dispersed electron spectra is due to electrons being trapped in subsequent bubbles of the plasma, that are not overlapped by the laser so those electrons are accelerated by the plasma wakefields only.

A second part of the work involved the usage of a long laser pulse available in the Lawrence Livermore National Laboratory (LLNL) National Ignition Facility (NIF) facility to generate hard x-rays was discussed. A 2D Osiris simulation was executed and discussed in which the laser front self-focuses and the central portion of the pulse suffers nonlinear effects that lead to its disruption and to the generation of plasma wakes off-axis, in an effect that is similar to a hosing like instability, while the back of the laser self-channels through the plasma ions generating a cavity where electrons can be trapped and directly accelerated by the laser. The experiment measured significant x-ray emission that was more closely reproduced by the simulation done with a laser normalized strength of  $a_0 = 3$  than the results of our simulation that used  $a_0 = 2$ . It is important to carry out this study to understand the unknown processes that are responsible for the disruption of the laser pulse peak region in this nonlinear self-modulation regime.

A, not related, novel tightly focused positron driven self-channeling plasma wakefield configuration was also proposed. It was validated and characterized by an analytical model corroborated by 3D and 2D simulations performed with the OSIRIS and QuickPIC Particle-In-Cell (PIC) codes. The channel provides the means of accelerating trailing positrons without jeopardizing their emittance as the transverse forces are reduced. The additional advantages of this structure include allowing nonlinear accelerating gradients to be sustained in the channel and the absence of neutral particles in the channel. In the future it will be interesting to set an upper limit to positron charge that can be loaded as a trailing bunch for reducing accelerated beam energy spread without jeopardizing its quality.

Lastly, this document includes an overview of the numerical results found for the National Accelerator Laboratory in California (SLAC) FACET E-209 long lepton beam plasma wakefield self-modulation instability experiment done at SLAC. These results were the first evidence of the self-modulation of long particle beams and depended on the particle charge sign. In fact, in the experiment and

simulations, stronger accelerating wakefields were found for the modulated electron bunch than the positron bunch. The need for the sharp rise time longitudinal profile of the bunches was evident in the challenge of producing significant signatures to be measured in the experiment. The ongoing AWAKE experiment at CERN has shed some new light into the self-modulation phenomena. Currently the greatest obstacle being addressed is controlling particle beam injection to use that phenomena for beam acceleration.



# 8

## **Appendix: State of the art laser and x-ray sources**

Different institutions are pursuing the path towards laser pulse short duration and high intensity/power optimization for applications like the ones mentioned in this chapter: in molecular, biomedical and material sciences; UV and x-ray generation; plasma physics and laboratory astrophysics; high-energy-density physics and particle acceleration. Table 8.2 contains the laser pulse peak power,  $P_L$ , energy  $En_L$ , duration  $\tau_L$  and operating repetition rate,  $R_L$ , that are planned (P), commissioning (C), or already operational (OP) for some of the recent laser technologies [183] of international facilities like the European Union's Extreme Light Infrastructure (ELI) sources and Gas High Harmonic Generation (GHHG), the Brookhaven National Laboratory (BNL) Accelerator Test Facility (ATF) CO<sub>2</sub> laser beamline, the Science & Technology Facilities Council Central Laser Facility (CLF) high power lasers, the X-Ray Laser Project XFEL, the European Laboratory for Non-Linear Spectroscopy (LaserLab); the Linac Coherent Light Source (LCLS) at National Accelerator Laboratory in California (SLAC); Helmholtz- Zentrum Dresden-Rossendorf (HZDR)'s ELBE center for high power radiation sources; Deutsches Elektronen-Synchrotron (DESY)'s Free-Electron LASer in Hamburg (FLASH) and synchrotron radiation source PETRA; Multidisciplinary research centre Elettra Sincrotrone Trieste (ELETTRA)'s FERMI; France's Laboratoire pour l'Utilisation des Lasers Intenses (LULI); USA's Berkeley Lab Laser Accelerator (BELLA); Japan's National Institute for Quantum and Radiological Science and Technology (QST) lasers and SPring-8 Angstrom Compact Free Electron Laser (SACLA) at RIKEN.

**Table 8.1:** Laser pulses peak power and energy from worldwide state-of-the-art infrastructures.

System	State	Location	Source	$P_L$	$En_L$	$\tau_L$	$R_L$
ELI Beamlines	P - 2018	Czech Republic	L1	~ TW	100 mJ	20 fs	1 kHz
			L2	~ TW	2/20 J	15 fs	10 Hz
			L3	~ TW	1/30 J	20 fs	10 Hz
			L4	1 PW 10 PW	150 J 1.8 kJ	150 fs 5 ns	-
ELI-ALPS	P-2017	Hungary	SYLOS	4.5 TW	45 mJ	10 fs	1 kHz
			HR1	100 W	1 mJ	6.2 fs	100 kHz
	P-2018		HFPW	2 PW	34 J	17 fs	10 Hz
	OP		MIR	15 W	150 $\mu$ J	150 fs	100 kHz
ELI-NP	P-2018	Romania	GBS	-	-	0.7/1.5 ps	100 Hz
	OP		HPLS	10 PW	150/250 J	15/25 fs	60 Hz
HZDR ELBE	C	Germany	DRACO	~ PW	30 J	30 fs	1 Hz
				150 TW	4.5 J	30 fs	10 Hz

**Table 8.2:** Laser pulses peak power and energy from worldwide state-of-the-art infrastructures (part II).

Berkeley	OP	USA	BELLA	1 PW	40 J	30 fs	1 Hz
SLAC	P-2020	USA	LCLS II	-	mJ	~ fs	120 Hz
				20 W	-	~ fs	~ MHz
LULI	OP	France	LULI2000	150 TW	100 J	1 ps	4 per day
			ELFIE	-	50 J	0.6 ns	1 mHz
RIKEN	OP	Japan	SACLA	10 GW	0.5 mJ	20-30 fs	10 Hz
QST	OP	Japan	J-KAREN-P	0.3 PW	~ 50 J	30 fs	0.1 Hz
			QUADRA-T	10 W	10 mJ	1.3 ps	1 kHz
DESY	OP	Germany	FLASH I	-	10 mJ	60 fs	10 Hz
				-	20 $\mu$ J	100 fs	1 MHz
EU	C	Germany	XFEL	-	-	100 fs	27 kHz
ELETTRA	OP	Italy	FERMI	~ GW	100 $\mu$ J	100 fs	10 Hz
BNL	OP	USA	ATF	TW	5 J	3 - 5 ps	20 - 500 Hz
CLF		UK	Astra-Gemini	0.5 PW	15 J	40 fs	0.05 Hz
	OP		Gemini	0.5 PW	15 J	30 fs	0.05 Hz
			Vulcan	3 PW	2.6 kJ	500 fs	-
GHHG	-	-	-	~ MW	~ $\mu$ J	~ fs	kHz-MHz
Synchrotron	-	-	-	~ W	~ fJ	~100 fs	~ MHz



# References

- [1] Accelerates extreme plasma physics group in university of lisbon, portugal. [Online]. Available: <http://epp.ist.utl.pt/wp/accelerates/>
- [2] Hoffman2 institute for digital research and education in university of california los angeles, united states. [Online]. Available: <https://www.hoffman2.idre.ucla.edu>
- [3] Fermi super computing applications innovation cineca in italy. [Online]. Available: <http://www.hpc.cineca.it>
- [4] Supermuc leibniz-rechenzentrum supercomputing center in germany. [Online]. Available: <https://www.lrz.de/english/>
- [5] Blue waters national centre for supercomputing applications in illinois, united states. [Online]. Available: <https://bluwaters.ncsa.illinois.edu>
- [6] N. Kikuzawa, R. Hajima, N. Nishimori, E. Minehara, T. Hayakawa, T. Shizuma, H. Toyokawa, and H. Ohgaki, "Nondestructive Detection of Heavily Shielded Materials by Using Nuclear Resonance Fluorescence with a Laser-Compton Scattering  $\gamma$ -ray Source," *Applied Physics Express*, vol. 2, no. 036502, March 2009.
- [7] A. L. C. and Toruun I. Yock, A. Mahajan, C. Hill-Kaiser, S. Keole, L. Loreda, O. Cahlon, K. P. McMullen, W. Hartsell, and D. J. Indelicato, "Pediatric Proton Therapy: Patterns of Care across the United States," *International Journal of Particle Therapy*, vol. 1, p. 357 to 367, 2014.
- [8] I. D. Young, M. Ibrahim, R. Chatterjee, S. Gul, F. D. Fuller, S. Koroidov, A. S. Brewster, R. Tran, R. Alonso-Mori, T. Kroll, T. Michels-Clark, H. Laksmono, R. G. Sierra, C. A. Stan, R. Hussein, M. Zhang, L. Douthit, M. Kubin, C. de Lichtenberg, L. V. Pham, H. Nilsson, M. H. Cheah, D. Shevela, C. Saracini, I. S. Mackenzie A. Bean, D. Sokaras, T.-C. Weng, E. Pastor, C. Weninger, T. Fransson, L. Lassalle, P. Bräuer, P. Aller, P. T. Docker, B. Andi, A. M. Orville, J. M. Glowina, S. Nelson, M. Sikorski, D. Zhu, M. S. Hunter, T. J. Lane, A. Aquila, J. E. Koglin, J. Robinson, M. Liang, S. Boutet, A. Y. Lyubimov, M. Uervirojnangkoorn, N. W. Moriarty, D. Liebschner, P. V. Afonine, D. G. Waterman, G. Evans, P. Wernet, H. Dobbek, W. I. Weis, A. T. Brunger, P. H. Zwart, P. D. Adams, A. Zouni, J. Messinger, U. Bergmann, N. K. Sauter, J. Kern, V. K. Yachandra, and J. Yano, "Structure of photosystem II and substrate binding at room temperature," *Nature*, vol. 540, no. 7633, p. 453 to 457, November 2016.
- [9] M. B. Bennett, C. Wrede, B. A. Brown, S. N. Liddick, D. Pérez-Loureiro, D. W. Bardayan, A. A. Chen, K. A. Chipps, C. Fry, B. E. Glassman, C. Langer, N. R. Larson, E. I. McNeice, Z. Meisel, W. Ong, P. D. O'Malley, S. D. Pain, C. J. Prokop, H. Schatz, S. B. Schwartz, S. Suchyta, P. Thompson, M. Walters, and X. Xu, "Isospin Mixing Reveals  $^{30}\text{P}(p,\gamma)^{31}\text{S}$  Resonance Influencing Nova Nucleosynthesis," *Physical Review Letters*, vol. 116, no. 102502, March 2016.
- [10] E. M. Oks, A. V. Tyunkov, Y. G. Yushkov, and D. B. Zolotukhin, "Ceramic coating deposition by electron beam evaporation," *Surface & Coatings Technology*, vol. 325, p. 1 to 6, June 2017.
- [11] A. Descoedres, S. Calatroni, and M. Taborelli, "DC Breakdown Experiments for CLIC," in *Proceedings of EPAC08, Genoa, Italy: 03 Linear Colliders, Lepton Accelerators and New Acceleration Techniques*, no. MOPP012, 2008, <https://accelconf.web.cern.ch/accelconf/e08/papers/mopp012.pdf>.
- [12] G. I. Budker, "Laser electron accelerator," *Proc. CERN symposium on High Energy Accelerators*, vol. 1, p. 68, 1956.
- [13] F. F. Chen, *Introduction to Plasma Physics and Controlled Fusion*, 2nd ed. Plenum, New York: Springer, 1983.
- [14] T. Tajima and J. M. Dawson, "Laser electron accelerator," *Physical Review Letters*, vol. 4, pp. 267–270, July 1979.

- [15] E. Esarey, P. Sprangle, J. Krall, and A. Ting, "Overview of Plasma-Based Accelerator Concept," *IEEE Transactions on Plasma Science*, vol. 24, no. 2, April 1996.
- [16] P. Gibbon, *Short Pulse Laser Interactions with Matter: An Introduction*. Imperial College Press, 2005. [Online]. Available: <https://books.google.pt/books?id=AlJDBqs0KaMC>
- [17] C. Joshi, "The development of laser- and beam-driven plasma accelerators as an experimental field," *Physics of Plasmas*, vol. 14, no. 5, p. 055501, February 2007.
- [18] V. Malka, J. Faure, Y. A. Gauduel, E. Lefebvre, A. Rousse, and K. T. Phuoc, "Principles and applications of compact laser-plasma accelerators," *Nat Phys*, vol. 4, no. 6, pp. 447–453, 06 2008. [Online]. Available: <http://dx.doi.org/10.1038/nphys966>
- [19] B. Holzer, V. Malka, P. Gibbon, B. Bingham, J. Vieira, Z. Najmudin, P. Muggli, J. Faure, M. Ferrario, A. Pukhov, B. Cros, M. Roth, E. Gschwendtner, S. Mangles, and J. Osterhoff, "Proceedings of the European Organization for Nuclear Research (CERN) Accelerator School: Plasma Wake Acceleration, Geneva, Switzerland, 23-29 November 2014," in *Proceedings of the CERN Accelerator School: Plasma Wake Acceleration, Geneva, Switzerland, 23-29 November 2014*, B. Holzer, Ed. CERN-2016-001, 2016, <https://e-publishing.cern.ch>
- [20] F. Albert and A. G. R. Thomas, "Applications of laser wakefield accelerator-based light sources," *Plasma Physics and Controlled Fusion*, vol. 58, no. 103001, September 2016.
- [21] C. E. Clayton, C. Joshi, C. Darrow, and D. Umstadter, "Relativistic Plasma-Wave Excitation by Collinear Optical Mixing," *Physical Review Letters*, vol. 54, no. 2343, May 1985.
- [22] P. Chen, J. M. Dawson, R. W. Huff, and T. Katsouleas, "Acceleration of Electrons by the Interaction of a Bunched Electron Beam with a Plasma," *Physical Review Letters*, vol. 54, no. 693, February 1985.
- [23] J. B. Rosenzweig, D. B. Cline, B. Cole, H. Figueroa, W. Gai, R. Konecny, J. Norem, P. Schoessow, and J. Simpson, "Experimental Observation of Plasma Wakefield Acceleration," *Physical Review Letters*, vol. 61, no. 1, July 1988.
- [24] K. Nakajima, D. Fisher, T. Kawakubo, H. Nakanishi, A. Ogata, Y. Kato, Y. Kitagawa, R. Kodama, K. Mima, H. Shiraga, K. Suzuki, K. Yamakawa, T. Zhang, Y. Sakawa, T. Shoji, Y. Nishida, N. Yugami, M. Downer, and T. Tajima, "Observation of Ultrahigh Gradient Electron Acceleration by a Self-Modulated Intense Short Laser Pulse," *Physical Review Letters*, vol. 74, no. 22, May 1995.
- [25] A. Modena, Z. Najmudin, A. E. Dangor, C. E. Clayton, K. A. Marsh, C. Joshi, V. Malka, C. B. Darrow, C. Danson, D. Neely, and F. N. Walsh, "Electron acceleration from the breaking of relativistic plasma waves," *Nature*, no. 377, pp. 606–608, October 1995.
- [26] D. Strickland and G. Mourou, "Compression of amplified chirped optical pulses," *Optics Communications*, vol. 56, no. 3, July 1985.
- [27] H. Hamster, A. Sullivan, S. Gordon, W. White, and R. W. Falcone, "Subpicosecond, Electromagnetic Pulses from Intense Laser-Plasma Interaction," *Physical Review Letters*, vol. 71, no. 17, October 1993.
- [28] S. P. D. Mangles, C. D. Murphy, Z. Najmudin, A. G. R. Thomas, J. L. Collier, A. E. Dangor, E. J. Divall, P. S. Foster, J. G. Gallacher, D. A. J. C. J. Hooker, A. J. Langley, W. B. Mori, P. A. Norreys, F. S. Tsung, R. Viskup, B. R. Walton, and K. Krushelnick, "Monoenergetic beams of relativistic electrons from intense laser-plasma interactions," *Nature*, vol. 431, pp. 535–538, 2004.
- [29] C. G. R. Geddes, C. Tóth, J. van Tilborg, E. Esarey, C. B. Schroeder, D. Bruhwiler, C. Nieter, J. Cary, and W. P. Leemans, "High-quality electron beams from a laser wakefield accelerator using plasma-channel guiding," *Nature*, vol. 431, pp. 538–541, September 2004.
- [30] J. Faure, Y. Glinec, A. Pukhov, S. Kiselev, S. Gordienko, E. Lefebvre, J. P. Rousseau, F. Burgy, and V. Malka, "A laser-plasma accelerator producing monoenergetic electron beams," *Nature*, vol. 431, p. 541, 2004.
- [31] T. Katsouleas, "Accelerator physics: Electrons hang ten on laser wake," *Nature*, vol. 431, pp. 515–516, September 2004.
- [32] I. Blumenfeld, C. E. Clayton, F.-J. Decker, M. J. Hogan, C. Huang, R. Ischebeck, R. Iverson, C. Joshi, T. Katsouleas, N. Kirby, W. Lu, K. A. Marsh, W. B. Mori, P. Muggli, E. Oz, R. H. Siemann, D. Walz, and M. Zhou, "Energy doubling of 42[thinsp]GeV electrons in a metre-scale plasma wakefield accelerator," *Nature*, vol. 445, no. 7129, pp. 741–744, February 2007.

- [33] M. Litos, E. Adli, W. An, C. I. Clarke, C. E. Clayton, S. Corde, J. P. Delahaye, R. J. England, A. S. Fisher, J. Frederico, S. Gessner, S. Z. Green, M. J. Hogan, C. Joshi, W. Lu, K. A. Marsh, W. B. Mori, P. Muggli, N. Vafaei-Najafabadi, D. Walz, G. White, Z. Wu, V. Yakimenko, and G. Yocky, "High-efficiency acceleration of an electron beam in a plasma wakefield accelerator," *Nature*, vol. 515, no. 7525, pp. 92–95, 11 2014. [Online]. Available: <http://dx.doi.org/10.1038/nature13882>
- [34] S. Corde, E. Adli, J. M. Allen, W. An, C. I. Clarke, C. E. Clayton, J. P. Delahaye, J. Frederico, S. Gessner, S. Z. Green, M. J. Hogan, C. Joshi, N. Lipkowitz, M. Litos, W. Lu, K. A. Marsh, W. B. Mori, M. Schmeltz, N. Vafaei-Najafabadi, D. Walz, V. Yakimenko, and G. Yocky, "Multi-gigaelectronvolt acceleration of positrons in a self-loaded plasma wakefield," *Nature*, no. 524, pp. 442–445, August 2015.
- [35] S. Steinke, J. van Tilborg, C. Benedetti, C. G. R. Geddes, C. B. Schroeder, J. Daniels, K. K. Swanson, A. J. Gonsalves, K. Nakamura, N. H. Matlis, B. H. Shaw, E. Esarey, and W. P. Leemans, "Multistage coupling of independent laser-plasma accelerators," *Nature*, vol. 530, no. 7589, pp. 190–193, 02 2016. [Online]. Available: <http://dx.doi.org/10.1038/nature16525>
- [36] J. M. Cole, J. C. Wood, N. C. Lopes, K. Poder, R. L. Abel, S. Alatabi, J. S. J. Bryant, A. Jin, S. Kneip, K. Mecseki, D. R. Symes, S. P. D. Mangles, and Z. Najmudin, "Laser-wakefield accelerators as hard x-ray sources for 3D medical imaging of human bone," *Nature Scientific Reports*, vol. 5, no. 13244, August 2015.
- [37] S. Kneip, C. McGuffey, F. Dollar, M. S. Bloom, V. Chvykov, G. Kalintchenko, K. Krushelnick, A. Maksimchuk, S. P. D. Mangles, T. Matsuoka, Z. Najmudin, C. A. J. Palmer, J. Schreiber, W. Schumaker, A. G. R. Thomas, , and V. Yanovsky, "X-ray phase contrast imaging of biological specimens with femtosecond pulses of betatron radiation from a compact laser plasma wakefield accelerator," *Applied Physical Letters*, vol. 99, no. 093701, September 2011.
- [38] N. Kumar, A. Pukhov, and K. Lotov, "Self-modulation instability of a long proton bunch in plasmas," *Physical Review Letters*, vol. 104, no. 255003, June 2010.
- [39] P. Muggli, O. Reimann, L. Amorim, N. Lopes, J. Vieira, S. Gessner, M. Hogan, S. Li, M. Litos, K. Marsh, W. Mori, C. Joshi, N. Vafaei-Najafabadi, E. Adli, and V. B. Olsen, "Electron Bunch Self-modulation in a Long Plasma at SLAC FACET," in *Proceeding of the IPAC Conference Dresden, Germany, 15-20 June 2014*, no. TUPME050, 2014, <http://accelconf.web.cern.ch/accelconf/IPAC2014/papers/tupme050.pdf>.
- [40] J. Vieira, W. B. Mori, and P. Muggli, "Hosing instability suppression in self-modulated plasma wakefields," *Physical Review Letters*, vol. 112, p. 205001, May 2014. [Online]. Available: <https://link.aps.org/doi/10.1103/PhysRevLett.112.205001>
- [41] A. Caldwell, E. Adli, L. Amorim, R. Apsimon, T. Argyropoulos, R. Assmann, A.-M. Bachmann, F. Batsch, J. Bauche, V. B. Olsen, M. Bernardini, R. Bingham, B. Biskup, T. Bohl, C. Bracco, P. Burrows, G. Burt, B. Buttenschön, A. Butterworth, M. Cascella, S. Chattopadhyay, E. Chevally, S. Cipiccia, H. Damerau, L. Deacon, P. Dirksen, S. Doebert, U. Dorda, E. Elsen, J. Farmer, S. Fartoukh, V. Fedosseev, E. Feldbaumer, R. Fiorito, R. Fonseca, F. Friebel, G. Geschonke, B. Goddard, A. Gorn, O. Grulke, E. Gschwendtner, J. Hansen, C. Hessler, S. Hillenbrand, W. Hofle, J. Holloway, C. Huang, M. Hüther, D. Jaroszynski, L. Jensen, S. Jolly, A. Joulaei, M. Kasim, F. Keeble, R. Kersevan, N. Kumar, Y. Li, S. Liu, N. Lopes, K. Lotov, W. Lu, J. Machacek, S. Mandry, I. Martin, R. Martorelli, M. Martyanov, S. Mazzoni, M. Meddahi, L. Meringa, O. Mete, V. Minakov, J. Mitchell, J. Moody, A.-S. Müller, Z. Najmudin, T. Noakes, P. Norreys, J. Osterhoff, E. Öz, A. Pardons, K. Pepitone, A. Petrenko, G. Plyushchev, J. Pozimski, A. Pukhov, O. Reimann, K. Rieger, S. Roesler, H. Ruhl, T. Rusnak, F. Salveter, N. Savard, J. Schmidt, H. von der Schmitt, A. Seryi, E. Shaposhnikova, Z. Sheng, P. Sherwood, L. Silva, F. Simon, L. Soby, A. Sosedkin, R. Spitsyn, T. Tajima, R. Tarkeshian, H. Timko, R. Trines, T. Tückmantel, P. Tüev, M. Turner, F. Velotti, V. Verzilov, J. Vieira, H. Vincke, Y. Wei, C. Welsch, M. Wing, G. Xia, V. Yakimenko, H. Zhang, and F. Zimmermann, "Path to awake: Evolution of the concept," *Nuclear Instruments and Methods in Physics Research Section A: Accelerators, Spectrometers, Detectors and Associated Equipment*, vol. 829, pp. 3 – 16, 2016, 2nd European Advanced Accelerator Concepts Workshop - EAAC 2015. [Online]. Available: <http://www.sciencedirect.com/science/article/pii/S0168900215016307>
- [42] E. Gschwendtner, E. Adli, L. Amorim, R. Apsimon, R. Assmann, A.-M. Bachmann, F. Batsch, J. Bauche, V. B. Olsen, M. Bernardini, R. Bingham, B. Biskup, T. Bohl, C. Bracco, P. Burrows, G. Burt, B. Buttenschön, A. Butterworth, A. Caldwell, M. Cascella, E. Chevally, S. Cipiccia, H. Damerau, L. Deacon, P. Dirksen, S. Doebert, U. Dorda, J. Farmer, V. Fedosseev, E. Feldbaumer, R. Fiorito, R. Fonseca, F. Friebel, A. Gorn, O. Grulke, J. Hansen, C. Hessler, W. Hofle, J. Holloway, M. Hüther, D. Jaroszynski, L. Jensen, S. Jolly, A. Joulaei, M. Kasim, F. Keeble, Y. Li, S. Liu, N. Lopes, K. Lotov, S. Mandry, R. Martorelli, M. Martyanov, S. Mazzoni, O. Mete, V. Minakov, J. Mitchell, J. Moody, P. Muggli, Z. Najmudin, P. Norreys, E. Öz, A. Pardons, K. Pepitone, A. Petrenko, G. Plyushchev, A. Pukhov, K. Rieger, H. Ruhl, F. Salveter, N. Savard, J. Schmidt, A. Seryi, E. Shaposhnikova, Z. Sheng,

- P. Sherwood, L. Silva, L. Soby, A. Sosedkin, R. Spitsyn, R. Trines, P. Tuev, M. Turner, V. Verzilov, J. Vieira, H. Vincke, Y. Wei, C. Welsch, M. Wing, G. Xia, and H. Zhang, "Awake, the advanced proton driven plasma wakefield acceleration experiment at cern," *Nuclear Instruments and Methods in Physics Research Section A: Accelerators, Spectrometers, Detectors and Associated Equipment*, vol. 829, pp. 76 – 82, 2016, 2nd European Advanced Accelerator Concepts Workshop - EAAC 2015. [Online]. Available: <http://www.sciencedirect.com/science/article/pii/S0168900216001881>
- [43] P. Sprangle, E. Esarey, and A. Ting, "Laser wakefield acceleration and relativistic optical guiding," *Applied Physics Letters*, vol. 53, no. 2146, November 1988.
- [44] T. C. Chiou, T. Katsouleas, C. Decker, W. B. Mori, J. S. Wurtele, G. Shvets, and J. J. Su, "Laser wakkefield acceleration and optical guiding in a hollow plasma channel," *Physics of Plasmas*, vol. 2, no. 1, pp. 310–318, 1995. [Online]. Available: <http://dx.doi.org/10.1063/1.871107>
- [45] T. Katsouleas, S. Wilks, P. Chen, J. M. Dawson, and J. J. Su, "Beam Loading in Plasma Accelerators," *Particle Accelerators*, vol. 22, p. 81 to 99, 1987.
- [46] J. M. Dawson, "Nonlinear Electron Oscillations in a Cold Plasma," *Physical Review*, vol. 113, no. 383, pp. 526–532, January 1959.
- [47] W. Lu, C. Huang, M. M. Zhou, W. B. Mori, and T. Katsouleas, "Limits of linear plasma wakefield theory for electron or positron beams," *Physics of Plasmas*, vol. 12, no. 063101, May 2005.
- [48] W. Lu, "Nonlinear plasma wakefield theory and optimum scaling for laser wakefield accelerator (lwfa) in the blowout regime," Ph.D. dissertation, University of California Los Angeles, 2006, [https://picksc.idre.ucla.edu/wp-content/uploads/2015/04/weilu\\_dissertation.pdf](https://picksc.idre.ucla.edu/wp-content/uploads/2015/04/weilu_dissertation.pdf).
- [49] P. Sprangle, E. Esarey, and A. Ting, "Nonlinear Theory of Intense Laser-Plasma Interactions," *Physical Review Letters*, vol. 64, no. 17, April 1990.
- [50] A. Pukhov and J. M. ter Vehn, "Laser wake field acceleration: the highly non-linear broken-wave regime," *Appl. Phys. B*, vol. 74, pp. 355–361, 2002.
- [51] I. Kostyukov, A. Pukhov, and S. Kiselev, "Phenomenological theory of laser-plasma interaction in bubble regime," *Physics of Plasmas*, vol. 13, no. 5256, 2004.
- [52] W. Lu, M. Tzoufras, C. Joshi, F. S. Tsung, W. B. Mori, J. Vieira, R. A. Fonseca, and L. O. Silva, "Generating multi-GeV electron bunches using single stage laser wakefield acceleration in a 3D nonlinear regime," *Physical Review Special Topics – Accelerators And Beams*, vol. 10, p. 061301, June 2007.
- [53] "Max iv infrastructure at the lund university in sweden," <https://www.maxiv.lu.se>
- [54] P. Mora and T. Antonsen, "Kinetic modeling of intense, short laser pulses propagating in tenuous plasmas," *Physics of Plasmas*, vol. 4, no. 1, pp. 217–229, 1997.
- [55] D. H. Whittum, "Electromagnetic instability of the ion-focused regime," *Physics of Fluids B: Plasma Physics*, vol. 4, pp. 730–739, 1992.
- [56] E. Esarey, P. Catravas, and W. P. Leemans, "Betatron radiation from electron beams in plasma focusing channels," *AIP Conference Proceedings*, vol. 569, no. 1, pp. 473–486, 2001.
- [57] E. Esarey, B. A. Shadwick, P. Catravas, and W. P. Leemans, "Synchrotron radiation from electron beams in plasma focusing channels," *Physical Review E*, vol. 65, no. 056505, 2002.
- [58] S. Corde, K. T. Phuoc, G. Lambert, R. Fitour, V. Malka, and A. Rousse, "Femtosecond x rays from laser-plasma accelerators," *Review on Modern Physics*, vol. 81, no. 1229, 2013.
- [59] N. Lemos, J. L. Martins, F. S. Tsung, J. L. Shaw, K. A. Marsh, F. Albert, B. B. Pollock, and C. Joshi, "Self-modulated laser wakefield accelerators as x-ray sources," *Plasma Physics and Controlled Fusion*, vol. 58, no. 3, p. 034018, 2016.
- [60] F. Albert, N. Lemos, J. L. Shaw, B. B. Pollock, C. Goyon, W. Schumaker, A. M. Saunders, K. A. Marsh, A. Pak, J. E. Ralph, J. L. Martins, L. D. Amorim, R. W. Falcone, S. H. Glenzer, J. D. Moody, and C. Joshi, "Observation of Betatron X-Ray Radiation in a Self-Modulated Laser Wakefield Accelerator Driven with Picosecond Laser Pulses," *Physical Review Letters*, vol. 118, no. 13, p. 134801, March 2017.
- [61] J. L. Shaw, "Direct laser acceleration in laser wakefield accelerators," Ph.D. dissertation, University of California Los Angeles, 2016.

- [62] J. L. Shaw, N. Lemos, L. D. Amorim, N. Vafaei-Najafabadi, K. A. Marsh, F. S. Tsung, W. B. Mori, and C. Joshi, "Role of direct laser acceleration of electrons in a laser wakefield accelerator with ionization injection," *Physical Review Letters*, vol. 118, no. 064801, p. 064801, February 2017.
- [63] S. Lee, T. Katsouleas, R. G. Hemker, E. S. Dodd, and W. B. Mori, "Plasma-wakefield acceleration of a positron beam," *Physical Review E*, vol. 64, no. 045501, 2001.
- [64] B. E. Blue, "Plasma wakefield acceleration of an intense positron beam," Ph.D. dissertation, University of California Los Angeles, 2003, <https://www.ncbi.nlm.nih.gov/pubmed/12786559>.
- [65] K. A. Marsh, B. E. Blue, C. E. Clayton, C. Joshi, W. B. Mori, F.-J. Decker, M. J. Hogan, R. Iverson, C. O'Connell, P. Raimondi, R. Siemann, D. Walz, T. C. Katsouleas, and P. Muggli, "Positron beam propagation in a meter long plasma channel," in *Proceedings of the 2003 Particle Accelerator Conference, 2003*, no. 731, 2003, <https://accelconf.web.cern.ch/accelconf/p03/PAPERS/FOAB011.PDF>.
- [66] P. Muggli, B. E. Blue, C. E. Clayton, F. J. Decker, M. J. Hogan, C. Huang, C. Joshi, T. C. Katsouleas, W. Lu, W. B. Mori, C. L. O'Connell, R. H. Siemann, D. Walz, and M. Zhou, "Halo formation and emittance growth of positron beams in plasmas," *Physical Review Letters*, vol. 101, p. 055001, Jul 2008. [Online]. Available: <https://link.aps.org/doi/10.1103/PhysRevLett.101.055001>
- [67] J. D. Jackson, *Classical Electrodynamics*, 2nd ed. New York: Wiley, 1975.
- [68] S. Wang, C. E. Clayton, B. E. Blue, E. S. Dodd, K. A. Marsh, W. B. Mori, C. Joshi, S. Lee, P. Muggli, T. Katsouleas, F. J. Decker, M. J. Hogan, R. H. Iverson, P. Raimondi, D. Walz, R. Siemann, and R. Assmann, "X-Ray Emission from Betatron Motion in a Plasma Wiggler," *Physics Review Letters*, vol. 88, p. 135004, 2002.
- [69] J. L. Martins, M. Vranic, T. Grismayer, J. Vieira, R. A. Fonseca, and L. O. Silva, "Modeling radiation emission in the transition from the classical to the quantum regime," *Plasma Physics and Controlled Fusion*, vol. 58, no. 1, November 2015.
- [70] J. L. Martins, S. Martins, R. Fonseca, and L. O. Silva, "Harnessing Relativistic Plasma Waves as Novel Radiation Sources from Terahertz to X-rays and Beyonds," in *SPIE conference proceedings*, D. A. Jaroszynsky and A. Rousse, Eds., vol. 7359, no. 73590V. SPIE, Bellingham, 2009.
- [71] J. L. Martins, S. F. Martins, R. A. Fonseca, and L. O. Silva, "Radiation in 1.5 gev and 12 gev laser wakefield acceleration stages from pic simulations," *AIP Conference Proceedings*, vol. 1299, pp. 191–196, June 2010.
- [72] —, "X-ray modeling in laser-wakefield accelerators," *IEEE Transactions on Plasma Science*, vol. 39, no. 11, pp. 2826–2827, July 2011.
- [73] R. A. Fonseca, L. O. Silva, F. S. Tsung, V. K. Decyk, W. Lu, C. Ren, W. B. Mori, S. Deng, S. Lee, T. Katsouleas, and J. C. Adam, "OSIRIS: A Three-Dimensional, Fully Relativistic Particle in Cell Code for Modeling Plasma Based Accelerators," in *Lecture Notes in Computer Science*, ser. Computational Science ICCS 2002, P. M. A. Sloot, A. G. Hoekstra, C. J. K. Tan, and J. J. Dongarra, Eds., vol. 2331. Springer, Berlin, Heidelberg, 2002.
- [74] C. Decker, W. Mori, and T. Katsouleas, "Particle-in-cell simulations of Raman forward scattering from short-pulse high-intensity lasers," *Physical Review E*, vol. 50, no. 5, pp. R3338–R3341, 1994.
- [75] J. Vay, "Noninvariance of space- and time-scale ranges under a Lorentz transformation and the implications for the study of relativistic interactions," *Physical Review Letters*, vol. 98, no. 13, 2007.
- [76] J. Vay, C. Geddes, E. Cormier-Michel, and D. Grote, "Effects of hyperbolic rotation in Minkowski space on the modeling of plasma accelerators in a Lorentz boosted frame," *Physics of Plasmas*, vol. 18, no. 3, 2011.
- [77] S. F. Martins, R. A. Fonseca, W. Lu, W. B. Mori, and L. O. Silva, "Exploring laser-wakefield-accelerator regimes for near-term lasers using particle-in-cell simulation in Lorentz-boosted frames," *Nature Physics*, vol. 6, no. 4, pp. 311–316, 2010.
- [78] P. Yu, X. Xu, A. Davidson, A. Tableman, T. Dalichaouch, F. Li, M. D. Meyers, W. An, F. S. Tsung, V. K. Decyk, F. Fiuza, J. Vieira, R. A. Fonseca, W. Lu, L. O. Silva, and W. B. Mori, "Enabling Lorentz boosted frame particle-in-cell simulations of laser wakefield acceleration in quasi-3D geometry," *Journal of Computational Physics*, vol. 316, pp. 747–759, April 2016.
- [79] A. Lifschitz, X. Davone, E. Lefebvre, J. Faure, C. Rechatin, and V. Malka, "Particle-in-cell modelling of laser-plasma interaction using Fourier decomposition," *Journal of Computational Physics*, vol. 228, no. 5, pp. 1803–1814, March 2009.

- [80] A. Davidson, A. Tableman, W. An, F. S. Tsung, W. Lu, J. Vieira, R. A. Fonseca, L. O. Silva, and W. B. Mori, "Implementation of a hybrid particle code with a PIC description in  $r$ - $z$  and a gridless description in  $\phi$  into OSIRIS," *Journal of Computational Physics*, vol. 281, pp. 1063–1077, November 2014.
- [81] K. S. Yee, "Numerical solution of initial boundary value problems involving maxwell's equations in isotropic media," *IEEE Transactions on Antennas and Propagation*, vol. 14, pp. 302–307, January 1966.
- [82] J.-L. Vay, "Noninvariance of Space- and Time-Scale Ranges under a Lorentz Transformation and the Implications for the Study of Relativistic Interactions," *Physical Review Letters*, vol. 98, no. 130405, March 2007.
- [83] P. Yu, X. Xu, A. Tableman, V. K. Decyk, F. S. Tsung, F. Fiuza, A. Davidson, J. Vieira, R. A. Fonseca, W. Lu, L. O. Silva, and W. B. Mori, "Mitigation of numerical Cerenkov radiation and instability using a hybrid finite difference-FFT Maxwell solver and a local charge conserving current deposit," *Computer Physics Communications*, vol. 197, pp. 144–152, August 2015.
- [84] E. Nerush, I. Kostyukov, A. Fedotov, N. Narozhny, N. Elkina, and H. Ruhl, "Laser field absorption in self-generated electron-positron pair plasma," *Physical Review Letters*, vol. 106, no. 035001, 2011.
- [85] M. Vranic, T. Grismayer, J. L. Martins, R. A. Fonseca, and L. O. Silva, "Particle merging algorithm for PIC codes," *Computer Physics Communications*, vol. 191, pp. 65–73, February 2015.
- [86] J. E. Moore and N. J. Fisch, "Guiding-center equations for electrons in ultra intense laser fields," *Physics of Plasmas*, vol. 1, no. 5, pp. 1105–1116, May 1994.
- [87] D. Gordon, W. Mori, and T. Antonsen, "A ponderomotive guiding center particle-in-cell code for efficient modeling of laser-plasma interactions," *IEEE Transactions on Plasma Science*, vol. 28, no. 4, pp. 1224–1232, 2000.
- [88] A. Helm, J. Vieira, L. O. Silva, and R. Fonseca, "Implementation of a 3d version of ponderomotive guiding center solver in particle-in-cell code osiris," 2017, in preparation.
- [89] D. Bruhwiler, D. Dimitrov, J. Cary, E. Esarey, W. Leemans, and R. Giacone, "Particle-in-cell simulations of tunneling ionization effects in plasma-based accelerators," *Physics of Plasmas*, vol. 10, no. 5, pp. 2022–2030, 2003.
- [90] F. Peano, M. Marti, L. Silva, and G. Coppa, "Statistical kinetic treatment of relativistic binary collisions," *Physical Review E*, vol. 79, no. 025701, 2009.
- [91] T. Grismayer, M. Vranic, J. L. Martins, R. A. Fonseca, and L. O. Silva, "Seeded QED cascades in counter-propagating laser pulses," *Physical Review E*, vol. 95, no. 023210, February 2017.
- [92] R. Courant, K. Friedrichs, and H. Lewy, "On the partial difference equations of mathematical physics," New York University, Institute of Fine Arts Library, New York, Tech. Rep. NYO-7689, September 1956.
- [93] C. Huang, V. Decyk, M. Zhou, W. Lu, and W. Mori, "QuickPIC: a highly efficient fully parallelized pic code for plasma-based acceleration," *J. Phys. Conf. Ser.*, vol. 46, pp. 190–199, 2006.
- [94] W. An, V. Decyk, W. Mori, and T. A. Jr., "An improved iteration loop for the three dimensional quasi-static particle-in-cell algorithm: QuickPIC," *Journal of Computational Physics*, vol. 250, pp. 165–177, 2013.
- [95] M. M. Aléonard *et al.*, "Eli - Extreme Light Infrastructure," in *Science and Technology with Ultra-Intense Lasers*, G. A. Mourou, G. Korn, W. Sandner, and J. L. Collier, Eds. Wolfshagener Str. 56 13187 Berlin, Germany: Andreas Thoss, THOSS Media GmbH, 2011, ch. Executive Summary, pp. 1–14.
- [96] K. Nakajima, T. Kawakubo, H. Nakanishi, A. Ogata, Y. Kato, Y. Kitagawa, R. Kodama, K. Mima, H. Shiraga, K. Suzuki, T. Zhang, Y. Sakawa, T. Shoji, Y. Nishida, N. Yugami, M. Downer, D. Fisher, B. Newberger, and T. Tajima, "A proof-of-principle experiment of laser wakefield acceleration," *Physica Scripta*, vol. T52, no. 61, November 1994.
- [97] F. Amoranoff, S. Baton, D. Bernard, B. Cros, D. Descamps, F. Dorchies, V. Malka, J. R. Marquès, G. Matthiessent, P. Miné, A. Modena, P. Mora, and J. M. Z. Najmudin, "Observation of Laser Wakefield Acceleration of Electrons," *Physics Review Letters*, vol. 81, no. 5, pp. 995–998, 1998.
- [98] V. Malka, S. Fritzler, E. Lefebvre, M. M. Aléonard, F. Burgy, J. P. Chambaret, J. F. Chemin, K. Krushelnick, G. Malka, S. P. Mangles, Z. Najmudin, M. Pittman, J. P. Rousseau, J. N. Scheurer, B. Walton, and A. E. Dangor, "Electron acceleration by a wake field forced by an intense ultrashort laser pulse," *Science*, vol. 298, no. 5598, pp. 1596–1600, November 2002.

- [99] W. Lu, C. Huang, W. B. Mori, and T. Katsouleas, "Nonlinear Theory for Relativistic Plasma Wakefields in the Blowout Regime," *Physics Review Letters*, vol. 96, no. 16, p. 165002, 2006.
- [100] J. B. Rosenzweig, B. Breizman, T. Katsouleas, and J. J. Su, "Acceleration and focusing of electrons in two-dimensional nonlinear plasma wake fields," *Physical Review A*, vol. 44, no. 10, p. 6189, 1991.
- [101] S. P. D. Mangles, A. G. R. Thomas, M. C. Kaluza, O. Lundh, F. Lindau, A. Persson, F. S. Tsung, Z. Najmudin, W. B. Mori, C. G. Wahlstrom, and K. Krushelnick, "Laser-Wakefield Acceleration of Monoenergetic Electron Beams in the First Plasma-Wave Period," *Nature*, vol. 431, pp. 535–538, 2004.
- [102] D. H. Froula, C. E. Clayton, T. Doepfner, K. A. Marsh, C. P. J. Barty, L. Divol, R. A. Fonseca, S. H. Glenzer, C. Joshi, W. Lu, S. F. Martins, P. Michel, W. B. Mori, J. P. Palastro, B. B. Pollock, A. Pak, J. E. Ralph, J. S. Ross, C. W. Siders, L. O. Silva, and T. Wang, "Measurements of the Critical Power for Self-Injection of Electrons in a Laser Wakefield Accelerator," *Physical Review Letters*, vol. 103, no. 215006, November 2009.
- [103] F. S. Tsung, R. Narang, W. B. Mori, and C. Joshi, "Near-GeV-Energy Laser-Wakefield Acceleration of Self-Injected Electrons in a Centimeter-Scale Plasma Channel," *Physical Review Letters*, vol. 93, no. 18, p. 185002, 2004.
- [104] E. Miura, K. Koyama, S. Kato, N. Saito, M. Adachi, Y. Kawada, T. Nakamura, and M. Tanimoto, "Demonstration of quasi-monoenergetic electron-beam generation in laser-driven plasma acceleration," *Applied Physics Letters*, vol. 86, p. 251501, 2005.
- [105] B. Hidding, K. U. Amthor, B. Liesfeld, H. Schwöerer, S. Karsch, M. Geissler, L. Veisz, K. Schmid, J. G. Gallacher, S. P. Jamison, D. Jaroszynski, G. Pretzler, and R. Sauerbrey, "Generation of Quasimonoenergetic Electron Bunches with 80-fs Laser Pulses," *Physical Review Letters*, vol. 96, p. 105004, March 2006.
- [106] W. P. Leemans, B. Nagler, A. J. Gonsalves, C. Tóth, K. Nakamura, C. G. R. Geddes, E. Esarey, C. B. Schroeder, and S. M. Hooker, "GeV electron beams from a centimetre-scale accelerator," *Nature Physics*, vol. 2, pp. 696–699, 2006.
- [107] N. A. M. Hafz, T. M. Jeong, I. W. Choi, S. K. Lee, K. H. Pae, V. V. Kulagin, J. H. Sung, T. J. Yu, K.-H. Hong, T. Hosokai, J. R. Cary, D.-K. Ko, and J. Lee, "Stable generation of GeV-class electron beams from self-guided laser plasma channels," *Nature Photonics*, vol. 2, pp. 571–577, 2008.
- [108] C. E. Clayton, J. E. Ralph, F. Albert, R. A. Fonseca, S. H. Glenzer, C. Joshi, W. Lu, K. A. Marsh, S. F. Martins, W. B. Mori, A. Pak, F. S. Tsung, B. B. Pollock, J. S. Ross, L. O. Silva, and D. H. Froula, "Self-Guided Laser Wakefield Acceleration beyond 1 GeV Using Ionization-Induced Injection," *Physical Review Letters*, vol. 105, p. 105003, September 2010.
- [109] B. B. Pollock, C. E. Clayton, J. E. Ralph, F. Albert, A. Davidson, L. Divol, C. Filip, S. H. Glenzer, K. Herpoldt, W. Lu, K. A. Marsh, J. Meinecke, W. B. Mori, A. Pak, T. C. Rensink, J. S. Ross, J. Shaw, G. R. Tynan, C. Joshi, and D. H. Froula, "Demonstration of a Narrow Energy Spread  $\approx 0.5$  GeV Electron Beam from a Two-Stage Laser Wakefield Accelerator," *Physical Review Letters*, vol. 107, p. 045001, July 2011.
- [110] H. T. Kim, K. H. Pae, H. J. Cha, I. J. Kim, T. J. Yu, J. H. Sung, S. K. Lee, T. M. Jeong, and J. Lee, "Enhancement of Electron Energy to the Multi-GeV Regime by a Dual-Stage Laser-Wakefield Accelerator Pumped by Petawatt Laser Pulses," *Physical Review Letters*, vol. 111, p. 165002, 2013.
- [111] X. Wang, R. Zgadzaj, N. Fazel, Z. Li, S. A. Yi, X. Zhang, W. Henderson, Y. Y. Chang, R. Korzekwa, H. E. Tsai, C. H. Pai, H. Quevedo, G. Dyer, E. Gaul, M. Martinez, A. C. Bernstein, T. Borger, M. Spinks, M. Donovan, V. Khudik, G. Shvets, T. Ditmire, and M. C. Downer, "Quasi-monoenergetic laser-plasma acceleration of electrons to 2 GeV," *Nature Communications*, vol. 4, June 2013.
- [112] W. P. Leemans, A. J. Gonsalves, H.-S. Mao, K. Nakamura, C. Benedetti, C. B. Schroeder, C. Tóth, J. Daniels, D. E. Mittelberger, S. S. Bulanov, J.-L. Vay, C. G. R. Geddes, and E. Esarey, "Multi-GeV Electron Beams from Capillary-Discharge-Guided Subpetawatt Laser Pulses in the Self-Trapping Regime," *Physical Review Letters*, vol. 113, p. 245002, December 2014.
- [113] "European plasma research accelerator with excellence in applications," 2015, <http://www.eupraxia-project.eu>
- [114] J. L. Shaw, F. S. Tsung, N. Vafaei-Najafabadi, K. A. Marsh, N. Lemos, W. B. Mori, and C. Joshi, "Role of direct laser acceleration in energy gained by electrons in a laser wakefield accelerator with ionization injection," *Plasma Physics and Controlled Fusion*, vol. 56, no. 8, p. 084006, July 2014.

- [115] J. L. Shaw, N. Lemos, K. A. Marsh, F. S. Tsung, W. B. Mori, and C. Joshi, "Estimation of direct laser acceleration in laser wakefield accelerators using particle-in-cell simulations," *Plasma Physics and Controlled Fusion*, vol. 58, no. 3, p. 034008, February 2016.
- [116] X. Zhang, V. N. Khudik, A. Pukhov, and G. Shvets, "Laser wakefield and direct acceleration with ionization injection," *Plasma Physics and Controlled Fusion*, vol. 58, no. 3, p. 034011, February 2016.
- [117] A. Pukhov and J. M. ter Vehn, "Relativistic Magnetic Self-Channeling of Light in Near-Critical Plasma: Three-Dimensional Particle-in-Cell Simulation," *Physical Review Letters*, vol. 76, no. 21, 1996.
- [118] A. Pukhov and Z. M. S. J. M. ter Vehn, "Particle acceleration in relativistic laser channels," *Physics of Plasmas*, vol. 6, no. 7, 1999.
- [119] A. Rousse, K. T. Phuoc, R. Shah, A. Pukhov, E. Lefebvre, V. Malka, S. Kiselev, F. Burgy, J.-P. Rousseau, D. Umstadter, and D. Hulin, "Production of a keV X-Ray Beam from Synchrotron Radiation in Relativistic Laser-Plasma Interaction," *Physics Review Letters*, vol. 93, p. 135005, 2004.
- [120] S. Cipiccia, M. R. Islam, B. Ersfeld, R. P. Shanks, E. Brunetti, G. Vieux, X. Yang, R. C. Issac, S. M. Wiggins, G. H. Welsh, M.-P. Anania, D. Maneuski, R. Montgomery, G. Smith, M. Hoek, D. J. Hamilton, N. R. C. Lemos, D. Symes, P. P. Rajeev, V. O. Shea, J. M. Dias, and D. A. Jaroszynski, "Gamma-rays from harmonically resonant betatron oscillations in a plasma wake," *Nature Physics*, vol. 7, pp. 867–871, November 2011.
- [121] S. Kneip, S. R. Nagel, C. Bellei, N. Bourgeois, A. E. Dangor, A. Gopal, R. Heathcote, S. P. D. Mangles, J. R. Marquès, A. Maksimchuk, P. M. Nilson, K. T. Phuoc, S. Reed, M. Tzoufras, F. S. Tsung, L. Willingale, W. B. Mori, A. Rousse, K. Krushelnick, and Z. Najmudin, "Observation of Synchrotron Radiation from Electrons Accelerated in a Petawatt-Laser-Generated Plasma Cavity," *Physical Review Letters*, vol. 100, p. 105006, March 2008.
- [122] A. Pak, K. A. Marsh, S. F. Martins, W. Lu, W. B. Mori, and C. Joshi, "Laser wakefield and direct acceleration with ionization injection," *Physical Review Letters*, vol. 104, p. 025003, January 2010.
- [123] A. Pak, "Injection of tunnel ionized electrons into laser-produced wakes," Ph.D. dissertation, University of California Los Angeles, 2010, <https://pdfs.semanticscholar.org/c92d/c08ddeb6f0a2584f21afc054e573a89e1383.pdf>.
- [124] C. McGuffey, A. G. R. Thomas, W. Schumaker, T. Matsuoka, V. Chvykov, F. J. Dollar, G. Kalintchenko, V. Yanovsky, A. Maksimchuk, K. Krushelnick, V. Y. Bychenkov, I. V. Glazyrin, and A. V. Karpeev, "Ionization Induced Trapping in a Laser Wakefield Accelerator," *Physical Review Letters*, vol. 104, p. 025004, January 2010.
- [125] Y. Xi, "Ionization injection plasma wakefield acceleration," Ph.D. dissertation, University of California Los Angeles, 2016, <http://escholarship.org/uc/item/5gh0k91r>.
- [126] D. Umstadter, S.-Y. Chen, A. Maksimchuk, R. F. Hubbard, B. Hafizi, H. R. Burris, C. Manka, and P. Sprangle, "Nonlinear Optics in Relativistic Plasmas and Laser Wake Field Acceleration of Electrons," *Science*, vol. 273, no. 5274, 1996.
- [127] W. B. Mori, "The physics of the nonlinear optics plasmas at relativistic intensities for short-pulse lasers," *IEEE Journal of Quantum Electronics*, vol. 33, no. 11, November 1997.
- [128] V. Malka, J. Faure, J. R. Marquès, F. Amiranoff, J. P. Rousseau, S. Ranc, J. P. Chambaret, Z. Najmudin, B. Walton, P. Mora, and A. Solodov, "Characterization of electron beams produced by ultrashort (30 fs) laser pulses," *Physics of Plasmas*, vol. 8, no. 2605, May 2001.
- [129] Z. Najmudin, K. Krushelnick, E. L. Clark, S. P. D. Mangles, B. Walton, A. E. Dangor, S. Fritzler, V. Malka, E. Lefebvre, D. Gordon, F. S. Tsung, and C. Joshi, "Self-modulated wakefield and forced laser wakefield acceleration of electrons," *Physics of Plasmas*, vol. 10, no. 2071, April 2003.
- [130] H. S. Brandi, C. Manus, G. Mainfray, T. Lehner, and G. Bonnaud, "Relativistic and ponderomotive self-focusing of a laser beam in a radially inhomogeneous plasma. I. Paraxial approximation," *Physics of Fluids B: Plasma Physics*, vol. 5, p. 3539, July 1993.
- [131] P. Sprangle, E. Esarey, J. Krall, and G. Joyce, "Propagation and Guiding of Intense Laser Pulses in Plasmas," *Physical Review Letters*, vol. 69, no. 2200, May 1992.
- [132] G.-Z. Sun, E. Ott, T. C. Lee, and P. Guzdar, "Self-focusing of short intense pulses in plasmas," *Physics of Fluids*, vol. 30, no. 2, pp. 526–532, February 1987.

- [133] P. Monot, T. Auguste, P. Gibbon, F. Jakober, G. Mainfray, A. Dulieu, M. Louis-Jacquet, G. Malka, and J. Miquel, "Experimental Demonstration of Relativistic Self-Channeling of a Multiterawatt Laser Pulse in an Underdense Plasma," *Physical Review Letters*, vol. 74, no. 15, p. 2953, April 1995.
- [134] J. Fuchs, G. Malka, J. C. Adam, F. Amiranoff, S. D. Baton, N. Blanchot, A. Héron, G. Laval, J. L. Miquel, P. Mora, H. Pépin, and C. Rousseaux, "Dynamics of Subpicosecond Relativistic Laser Pulse Self-Channeling in an Underdense Preformed Plasma," *Physical Review Letters*, vol. 80, no. 8, p. 1658, February 1998.
- [135] E. Oz, S. Deng, T. Katsouleas, P. Muggli, C. D. B. I. Blumenfeld, F. J. Decker, P. Emma, M. J. Hogan, R. Ischebeck, R. H. Iverson, N. Kirby, P. Krejcik, C. O'Connell, R. H. Siemann, D. Walz, D. Auerbach, C. E. Clayton, C. Huang, D. K. Johnson, C. Joshi, W. Lu, K. A. Marsh, W. B. Mori, and M. Zhou, "Ionization-Induced Electron Trapping in Ultrarelativistic Plasma Wakes," *Physical Review Letters*, vol. 98, no. 084801, February 1999.
- [136] E. D. Courant, C. Pellegrini, and W. Zakowicz, "High-energy inverse free-electron-laser accelerator," *Physical Review A*, vol. 32, no. 5, p. 2813, November 1985.
- [137] L. D. Landau and E. M. Lifshitz, *The Classical Theory of Fields.*, 4th ed. Butterworth-Heinemann: Elsevier, 1980.
- [138] C. D. Decker, W. B. Mori, T. Katsouleas, and D. E. Hinkel, "Spatial temporal theory of Raman forward scattering," *Physics of Plasmas*, vol. 3, no. 1360, 1996.
- [139] J. L. Shaw, "Characterization of sub-millimeter-scale gas cells as possible injectors for staged laser wakefield acceleration," Master's thesis, University of California Los Angeles, 2013.
- [140] M. Chen, E. Esarey, C. B. Schroeder, C. G. R. Geddes, and W. P. Leemans, "Theory of ionization-induced trapping in laser-plasma accelerators," *Physics of Plasmas*, vol. 19, no. 033101, March 2012.
- [141] R. Lehe, C. Thaury, E. Guillaume, A. Lifschitz, and V. Malka, "Laser-plasma lens for laser-wakefield accelerators," *Physical Review Special Topics - Accelerators and Beams*, vol. 17, no. 121301, December 2014.
- [142] L.-W. Zhu, Z.-M. Sheng, and M. Y. Yu, "Direct acceleration of electrons by a circular polarized laser pulse with phase modulation," *Physics of Plasmas*, vol. 20, no. 113112, 2013.
- [143] C. Gahn, G. D. Tsakiris, A. Pukhov, J. M. ter Vehn, G. Pretzler, P. Thirolf, D. Habs, and K. J. Witte, "Multi-MeV Electron Beam Generation by Direct Laser Acceleration in High-Density Plasma Channels," *Physical Review Letters*, vol. 83, no. 23, p. 4772, June 1999.
- [144] F. Albert, N. Lemos, J. L. Shaw, B. B. Pollock, C. Goyon, W. Schumaker, A. M. Saunders, K. A. Marsh, A. Pak, J. E. Ralph, J. L. Martins, L. D. Amorim, R. W. Falcone, S. H. Glenzer, J. D. Moody, and C. Joshi, "Observation of betatron x-ray radiation in a self-modulated laser wakefield accelerator driven with picosecond laser pulses," *Physical Review Letters*, vol. 118, p. 134801, Mar 2017. [Online]. Available: <https://link.aps.org/doi/10.1103/PhysRevLett.118.134801>
- [145] P. Monot, T. Auguste, L. A. Lompré, G. Mainfray, and C. Manus, "Focusing limits of a terawatt laser in an underdense plasma," *Journal of the Optical Society of America B*, vol. 9, no. 9, pp. 1579–1584, Sep 1992. [Online]. Available: <http://josab.osa.org/abstract.cfm?URI=josab-9-9-1579>
- [146] W. Horton and T. Tajima, "Pump depletion in the plasma-beat-wave accelerator," *Physical Review A*, vol. 34, pp. 4110–4119, Nov 1986. [Online]. Available: <https://link.aps.org/doi/10.1103/PhysRevA.34.4110>
- [147] C. Decker and W. Mori, "Group velocity of large amplitude electromagnetic waves in a plasma," *Physical Review Letters*, vol. 72, no. 4, pp. 490–493, 1994.
- [148] M. D. Perry and G. Mourou, "Terawatt to petawatt subpicosecond lasers," *Science*, vol. 264, no. 5161, pp. 917–924, 1994. [Online]. Available: <http://science.sciencemag.org/content/264/5161/917>
- [149] W. B. Mori, C. D. Decker, D. E. Hinkel, and T. Katsouleas, "Raman forward scattering of short-pulse high-intensity lasers," *Physical Review Letters*, vol. 72, pp. 1482–1485, Mar 1994. [Online]. Available: <https://link.aps.org/doi/10.1103/PhysRevLett.72.1482>
- [150] P. Sprangle, A. Ting, and C. M. Tang, "Analysis of radiation focusing and steering in the free-electron laser by use of a source-dependent expansion technique," *Physical Review A*, vol. 36, pp. 2773–2781, Sep 1987. [Online]. Available: <https://link.aps.org/doi/10.1103/PhysRevA.36.2773>

- [151] T. M. Antonsen and P. Mora, "Self-focusing and raman scattering of laser pulses in tenuous plasmas," *Physical Review Letters*, vol. 69, pp. 2204–2207, Oct 1992. [Online]. Available: <https://link.aps.org/doi/10.1103/PhysRevLett.69.2204>
- [152] E. Esarey, J. Krall, and P. Sprangle, "Envelope analysis of intense laser pulse self-modulation in plasmas," *Physical Review Letters*, vol. 72, pp. 2887–2890, May 1994. [Online]. Available: <https://link.aps.org/doi/10.1103/PhysRevLett.72.2887>
- [153] A. B. Borisov, A. V. Borovskiy, O. B. Shiryayev, V. V. Korobkin, A. M. Prokhorov, J. C. Solem, T. S. Luk, K. Boyer, and C. K. Rhodes, "Relativistic and charge-displacement self-channeling of intense ultrashort laser pulses in plasmas," *Physical Review A*, vol. 45, pp. 5830–5845, Apr 1992. [Online]. Available: <https://link.aps.org/doi/10.1103/PhysRevA.45.5830>
- [154] M. D. Feit, J. C. Garrison, and A. M. Rubenckick, "Channeling of intense laser beams in underdense plasmas," *Physical Review E*, vol. 56, pp. R2394–R2397, April 1997. [Online]. Available: <http://www.mfeit.net/physics/papers/pre5697.pdf>
- [155] M. Borghesi, A. J. MacKinnon, L. Barringer, R. Gaillard, L. A. Gizzi, C. Meyer, O. Willi, A. Pukhov, and J. Meyer-ter Vehn, "Relativistic channeling of a picosecond laser pulse in a near-critical preformed plasma," *Physical Review Letters*, vol. 78, pp. 879–882, Feb 1997. [Online]. Available: <https://link.aps.org/doi/10.1103/PhysRevLett.78.879>
- [156] N. Naseri, S. G. Bochkarev, and W. Rozmus, "Self-channelling of relativistic laser pulses in large-scale underdense plasmas," *Physics of Plasmas*, vol. 17, no. 3, p. 033107, 2010.
- [157] J. Peñano, J. P. Palastro, B. Hafizi, M. H. Helle, and G. P. DiComo, "Self-channeling of high-power laser pulses through strong atmospheric turbulence," *Physical Review A*, vol. 96, p. 013829, Jul 2017. [Online]. Available: <https://link.aps.org/doi/10.1103/PhysRevA.96.013829>
- [158] C. B. Schroeder, E. Esarey, C. Benedetti, and W. P. Leemans, "Control of focusing forces and emittances in plasma-based accelerators using near-hollow plasma channels," *Physics of Plasmas*, vol. 20, no. 8, p. 080701, 2013. [Online]. Available: <http://dx.doi.org/10.1063/1.4817799>
- [159] L. Yi, B. Shen, L. Ji, K. Lotov, A. Sosedkin, XiaomeiZhang, W. Wang, J. Xu, Y. Shi, L. Zhang, and Z. Xu, "Positron acceleration in a hollow plasma channel up to tev regime," *Scientific Reports*, vol. 4, p. 4171, 2014. [Online]. Available: <http://www.ncbi.nlm.nih.gov/pmc/articles/PMC3933876/>
- [160] A. Pukhov, O. Jansen, T. Tueckmantel, J. Thomas, and I. Y. Kostyukov, "Field-reversed bubble in deep plasma channels for high-quality electron acceleration," *Phys. Rev. Lett.*, vol. 113, p. 245003, Dec 2014. [Online]. Available: <https://link.aps.org/doi/10.1103/PhysRevLett.113.245003>
- [161] S. Gessner, E. Adli, J. M. Allen, W. An, C. I. Clarke, C. E. Clayton, S. Corde, J. P. Delahaye, J. Frederico, S. Z. Green, C. Hast, M. J. Hogan, C. Joshi, C. A. Lindstrom, N. Lipkowitz, M. Litos, W. Lu, K. A. Marsh, W. B. Mori, B. O'Shea, N. Vafaei-Najafabadi, D. Walz, V. Yakimenko, and G. Yocky, "Demonstration of a positron beam-driven hollow channel plasma wakefield accelerator," *Nature Communications*, vol. 7, pp. 11 785 EP –, 06 2016. [Online]. Available: <http://dx.doi.org/10.1038/ncomms11785>
- [162] J. Vieira and J. T. Mendonça, "Nonlinear laser driven donut wakefields for positron and electron acceleration," *Physical Review Letters*, vol. 112, p. 215001, May 2014. [Online]. Available: <https://link.aps.org/doi/10.1103/PhysRevLett.112.215001>
- [163] J. Vieira, R. M. G. M. Trines, E. P. Alves, R. A. Fonseca, J. T. Mendonça, R. Bingham, P. Norreys, and L. O. Silva, "High orbital angular momentum harmonic generation," *Physical Review Letters*, vol. 117, p. 265001, Dec 2016. [Online]. Available: <https://link.aps.org/doi/10.1103/PhysRevLett.117.265001>
- [164] J. T. Mendonça and J. Vieira, "High harmonic generation in underdense plasmas by intense laser pulses with orbital angular momentum," *Physics of Plasmas*, vol. 22, no. 12, p. 123106, 2015. [Online]. Available: <http://dx.doi.org/10.1063/1.4936824>
- [165] L. D. Amorim, J. Vieira, R. A. Fonseca, and L. O. Silva, "Positron plasma wakefield acceleration in a self-driven hollow channel," *AIP Conference Proceedings*, vol. 1777, no. 1, p. 070001, 2016. [Online]. Available: <http://aip.scitation.org/doi/abs/10.1063/1.4965644>
- [166] —, "Positron acceleration in non-linear plasma wakefields driven by tightly focused particle bunches," in *Proceeding of the 41st EPS Conference on Plasma Physics Berlin, Germany, 23-27 June 2014*, no. O5.224, 2014, <http://ocs.ciemat.es/EPS2014PAP/pdf/O5.224.pdf>.
- [167] D. A. Hammer and N. Rostoker, "Propagation of High Current Relativistic Electron Beams," *The Physics of Fluids*, vol. 13, no. 1831, 1970.

- [168] V. Marinca and N. Herisanu, *Nonlinear Dynamical Systems in Engineering: Some Approximate Approaches*, ser. SpringerLink : Bücher. Springer Berlin Heidelberg, 2012. [Online]. Available: <https://books.google.pt/books?id=CgxDd9P2Rc0C>
- [169] A. Caldwell, K. Lotov, A. Pukhov, and F. Simon, "Proton-driven plasma-wakefield acceleration," *Nat Phys*, vol. 5, no. 5, pp. 363–367, 05 2009. [Online]. Available: <http://dx.doi.org/10.1038/nphys1248>
- [170] A. Caldwell and K. V. Lotov, "Plasma wakefield acceleration with a modulated proton bunch," *Physics of Plasmas*, vol. 18, no. 10, p. 103101, 2011. [Online]. Available: <http://dx.doi.org/10.1063/1.3641973>
- [171] A. Pukhov, N. Kumar, T. Tückmantel, A. Upadhyay, K. Lotov, P. Muggli, V. Khudik, C. Siemon, and G. Shvets, "Phase velocity and particle injection in a self-modulated proton-driven plasma wakefield accelerator," *Phys. Rev. Lett.*, vol. 107, p. 145003, Sep 2011. [Online]. Available: <https://link.aps.org/doi/10.1103/PhysRevLett.107.145003>
- [172] K. V. Lotov, A. P. Sosedkin, A. V. Petrenko, L. D. Amorim, J. Vieira, R. A. Fonseca, L. O. Silva, E. Gschwendtner, and P. Muggli, "Electron trapping and acceleration by the plasma wakefield of a self-modulating proton beam," *Physics of Plasmas*, vol. 21, no. 12, p. 123116, 2014.
- [173] P. Muggli, N. C. Lopes, **L. D. Amorim**, J. Vieira, and S. K. L. O. Silva, "Injection of a LWFA Electron Bunch in a PWFA Driven by a Self-modulated Proton Bunch," in *Proceeding of the IPAC Conference Dresden, Germany, 15-20 June 2014*, no. TUPME048, 2014, <http://accelconf.web.cern.ch/accelconf/IPAC2014/papers/tupme048.pdf>.
- [174] Y. Fang, J. Vieira, L. D. Amorim, W. Mori, and P. Muggli, "The effect of plasma radius and profile on the development of self-modulation instability of electron bunches," *Physics of Plasmas*, vol. 21, no. 5, p. 056703, 2014. [Online]. Available: <http://dx.doi.org/10.1063/1.4872328>
- [175] J. Vieira, Y. Fang, W. B. Mori, L. O. Silva, and P. Muggli, "Transverse self-modulation of ultra-relativistic lepton beams in the plasma wakefield accelerator," *Physics of Plasmas*, vol. 19, no. 6, p. 063105, 2012.
- [176] J. Vieira, L. D. Amorim, Y. Fang, W. B. Mori, P. Muggli, and L. O. Silva, "Self-modulation instability of ultra-relativistic particle bunches with finite rise times," *Plasma Physics and Controlled Fusion*, vol. 56, no. 8, p. 084014, 2014. [Online]. Available: <http://stacks.iop.org/0741-3335/56/i=8/a=084014>
- [177] P. Muggli, O. Reimann, J. Vieira, N. Lopes, L. D. Amorim, L. Silva, S. Gessner, M. J. Hogan, S. Li, M. Litos, N. Vafaei-Najafabadi, C. Joshi, W. Mori, K. Marsh, E. Adli, V. K. B. Olsen, and Y. Fang, "Self-modulation of ultra-relativistic slac electron and positron bunches," in *2014 IEEE 41st International Conference on Plasma Sciences (ICOPS) held with 2014 IEEE International Conference on High-Power Particle Beams (BEAMS)*, May 2014, pp. 1–1.
- [178] P. Muggli, O. Reimann, **L.D. Amorim**, N. Lopes, J. Vieira, S. Gessner, M. Hogan, S. Li, M. Litos, K. Marsh, W. Mori, C. Joshi, N. Vafaei-Najafabadi, E. Adli, and V. B. Olsen, "Electron Bunch Self-modulation in a Long Plasma at SLAC FACET," in *Proceeding of the IPAC Conference Dresden, Germany, 15-20 June 2014*, no. TUPME050, 2014, <http://accelconf.web.cern.ch/accelconf/IPAC2014/papers/tupme050.pdf>.
- [179] L. D. Amorim, J. Vieira, L. O. Silva, and P. Muggli, "Numerical Modelling of the E-209 Self-modulation Experiment at SLAC - FACET," in *Proceeding of the IPAC Conference Dresden, Germany, 15-20 June 2014*, no. TUPME076, 2014, <http://accelconf.web.cern.ch/accelconf/IPAC2014/papers/tupme076.pdf>.
- [180] P. Muggli, O. Reimann, L. Amorim, L. S. N.C. Lopes, J. Vieira, J. Allen, S. Gessner, M. Hogan, S. Green, M. Litos, B. O'Shea, V. Yakimenko, G. Andonian, C. Joshi, K. Marsh, W. B. Mori, N. Vafaei-Najafabadi, O. Williams, E. Adli, C. Lindstrom, and V. Olsen, "Measuring the self-modulation instability of electron and positron bunches in plasmas," in *Proceedings of the 6th IPAC Conference Richmond, VA - USA, June 2015*, no. WEPWA008, 2014, <http://accelconf.web.cern.ch/accelconf/IPAC2015/papers/WEPWA008.pdf>.
- [181] E. Adli, V. B. Olsen, C. Lindstrom, P. Muggli, O. Reimann, J. Vieira, L. Amorim, C. Clarke, S. Gessner, S. Green, M. Hogan, M. Litos, B. O'Shea, V. Yakimenko, C. Clayton, K. Marsh, W. Mori, C. Joshi, N. Vafaei-Najafabadi, and O. Williams, "Progress of plasma wakefield self-modulation experiments at {FACET}," *Nuclear Instruments and Methods in Physics Research Section A: Accelerators, Spectrometers, Detectors and Associated Equipment*, vol. 829, pp. 334 – 338, 2016, 2nd European Advanced Accelerator Concepts Workshop - {EAAC} 2015. [Online]. Available: <http://www.sciencedirect.com/science/article/pii/S0168900216002515>
- [182] P. Muggli, "Coherent transition radiation interferometric diagnostic for charged particle bunch self-modulation," *AIP Conference Proceedings*, vol. 1777, no. 1, p. 070008, 2016.
- [183] Y. Makina and T. Hitoshi, "The next ten years of x-ray science," *Nature Photon*, vol. 11, no. 1, pp. 12–14, 01 2017.

***"I find I'm so excited, I can barely sit still or hold a thought in my head. I think it is the excitement only a free man can feel, a free man at the start of a long journey whose conclusion is uncertain."***

Stephen King

***"Recomeça...  
Sempre a sonhar e vendo  
O logro da aventura."***

Miguel Torga